ERROR CORRECTION OF THE NORMALIZED DIFFERENCE VEGETATION INDEX AND BRIGHTNESS TEMPERATURE CALCULATED FROM THE AVHRR OBSERVATIONS

By

MOHAMMED ZAHIDUR RAHMAN

A dissertation submitted for the Graduate Faculty in Engineering in partial fulfillment of the requirements for the degree of Doctor of philosophy. The City University of New York

2008

UMI Number: 3296936

UMI Microform 3296936

ProQuest Information and Learning Company
300 North Zeeb Road
P.O. Box 1346
Ann Arbor, MI 48106-1346

This manuscript has been read and accepted for the Graduate Faculty in Engineering in satisfaction of the dissertation requirement for the degree of Doctor of philosophy.

Date

Chair of Examining Committee
Dr. Leonid Roytman

Date

Executive Officer
Dr. Mumtaz Kassir

Dr. Reza M. Khanbilvardi

Dr. Hoang Joon Kim

Dr. Mohamad M. Zahran

Dr. Felix Kogan

Supervision Committee

THE CITY UNIVERSITY OF NEW YORK

ABSTRACT

ERROR CORRECTION OF THE NORMALIZED DIFFERENCE VEGETATION INDEX AND BRIGHTNESS TEMPERATURE CALCULATED FROM THE AVHRR OBSERVATIONS

by

Mohammed Zahidur Rahman

Advisor: Professor Leonid Roytman

This thesis investigates Normalized Difference Vegetation Index (NDVI) and Brightness Temperature (BT) stability in the NOAA/NESDIS Global Vegetation Index (GVI) data during 1982-2003. This data was collected from five NOAA series satellites. We have proposed to apply Empirical distribution function (EDF) to improve the stability of the NDVI and BT data derived from the AVHRR sensor on NOAA polar orbiting satellite. The instability of data results from orbit degradation as well as the circuit drifts over the life or a satellite. Degradation of NDVI and BT over time and shifts of NDVI and BT between the satellites was estimated China data set, for it includes a wide variety or different ecosystems represented globally. It was found that data for the years 1988, 1992, 1993, 1994, 1995 and 2000 are not stable enough compared to other years because of satellite orbit drift, AVHRR sensor degradation, and also Mt Pinatubo volcanic eruption in 1992. We assume data from NOAA-7(1982, 1983), NOAA-9 (1985, 1986), NOAA-11(1989, 1990), NOAA-14(1996, 1997), and NOAA-16 (2001, 2002) to be standard because theses satellite's equator crossing time falls between 1330 and 1500. Data from this particular period of the day maximized the value of coefficients. The crux

of the proposed correction procedure consists of dividing standard year's data sets into two subsets. The subset 1(standard data correction sets) is used for correcting unstable years and then corrected data for this years compared with the standard data in the subset 2 (standard data validation sets). In this dissertation, we apply EDF to correct this deficiency of data for the affected years. We normalize or correct data by the method of empirical distribution functions compared with the standard. Using these normalized values, we estimate new NDVI and BT time series which provides NDVI and BT data for these years that match in subset 2 that is used for data validation.

ACKNOWLEDGEMENTS

First of all, I would like to express my gratitude to my advisor, Dr. Leonid Roytman, for his support, patience, and encouragement throughout my graduate studies. Many opportunities he gave me to practice have stimulated many of my interests and enable me to gain more experiences in my research field.

I am especially grateful to Dr. Felix Kogan for his kind and all-aspect help. His unreserved kindness has made the past years an ever-good memory in my life. His supervision and continuous supports laid a smooth way for my studies and research work.

Special thanks also go to Dr. Reza Khanbilvardi. While serving my dissertation committee, he offered many constructive comments and suggestions. His comments and suggestions to my dissertation are valuable.

I wish to express my sincere appreciation to my friend Dr. Mahbub Rabbani. Our friendship has led to many interesting and good-spirited discussions relating to this research.

Finally, I want to express my gratitude to my wife Dr. Rosy Rahman, for her emotional encouragement and support, and to my parents for their dedication and so many years of support during my studies.

Contents

LIST OF FIGURES

LIST OF TABLES

CHAPTER 1

INTROCUCTION

1.1 Research Motivations and Problem Statement

For almost two decades, the Advanced Very High Resolution Radiometer (AVHRR) on NOAA polar-orbiting satellites have observed radiances, which were collected, sampled, and stored for the entire world. These data were intensively used by the global community for studying and monitoring land surface, atmosphere, and recently for analyzing climate and environmental changes [37, 40]. AVHRR data, though informative, can not be directly used in climate change studies because of the orbit drift in the NOAA satellites (particularly, NOAA-9, -11, and -14) over these satellites' life time [23, 50]. **P**rice 1991 attributed this drift to the selection of a satellite orbit designed to avoid direct sunshine on the instruments. This orbital drift leads to the measurements of Normalized Difference Vegetation Index (NDVI) and Brightness Temperature (BT) are being taken at different local times during the satellites' life time, thereby introducing a temporal inconsistency in the NDVI and BT data. Consequently, a declining trend results in the NDVI and BT data calculated by some satellites. It was found that data for the years 1988, 1992, 1993, 1994, 1995 (first eight weeks), and 2000 are not stable enough compared to other years because of satellite orbit drift, AVHRR sensor degradation and also Mt Pinatubo volcanic eruption in 1992. For our research the data for NOAA-7(1982, 1983), NOAA-9 (1985, 1986), NOAA-11(1989, 1990), NOAA-14(1996, 1997), and NOAA-16 (2001, 2002) are assumed to be standard due to the fact, that equator crossing time of satellite between 1330 and 1500, which maximized the value of coefficients. For the purpose of this study this years are called standard. The crux of the

proposed correction procedure consists of dividing standard year's data sets into two subsets. The subset 1 (1982, 1985, 1989, 1996, 2001) called standard data correction sets is used for correcting unstable years and then corrected or normalized data for this years compared with the standard data in the subset 2 (1983, 1986, 1990, 1997, 2002). The subset 2 also called standard data validation sets that are used for data validation.

This research investigates NDVI and BT stability in the NOAA/NESDIS Global Vegetation Index (GVI) data for the period 1982-2003 [32, 34]. AVHRR weekly data for the five NOAA afternoon satellites NOAA-7, NOAA-9, NOAA-11, NOAA-14, and NOAA-16 are used for the China dataset, for it includes a wide variety or different ecosystems represented globally. These observations were made only under clear skies and thus some regions and seasons may be poorly sampled due to the contamination of clouds. To avoid misinterpretation of signals due to orbit drift and satellite changes, correction must be applied to remove or, at least, reduce these effects from the AVHRR data so one can use a long-term time-series for study. This research introduces a scientific methodology that can be easily implementable to generate the desired long-term time-series. The main goal of this dissertation is to correct the NDVI and BT data calculated from the AVHRR observations for the years 1988, 1992, 1993, 1994, 1995, and 2000 by the method of empirical distribution functions (EDF) compared to the standard data. We can use the same methodology globally to create vegetation index to improve the climatology. The corrected datasets can be used as proxy to study climate change, epidemic analysis, and drought prediction etc.

1.2 Organization of This Dissertation

This dissertation is organized into eight chapters. Chapter one introduces the research motivations and problem statement. Chapter two describes the background related to the research. Chapter three briefly outlines the AVHRR data and processing. Chapter four describes landscape in the study area – China and part of Mongolia, North Korea, Bhutan, Nepal, and India. Chapter five presents several methods for correction of the satellite data and describes the theoretical principles behind them. Chapter six demonstrates experimental results involved in this research to show how the statistical technique developed here. Chapter seven describes validation for other countries such as Mongolia, North Korea, Bhutan, Nepal, and part of India. Chapter eight concludes the dissertation research and provides direction for further research.

CHAPTER 2

BACKGROUND

In this chapter we present a brief overview of theoretical background and of results related to the topics of our research.

2.1 Normalized Difference Vegetation Index (NDVI)

To determine the density of green on a patch of land, researchers must observe the distinct colors (wavelengths) of visible and near-infrared sunlight reflected by the plants. As can be seen through a prism, many different wavelengths make up the spectrum of sunlight. When sunlight strikes objects, certain wavelengths of this spectrum are absorbed and other wavelengths are reflected. The pigment in plant leaves, chlorophyll, strongly absorbs visible light (from 0.4 to 0.7 μm) for use in photosynthesis. The cell structure of the leaves, on the other hand, strongly reflects near-infrared light (from 0.7 to 1.1 μm).

The NOAA AHVRR instrument has five detectors, two of which are sensitive to the wavelengths of light ranging from 0.58–0.68 and 0.725–1.0 micrometers. With AHVRR's detectors, researchers can measure the intensity of light coming off the Earth in visible and near-infrared wavelengths and quantify the photosynthetic capacity of the vegetation in a given pixel (an AVHRR pixel is 4 square km) of land surface.

Nearly all satellite Vegetation Indices employ this difference formula to quantify the density of plant growth on the Earth-near-infrared radiation minus visible radiation divided by near-infrared radiation plus visible radiation. The reflectance measured from

Channel 1 (visible: 0.58 - 0.68 microns) and Channel 2 (near infrared: 0.725 - 1.0 microns) are used to calculate the index:

$$NDVI = (Ch2-Ch1)/ (Ch2+Ch1)$$

Figure 2.1 below shows the spectral reflectance response characteristic for green vegetation, soil and water compared with the bandwidth of the AVHRR Channels 1 and 2 used to create the index.

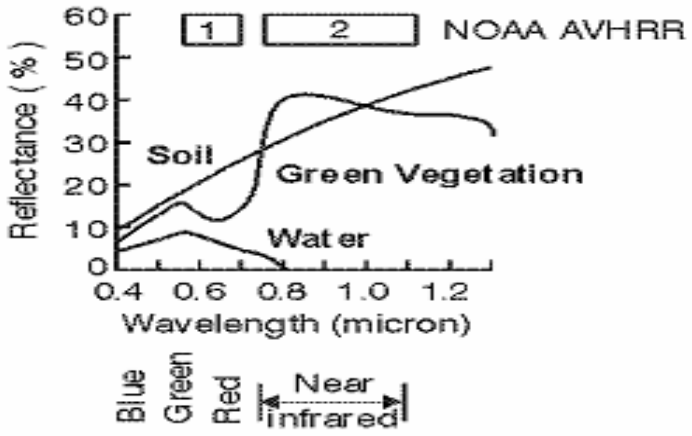

Figure 2.1 Spectral reflectance characteristics of common earth surface materials.

The differential reflectance in these bands provides a means of monitoring density and vigor of green vegetation growth using the spectral reflectivity of solar radiation. Green leaves commonly have larger reflectances in the near infrared than in the visible range. As the leaves come under water stress, become diseased or die back, they become more yellow and reflect significantly less in the near infrared range. Clouds, water, and snow have larger reflectances in the visible than in the near infrared while the difference is almost zero for rock and bare soil. Vegetation NDVI typically ranges from 0.1 up to 0.6, with higher values associated with greater density and greenness of the plant canopy.

Surrounding soil and rock values are close to zero while the differential for water bodies such as rivers and dams have the opposite trend to vegetation and the index is negative. A range of errors such as scattering by dust and aerosols, Rayleigh scattering, subpixel-sized clouds, plus large solar zenith angles and large scan angles all act to increase Ch1 with respect to Ch2 and reduce the computed NDVI.

For example, NDVI is calculated from the visible and near-infrared light reflected by vegetation. Healthy vegetation (left) in Figure 2.2 absorbs most of the visible light that hits it, and reflects a large portion of the near-infrared light. Unhealthy or sparse vegetation (right) reflects more visible light and less near-infrared light.

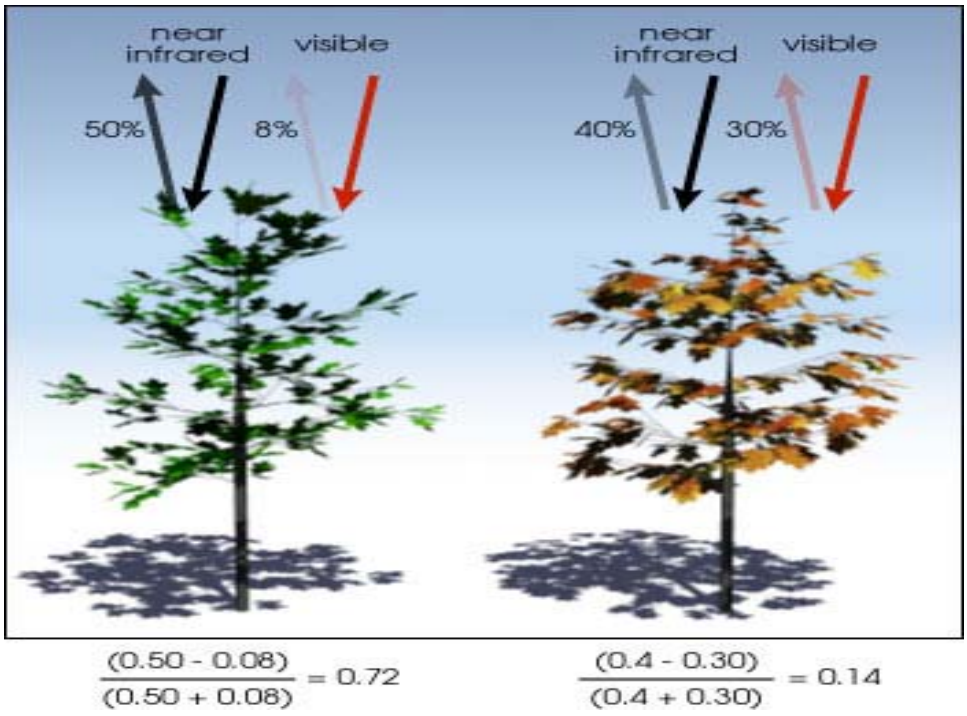

Figure 2.2 NDVI is calculated from the visible and near-infrared light reflected by vegetation [Robert Simmon, 46]

The numbers on the figure above are representative of actual values, but real vegetation is much more varied (Robert Simmon, [46]).

2.2 Brightness Temperature (BT)

A material's surface emissivity is a measure of the energy emitted when a surface is directly viewed. Surface emissivity is generally measured indirectly by assuming that it is equal to one minus reflectivity. Setting emissivity to one is equivalent to assuming that the target is a blackbody. Therefore the brightness temperature is defined as the temperature a blackbody would be in order to produce the radiance perceived by the sensor. Brightness Temperature is a descriptive measure of radiation in terms of the temperature of a hypothetical blackbody emitting an identical amount of radiation at the same wavelength. The brightness temperature is obtained by applying the inverse of the Planck function to the measured radiation. Depending on the nature of the source of radiation and any subsequent absorption, the brightness temperature may be independent of, or highly dependent on, the wavelength of the radiation.

Computation of BT

The aim is to produce a calibrated AVHRR image, i.e. converted into brightness temperature and reflectance from the raw AVHRR data. This is the computation of "raw" data transfer functions (digital counts of the radiometer measurement) for radiance. The computation requires real time knowledge of at least 2 measurement points (view of a hot target assumed to be the black body, and space view serving as a cold target). The temperature of both targets is obtained through onboard thermistor measurements for the hot target and a fixed measurement of 2 Kelvin for the space target. The assumption of linearity for digital count conversion into radiance is only checked

rarely. Hence, manufacturers offer nonlinearity correction techniques that are applied to the calibration algorithms. The following must be known:

- the radiometer spectral response, i.e. its wavelength sensitivity (for computing the theoretical radiance of the hot target according to its temperature by integrating it throughout the spectrum). This spectral response curve can be replaced by an approximation that models the filter by a central wave number and 2 correction coefficients,
- the polynomials for converting thermistor counts into temperature, for computing the temperature measured by each thermistor on the hot target. Based on **C**racknell, (1997, [53]) we can write the following equations (2.2.1- 2.2.8)

  $T = Sa_j Xj$ (where X is the thermostat count) (2.2.1)

- Planck's formula, enabling the spectral radiance at a wave number to be calculated as a function of the black body temperature,

  $B(n, T) = c_1 n^3 / (\exp(c_2 n / T)) - 1$ (2.2.2)

  where n is the central wave number (in cm^{-1}) and T the target's temperature (in Kelvin)*, c_1 equals 1.1910659 10^{-5} $mW.m^{-2}.sr^{-1}.cm^4$, c_2 equals 1.438833 K.cm .

For a given filter, the integrated radiance for the entire filter interval must be calculated

$R(T) = {}_S B(n,T) F(n) dn / {}_S F(n) dn$ (between filter terminals n_1 and n_2) (2.2.3)

The warm target temperature is averaged by

$$T = Sb_iT_i \quad (2.2.4)$$

Assuming conversion linearity, we obtain the following for each view X count

$$Rlin = GX + I \quad (2.2.5)$$

If R_c is the target radiance, R_{sp} the space radiance, X_c the average of the hot view counts and X_{sp} the average of the space counts, one obtains

$$G = (R_c - R_{sp}) / (X_c - X_{sp}) \quad (2.2.6)$$

$$I = R_{sp} - GX_{sp} \quad (2.2.7)$$

where R_c is the theoretical hot target radiance (result of the temperature conversion of the target given by the thermistors), R_{sp} is the radiance of space. It equals zero or a non-linearity correction term, X_t and X_{sp} are respectively the average digital counts of the radiometric views of the hot target and space.

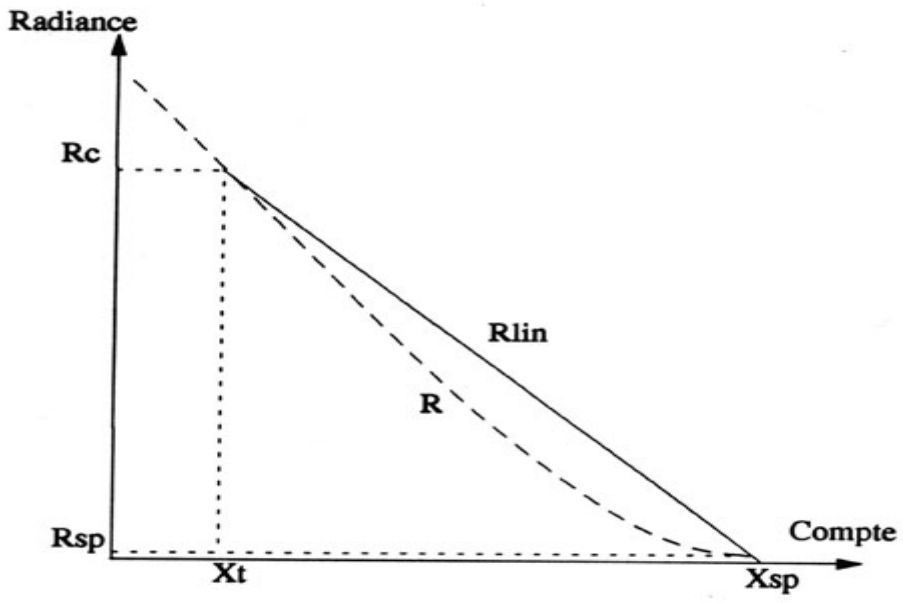

Figure 2.3 Compute (count) vs. radiance [45, 53]

The nonlinearity correction is applied as follows to the AVHRR: NOAA/NESDIS supply users with correction coefficients of the form $R = A\ Rlin + B\ Rlin^2 + C$, together with a space radiance correction term R_{sp}

The coefficients supplied to the user are those enabling the conversion of the X count into radiance (quadratic polynomial). This technique has only been used by NOAA/NESDIS since NOAA-13. The CMS has used this technique since NOAA-12 and NOAA-14.

Calibration cycle:

It has been seen that the average values for different parameters must be calculated. The calibration cycle is the number of radiometer scan lines required for data accumulation. This number depends on the instrument. For the AVHRR, the pattern is as follows [53]

HRPT message	Parameter sample
n	R_{ef}
n + 1	Thermistor 1 C_n
n +2	Thermistor 2 C_n
n +3	Thermistor 3 C_n
n +4	Thermistor 4 C_n
n +5	R_{ef}

The target views C_n are provided for channels 3, 4 and 5 in each message and R_{ef} refers to the reference value.

Interpolation between calibration cycles:

To prevent "hops" between calibration cycles, a linearization is generally carried out between two consecutive cycles to smooth out any variations.

Elimination of noisy digital counts:

The calibration uses average values on the digital counts coming from the raw data flow. A two-pass filter technique is used to ensure that the average value is calculated correctly:

- Coarse filter, counts outside the min. and max. limits are eliminated,
- Fine filter, after an initial elimination, an average value and standard deviation can be calculated. Both values are used again to determine two min. and max. Limits (min. = average - 2 standard deviations, max. = average + 2 standard deviations) serving in the second elimination. The final value of any average computed from the remaining population will be used to calculate the coefficients.

Conversion of radiance into brightness temperature:

The brightness temperature is the temperature of the black body emitting the radiance observed. Hence, this means inverting Planck's formula. The wave number formula is

$$T(R) = c_2 n / \text{Log}\,(1 + (c_1 n^3 / R) \qquad (2.2.8)$$

Applications of Brightness Temperature:

Brightness temperature has been used to observe volcanic ash clouds, detect ice leads in the Arctic, and to identify anthropogenic and natural fires, to name a few examples. The ASTER brightness temperature will be used as an alternate to radiance in the temperature/emissivity separation algorithm to report relative cloud-top temperature because there will be no routinely available applicable atmospheric correction to enable a calculation of exact cloud-top temperature. ASTER brightness temperatures can be acquired during the day or night and over all surface types (land, water, cloud, etc.).

2.3 The AVHRR Instrument

The AVHRR instrument is the primary focus of this educational module on global vegetation. The instrument is not considered one of the more sophisticated remote sensing scanners flying today but the fact that it has been providing consistent global coverage of the Earth since 1978 makes it a valuable tool for consistent monitoring of global changes in vegetation.

2.3.1 Scientific Objective

The AVHRR was designed to measure cloud cover, day and nighttime sea surface temperature, cloud formations, and surface reflectance properties (from which vegetation indices were later derived). The objective was to fly this instrument in order to obtain contiguous global coverage on a daily basis.

2.3.2 Instrument Description

The Advanced Very High Resolution Radiometer (AVHRR) is actually not that advanced by today's standards. Compared to many other environmental remote sensing sensors it does not provide high spatial resolution data. Compared to other satellites designed to measure meteorological phenomena, however, the spatial resolution of the AVHRR can be considered high. The AVHRR instrument has a reasonably high radiometric resolution. This means that the instrument can measure reflected and emitted energy with a higher precision than most other sensors. Energy recorded by the AVHRR instrument is given a value between 0 and 1023 as compared to most other sensors which record values

between 0 and 255. This difference allows the AVHRR instrument to record finer differences in reflectance and emission.The AVHRR is a scanning radiometer which uses five detectors that collect different bands of radiation wavelengths. The AVHRR scanner uses a mirror which allows it to collect data 55 degrees east and west of nadir (vertical). This gives a swath width of approximately 2600 kilometers. The data capture rate is such that one scan line (one swing of the mirror) is made up of 2048 pixels. The scanner has an instantaneous field of view (IFOV) of approximately 1.4 milliradians which produces a resolution of about 1.1 kilometers at nadir and expands to approximately 17 kilometers at its extreme angle of 55 degrees.

The instrument records data for five wavelengths as listed in Table 2.1. The first channel is in the orange and red portion of the spectrum and the second channel in the near infrared portion. These two channels are used to observe vegetation, clouds, lakes, shorelines, snow, and ice. The third channel is in the mid-infrared portion, however, it is located so that it detects a mixture of reflected and emitted energy. This channel is used extensively for detecting fires and other very hot objects. The last two channels are located in the far infrared region of the spectrum and are sensitive primarily to emitted thermal radiation. These two channels are used primarily to detect the surface temperature of sea and land. These last three channels are often used to identify clouds and calibrate the first two channels. The three IR channels are calibrated in-flight using a view of a stable blackbody and space as a reference. No in-flight visible channel calibration is performed.

Table 2.1: Wavelength Sensitivity for Each Channel of the AVHRR Sensors.

Channel #	**TIROS-N**	**NOAA-6,-8,-10**	**NOAA-7, -9,-11, -12,-14**	**NOAA-13**
1	0.55-0.90µm	0.58-0.68µm	0.58-0.68µm	0.58-0.68µm
2	0.725-1.10µm	0.725-1.10µm	0.725-1.10µm	0.725-1.0µm
3	3.55-3.93µm	3.55-3.93µm	3.55-3.93µm	3.55-3.93µm
4	10.5-11.5µm	10.5-11.5µm	10.5-11.3µm	10.5-11.3µm
5	Channel 4 repeated	Channel 4 repeated	11.5-12.5µm	11.4-12.4µm

2.3.3 Future AVHRR Instruments

2.3.3.1 Introduction

A new series of AVHRR instruments, known as AVHRR/3, first carried on NOAA-15 launched in May 1998. The AVHRR/3 scans the Earth surface in six spectral bands in the range of 0.58 - 12.5 microns (Table 2.3.3.1). It provides day and night imaging of land, water and clouds, measures sea surface temperature, ice, snow and vegetation cover. The AVHRR/3 is a six-channel imaging radiometer that detects energy in the visible and infrared (IR) portions of the electromagnetic spectrum [47]. The instrument measures reflected solar (visible and near-IR) energy and radiated thermal energy from land, sea, clouds, and the intervening atmosphere. The instrument provides spectral and gain improvements to the solar visible channels that provide low light energy detection. Channel 3A, at 1.6 microns, provides snow, ice, and cloud discrimination. Channel 3A will be time-shared with the 3.7-micron channel, designated 3B, to provide five channels of continuous data. An external sun shield and an internal baffle have been added to reduce sunlight impingement into the instrument's optical cavity and detectors. A summary of the AVHRR/3 Channel characteristics are given in Tables 2.3

Table 2. 3. AVHRR/3 Channel Characteristics

Resolution at Nadir	Wavelength (um)	Typical Use
1.09 km	0.58-0.68	Day time cloud and surface mapping
1.09 km	0.725-1.00	Land-water boundaries
1.09 km	1.58-1.64	Snow and ice detection
1.09 km	3.55-3.93	Night cloud mapping, sea surface temperature
1.09 km	10.30-11.30	Night cloud mapping, sea surface temperature

2.3.3.2 Instrument Operations

The AVHRR/3 is an imaging system in which a small field of view (1.3 milliradians by 1.3 milliradians) is scanned across the earth from one horizon to the other by continuous 360 degree rotation of a flat scanning mirror. The orientation of the scan lines is perpendicular to the spacecraft orbit track and the speed of rotation of the scan mirror is selected so that adjacent scan lines are contiguous at the sub satellite (nadir) position. Complete strip maps of the earth from pole to pole are thus obtained as the spacecraft travels in orbit at an altitude of approximately 833 km (450 n. miles). The analog data output from the sensors is digitized on board the satellite at a rate of 39,936 samples per second per channel. Each sample step corresponds to an angle of scanner rotation of 0.95

milliradians. At this sampling rate, there are 1.362 samples per IFOV. A total of 2048 samples will be obtained per channel per Earth scan, which will span an angle of ±55.4 degrees from the nadir (subpoint view). All six spectral channels of the AVHRR/3 are registered so that they all measure energy from the same spot on the earth at the same time. All six channels are also calibrated so that the signal amplitude in each channel is a measure of the scene radiance. Although the AVHRR/3 has six channels, only five are transmitted to the ground at any one time. The radiometers are designed to operate within specification for a period of three years in orbit.

2.4 NOAA Series of Satellites

This section provides a history and description of the various properties of the satellites that carry the AVHRR instrument. All of the satellites are part of the NOAA Polar orbiting Operational Environmental Satellite (POES) series. NASA funded the development and launch of the first satellite but subsequent satellites were procured and launched by NASA using NOAA funds.

2.4.1 History

All of the AVHRR sensors have been housed on the TIROS-N and NOAA-6 through NOAA-15 polar orbiting satellites. Starting with NOAA-8 this series of satellites is also referred to as the Advanced TIROS-N (ATN) series. To date, eleven such satellites have been launched. The first one, launched in 1978, was called the Television and Infrared Observation Satellite (TIROS-N). This was followed by the National Oceanic and

Atmospheric Administration's (NOAA) NOAA-A satellite which was renamed NOAA-6 after its launch. Table 2.4 shows the dates and names of the various satellites which carry the AVHRR instrument.

Table 2. 4: NOAA POES Launch Dates

Name after launch	**Name before launch**	**Date of launch**
TIROS-N	TIROS-N	October, 1978
NOAA-6	NOAA-A	June, 1979
NOAA-7	NOAA-C	June, 1981
NOAA-8	NOAA-E	March, 1983
NOAA-9	NOAA-F	December, 1984
NOAA-10	NOAA-G	September, 1986
NOAA-11	NOAA-H	September, 1988
NOAA-12	NOAA-D	May, 1991
NOAA-13	NOAA-I	August, 1993
NOAA-14	NOAA-J	December, 1994
NOAA-15	NOAA-k	February, 1998
NOAA-16	NOAA-L	September, 2000
NOAA-17	NOAA-M	June, 2004
NOAA-18	NOAA-N	May, 2005

2.4.2 Instrument Packages on the Polar Orbiting Observational Satellite Series

The TIROS-N and NOAA satellites 6 through 15 all carried at least two instrument packages. The first was the AVHRR which will be discussed in detail. The other package was the TIROS Operational Vertical Sounder (TOVS). TOVS is comprised of three sensors: Microwave Sounding Unit (MSU), Stratospheric Sounding Unit (SSU), and the High Resolution Infrared Radiation Sounder/2 (HIRS/2). TOVS was designed so that the data from the HIRS/2, SSU and MSU instruments could be combined to compute: 1) atmospheric temperature profiles from the surface to 10 millibars (mb), 2) water vapor content at three levels of the atmosphere, and 3) total ozone content. Another sensor, a Solar Backscattered Ultraviolet system (SBUV/2) for ozone measurement, was added starting with the NOAA-9 spacecraft. Incrementally added to the payload were a Search and Rescue Demonstration System (SAR), and an Earth Radiation Budget Experiment (ERBE) flown on NOAA-9 and NOAA-10 only.

2.4.3 Satellite Characteristics

The TIROS-N series satellites (Figure 2.3) weigh about 1700 kilograms (about 3.7 U.S. tons). The dimensions of the satellites are 1.8 meters X 4.18 meters. The sensors are designed to last for two years although they typically last longer. Also onboard are solar panels which are designed to provide 1500 watts of power to the sensor and navigation systems.

Figure 2.4 Images of a NOAA POES (NOAA/NESDIS, [47])

The spacecraft structure consists of four components: 1) the Reaction System Support Structure (RSS); 2) the Equipment Support Module (ESM); 3) the Instrument Mounting Platform (IMP); and 4) the Solar Array (SA). Instruments are located on both the IMP and the ESM. All the instruments listed above face the Earth when the satellite is in mission orientation.

Onboard the satellites are systems which can transmit the data and record the data so it can be stored and then transmitted at a later time. The TIROS Information Processor (TIP) formats data available for transmission from the satellite. It also controls the data outputs from these sources and accepts command verification data.

The on-orbit Attitude Determination and Control Subsystem (ADACS) provides three axis pointing control for the satellite. The ADACS maintains system pointing by controlling torque in three mutually orthogonal wheels (a fourth skewed wheel is available in the event of failure of one of these three). The torque is determined by analysis of spacecraft orientation in space. Inputs to these computations are acquired from the Earth Sensor Assembly (ESA) for pitch and roll, and an inertial reference with sun updates for yaw.

The ADACS is required to control spacecraft attitude so that orientation of the three axes is maintained to within plus or minus 0.2 degrees of the local geographic reference. Information to permit computation of yaw, pitch, and roll to within 0.1 degrees by computer processing on the ground, after the fact, is also available.

CHAPTER 3

AVHRR DATA AND PROCESSING

3.1 Satellite Data

Satellite data were collected from the NOAA/NESDIS Global Vegetation Index (GVI) data set [32, 34] which is one of the most widely used satellite products worldwide. The GVI is produced by sampling and mapping the 4-km daily radiance in the VIS (Ch1, 0.58-0.68 μm), NIR (Ch2, 0.72-1.1 μm), and two thermal bands (Ch4, 10.3-11.3 μm and Ch5, 11.5-12.5 μm) in Figure 3.1 measured onboard NOAA polar-orbiting satellites, to a 16-km map. To minimize cloud effects, these maps, including the NDVI, solar zenith angle, and satellite scan angle, are composited over a 7- day period by saving those values that have the largest difference between VIS and NIR reflectance for each map cell. The weekly GVI data from January 1982 through January 1985 for NOAA-7, from April 1985 through September 1988 for NOAA-9, from October 1988 through August 1994 for NOAA-11, from March 1995 through December 2000 for NOAA-14, and from January 2001 through December 2003 for NOAA-16 were used here.

During 1985-2000, the performance of the channel 1 and 2 differed between NOAA-9, NOAA-11, and NOAA-14 satellites and most importantly, degraded over time for each satellite differently. Since there is no in-flight calibration of channel 1 and 2 of the AVHRR, the question arises as to the validity of the pre-launch calibration coefficients, both in the early days after launch and, perhaps more seriously, after the AVHRR has been in space for a long time. There is a clear evidence in several environmental products, such as the normalized difference vegetation index , global cloud morphology,

and earth radiation budget [53] , that are generated from channel -1 and channel-2 AVHRR data to indicate that the performance of the instrument these two channels has deteriorated after launch. The need to correct for this in-orbit degradation has been keenly felt recently since it is now being proposed to use the long-term records of AVHRR-derived environmental products in climate and global change studies [48, 49, 6, 2, 54, 55, 56, and 71] and the degradation of the instrument with time is clearly illustrated by the results shown in Figure 3.2. The average degradation rates were for NOAA-7 (1.36% and 4.3% per year), for NOAA-9 (5.9% and 3.5% per year), and NOAA-11 (1.2% and 2% per year) for channels 1 and 2, respectively [56].

Therefore, the standard data preparation procedure for the 7-day composite time series now includes a correction of Ch1 (VIS) and Ch2 (NIR) values following Rao and Chen [58]. The post-launch correction considerably improves the stability of NDVI over time, especially for NOAA-9, and almost eliminates the difference between the level of NDVI for the end of NOAA-9 and beginning of NOAA-11 satellite data [36].The thermal brands' measurements were converted to brightness temperature using look-up table, and a nonlinear correction was applied following Weinreb et al. [74].

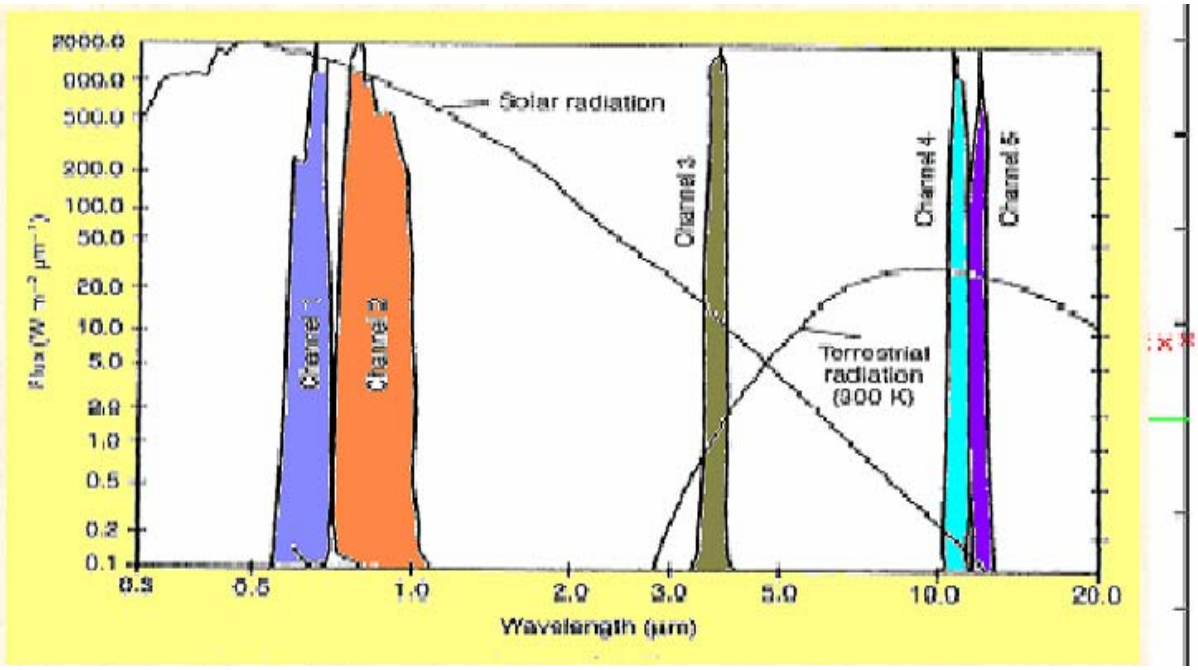

Figure 3.1 Normalized spectral response of AVHRR

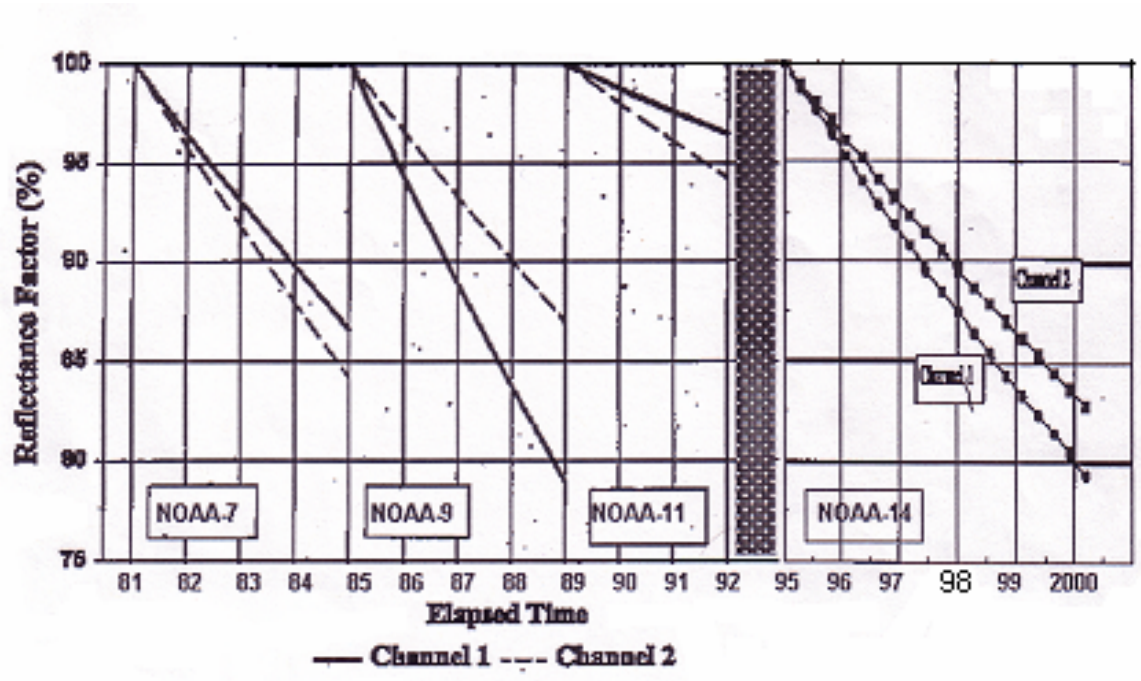

Figure 3.2 Degradation of AVHRR Channels 1 and 2 [56, 1994]

3.2 Composite Data Set

The Composite Data Set is similar to the daily data in structure and is derived from the Daily Data Set, however the process of compositing removes much of the cloud cover present in the Daily Data Set [25] is generated by comparing the NDVI values for each 4 km bin from 7 consecutive Daily Data Sets. Because data at the edge of a scan may contain distortion and bidirectional effect biases, only data within 42 deg of nadir are used in the composite. The pixel with the highest NDVI for the 7 days is chosen as the date for the inclusion in the composite, and all 12 data layers are updated with data from that date. This compositing process is effective for removing most of the clouds and atmospheric contaminants thus providing as close to a cloud free field in each of the data layers as is possible. However, in areas of persistent cloudiness, cloudy pixels will remain.

Compositing the seven day composites will often be necessary to provide sufficiently cloud free images for many parts of the world. There are four composites per month. The first composite of each month is for days 1 to 7, the second composite is for days 8 to 15 and the third composite is for days 16 to 23 and the fourth composite the remaining days. This convention was chosen so that these data could be used with many climatologies and meteorological data which are provided in monthly averages.

Some of the features described in the Daily Data Set are not present or are not as pronounced in the Composite Data Set. The contrast in the areas of orbital overlap is no longer present (because pixels outside 42 deg. are not used). In generating the 7-day composite, pixels flagged out of range or with NOAA QC flags (in the QC layer) are not

included. This helps, but does not totally eliminate, the selection of data with abnormally high NDVI's resulting from bad calibration. However, there are frequent cases of good channel 1 and 2 data where the thermal data are missing or incorrect due to lack of calibration coefficients. These areas of bad data should be noted in the QC comments.

The Composite Data Set is particularly useful for studies of temporal and interannual behavior of surface vegetation and for developing surface background characteristics for use in climate modeling. The most useful data layer is the Normalized Difference Vegetative Index (NDVI) which represents the green leaf biomass

The Composite data set contain the following parameters which is described in Table 3.2

- NDVI
- Clouds from AVHRR (CLAVR) flag
- Quality Check flag
- Scan Angle
- Solar Zenith Angle
- Relative Azimuth Angle
- Channel-1, and -2 Reflectances
- Channel-3, -4, and -5 Brightness Temperatures
- Day of Year

Table 3. 2 Composite data set parameters

Parameter/ Variable	Variable Definition	Unit of Measurement	Data Range
NDVI	Normalized Difference Vegetation Index of pixel.	NONE	min = -1 min = +1
CLAVR Flag	Cloudiness indicator from CLAVR algorithm.	NONE	min = 0 min = 30
QC Flag	Data Quality flag.	NONE	min = 0 min = 16
Scan Angle	Scan Angle of Sensor.	RADIANS	min = -1.0471976 max = +1.0471976
Solar Zenith Angle	Solar Zenith Angle of pixel.	RADIANS	min = 0 max = 1.396256
Relative Azimuth Angle	Relative Azimuth Angle of Sensor.	RADIANS	min = -1.0471976 max = +1.0471976
Ch1 Reflectance	Reflectance value for Channel 1 (0.58-0.68 µm).	PERCENT	min = 0 max = 100
Ch2 Reflectance	Reflectance value for Channel 2 (0.72-1.10 µm).	PERCENT	min = 0 max = 100
Ch3 Btemp	Brightness Temperature value for Channel 3 (3.55-3.95 µm).	KELVIN	min = 160 max = 340
Ch4 Btemp	Brightness Temperature value for Channel 4 (10.3-11.3 µm).	KELVIN	min = 160 max = 340
Ch5 Btemp	Brightness Temperature value for Channel 5 (11.5-12.5 µm).	KELVIN	min = 160 max = 340

Normalized Difference Vegetation Index:

The Normalized Difference Vegetation Index (NDVI), which is related to the proportion of photosynthetically absorbed radiation, is calculated from atmospherically corrected reflectances from the visible and near infrared AVHRR channels as:

$$(CH2 - CH1) / (CH2 + CH1)$$

Where CH1 is the reflectance in the visible wavelengths (0.58-0.68 um) and CH2 is the reflectance in the reflective infrared wavelengths (0.725-1.1 um). The principle behind this is that Channel 1 is in a part of the spectrum where chlorophyll causes considerable

absorption of incoming radiation, and the Channel 2 is in a spectral region where spongy mesophyll leaf structure leads to considerable reflectance [27, 69, and 70].

Clouds from AVHRR (CLAVR) Flags:

The Pathfinder data includes cloud flags produced by the NOAA Clouds from AVHRR (CLAVR) algorithm [63]. The CLAVR algorithm performs a series of threshold and uniformity tests on a 2 x 2 array of pixels. If 1-3 pixels in the array are flagged as cloudy, all four pixels are flagged as mixed. Otherwise, the array is flagged as clear or cloudy. Zero values mean no decision was made because of missing data.

A mapping of NOAA CLAVR values in the Pathfinder data to the NOAA values can be found in the Pathfinder Data Set User's Manual which is available from the archive. The numeric values were reorganized to simplify value lookups for users who are interested in simple discrimination between clear (values 22-30), mixed (values 12-21) and cloudy (values 1-11) pixels.

The CLAVR flags are calculated using top of atmosphere reflectances which are slightly different from the surface reflectances which are stored in the Daily and Composite Data Set layers.

Quality Control Flags (QC flag):

The QC flag is based on error or warning conditions that are identified during processing. These conditions are encoded in an additive fashion so that any specific condition or combination of conditions can be used and easily interpreted. For example, a QC flag

with a value of **5** indicates that both the "filled data gap" bit **4** and the "Channel 1, 2 processing non-standard" bit **1** were set [32]. It should be noted that these conditions do not always indicate invalid values. Some QC flags, such as a range check failure, do mean that data in at least one layer are incorrect, however, some error conditions are informational and do not necessarily mean the data are not usable.

Scan Angle:

Sensor scan angle is the angle between the sensor view vector and the downward pointing (to nadir) axis. Figure 3.3 shows the solar/satellite geometry. The sensor zenith angle, which is not stored as part of the data set, is the angle between the sensor view vector and the local vertical to the pixel. The sensor zenith angle is used in the calculation of the relative azimuth.

Scan angle is particularly important in that data with very large scan angles generally are greatly distorted and navigation of extremely off-nadir pixels may have large errors. In addition, bi-directional effects are more pronounced at extreme off-nadir pixels. In addition, at approximately 42 degrees of nadir, the pixel width is greater than 8 km. For these reasons, in producing the Daily Data Set pixels within 42 degrees of nadir are selected preferentially to pixels outside 42 degrees and in the composite data set pixels outside 42 deg. are excluded.

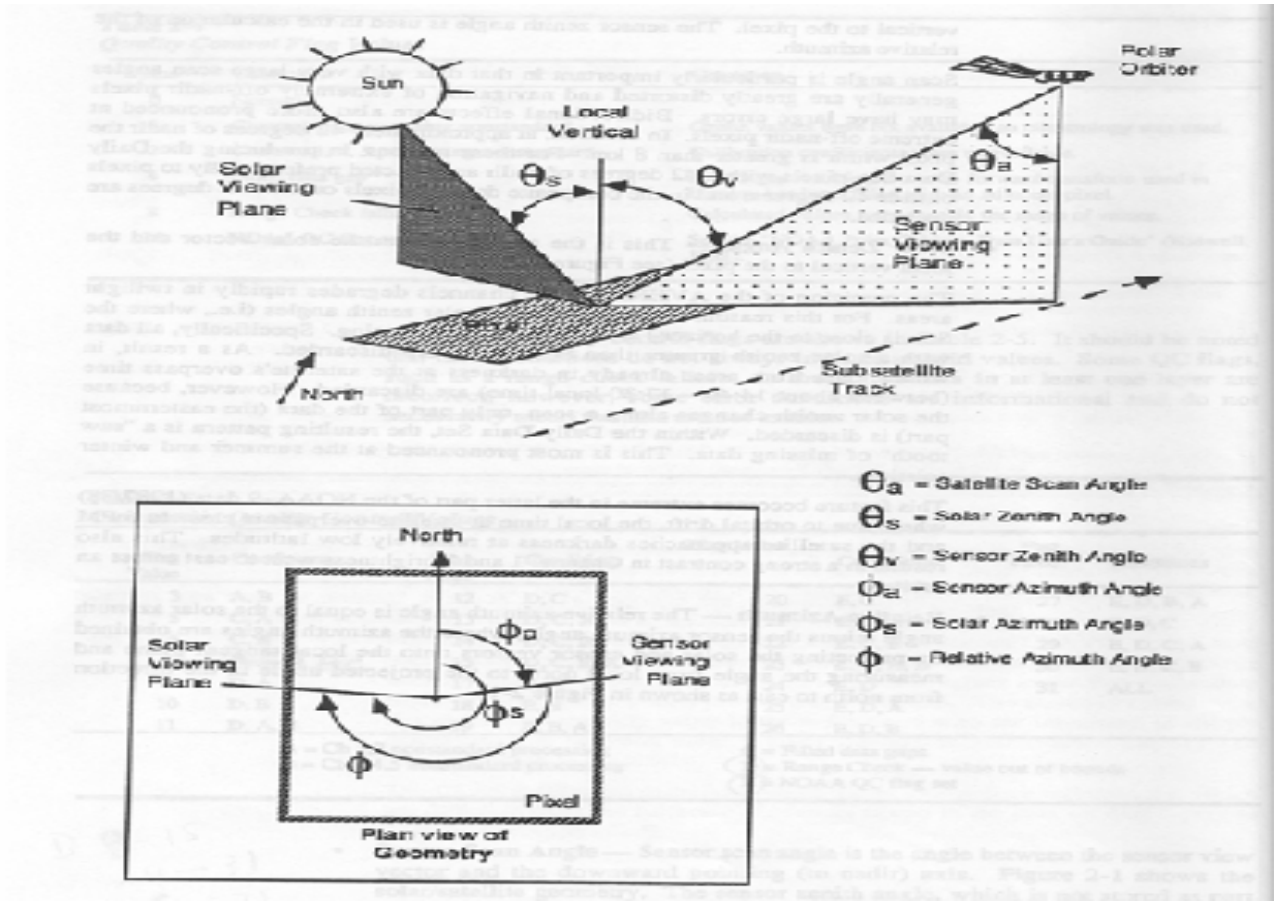

Figure 3.3 Solar and scan Geometry [77, 1994]

Solar Zenith Angle**:**

The angle between the solar vector and the local vertical to the pixel (Figure 3.3). The precision of the AVHRR visible channels degrades rapidly in twilight areas. For this reason, all data with high solar zenith angles (i.e., where the sun is close to the horizon) are discarded in processing. Specifically, all data with a solar zenith greater than 80 deg. are discarded. As a result, in winter time, areas already in darkness at the satellite's overpass time (between about 14:40 - 17:30 local time) data are discarded. However, because the solar zenith changes along a scan only part of the data (the easternmost part)

is discarded. Within the Daily Data Set, the resulting pattern is a "saw tooth" of missing data. This is most pronounced at the summer and winter solstice.

This feature becomes extreme in the latter part of the NOAA-9 data (1987/88) when, due to orbital drift, the local time at satellite overpass is close to 6 PM and the satellite approaches darkness at relatively low latitudes. This also results in a strong contrast in channel 1 and 2 brightness west to east across an orbit.

Relative Azimuth**:**

The relative azimuth angle is equal to the solar azimuth angle minus the sensor azimuth angle where the azimuth angles are obtained by projecting the solar and sensor vectors onto the local tangent plane and measuring the angle from local north to the projected angle in the direction from north to east as shown in Figure 3.3

Visible and Near-infrared Reflectance:

The Daily and Composite Data Sets include reflectances derived from Channel 1 (0.58 - 0.68 micrometer) and Channel 2 (0.73 - 1.10 micrometer) of the AVHRR instrument. The reflectance is corrected for Rayleigh Scattering and ozone absorption as described in James and Kalluri [28].

Brightness Temperature:

There are three brightness temperature fields in Composite Data Set:

Channel 3 Brightness Temperatures:

This is the top of the atmosphere brightness temperature, in Kelvin, derived from Channel 3 of the AVHRR (3.55-3.93 micrometer).

Channel 4 Brightness Temperatures:

This is the top of the atmosphere brightness temperature, in Kelvin, derived from Channel 4 of the AVHRR (10.3 - 11.3 micrometer).

Channel 5 Brightness Temperature: This is the top of the atmosphere brightness temperature, in Kelvin, derived from Channel 5 of the AVHRR (11.5 - 12.5 micrometer).

A team of scientists formed the calibration working group and made recommendations on the appropriate calibration coefficients to be used in data processing. A report of the calibration working committee is given in Rao [54, 55]. However, no recommendations were made for the channel 3, so the Pathfinder processing system uses the gains and offsets provided in the NOAA 1b data record and calibrate the radiances using the procedures described in the Polar Orbiter Users Guide [32].

The calibrated fluxes are then converted to brightness temperatures. In order to save computation time, calibrated radiances are converted to temperatures using pre-computed radiance to temperature conversion tables based on the response curves of each of the AVHRR thermal detectors. Calibration of AVHRR thermal channels are detail discussed Brown, O.W [5], Steyn-Ross [64], and Weinreb, M.P., [73].

3.3 Data Format

All Pathfinder AVHRR Land data are stored in the National Center for Supercomputing Applications' (NCSA) Hierarchical Data Format (HDF) [4]. HDF allows data (scientific data and metadata) to be implemented in several ways including Scientific Data Sets (SDS) and 8-bit Raster Image (RIS8) data sets. The SDS implementation has more flexibility in including metadata and allows data of a variety of word sizes (8- to 64-bit data). The Daily, Composite, Climate, and Ancillary data are stored as HDF SDS, but the Browse data is stored as HDF RIS8.

3.4 Calibration of AVHRR Data

There are various aspects of the calibration of the AVHRR instruments. These include:

- Determination of the spectral response function of each spectral channel
- Pre-launch radiometric calibration of all five spectral channels
- In-flight calibration of the thermal infrared channels, i.e. channels 3,4 and 5 of HRPT/LAC data
- In-flight calibration of APT data
- Post launch calibration studies

The first two of these are done on the ground before launch and give results which are provided by NOAA to the users of AVHRR data. The third and fourth (in-flight calibration) occur on board and many users need to incorporate this in-flight calibration data into their own processing of the AVHRR data which described in section 2.2 for Brightness Temperature. The fifth is still an area of active research and development work which is described as follow as.

Post-Launch Calibration

It is observed that the visible channel of the imager degrades in orbit. Since the sensor has no onboard calibration device, it is necessary to develop post-launch calibration coefficients (or slopes) which take into account the in-orbit degradation of the sensor so that the derived products are rendered accurate. Therefore, the post-launch calibration of the imager visible channel has been determined using a vicarious technique that has been developed at the NOAA/NESDIS Office of Research and Applications for the calibration of broad band sensors in the visible, and near infrared. The post-launch operation is an attempt to recalibrate channels 1 and 2 to account for the degradation of the instruments. However, the NOAA-NASA AVHRR pathfinder program, which has been entrusted with the task of the reprocessing and rehabilitation of the AVHRR records for the period 1981-1990 (which has been termed the pathfinder period) for the purpose of the production of long-term records for climate studies, set up the AVHRR Pathfinder Calibration Working group in March 1991 to assess the degradation of channels 1 and 2 on the NOAA-7, -9, –11, and –14 spacecraft (referred to as the afternoon satellites since they cross the equator traveling north-wards in the afternoon) and to make recommendations for implementing appropriate corrections for the observed degradation . The report of this working group has now been published Rao and Chen [55].

In the Pathfinder Calibration Working Group report [55] four approaches for the post-launch calibration of channels 1 and 2 were used:

(a) the determination of relative trends in the calibration of channels 1 and 2 using the southeastern Libyan desert as a time-invariant calibration target.

(b) the determination of relative trends based on the global ISCCP data sets.

(c) Absolute calibration using ocean targets

(d) the use of congruent path airborne and satellite measurements over the White Sands Missile Range in New Mexico

These various approaches are described [55] in some detail and with many references cited.

The post-launch calibration coefficients were developed from southeastern Libyan desert (21-23^0 N and 28-29^0 E) data, which are assumed to be time invariant [57]. The CH1 and CH2 were calibrated using the updated Pathfinder coefficients, normalized by the cosine of the solar zenith angle and corrected for sun-earth distance. The resulting reflectances are in percent and packed into 8-bit values. The following formulas were used

NOAA-9; CH1: $0.105*\exp[166*10^{-6}*(d9-65)]*(4Ch1_8 - 37)$ (3.4.1)

CH2: $0.1143*\exp[98*10^{-6}*(d9-65)]*(4Ch2_8 - 39.6)$ (3.4.2)

NOAA-11; CH1: $0.106*\exp[33*10^{-6}*(d11-65)]*(4Ch1_8 - 40)$ (3.4 .3)

CH2: $0.1098*\exp[55*10^{-6}*(d11-65)]*(4Ch2_8 - 40)$ (3.4. 4)

NOAA-14; CH1: $(23.2*10^{-6}*d14 + 0.109)*(4Ch1_8 - 41)$ (3.4.5)

CH2: $(37.3*10^{-6}*d14 + 0.129)*(4Ch2_8 - 41)$ (3.4.6)

Where d9= 18 +365*(year-1985) + Julian day; d11= 98+356 (year-1989) + Julian day; d14 = 365 (year-1995) + Julian day. The $Ch1_8$, $Ch2_8$ are digital counts in 8-bit format; they are multiplied by 4 to convert into 10-bit format. These formulas were used to correct channel data from which NDVI was calculated in section 2.1.

CHAPTER 4

STUDY AREA

4.1 Introduction

For our research, we wanted to choose an area with diverse ecosystems. China has all major types of ecosystems present in the world. Therefore, we investigate NDVI and BT stability over China. It also reduces the amount of data to a manageable state and captures global variety of ecosystems in a single geographic region. It is very difficult to analysis of AVHRR data globally because of the huge volume of data. We can use the same methodology (EDF) globally to create vegetation index to improve the climatology because characteristics of ecosystems are same all over the world based on climate and human activities.

The study area, China, is located in central Asia The People's Republic of China lies between 25^0 N to 45^0 N in latitude and 70^0 E to 133^0 E in longitude (Figure 4.1).It is bound by Mongolia, Russia and Kazakhstan to the north, North Korea, the Yellow Sea and the East China Sea to the east, the South China Sea, the Gulf of Tonkin, Vietnam, Laos, Myanmar, India, Bhutan and Nepal to the south as well as India, Afghanistan, Pakistan, Tajikistan and Kyrgyzstan to the west. Over 66% of the study area is upland hill, mountains and plateau while the highest mountains and plateau are found to the west of China including part of Nepal, Bhutan and India. To the north and east of the Tibetan Plateau, the land decreases to the desert or semi desert areas of Sinkiang, Inner Mongolia, and southern part of Mongolia (Gobi desert). To the northeast of China is the broad fertile Manchurian Plains which are separated from North Korea by the densely forested uplands of Changpai Shan. Therefore, part of forested region North Korea based is

included in the study area. East of the Tibetan Plateau in China and south of Inner Mongolia is the Sichuan Basin, which is drained by the Yangtze River that flows east across the southern plains to the East China Sea. The southern plains along the east coast of China have rich, fertile soils and are protected from the north winds.

4.2 Land Targets

The land targets approximately between 25^0 N to 45^0 N in latitude and 70^0 E to 133^0 E in longitude were selected for Central Asia (Figure 4.1). Most of the study area covers China and it includes a wide variety or different ecosystems represented globally. It also covers part of the following countries: Mongolia, Russia, North Korea, Nepal, Bhutan, and India.

Figure 4.1 Geographical location of study area (bordered area).

We attempt to select relatively small uniform areas using common knowledge of geography, climate, ecosystem, and human activities. The main cover types are desert,

forest, and grassland. The information collected by the ground truth survey is useful for the classification of NOAA AVHRR weekly-composted NDVI and BT data.

CHAPTER 5

METHODOLOGY

5.1 Introduction

For each satellite, we construct the NDVI and BT time series and also approximate linear trend using least square technique. From trend equation, we estimate two values: the largest difference ((dN_t) between NDVI or BT at the beginning (N_b) and the end (N_e) of satellite life and difference (dN_s) between NDVI or BT at the beginning of the next (n) satellite (N_{bn}) and at the end of the previous (p) one ($N_{ep)}$. Both differences are normalized in order to compare NDVI and BT performance for different ecosystems.

$dN_t = 100* (N_e – N_b)/(N_b)$; $dN_s = 100*(N_{bn} –N_{ep})/N_{ep}$ ----------(5.1)

If the dN_t values are positive then the NDVI time series upward trend and downward for negative value; positive dN_s indicate larger NDVI at the end of the previous satellite and smaller NDVI in the opposite case.

There is no available physical method that can be used to correct for the stability of NDVI and BT. Therefore, we developed a statistical model for the correction of NDVI and BT. The empirical distribution function (EDF) is a statistical technique which is used to generate a normalization data of the years 1988, 1992, 1993, 1994, 1995 and 2000 compared with standard years data.

Standard Year

We designate several years data as standard in this study. Then the outputs of the other years are adjusted so that their distributions are the same as that of the standard. A standard year data should meet certain criteria [26, 74]. Its output should cover as much of the dynamic range[1] of the data (265^0 k < BT < 325^0 k) and 0.05 < NDVI< 0.35) system as possible without clipping at either the low or high ends. For example, based on the criteria of the standard year, data for the years 1986 and 1990 are designate as the standard (Figure 5.1). We chose

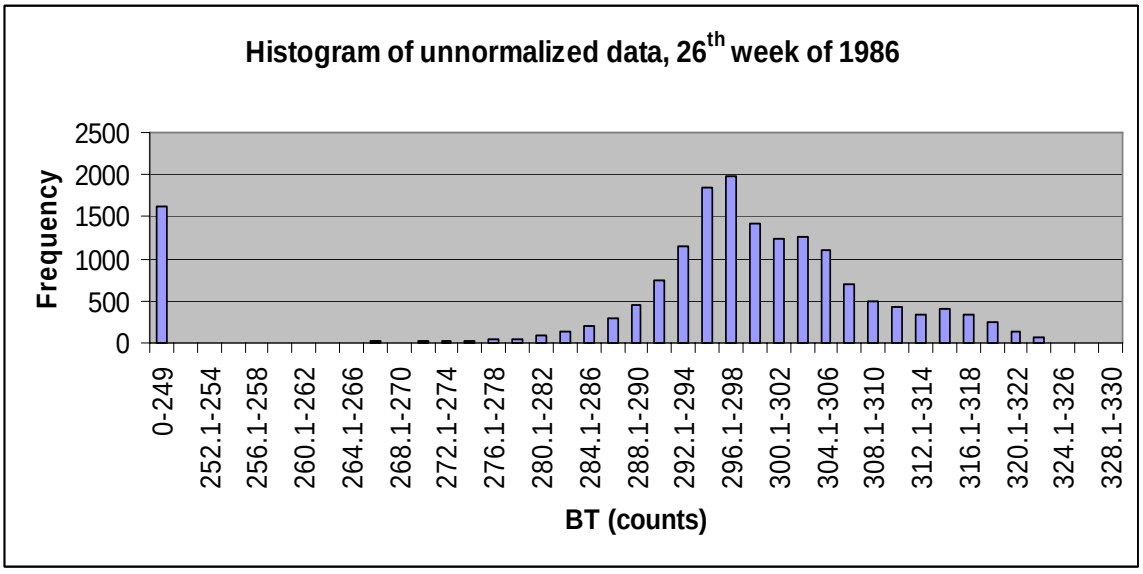

Figure 5.1 (a). Histogram of unnormalized data, 26th week of standard year (1986)

[1] Dynamic range is a flexible range of BT (counts) which may gradually vary overtime

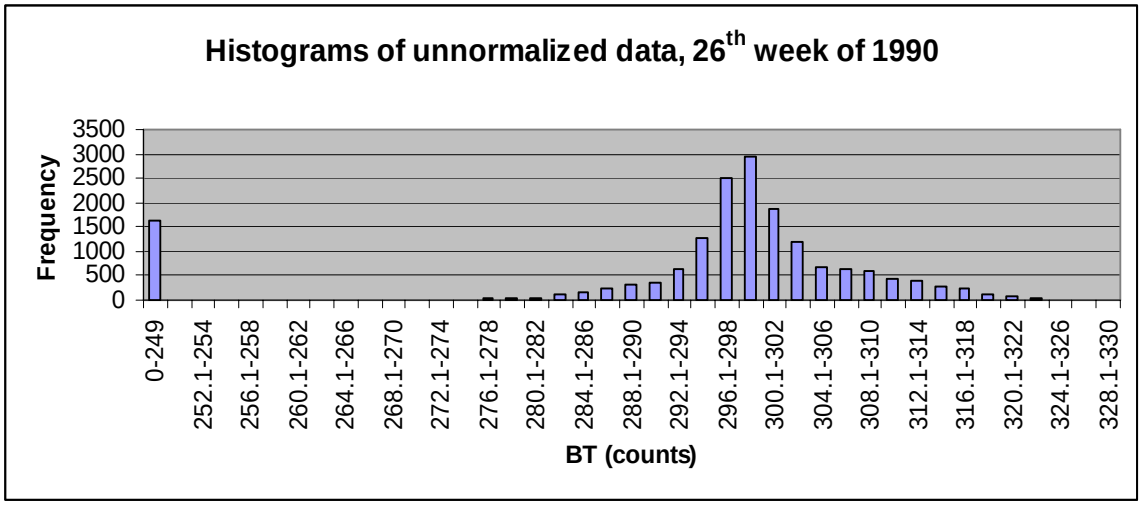

Figure 5.1 (b). Histogram of unnormalized data, 26th week of standard year (1990)

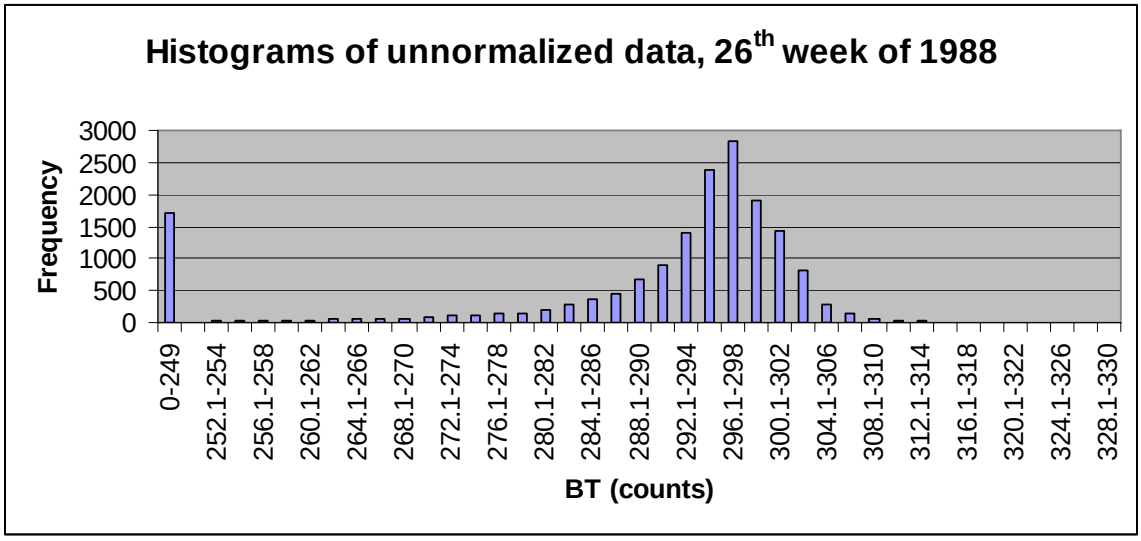

Figure 5.1 (c). Histogram of unnormalized data, 26th week of 1988

data for the years 1988 as an example because of histograms of data for the years 1988, are the most different from the standard year. The histogram of the year of 1988 is shifted towards the lower intensities relative to that of the standard year and its lower end is clipped in Figure 5.1 (c). Also standard year data should have low noise and a stable gain, one that does not change rapidly with time. Because the characteristics of the detectors of

AVHRR sensors are expected to be stable in time , a particular year may be usable as a standard for years, and normalization data may be effective for years. Data for the years 1982, 1983, 1985, 1986, 1989, 1990, 1996, 1997, 2001, and 2002 are stable in time (For example histograms of 1986, 1990 etc.) and can be used as standard for other years, because of equatorial crossing time of those years are between 13:30 and 15:00 local time (Figure 5.2) which maximized the value of coefficients. In other years, quality of satellite

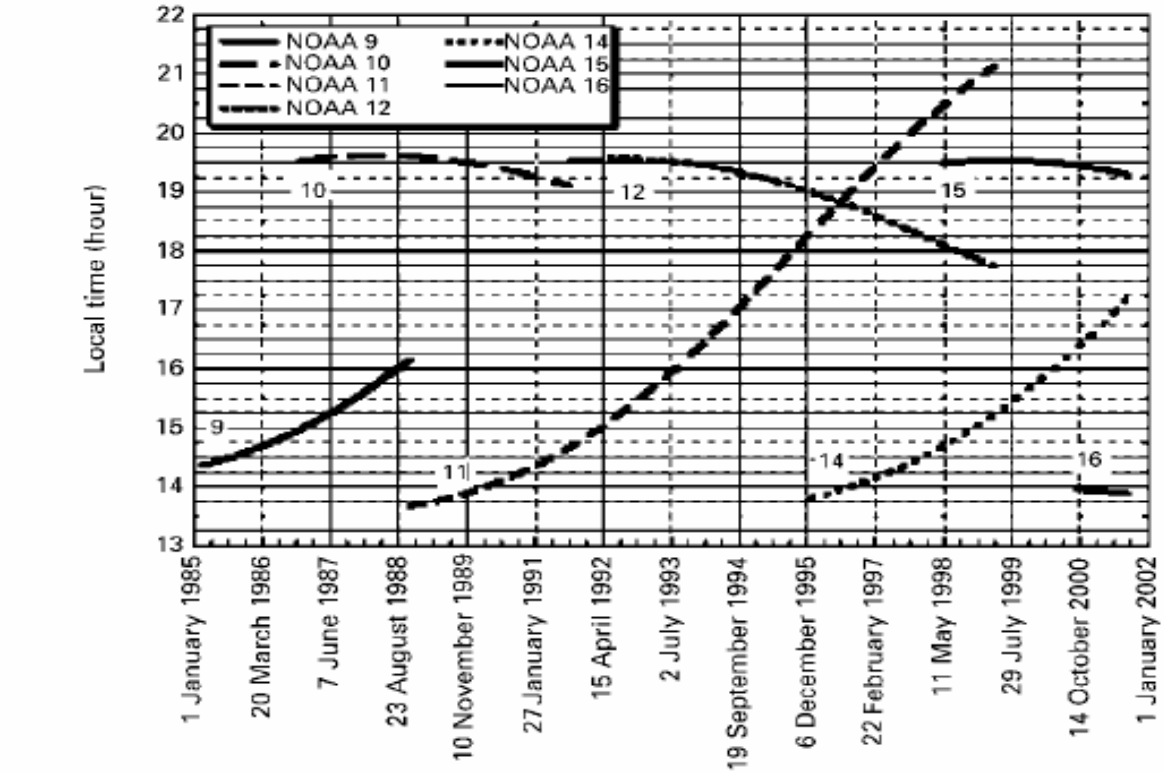

Figure 5.2. Schematic diagram of the equatorial crossing time for NOAA -9, -10, -11, -12, -14, -15, and -16. The y direction is local equatorial crossing time, and the x direction is time of year. NOAA-7 is not shown here but has similar orbital drift as the afternoon satellites NOAA-9, -11, and 14 [30, 2003].

observations significantly deviates from the standard. Also Data from the afternoon passes of the satellites are affected by a drift of 1-2 hours in local overpass time, during a

nominal three-four year life time [50]. Image data from the AVHRR slowly shift as the overpass time gets later and later. This interferes with the estimation of long-term changes in surface properties such as vegetation conditions, albedo etc because the changing angle of solar incidence causes variation in observed radiances as the AVHRR scans the earth. Therefore data for these years are considerably stable compared to data for other years. For that reason, we use those as standard years for normalized data.

5.2 Empirical Distribution Function (EDF) Method for Normalization of Satellite Data

Empirical distribution function (EDF) approach is based on the physical reality, that each ecosystem may be characterized by very specific statistical distribution, independent of the time of observation. It is the best available technique to normalize satellite data. It allows us to represent global ecosystem from desert to tropical forest and to correct extreme distortions in satellite data related to technical problem. To generate the normalization data, we begin by selecting samples of unnormalized earth-scene data covering as much of the range intensities as possible. For NOAA satellites, the area will be rectangular, extending several thousand pixels from desert to tropical forest (both east to west and north to south). Corresponding to the incoming radiance from any pixel, the instrument will respond with an output x, in digital counts. One can compile the discrete density function, i.e., the histogram, describing the relative frequency of occurrence of each possible count value, for each year. For year **i**, which is the year to be normalized, let the histogram be $P_i(x)$. An empirical distribution function (EDF) $P_i(x)$ can then be generated; viz.[74, 1989],

$$P_i(x) = \sum_{t=0}^{x} p_i(t). \qquad (5.2)$$

The EDF is also known as a cumulative histogram of relative frequency. It is a non-decreasing function of x, and its maximum value is unity.

For convenience, however, we have chosen the maximum value to be 1; i.e., if the maximum possible output in counts is x, then $P_i(x) = 1$, as shown in Figure 5. 3

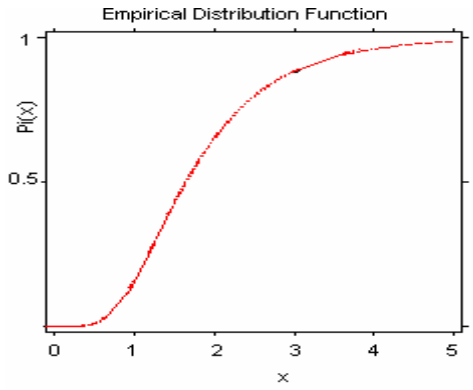

Figure 5.3. Empirical Distribution Function

For example, Figure 5.4 shows the histogram of 26th week number of 1988 represents AVHRR output data from 16905(161*105) pixels. The abscissa, labelled "Brightness temperature (counts)" is the output levels and the ordinates, labelled "Frequency", is the frequencies of occurrence of the outputs at each level. Figure 5.5 show the EDF of 1988, which computed from the histogram in Figure 5.4. The abscissas, labelled "Brightness temperature (counts)" is the output levels and the ordinates, labelled "EDF (0 to 1)", is the percentage of the data with the outputs at or below that level.

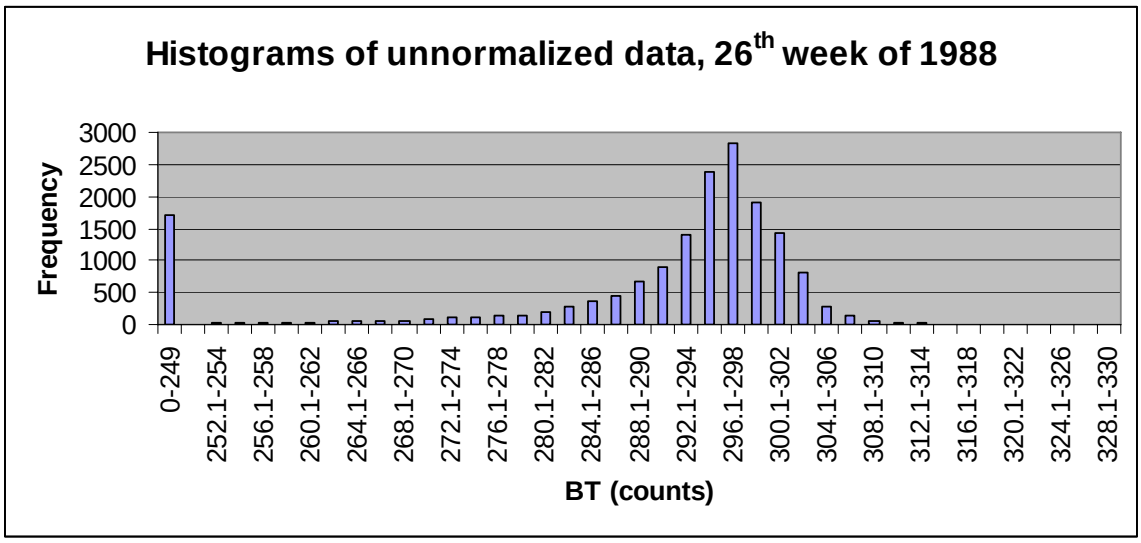

Figure 5.4. Histogram of unnormalized data, 26th week of 1988

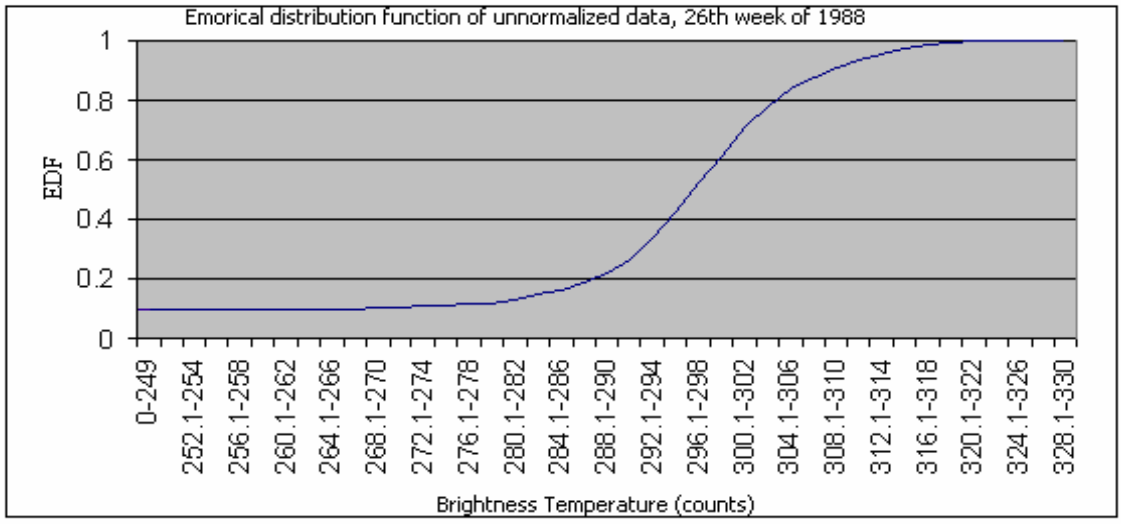

Figure 5.5. Empirical distribution function of unnormalized data, 26th week of 1988

In these terms, the basic premise of normalization is that for each output value x in year i, the normalized value x' should satisfy [74, 1989]

$$P_s(x') = P_i(x), \tag{5.3}$$

Where the subscript **s** refers to the standard year. In practice, not only is P_s non-decreasing, but it is also monotonically increasing as a function of x' in the domain of x' where there are data. Therefore, it can be inverted, yielding the solution for x', [74, 1989]

$$x' = P_s^{-1}(P_i(x)) \tag{5.4}$$

When it is applied sequentially for every possible count value x, eq. (5.4) generates the normalization data relating each x to an x'. Figure 5.6 shows how the procedure is applied in actual practice to generate the normalization data [26, 74]. The figure shows idealized EDF's for the standard and unnormalized years i. In the figure the EDF's are continuous, but in practice they are discrete, being specified only integer values of x.

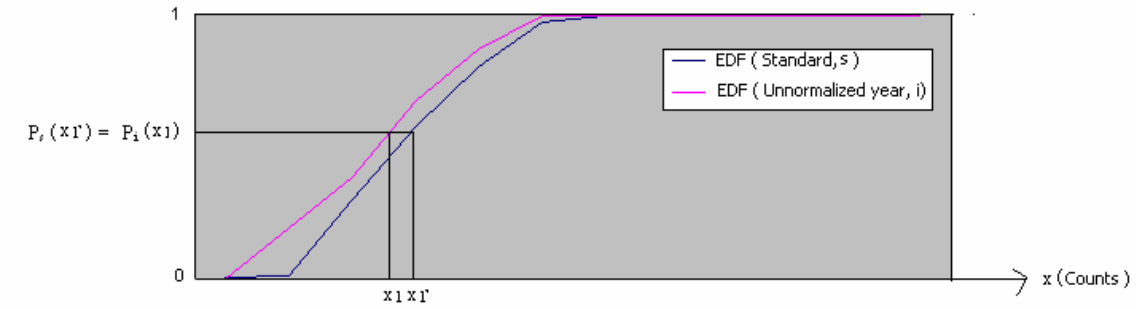

Illustration in Figure 5.6 procedure to generate normalization data

To find x'_1 , the normalized count value corresponding to the unnormalized count value of x_1 , the following is the procedure: First, for the count value x_1 in unnormalized year i, , find the decimal or percentage value from the EDF of year i. In the illustration it is Pi (x_1). Then find the point on the standard year's EDF with the same decimal or percentage value. According to equation (5.3), that decimal or percentage can also be expressed as P_s (x'_1). Finally, use the EDF of the standard year to find the normalized count value x'_1 .

Since the data are actually discrete, we will need to interpolate within the EDF of the standard year to find the value x'_1. Using this technique, we can generate the normalization data. Therefore, we choose EDF method for the normalization of satellite data.

Error exists when the EDF's of unnormalized year i and the standard years are not identical. As a quantitative measure of the error, we express the differences in counts or percent, between the EDF of the standard and unnormalized years. In the terminology of equation 5.4 , the count differences are x'-x, and the percent differences are $P_s(x') - Pi(x)$.

5.3 Comparison of EDF with Other Methods

5.3.1 Method 1: Trend Estimation (Based on Same Value)

We use trend estimation method for the correction of satellite data. Given the monotonic decrease in reflectance, we chose to fit a trend line to the NDVI data (parallel to the X-axis), using the monitor output from NOAA-7 (January 1982- January 1985), NOAA-9 (April 1985 - September 1988), NOAA-11 (October 1988-August 1994), and NOAA-14 (March 1995-December 2000) satellites. We derive the trend line for unnormalized NDVI value for each satellite. We normalize the degradation trend by comparing with the trend which is a straight line in Figure 5.7 for each week of each satellite. For example, unnormalize NDVI value of 18^{th} week number of 1988 is 0.18, First we find the NDVI value for same week on trend of straight line. The NDVI value is 0.20 for same week (18^{th} week). Then find the difference of two NDVI values for same week. The difference is 0.02, and then adds 0.02 to 0.18 and thus derives the normalized NDVI value for that week. Similarly, we normalize the NDVI value for each week of NOAA-7, NOAA-9, NOAA-11, and NOAA-14. After that we produce new NDVI time series using the new value of each satellite. Figure 5.7 shows the new NDVI for each satellite (yellow line). We did not normalize NDVI value of NOAA-16 satellite using this method because this satellite doesn't have trend.

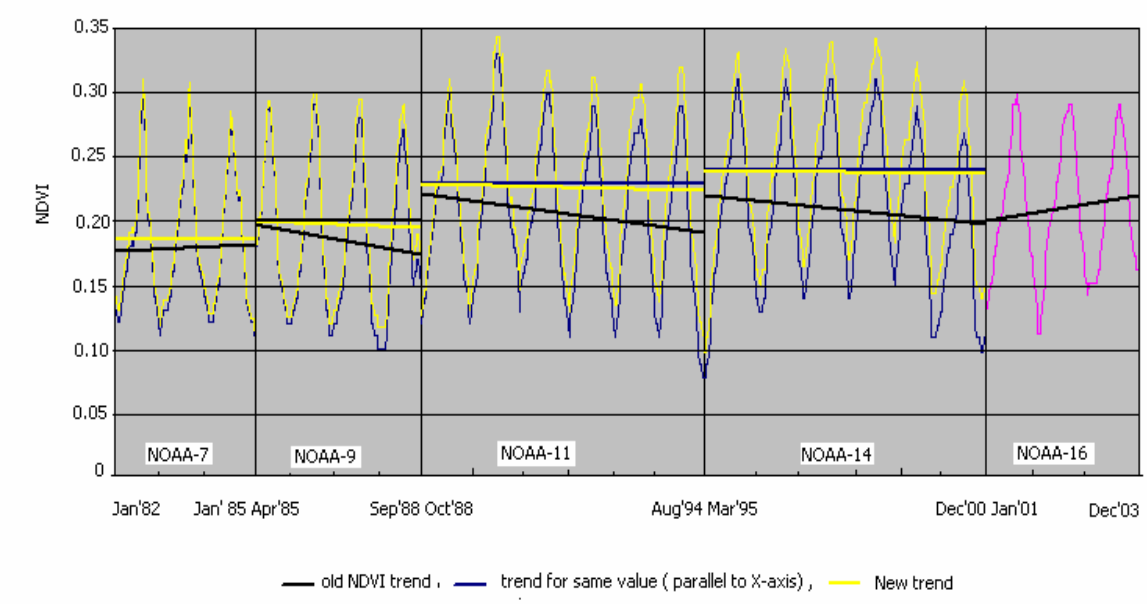

Figure 5.7 Corrected NDVI time series (yellow line) by the trend estimation method

We compared this method with the EDF method (Figure 5.8), we see that the EDF method is better because the Trend Estimation Method corrects all years (Figure 5.7).But when using EDF Method, we do not need to correct the first two years for each satellite since the first two years produce data of good quality. Therefore, we use the EDF method to correct satellite data in this dissertation because normalized data are relatively closer to the standard data. In addition, unlike the trend estimation method, we do not need to correct all year's data.

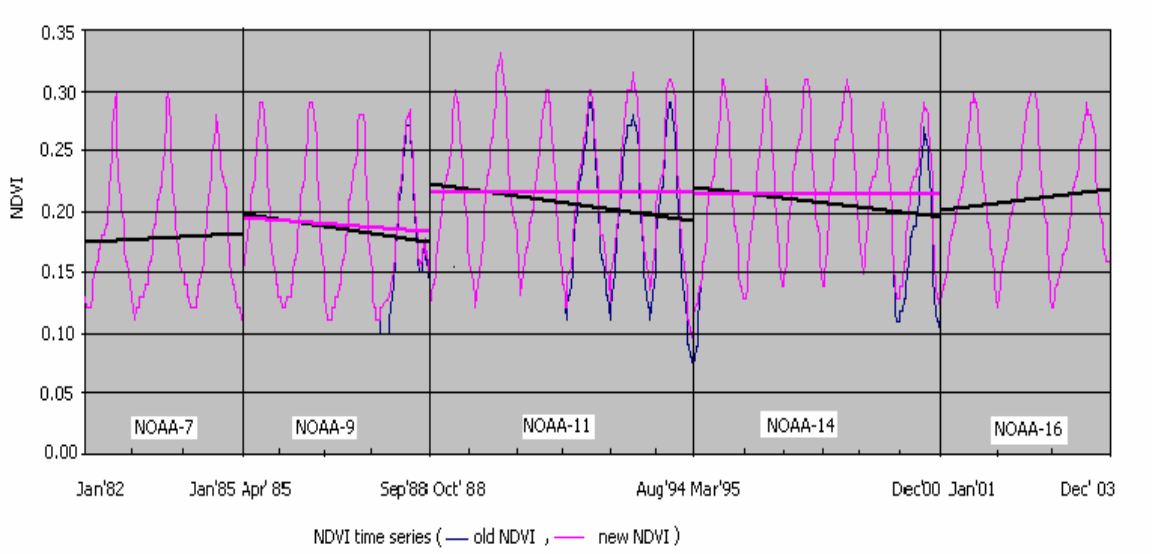

Figure 5.8 Corrected NDVI time series (pink line) by the EDF method

5.3.2 Method 2: Trend Estimation (Based on Standard Years).

We estimate trend equation for the first two years (104 weeks) of each satellite's life because we use these years as standard. We use X-axis as number of week and Y-axis as NDVI value. After that we calculate the trend equation for total week number of each satellite. For example NOAA-9 (April 1985- September 1988) we use total weeks (x =183) for finding the trend equation of that satellite. We also derive the decline trend for old NDVI value of each satellite. We normalized the decline trend by comparing it with the trend equation based on standard years of each satellite. For example, old NDVI value of the 26th week of 1988 is 0.25, First, we find the NDVI value for the169th week by using the old NDVI trend equation. The NDVI value is (y= -0.0001x + 0.1983, x =169) 0.18. Second, we estimate the NDVI value for same week by using the trend equation (y = 0.0003x + 0.1705, x = 169) based on standard years (1985 and 1986). The estimated NDVI value is 0.22. Then we find the difference of two NDVI values for the same week.

The difference is 0.04. Then we add 0.04 to 0.25 and thus derive the normalized NDVI value for that week. Similarly, we normalize the NDVI value for each week of NOAA-7, NOAA-9, NOAA-11, and NOAA-14 except standard years. After that we produce the new NDVI time series using the new value of each satellite. Figure 5.9 shows the new NDVI time series for the satellites (pink line).

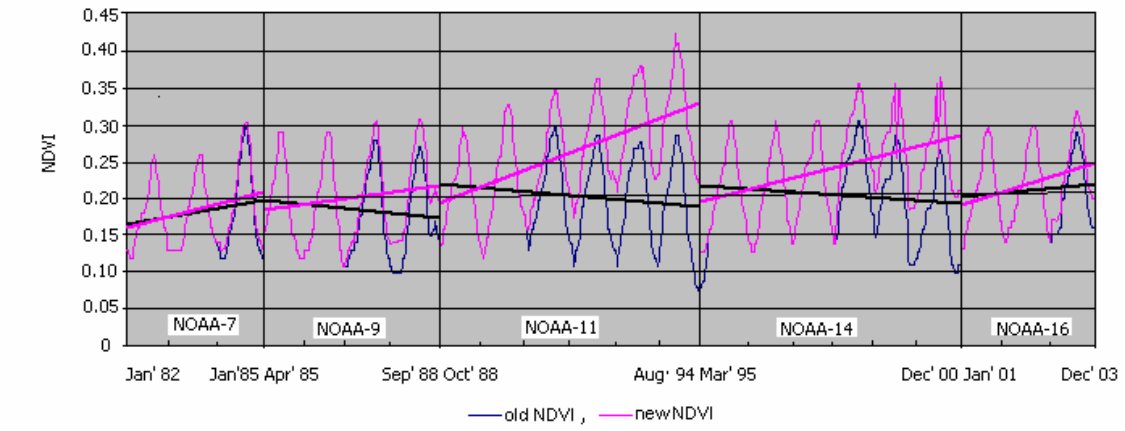

Figure 5.9 Corrected NDVI time series (pink line) by the trend estimation method (based on standard years)

The main disadvantage of that method is that there is a bigger shift between estimated data from two satellites during transition between satellites. Consequently, data for all years are shifted except the standard year which is not desirable. Therefore, we use the EDF method to correct satellite data (Figure 5.8) in this dissertation because normalized data are relatively closer to the standard data. In addition, we do not need to correct all year's data when using the EDF method.

5.3.3 Method 3: Typical Pattern Technique

Typical pattern is a statistical technique which is used for normalization of satellite data for removing orbit drift on AVHRR temperature measurement [31]. The brightness temperature diurnal cycle (Ts (t), t =1 to 24) is decomposed into three parts: a climate mean diurnal cycle $T'_s(t)$ instantaneous variations (Ts'), and noise N(t) [31, 1999]:

$$Ts(t) = T''_s(t) + T' s(t) + N(t) \qquad (5.3.1)$$

with t ranging from 1 to 24. The climatological mean (Ts (t), t =1 to 24) represents the typical diurnal cycle pattern. The noise term represents small-scale fluctuations or random measurement error. T's is the instantaneous disturbance from mean condition. The disturbance can be largely explained as the response of the atmospheric surface layer to short time-scale atmospheric forcing. Taking N(t) to be negligible with respect to the typical pattern which represents most of the Ts diurnal cycle, the brightness temperature diurnal cycle can be described as a combination of the typical pattern and instantaneous variations $Ts(t) = T''_s(t) + Ts'(t)$, t = 1 to 24.

The underlying physical basis for this decomposition is as follows. The diurnal cycle of brightness temperature is dominated by the absorbed surface insolation. This forcing evolves over longer time-scales, i.e. climatology. However, the actual brightness temperature also depends on the instantaneous state of the atmosphere and surface properties, such as wind and soil moisture. The first term in equation (5.3.1) corresponds to the typical diurnal cycle of Ts, which is a function of season, latitude and surface type [31].

The typical patterns are normalized using the equation: [31, 1999]

$$\hat{T}_s(t) = (T_s(t) - T_{min}) / (T_{max} - T_{min.}) \quad (5.3.2)$$

where Tmax and Tmin are the maximum and minimum temperatures of that typical pattern. This normalization can be used to facilitate easy comparison between typical diurnal variations. We have to use look-up table for typical pattern of the T_s diurnal cycle which can be obtained from CCM3/BATS (National Center for Atmospheric Research (NCAR) Climate Community Model / the Biosphere–Atmosphere Transfer Scheme BATS) for all land covers, seasons and latitudes. The look-up table can be used to correct the orbital drift effect on the brightness temperature and, consequently, to derive the temperature at a consistent time over the lifetime of each NOAA afternoon satellite.

To correct data, we have to use the following three steps using this technique. First, for a given pixel, obtain the satellite Ts observation and extract the corresponding typical pattern from the look-up table based on land cover/ vegetation type, season and latitude. Second, fit the satellite measurement with the typical pattern to provide the diurnal cycle. Third, select the temperature at a consistent time to output, for example, 14:00LT, from which to build the drift corrected Ts dataset. For NDVI data we can apply same procedure.

We compared this method with the EDF method and we notice that the EDF method is better because the EDF method does not need to correct all year's data. When using typical pattern technique, we have to correct all year's data. We do not need to correct the

first two years of each satellite since the first two years produce data of good quality. For this technique we have to use look-up table which depend on CCM3/BATS for all land cover/ vegetation type, season and latitude. For the EDF method, we have to generate look-up table for data normalization which does not depend on CCM3/BATS. Therefore, we use the EDF method to correct satellite data in this dissertation.

5.3.4 Method 4: Weighted Least-Squares Method

This method generates the average annual profile of NDVI and channels 4 brightness temperatures of all ecosystems in China. The NOAA / NASA Pathfinder data keep only observations with the solar zenith angle smaller than 70°. Some cover types distributed in the high-latitude regions may have many missing pixels in the winter seasons, which corresponds to the channel 4 brightness temperature as low as 160° .In the winter of 1988, NOAA-9 reached the end of its lifetime. Because of satellite orbit drifts [15, 52, 62] the solar zenith angle is very low in the winter so that many cover types do not have any observations during that period (For example 1988, 1993, 1994, and 2000). We can produce average annual NDVI profile for unnormalized years and standard years in Figure 5.10. After that, we can normalize data of unnormalized years compared with the standard years. Using this normalized value we can produce new NDVI time series. Figure 5.10 (b) shows that normalized data does not match perfectly with standard data because we use monthly NDVI value in this method. This method is very effective for monthly composite data [65] . But we used seven days composite data in our research. Therefore, we can not use this method for data normalization.

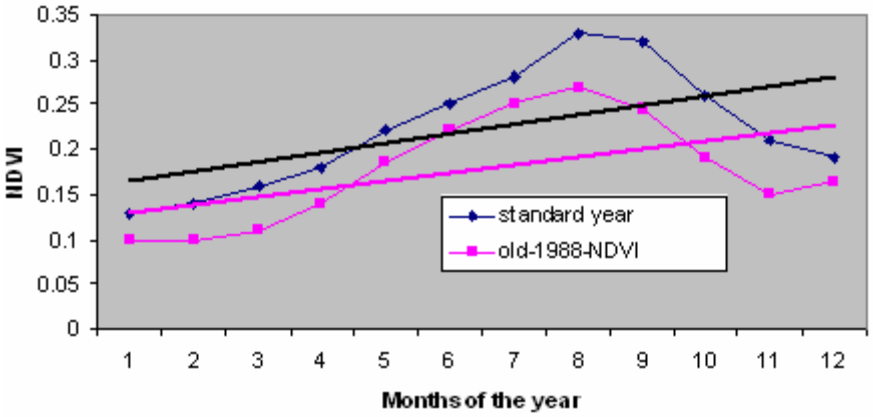

Figure 5.10 (a) Average annual profiles of unnormalized data of 1988 compared with standard

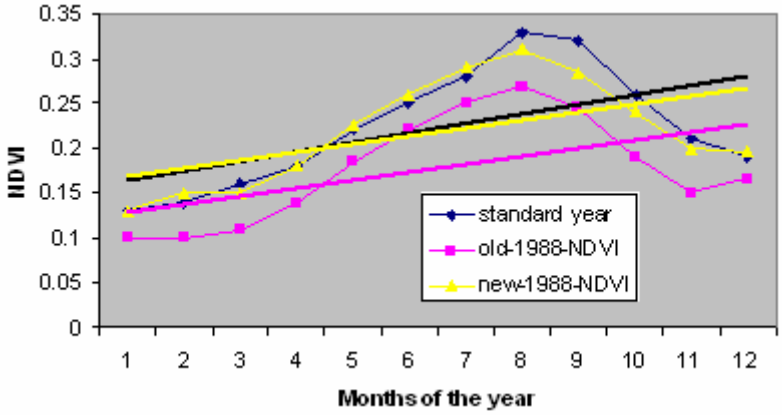

Figure 5.10 (b) Average annual profiles of normalized data of 1988 compared with standard

We compared this method with the EDF method, we see that the EDF method is better because normalized data in this method matches with standard and also does not correct data for all years. For this reason, we decided not to use weighted least-square method. As the EDF method is better than weighted least-square method.

5.3.5 Method 5: Correction of Solar Zenith Angle and Calibration Adjustments

Technique:

Although the calibration is available for all satellites, only NOAA-9 has it been verified with extensive series of studies and underflight experiments and general consensus developed. The NOAA-11 calibration has greater uncertainties merely because of the lack of reliable data after the Pinatubo event, satellite orbit degradation, and some disagreements still remain [14]. The NOAA -14 period is, perhaps, too recent to have been sufficiently explored and documented. As for Solar Zenith Angle (SZA) effects, they are often accounted for in some studies with atmospheric radioactive models and empirical relationships. The disagreement in model results is still substantial [7].

Our two basic assumptions are (1) the NOAA-9 calibration is correct (2) globally averaged deserts and rain forests do not have trends in time. The justification for using the NOAA-9 calibration as a baseline was proposed by **R**ao and **C**hen [57] and is discussed in detail by Brest et al [78]. The second assumption, namely, stability of global aggregates, prohibits "global desert greening" or "global tropical deforestation," essentially implying that anomalies are mutually compensated on a global scale for most of the time because of counteracting effects.

This technique can correct the orbital drift on AVHRR data by dividing the global land areas into different NDVI- based classes and then regressing the satellite solar zenith angle against the NDVI for each class. The global data are stratified into six classes (class1-deserts, class 2-semi-arid, class 3-boreal forests/tundra, class 4- mixed/decidous forests, class 5-wooded grasslands, and class 6-rain forests) with common surface type characteristics based on snow-free annual range and mean as clustering variables [23].

For this technique, we can parameterize the SZA trend using a data subset for which stability in time and correct calibration are assumed; then, can remove this effect from rest of full time series of the stable classes and derive corrections/adjustments to the residual trends, attributed to calibration discrepancies; further develop calibration adjustments to all the classes based on the corrections derived for the two extreme classes; and then can apply these calibration adjustments to all the data, and develop SZA corrections for all classes. After application of SZA and calibration corrections, the time series would have a smaller variance. The results of such a procedure may still be inadequate for global time series analysis because the uncertainties in the statistical analysis of 20-25 years of data may be as large as the climate signal. As shown by **W**eatherhead et al. [75] the precision of trend estimate depends on the number of years used for analysis, the magnitude of variation and the autocorrelation of the noise, and possible level shifts, e.g., due to change of sensors. Even for small autocorrelation, low variability, and consistent calibration, much longer periods than one decade may be required to detect a statistically trend of time series.

The advantage of this method is its simplicity. But it suffers from some limitations. First it suffer from limitations in the determination of vegetation classes. Second it uses unrepresentative samples to compute the regression coefficients [20, 23, and 30]. Another disadvantage of this method is that it corrects all year's data. But when using the EDF method, we do need to correct all year's data because first two years produce data of good quality. Therefore EDF is the best technique to normalize satellite data compared to all other methods which mentioned above.

CHAPTER 6

RESULTS AND DISCUSSION

6.1 Analysis of NDVI Time Series for Study Area

We produce NDVI time series of five NOAA satellites, which is illustrated in figure 6.1.

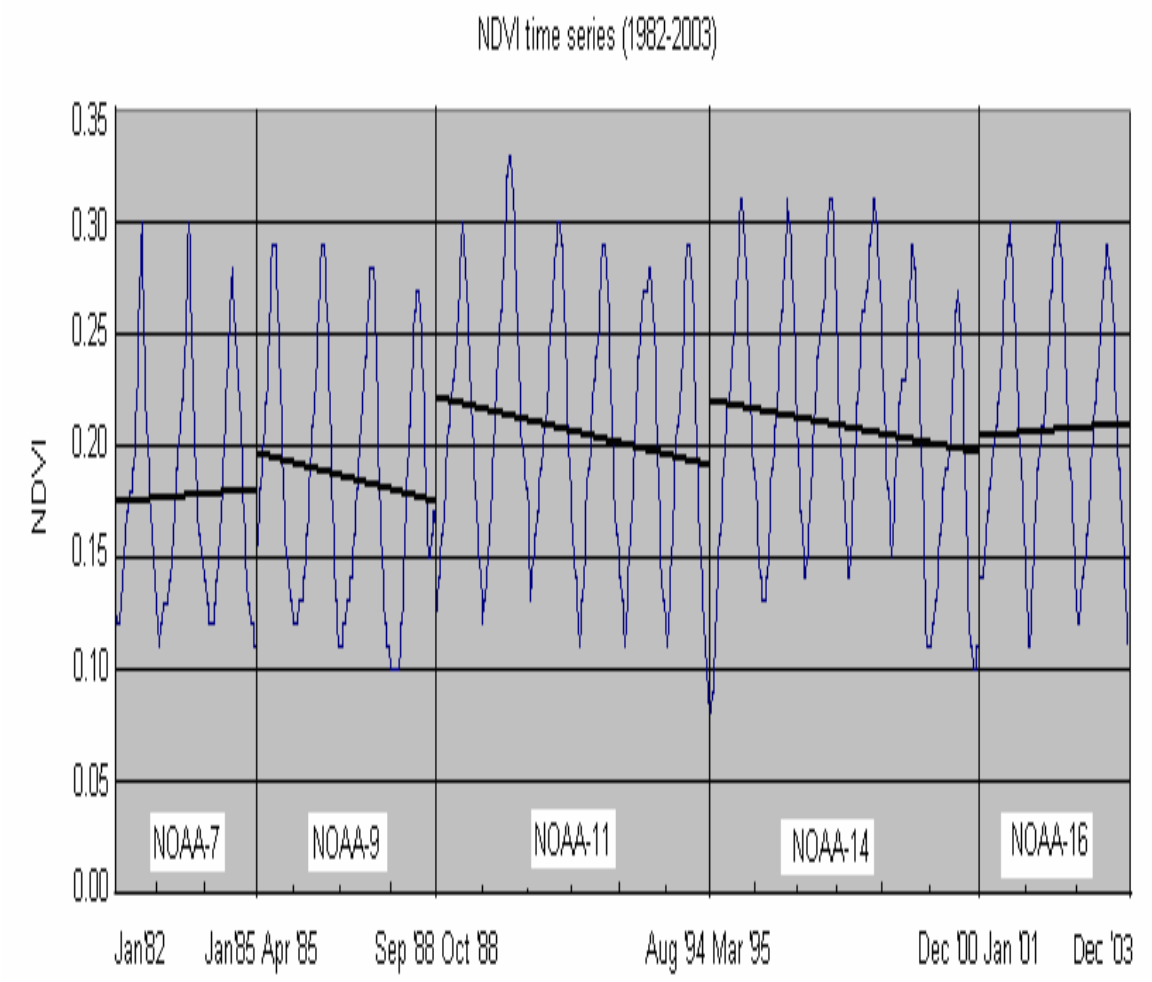

Figure 6.1 NDVI time series (yearly old NDVI data) for study area.

We found NDVI range for the study area between 0.07 and 0.33 approximately because major part of the study area covers grassland, desert, semi desert (mixed) and forest,

which usually have NDVI value over 0.25. Vegetation NDVI typically ranges from 0.1 to 0.6, with higher values associated with greater density and greenness of the plant canopy. Surrounding soil and rock NDVI values are close to zero while the NDVI differential for water bodies such as rivers and dams have the opposite trend to vegetation with negative NDVI index. We assume for desert areas, the NDVI value is less than or equal to 0.12; for semi-desert (mixed) area, the NDVI value between 0. 12 and 0.19; for grassland area, the NDVI value between 0.2 and 0.25; and for forest area, the NDVI value is greater than 0.25 because the NDVI value is usually lower in unfavorable weather (desert) than in normal and wet weather (forest) [39].

Data from the afternoon polar orbiters is preferred for producing the NDVI time series because of the high sun elevation angle (low solar zenith angle). However, the equator crossing time drifts to a later hour as the satellites age [50]. Satellite orbit drift results in a systematic change of illumination conditions which is one of the main sources of non-uniformity in multi annual NDVI time series.

Figure 6.1 shows that the NDVI data of 1988, 1992, 1993, 1994, 1995 (week # 1-8), and 2000 are nonuniform compare to other years because of satellite orbital drift, Mt Pinatubo, and sensor degradation. Therefore, we need to correct the data of those years. We apply EDF for the correction of data of those years compared with standard year's data. The subset 1(standard data correction sets) is use for correcting unstable years and then corrected data for this years compared with the standard data in the subset 2 (standard data validation sets). First, EDF construct for unnormalized data and than generate the normalize data compared with subset1. Then corrected or normalized data for this years compared with subset 2 which provides NDVI data for these years that

match in subset 2. Figure 6.2 shows how the procedure is applied in actual practice to generate normalization NDVI value [26, 74].The figure shows idealized EDF's for the standard and the year of 1988. As EDF are based on cumulative histogram, they are discrete. But in Figure 6.2, they are shown as continuous function.

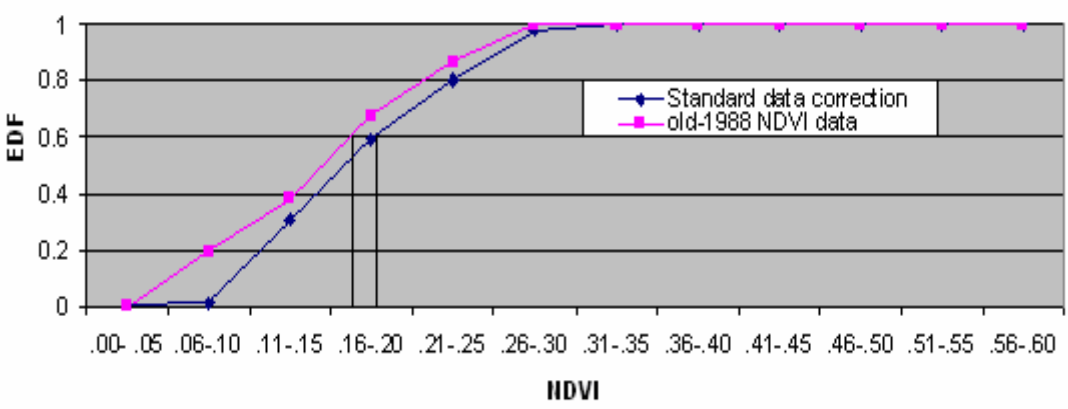

Figure 6.2 Illustration of procedure to generate normalization NDVI data.

For example, for the NDVI value 0.16 in year 1988 (Figure 6.2) find the value from the EDF of year 1988. In the illustration it the EDF_{88} is 0.6. Then find the point on the standard data correction sets EDF with the same EDF value. According to equation 5.3, that the EDF value can also be expressed as the $EDF_{standard}$ is 0.6. Finally, use the EDF of the standard data correction to find the normalized count value 0.18. Since the data are actually discrete, we will need to interpolate within the EDF of the standard data correction sets to find the value of 0.18. Therefore,

$$\text{New NDVI value for 1988} = NDVI_{1988} + (NDVI_{standard} - NDVI_{1988}) \text{ or}$$

$$\text{New NDVI value for 1988} = 0.16 + (0.18 - 0.16) = 0.18$$

Using this technique, EDF's produce to normalize or correct data for the years 1988, 1992, 1993, 1994, 1995(week#1-8), and 2000 compared with standard year's data which are illustrated in following Figures.

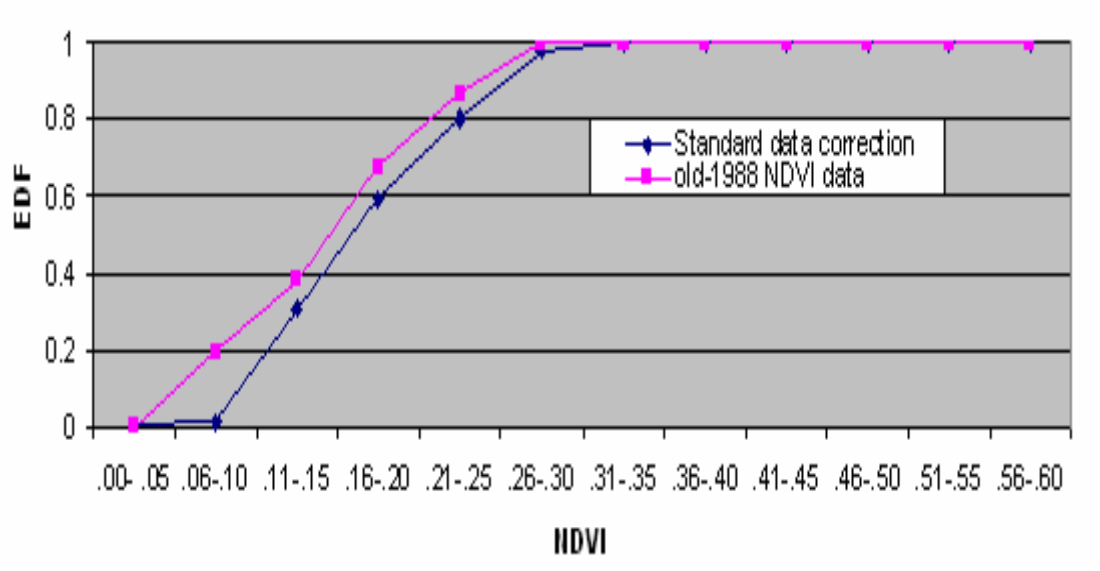

Figure 6.3 (a). Empirical distribution functions for unnormalized data of 1988 compared with standard data correction sets (subset1)

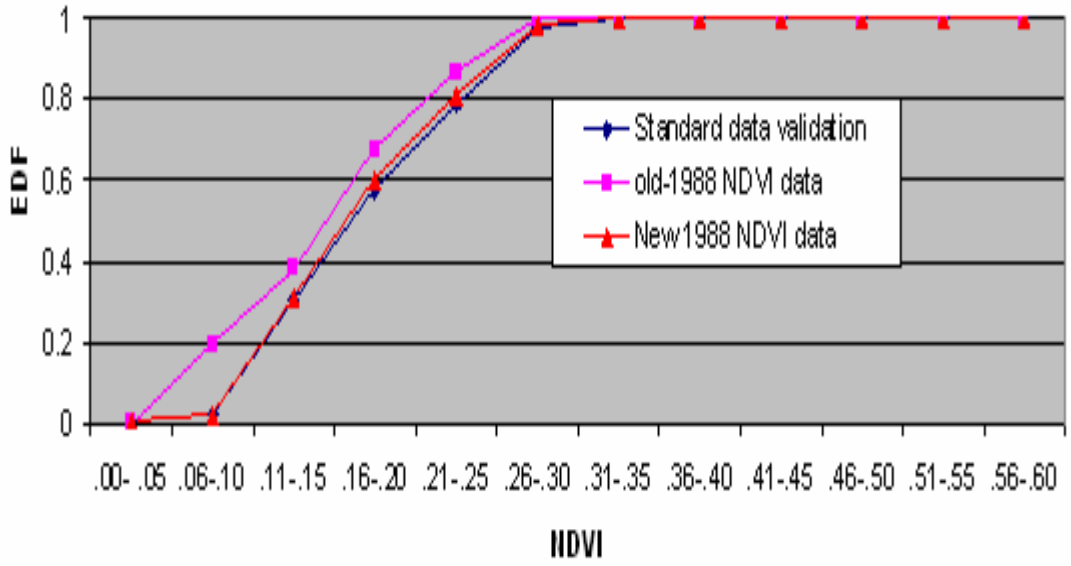

Figure 6.3 (b). Empirical distribution functions for normalized data of 1988 compared with standard data validation sets (subset 2)

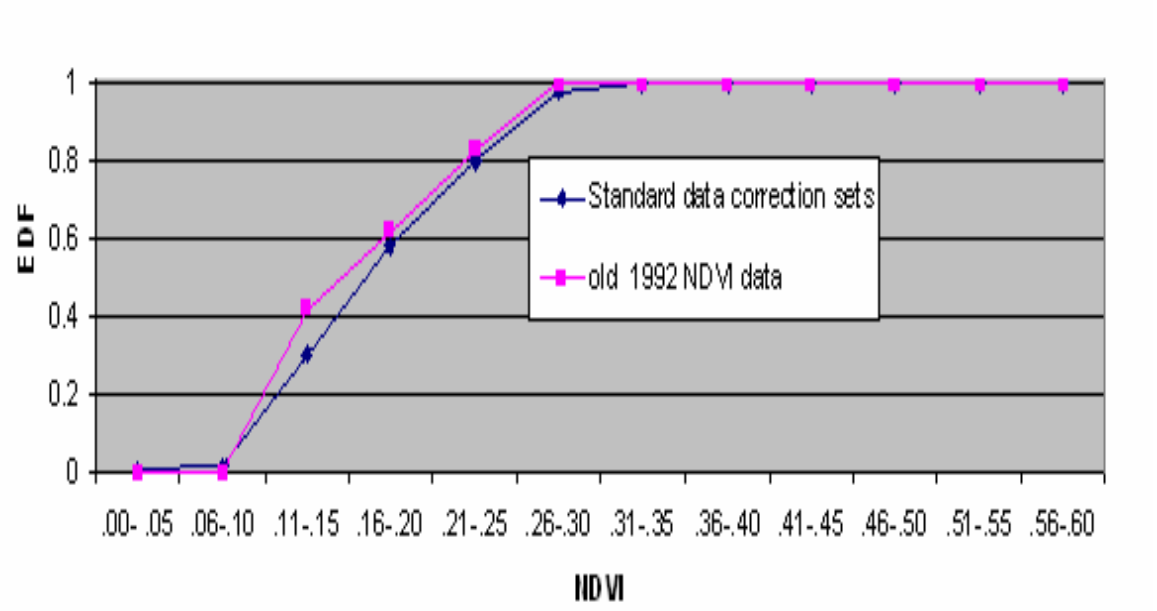

Figure 6.4 (a) Empirical distribution functions for unnormalized data of 1992 compared with standard data correction sets (subset 1).

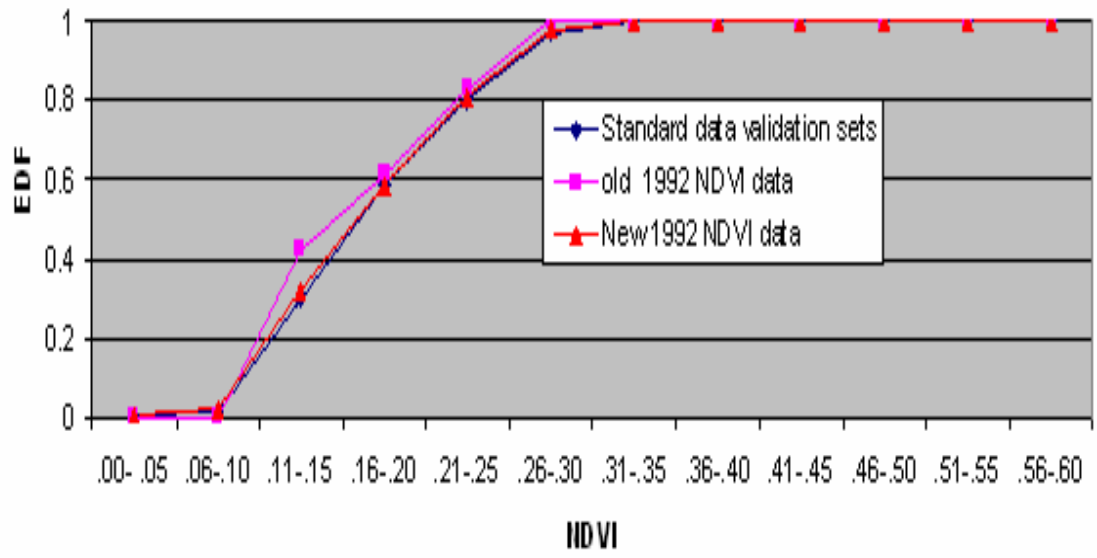

Figure 6.4 (b) Empirical distribution functions for normalized data of 1992 compared with standard data validation sets (subset 2).

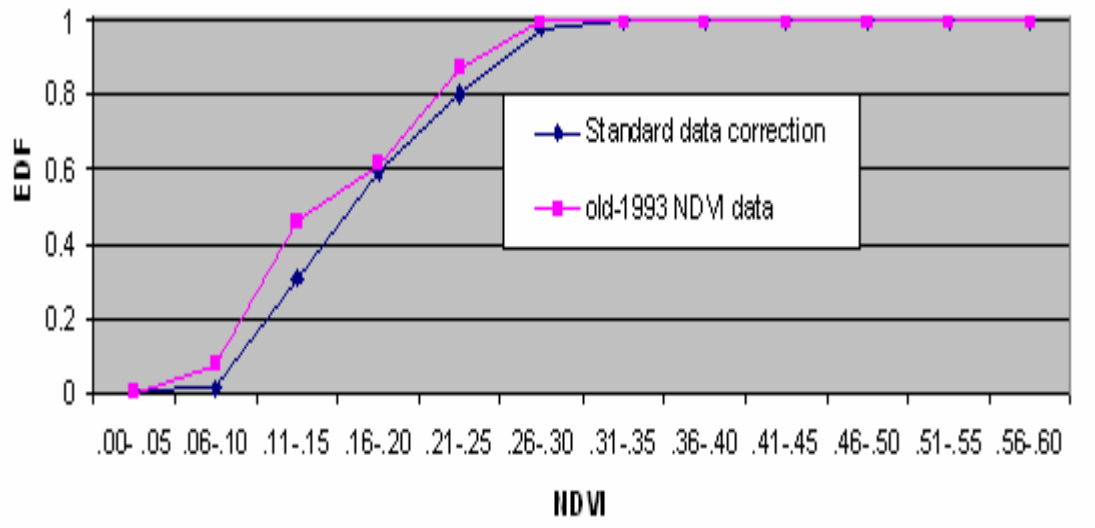

Figure 6.5 (a) Empirical distribution functions for unnormalized data of 1993 compared with standard data correction sets (subset 1).

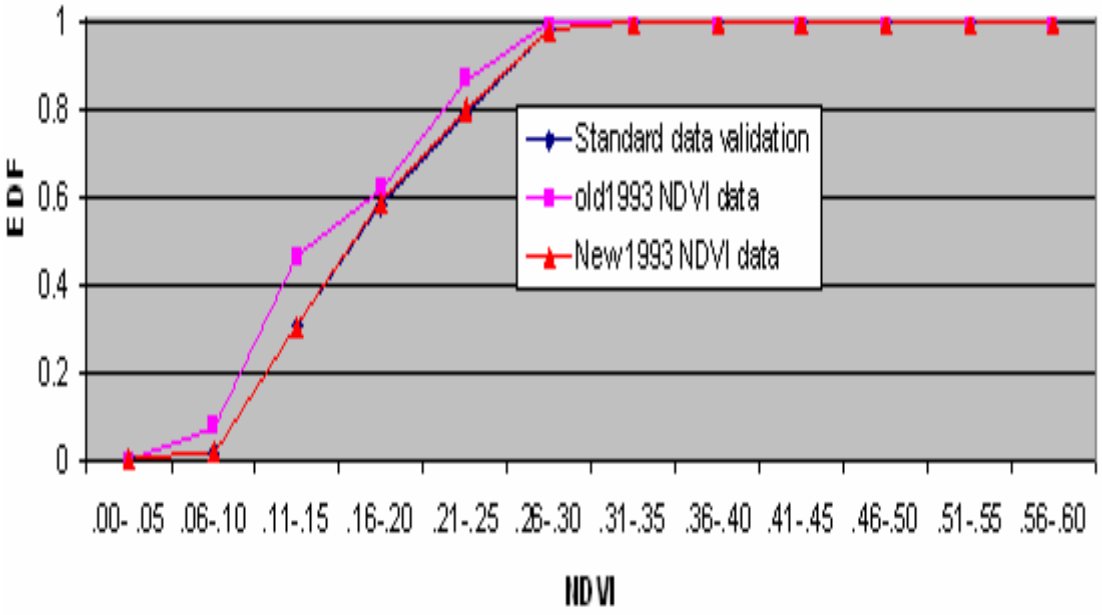

Figure 6.5 (b) Empirical distribution functions for normalized data of 1993 compared with standard data validation sets (subset 2).

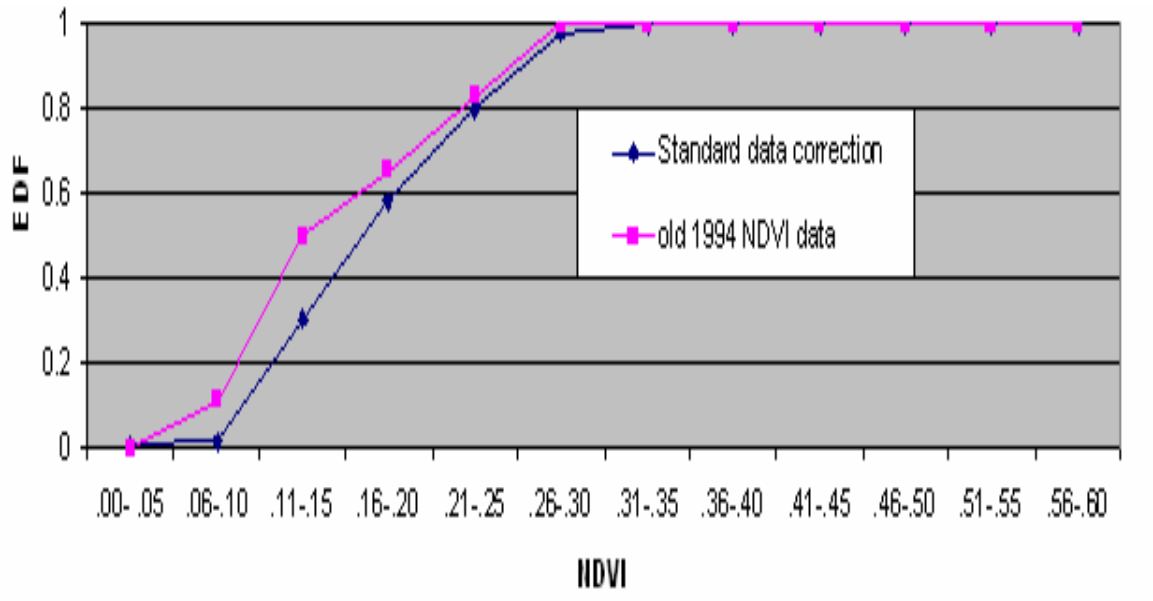

Figure 6.6 (a) Empirical distribution functions for unnormalized data of 1994 compared with standard data correction sets (subset 1).

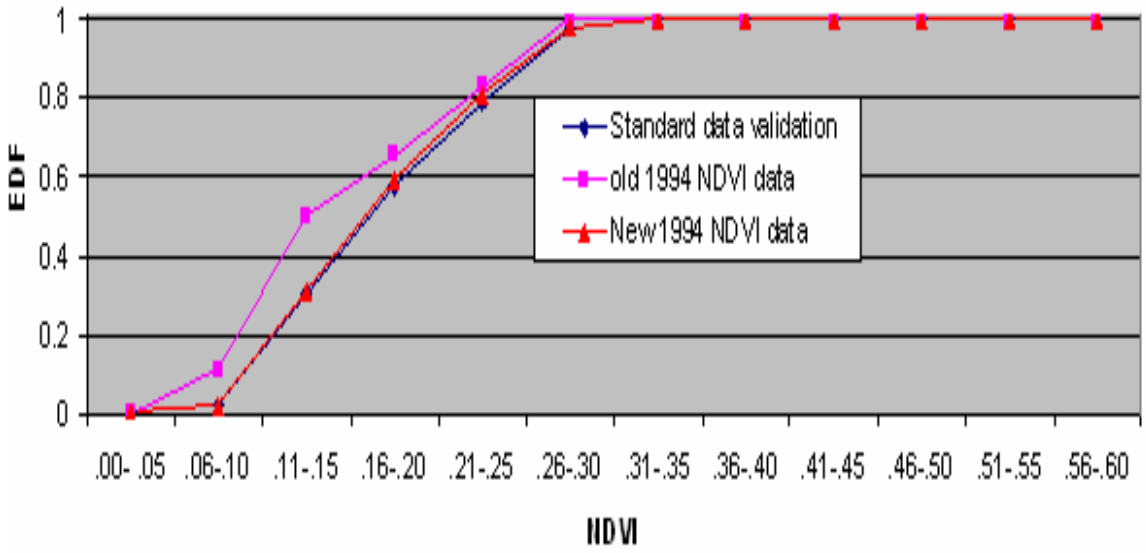

Figure 6.6 (b) Empirical distribution functions for normalized data of 1994 compared with standard data validation sets (subset 2).

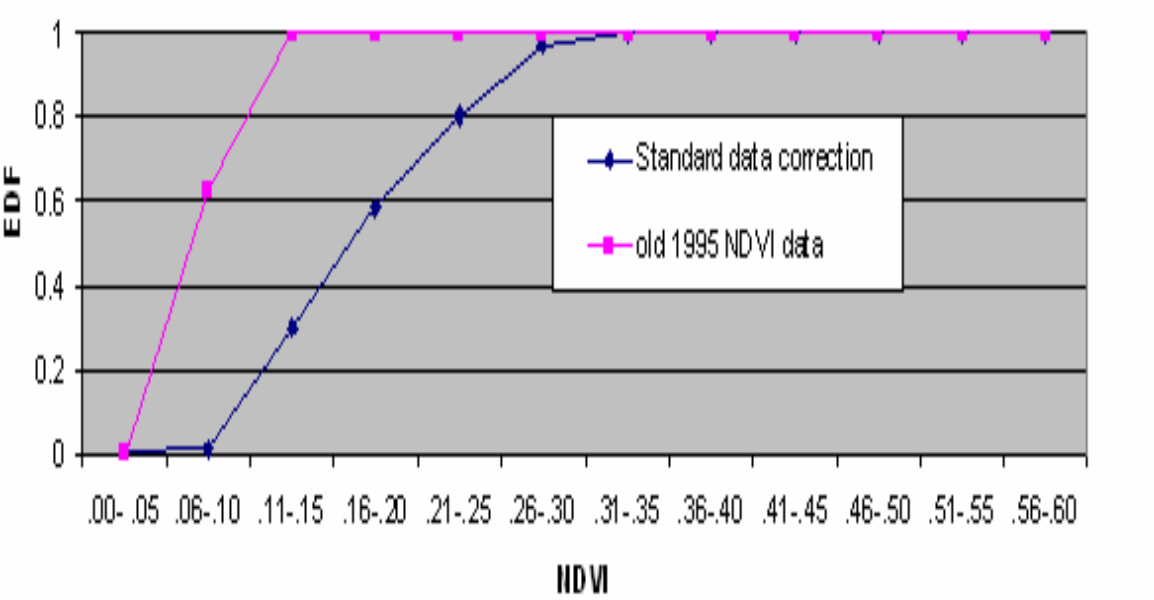

Figure 6.7 (a) Empirical distribution functions for unnormalized data of 1995 compared with standard data correction sets (subset 1).

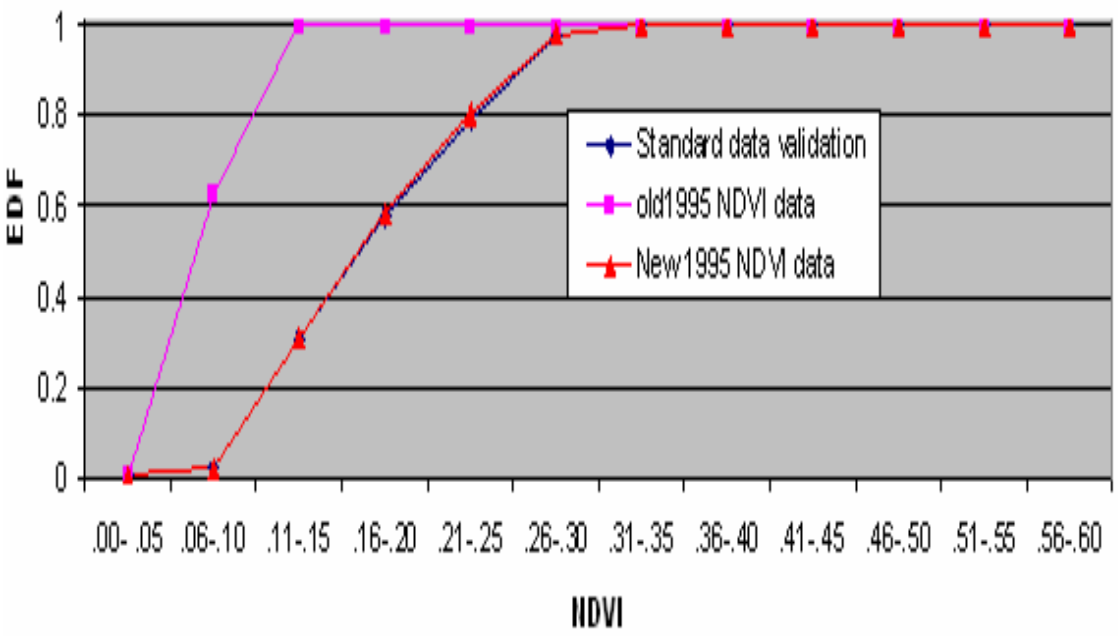

Figure 6.7 (b) Empirical distribution functions for normalized data of 1995 compared with standard data validation sets (subset 2).

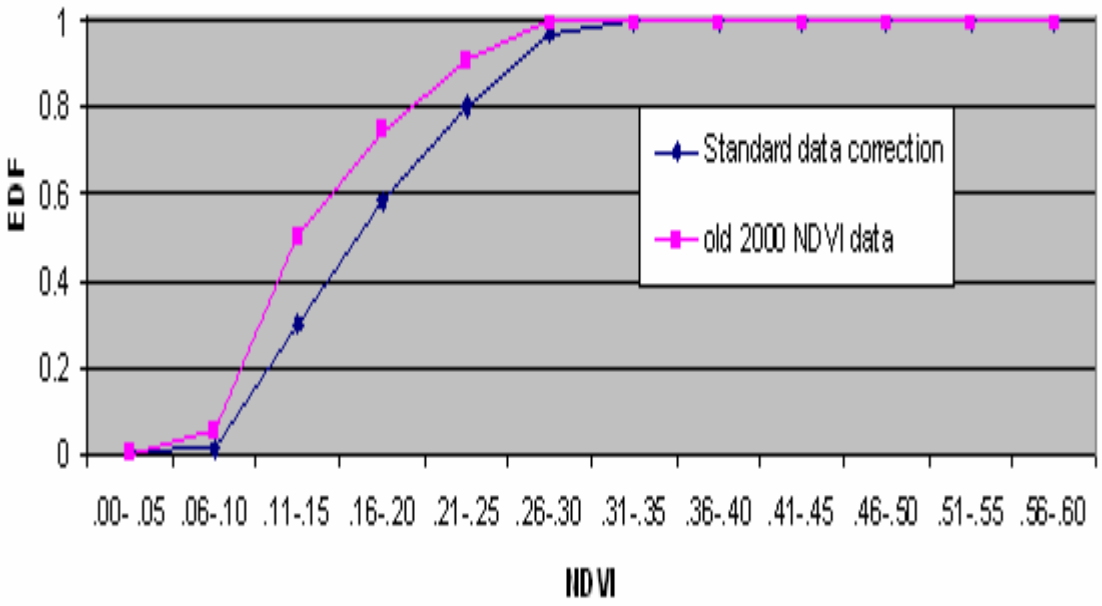

Figure 6.8 (a) Empirical distribution functions for unnormalized data of 2000 compared with standard data correction sets (subset 1).

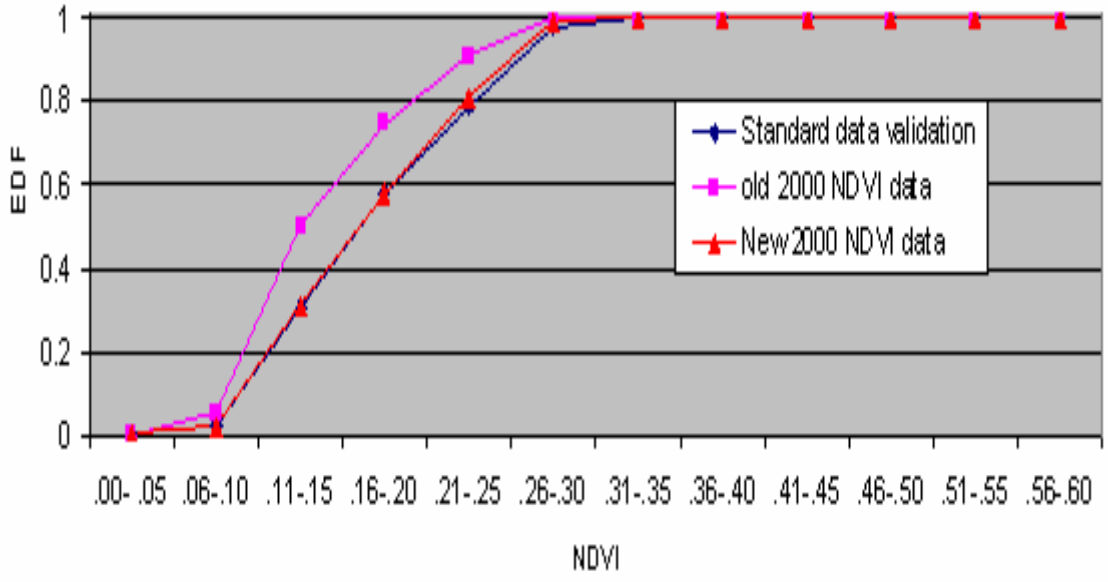

Figure 6.8 (b) Empirical distribution functions for normalized data of 2000 compared with standard data validation sets (subset 2).

Figure 6.3-6.8 (part a) shows the EDF's of unnormalize data for the years 1988, 1992, 1993, 1994, 1995, and 2000 as well as the EDF of the standard data correction sets (subset 1). The abscissa labeled "NDVI" value and ordinate labeled "EDF" (0 to 1). Figure 6.3-6.8 (part b) shows the EDF's of the normalize data for each of those years and indicates that the normalization was successful in making the EDF's of the unnormalized and standard data validation years nearly identical. This implies that the relationships between the EDF's remained essentially the same between two years. Those relationships, in fact, depend only on the relative function between two years. As long as the relative functions remain in the same, the normalization data remain effective. Using normalized value, we produce new NDVI time series for study area in China as shown in Figure 6.9 which shows improve the NDVI data (pink line) of the year of 1988, 1992, 1993, 1994, 1995, and 2000.

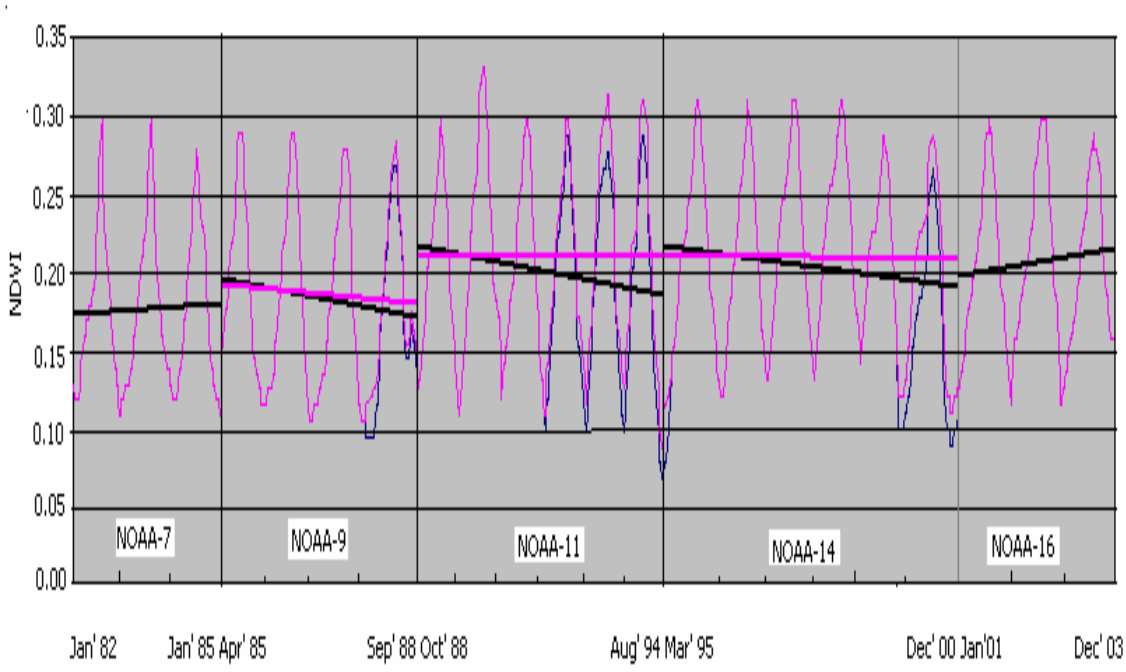

Figure 6.9 New NDVI time series (yearly) for study area in China (old NDVI data—— , and new NDVI data——).

NDVI trends for china and jumps between the satellites are illustrated in Figure 6.9 and the errors are estimated in Table 6.1. Figure 6.9 shows some NDVI trends for each satellite and jump from one satellite to the next one. Considering old NDVI trend (Table 6.1), for china, NOAA-9, -11, and -14 have negative trend and NOAA-7, -16 have positive trend. Therefore, NOAA-7, and -16 shows clear tendency to NDVI increase during its three years in operation. However, important is trend rate. Analysis shows that high rate of NDVI change for NOAA-9,-11, and -14 by reduction of NDVI in 1988, 1992-1994, and 2000 due to elevated amount of stratospheric aerosol from Mt. Pinatubo and considerable degradation of satellite orbit.

Regarding NDVI jump from one satellite to the next in Table 6.1(B), general tendency is a reduction of NDVI between beginning of NOAA-9 and the end of NOAA-7, between beginning of NOAA-16 and the end of NOAA-14. An increase in NDVI is observed only during satellite change from NOAA-9 to NOAA-11, NOAA-11 to NOAA-14, and NOAA-14 to NOAA-16 due to already mentioned sharp stratospheric aerosols increase and orbit drift of satellite.

After correction of NDVI, we also estimate errors (new NDVI) in Table 6.1 of NDVI trends and jumps between the satellites. This table shows improve the NDVI trends for each satellite and jump from one satellite to the next one. But there remain other potential sources of error in NDVI such as an incomplete drift correction, inaccurate NDVI calculation, and influence from Mt. Pinatubo. The EDF method is designed to reduce only errors due to orbit drift, the dominant uncertainty in temperature variation during the satellite life time [50]. However, it may be difficult to accurately and completely remove

this effect and thus orbit remains as an error source, though at a reduced level. Another large uncertainty lies in NDVI calibration and Mt. Pinatubo which includes all errors such as incomplete atmospheric corrections, surface corrections, sensor degradation and volcanic eruptions.

Table 6.1: Estimation of Errors in (A) NDVI trend at the End of a Satellite Life and (B) Jumps between the Satellites (% to the beginning level)

Target		A					B			
		N-7	N-9	N-11	N-14	N-16	N-7/9	N-9/11	N-11/14	N-14/16
China	Old NDVI	3	-10	-12	-11	7	10	30	16	5
	New NDVI	3	-5	0	0	7	7	19	0	-5

6.2 Analysis of NDVI Time Series for China

We extract the NDVI data for China from the original data set. We divide whole China area into rectangles based (Figure 6.10) on longitude and latitude. Then we use the following formula to convert row and column score corresponding to longitude and

Figure 6.10 Geographical location of study area in China

latitude. These row and column scores are used to segment data from the original data set: [36]

$$\text{Column} = \text{longitude} * 2500/360 + 1250 \quad (6.1)$$

$$\text{Row} = -\text{Lattitude} * 904/130+523 \quad (6.2)$$

We produce NDVI time series for China which is illustrated in Figure 6.11. The comparison of NDVI time series with the original NDVI time series (Figure 6.1) shows that both time series are almost similar but NDVI value varies from year to year. Based our comparison of the two data sets, the NDVI data for China shows similar results. Therefore, we apply the method of empirical distribution functions to correct the data for

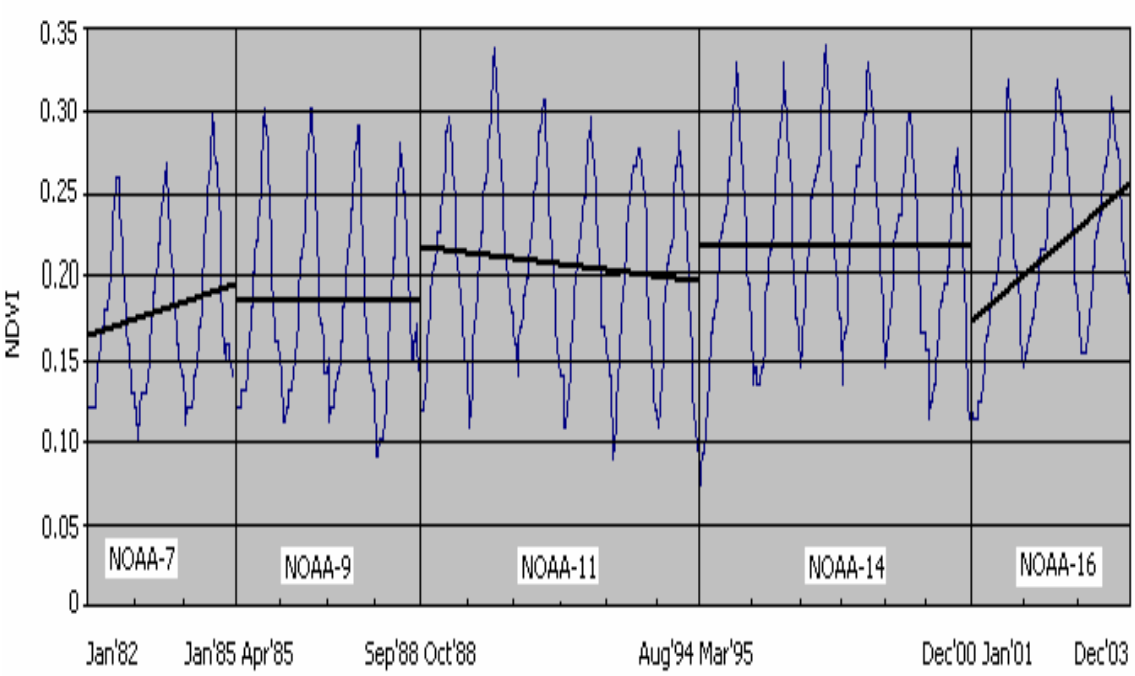

Figure 6.11 NDVI time series (yearly) for study area in China

affected years. We normalize data by the EDF's compared with standard data correction sets (subset 1) according to equations 5.3 and 5.4. Then corrected or normalized data for this years compared with subset 2 (standard data validation sets) which provides NDVI data for these years that match in subset 2.

Using this technique, we produced EDF's to normalize or correct data for the years 1988, 1992, 1993, 1994, and 2000 compared with standard data correction sets (subset 1) and

then corrected or normalized data compared with standard data validation sets (subset 2) which are illustrated in following Figures.

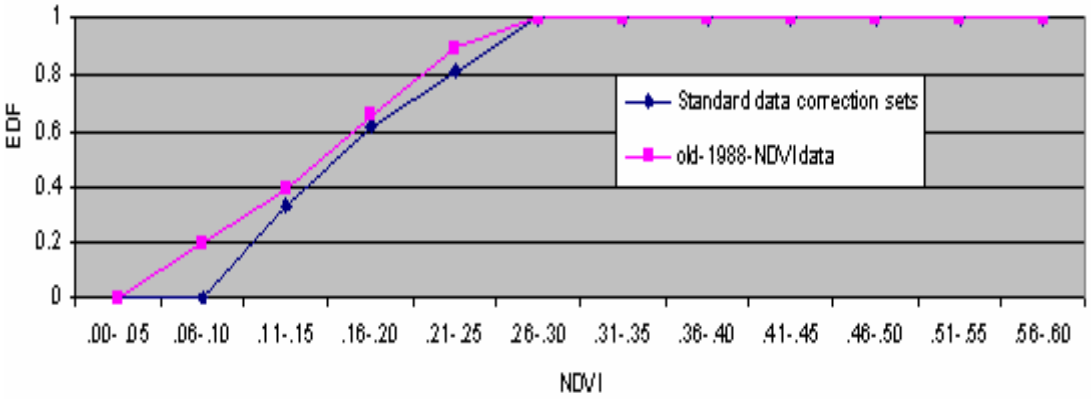

Figure 6.12 (a) Empirical distribution functions for unnormalized data of 1988 compared with standard data correction sets (subset 1).

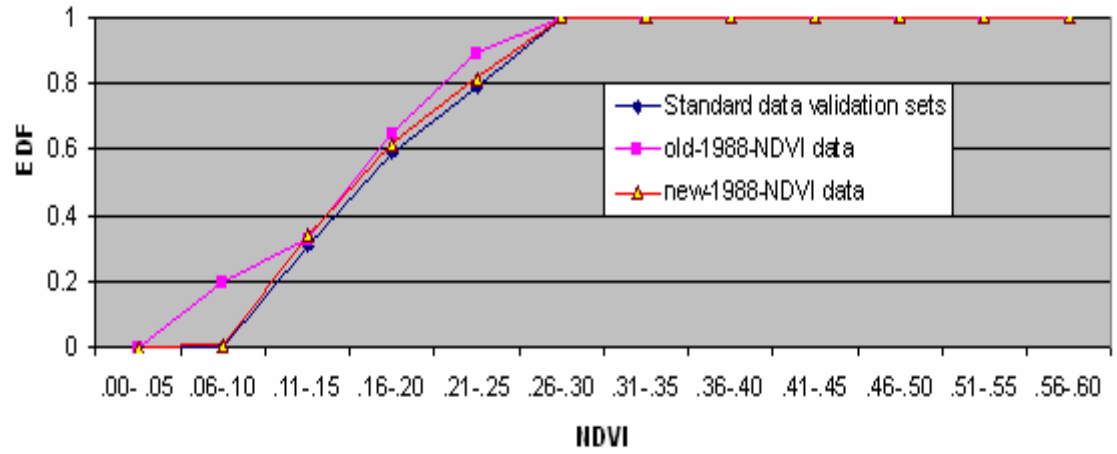

Figure 6.12 (b) Empirical distribution functions for normalized data of 1988 compared with standard data validation sets (subset 2).

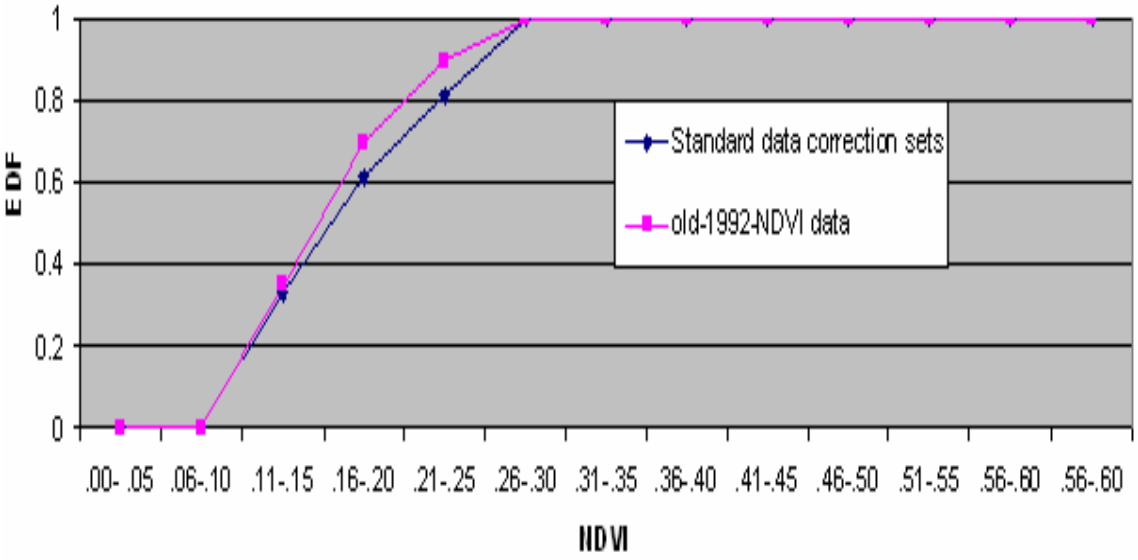

Figure 6.13 (a) Empirical distribution functions for unnormalized data of 1992 compared with standard data correction sets (subset 1).

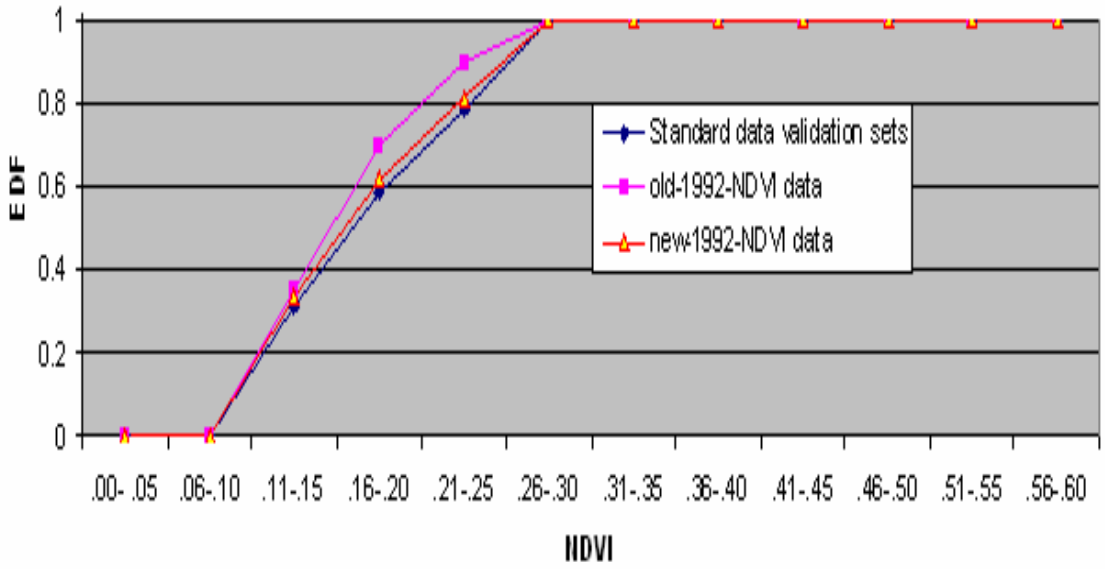

Figure 6.13 (b) Empirical distribution functions for normalized data of 1992 compared with standard data validation sets (subset 2).

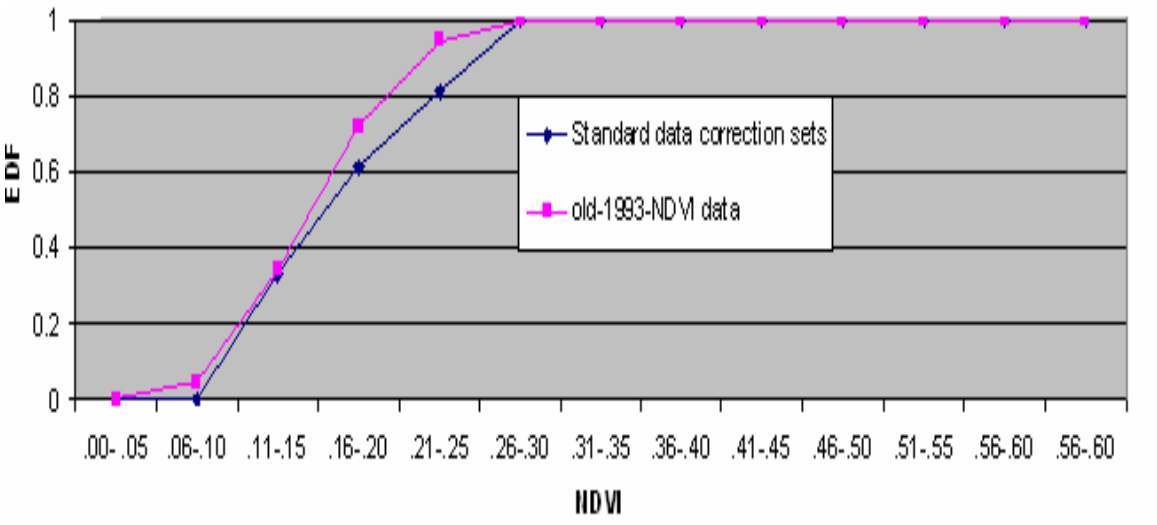

Figure 6.14 (a) Empirical distribution functions for unnormalized data of 1993 compared with standard data correction sets (subset 1).

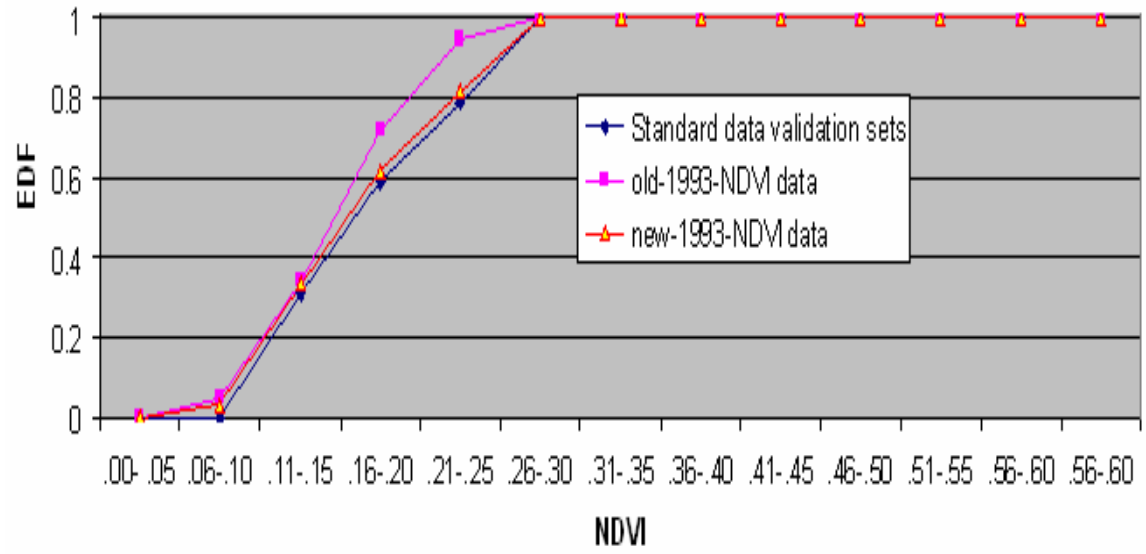

Figure 6.14 (b) Empirical distribution functions for normalized data of 1993 compared with standard data validation sets (subset 2).

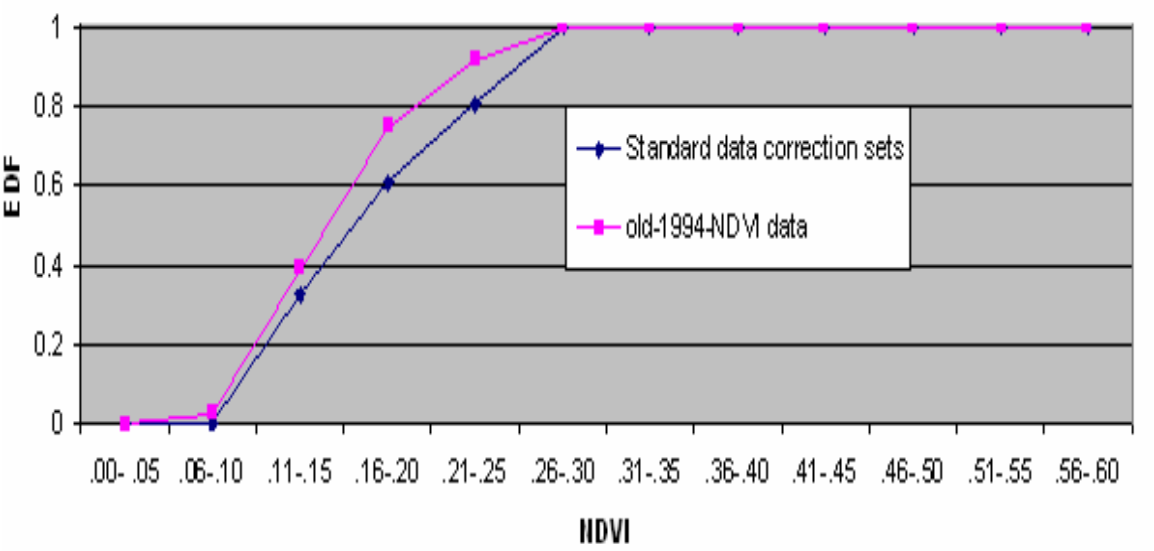

Figure 6.15 (a) Empirical distribution functions for unnormalized data of 1994 compared with standard data correction sets (subset 1).

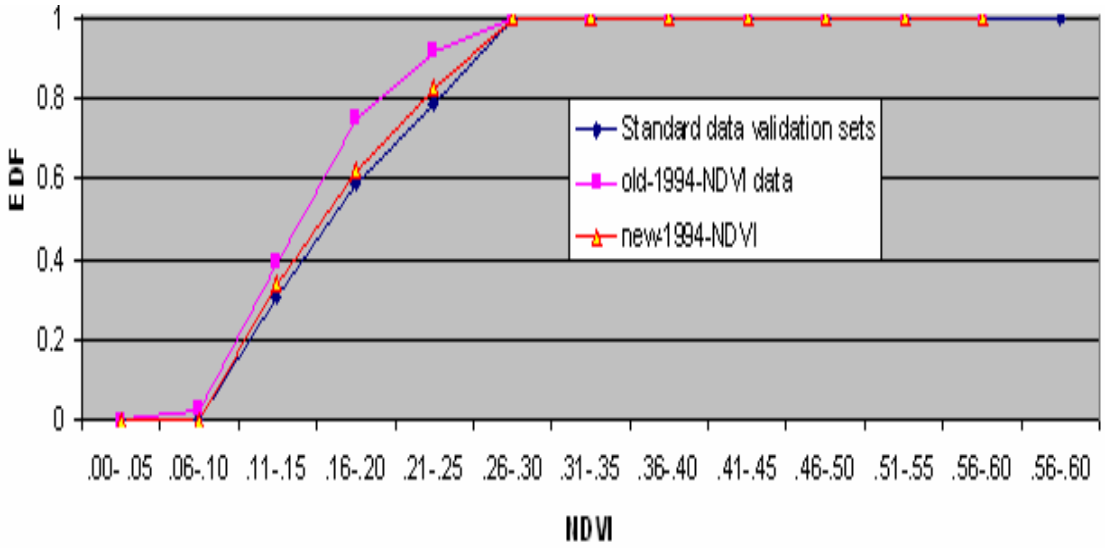

Figure 6.15 (b) Empirical distribution functions for normalized data of 1994 compared with standard data validation sets (subset 2).

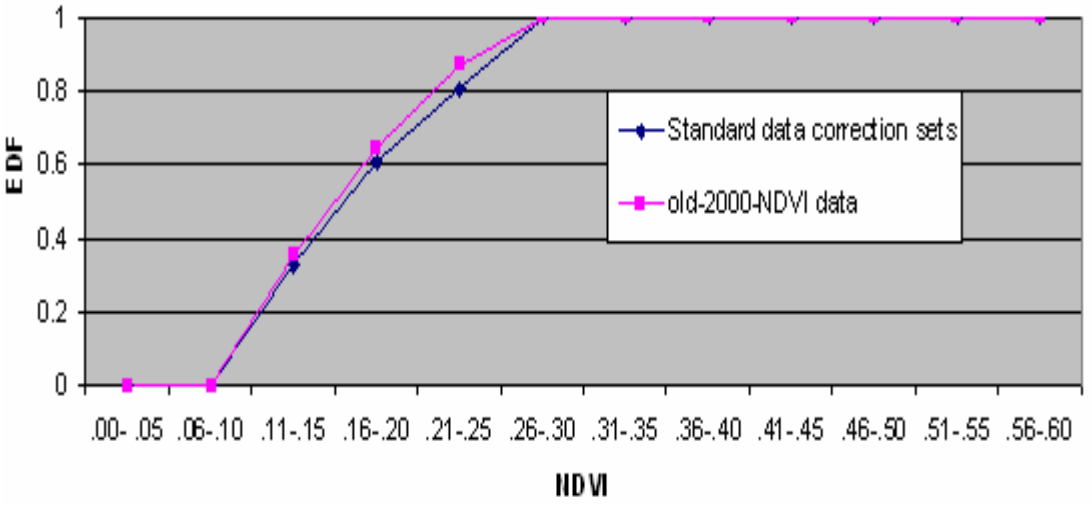

Figure 6.16 (a) Empirical distribution functions for unnormalized data of 2000 compared with standard data correction sets (subset 1).

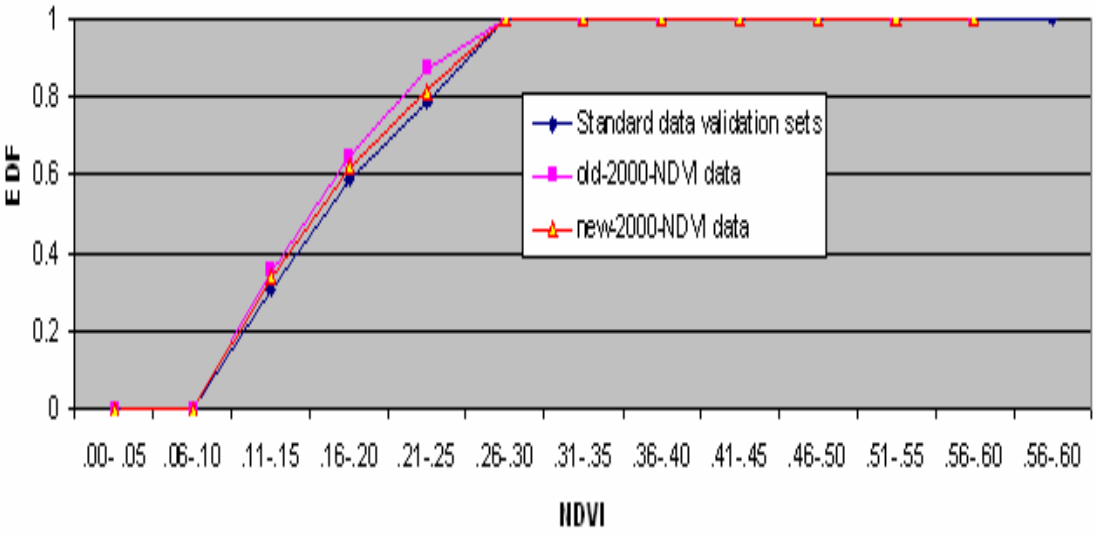

Figure 6.16 (b) Empirical distribution functions for normalized data of 2000 compared with standard data validation sets (subset 2).

Using normalized NDVI value, we produce new NDVI time series for study area in China as shown in Figure 6.17 which shows improvement of the NDVI data (pink line) of the year of 1988, 1992, 1993, 1994, and 2000.

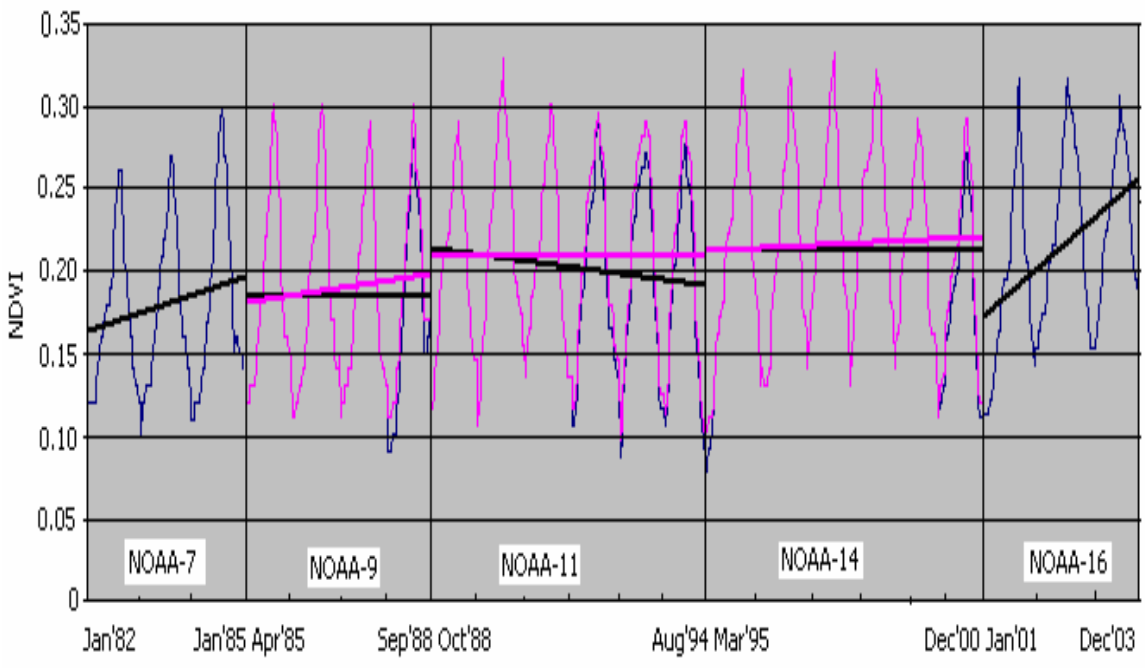

Figure 6.17 New NDVI time series (yearly) for study area in China

(old NDVI —, new NDVI —)

6.3 Analysis of NDVI Time Series for Different Ecosystems in China

In this section, we produce NDVI time series for different ecosystems in China such as desert, grassland, mixed, and forests separately as shown in Figure 6.18. The differences of ecosystem component become more apparent which is due to weather variation. For example in unfavorable weather (mostly dry and hot) the NDVI curve will be lower than in normal and wet weather (forest).

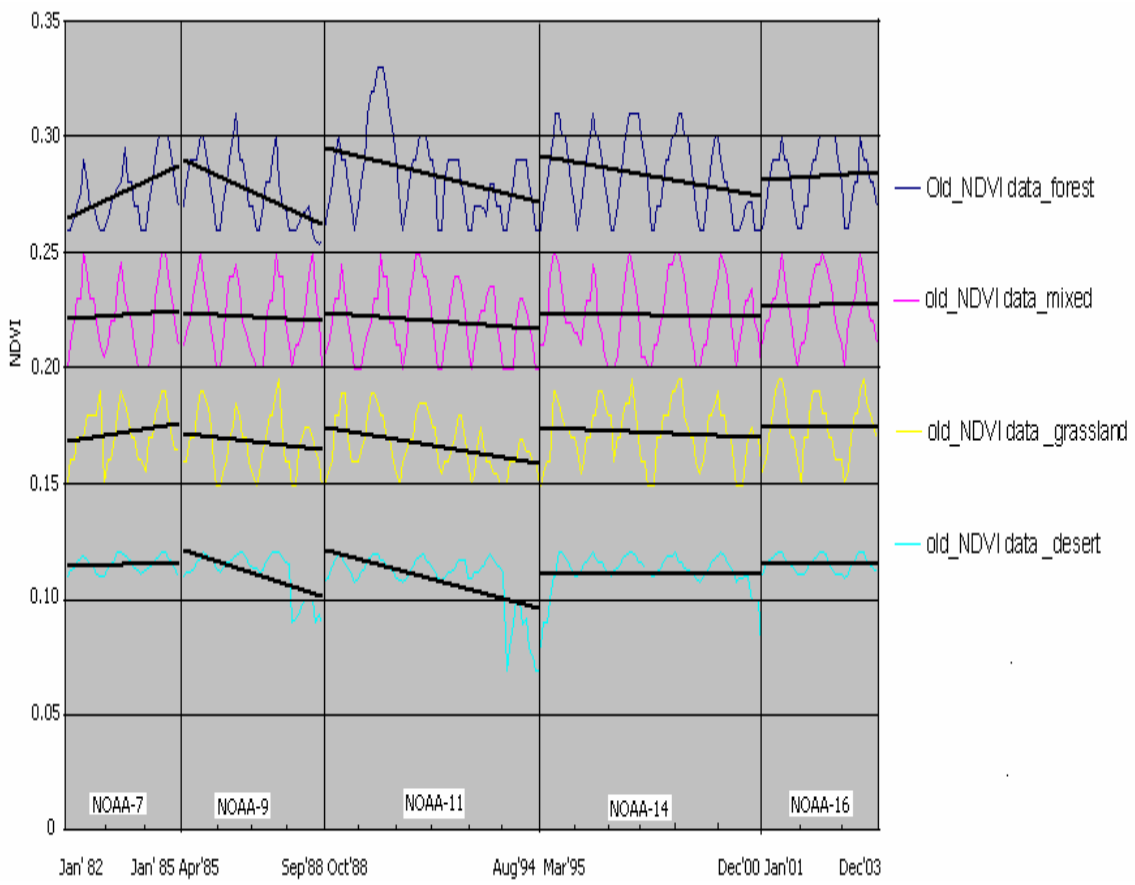

Figure 6. 18. NDVI time series (yearly) for different ecosystems in selected study area of China

Figure 6.18 shows that data are not uniform compare to other years because of satellite orbit drift and sensor degradation. Therefore, we need to correct the data of the year of

1988, 1992, 1993, 1994, 1995 (week#1-8), and 2000 for different ecosystems. We normalize the NDVI data by EDF compared with standard data correction sets according to equation 5.3-5.4 for affected years which are illustrated in following figures.

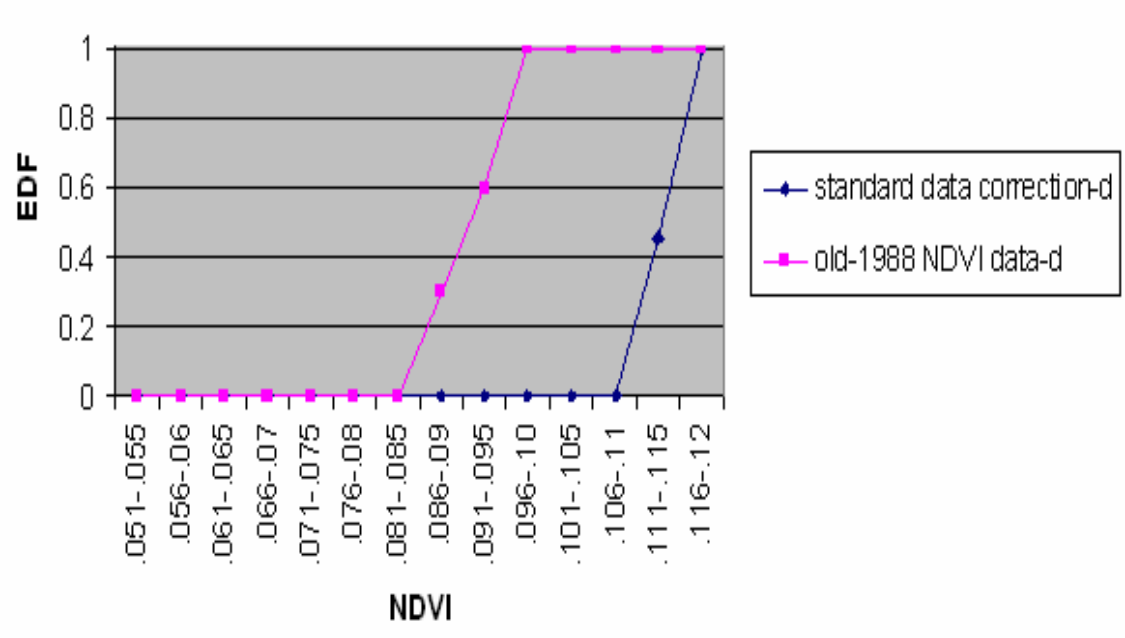

Figure 6.19 (a) Empirical distribution functions for unnormalized NDVI data (d-desert) of 1988 compared with standard data correction sets (subset 1).

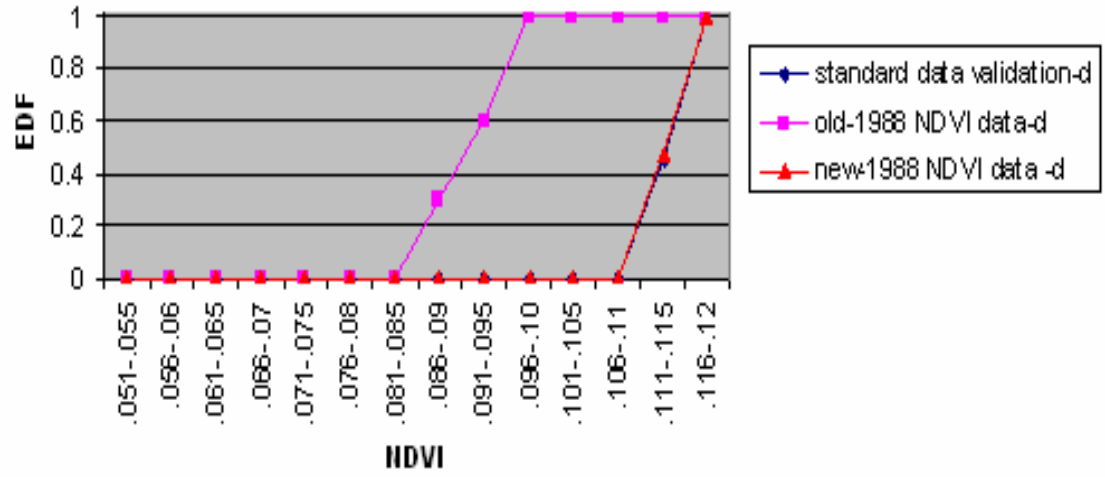

Figure 6.19 (b) Empirical distribution functions for normalized NDVI data (d-desert) of 1988 compared with standard validation sets (subset 2).

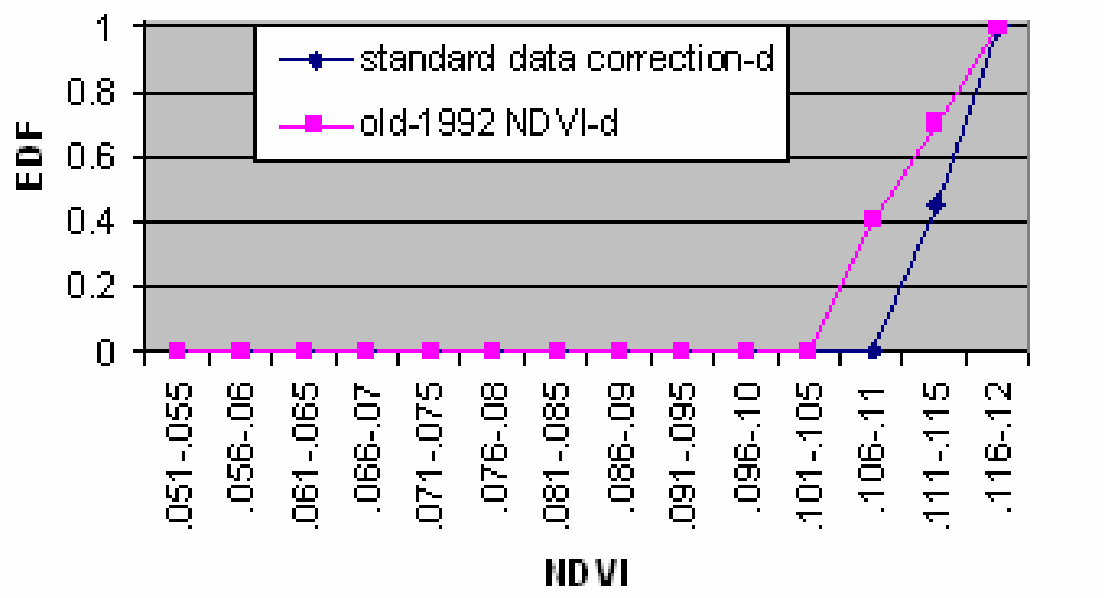

Figure 6.20 (a) Empirical distribution functions for unnormalized NDVI data (d-desert) of 1992 compared with standard data correction sets (subset 1).

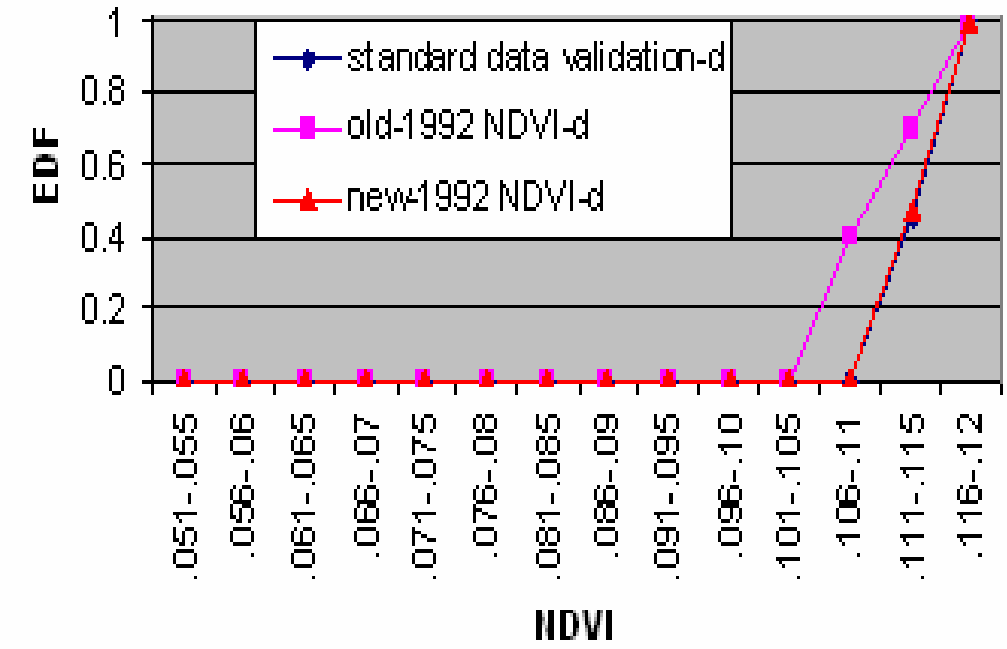

Figure 6.20 (b) Empirical distribution functions for normalized NDVI data (d-desert) of 1992 compared with standard data validation sets (subset 2).

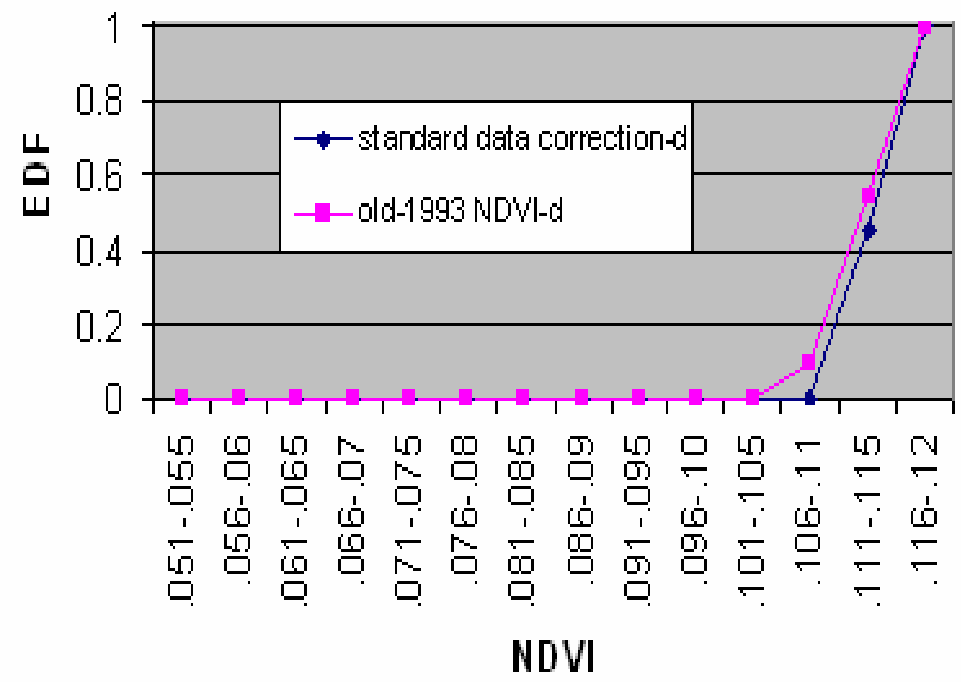

Figure 6.21 (a) Empirical distribution functions for unnormalized NDVI data (d-desert) of 1993 compared with standard data correction sets (subset 1).

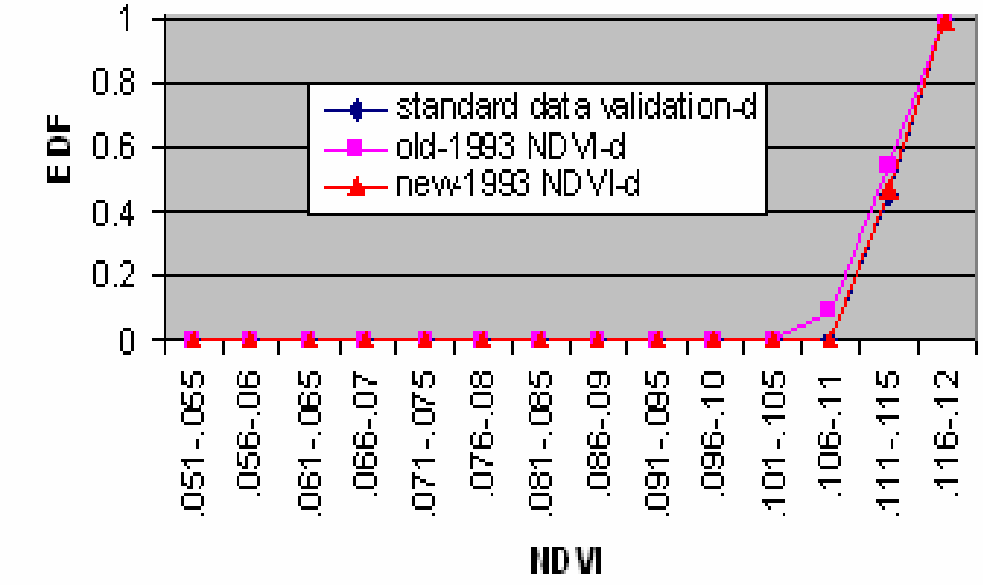

Figure 6.21 (b) Empirical distribution functions for normalized NDVI data (d-desert) of 1993 compared with standard data validation sets (subset 2).

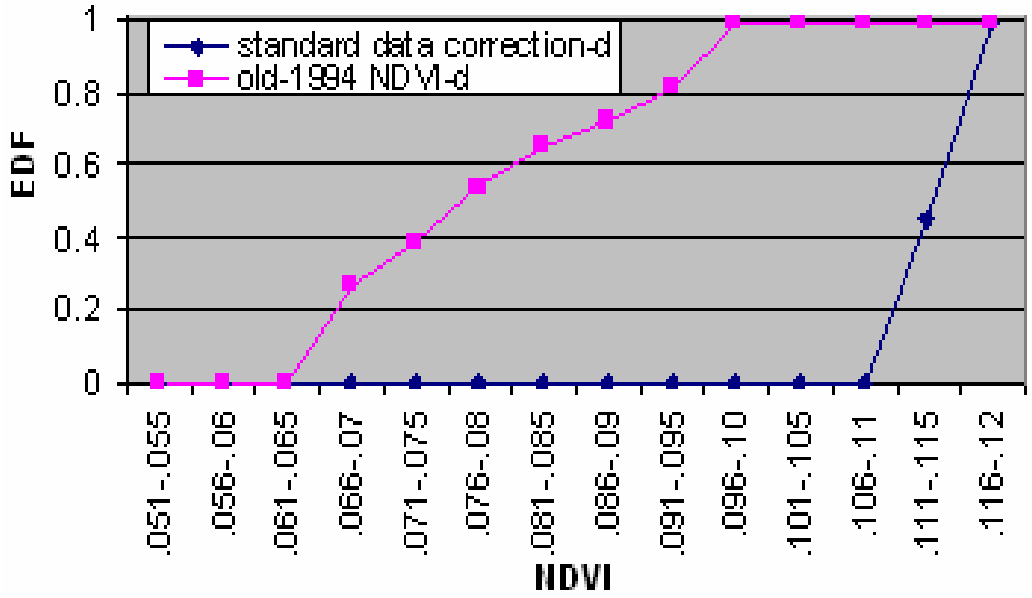

Figure 6.22 (a) Empirical distribution functions for unnormalized NDVI data (d-desert) of 1994 compared with standard data correction sets (subset 1).

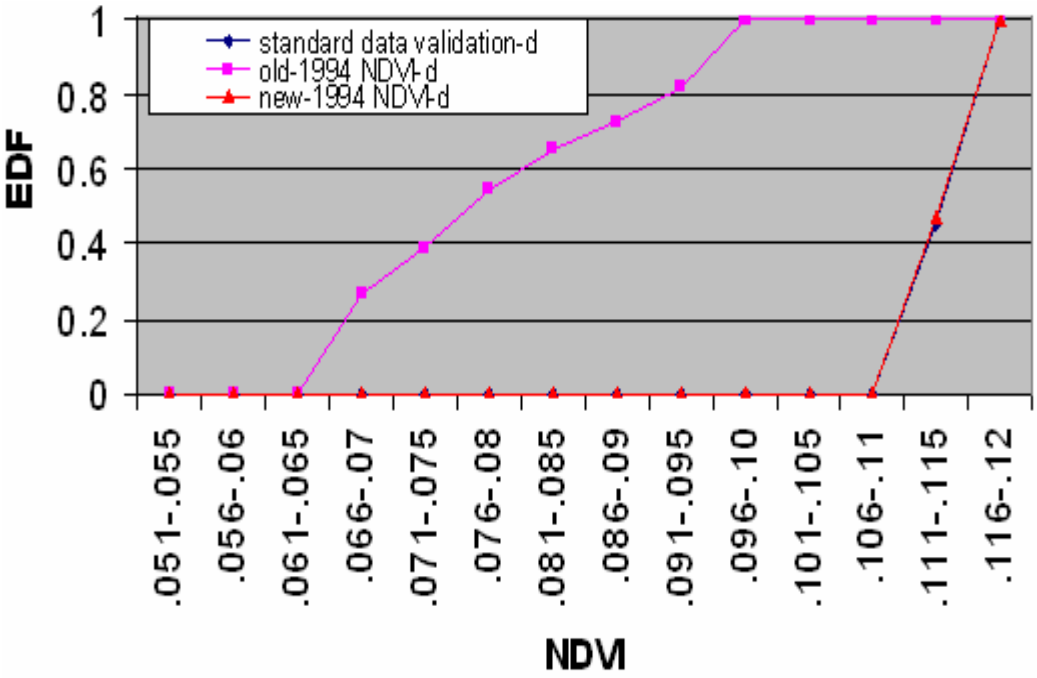

Figure 6.22 (b) Empirical distribution functions for normalized NDVI data (d-desert) of 1994 compared with standard data validation sets (subset 2).

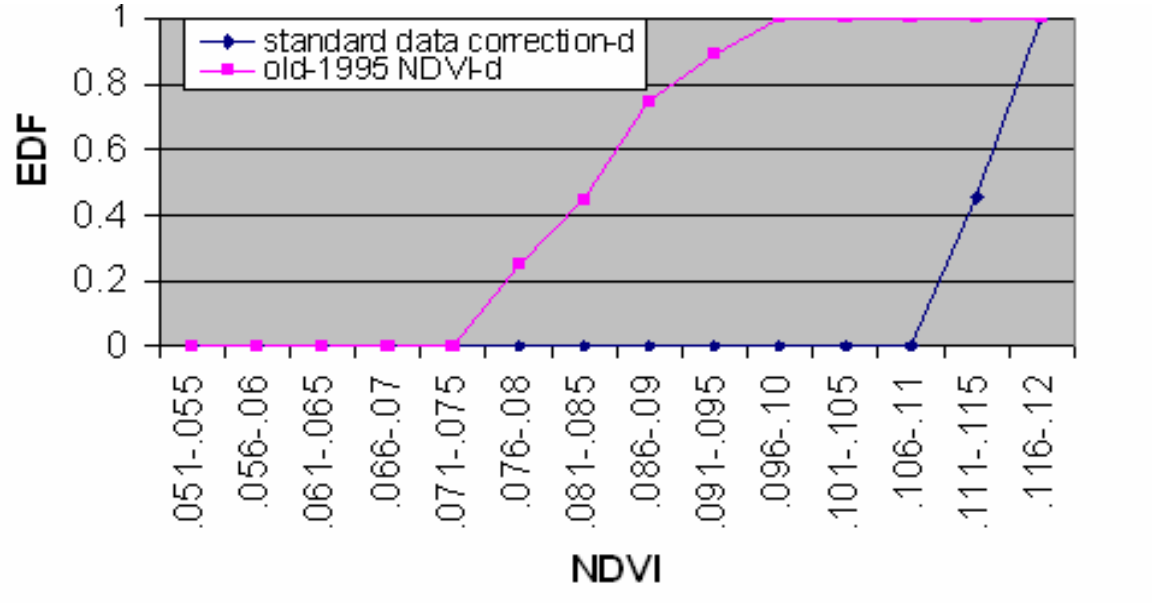

Figure 6.23 (a) Empirical distribution functions for unnormalized NDVI data (d-desert) of 1995 compared with standard data correction sets (subset 1).

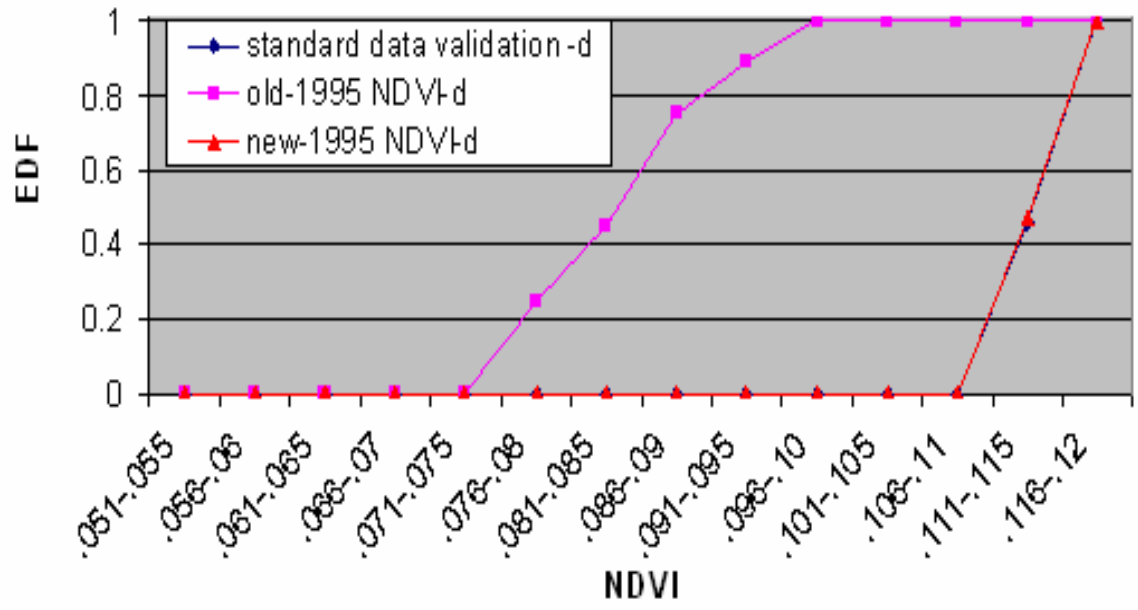

Figure 6.23 (b) Empirical distribution functions for normalized NDVI data (d-desert) of 1995 compared with standard data validation sets (subset 2).

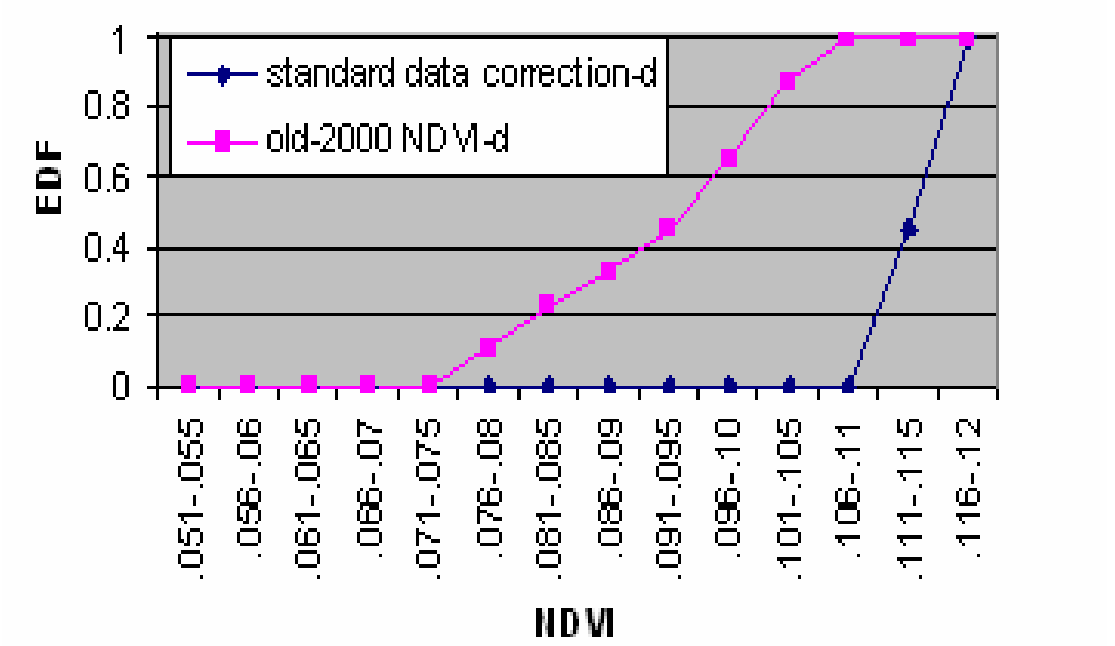

Figure 6.24 (a) Empirical distribution functions for unnormalized NDVI data (d-desert) of 2000 compared with standard data correction sets (subset 1).

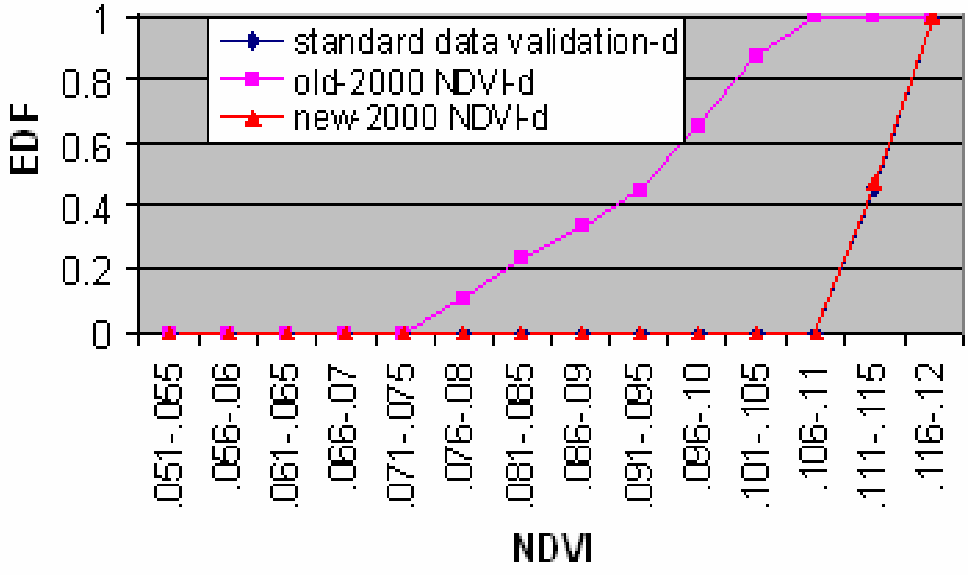

Figure 6.24 (b) Empirical distribution functions for normalized NDVI data (d-desert) of 2000 compared with standard data validation sets (subset 2).

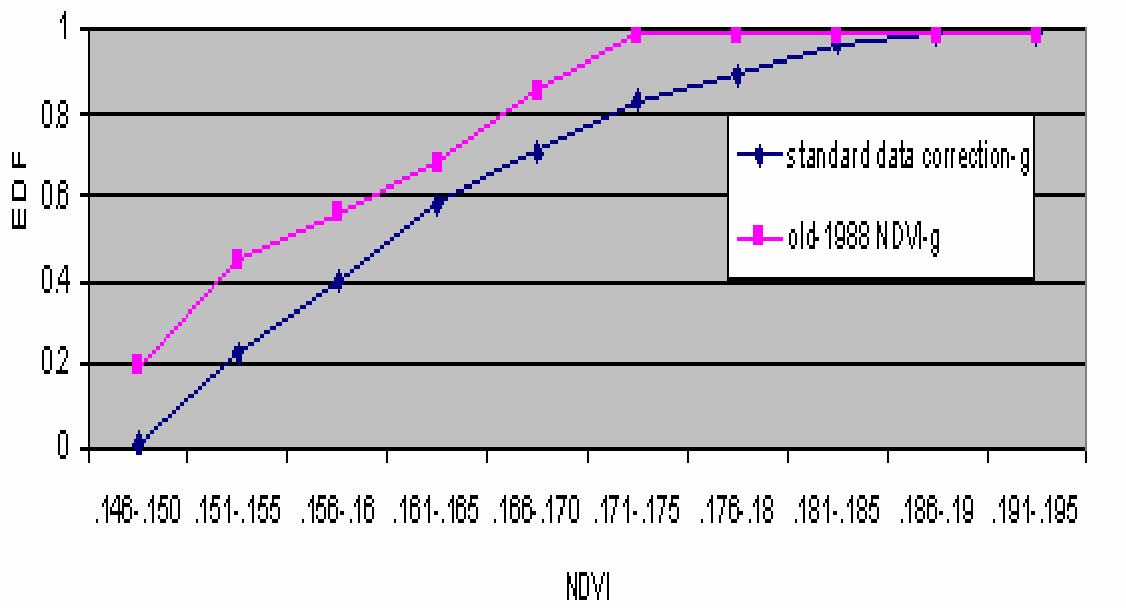

Figure 6.25 (a) Empirical distribution functions for unnormalized NDVI data (g-grassland) of 1998 compared with standard data correction sets (subset 1).

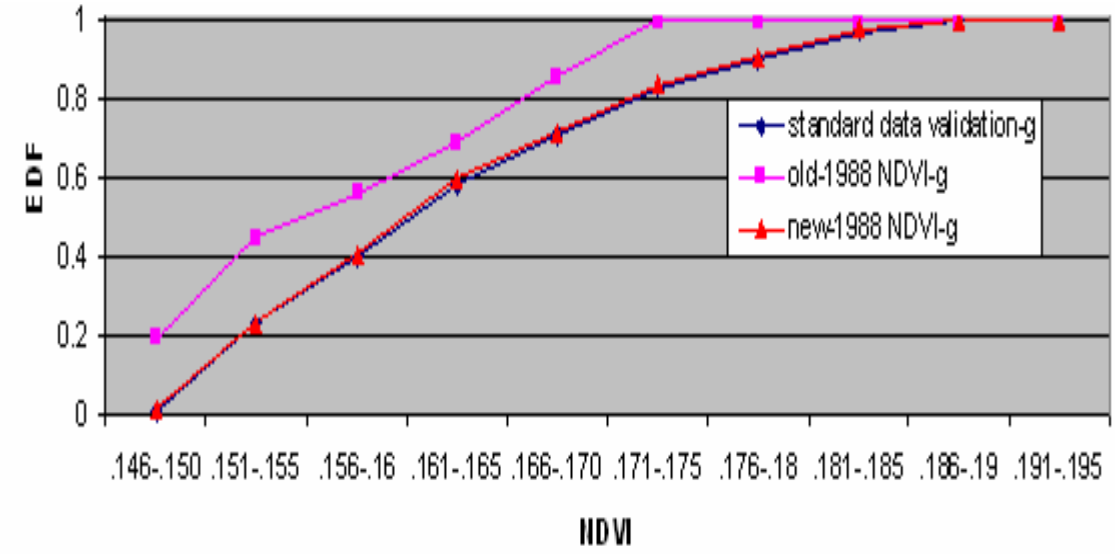

Figure 6.25 (b) Empirical distribution functions for normalized NDVI data (g-grassland) of 1998 compared with standard data validation sets (subset 2).

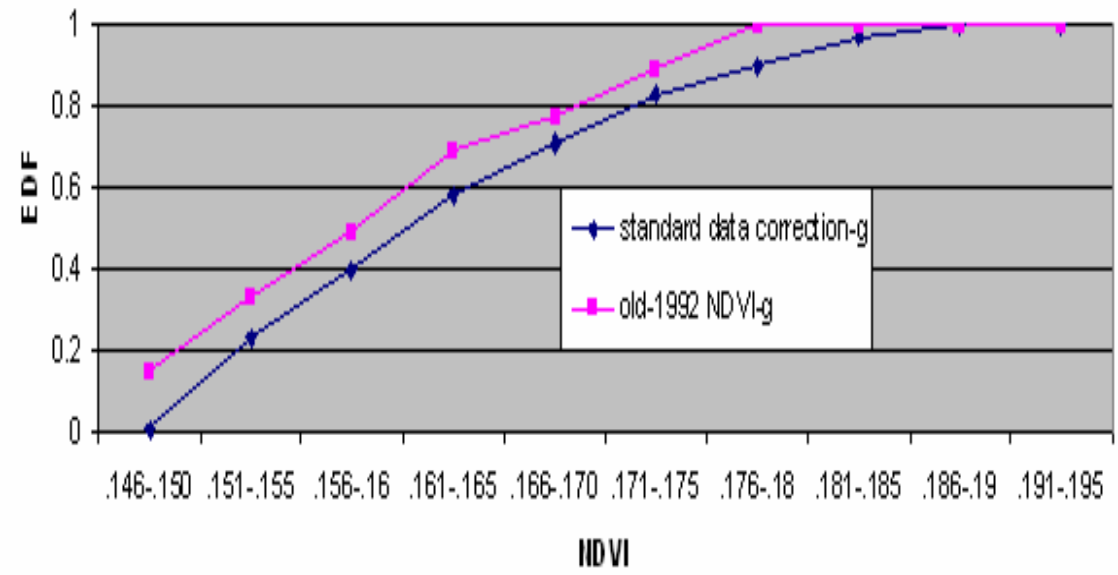

Figure 6.26 (a) Empirical distribution functions for unnormalized NDVI data (g grassland) of 1992 compared with standard data correction sets (subset 1).

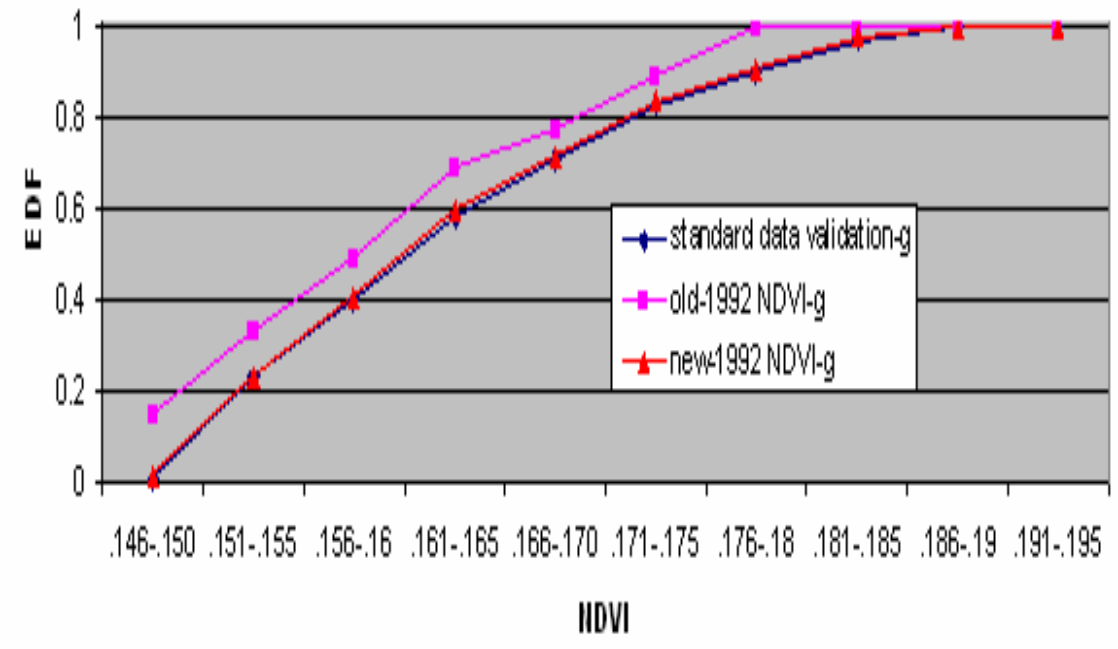

Figure 6.26 (b) Empirical distribution functions for normalized NDVI data (g-grassland) of 1992 compared with standard data validation sets (subset 2).

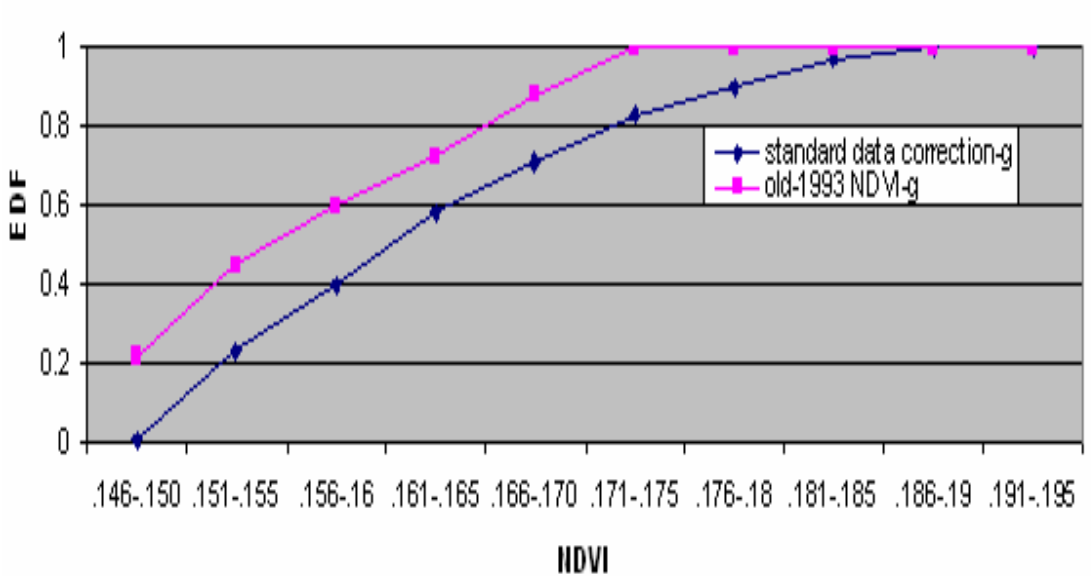

Figure 6.27 (a) Empirical distribution functions for unnormalized NDVI data (g-grassland) of 1993 compared with standard data correction sets (subset 1).

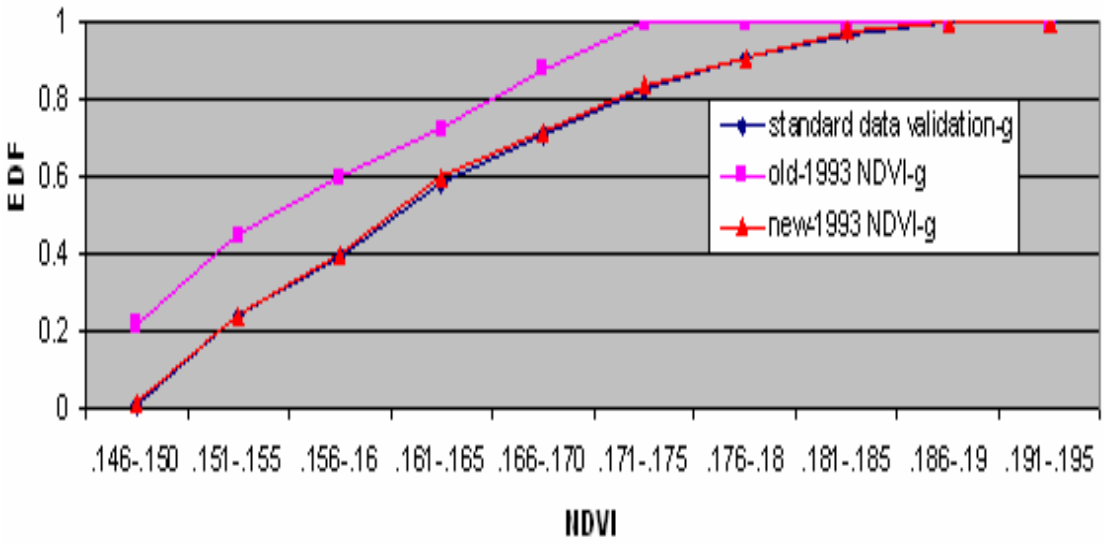

Figure 6.27 (b) Empirical distribution functions for normalized NDVI data (g-grassland) of 1993 compared with standard data validation sets (subset 2).

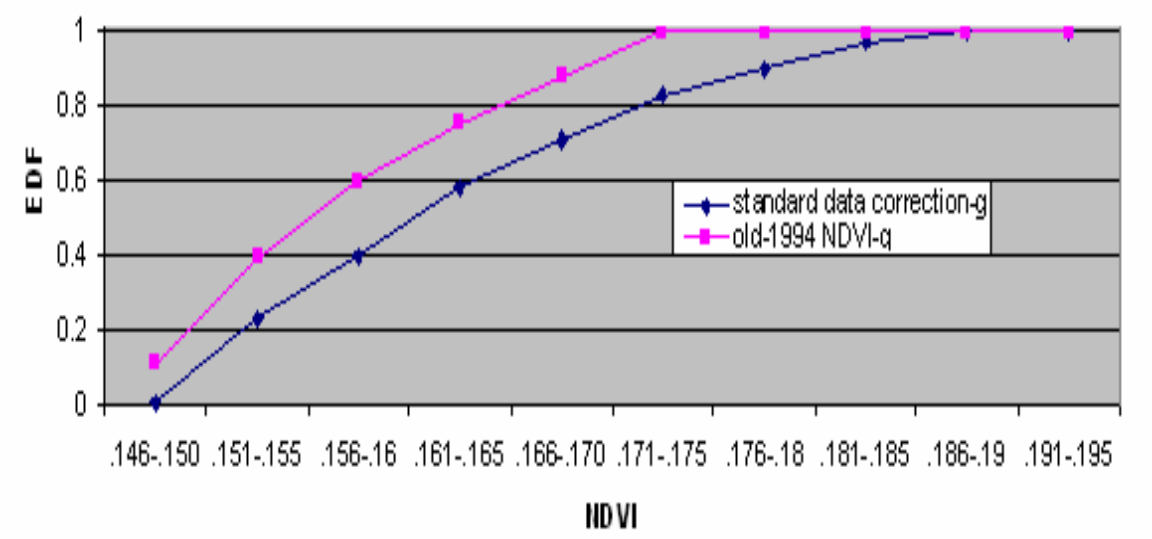

Figure 6.28 (a) Empirical distribution functions for unnormalized NDVI data (g-grassland) of 1994 compared with standard data correction sets (subset 1).

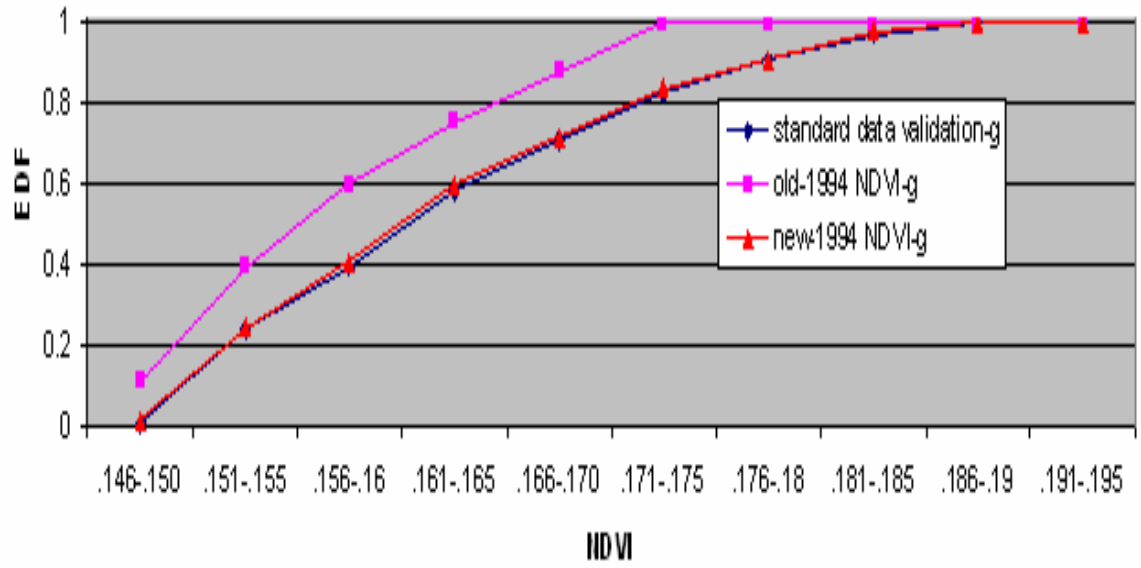

Figure 6.28 (b) Empirical distribution functions for normalized NDVI data (g-grassland) of 1994 compared with standard data validation sets (subset 2).

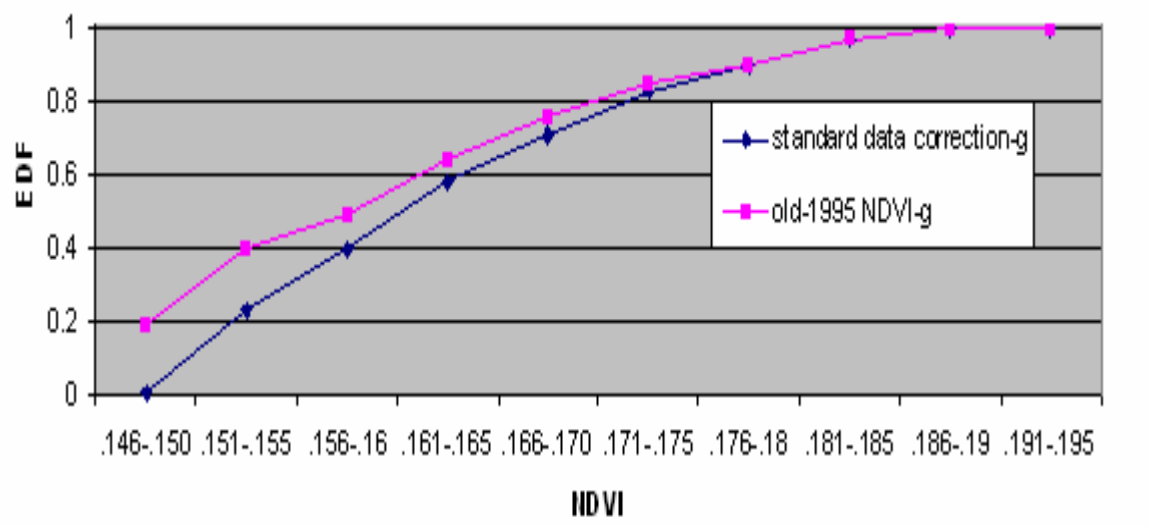

Figure 6.29 (a) Empirical distribution functions for unnormalized NDVI data (g-grassland) of 1995 compared with standard data correction sets (subset 1).

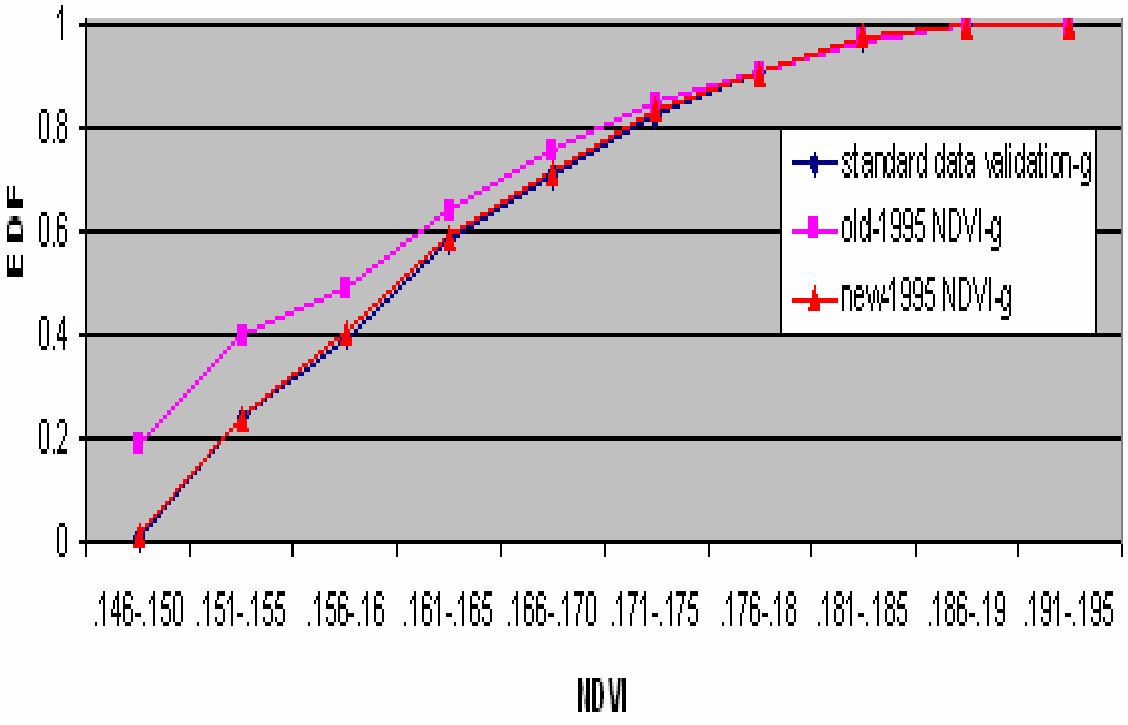

Figure 6.29 (b) Empirical distribution functions for normalized NDVI data (g-grassland) of 1995 compared with standard data validation sets (subset 2).

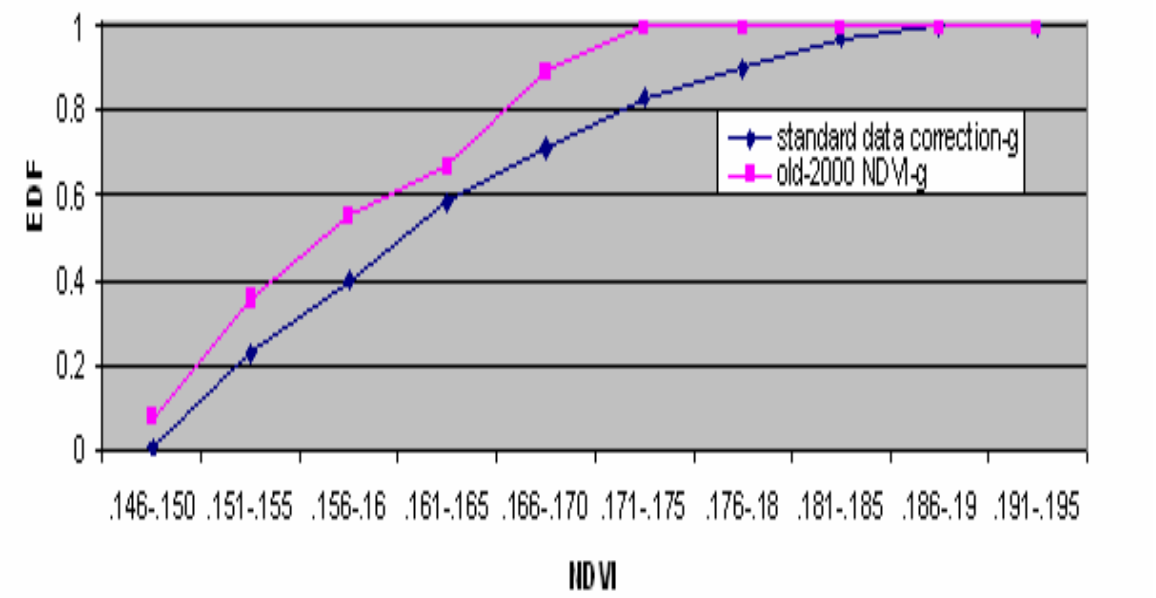

Figure 6.30 (a) Empirical distribution functions for unnormalized NDVI data (g-grassland) of 2000 compared with standard data correction sets (subset 1).

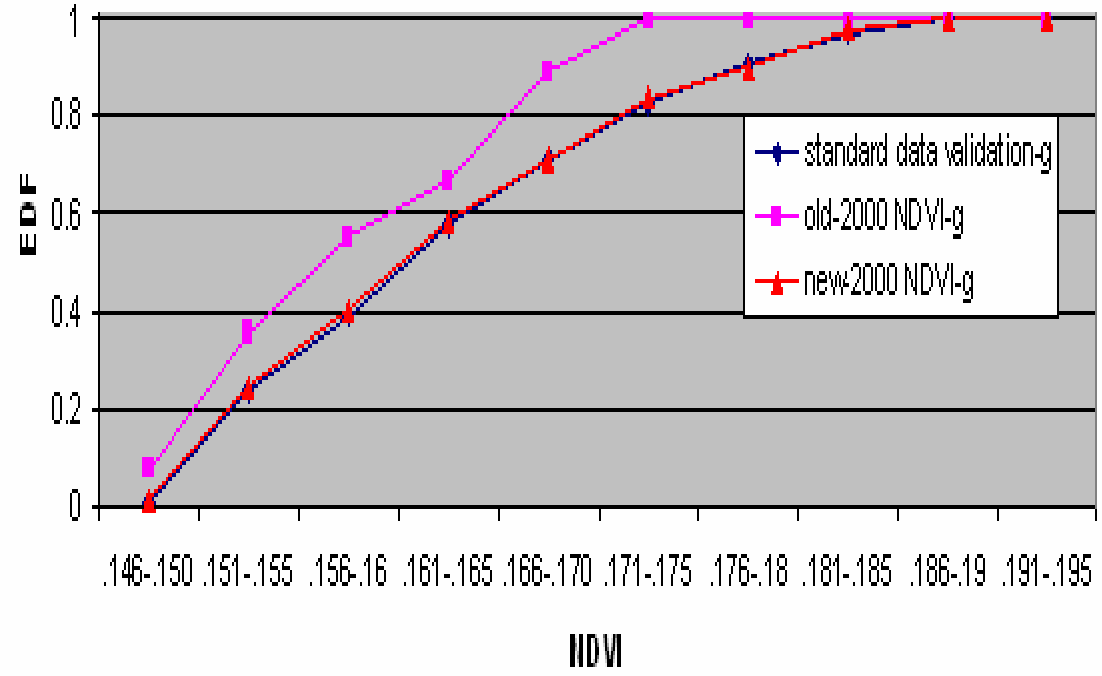

Figure 6.30 (b) Empirical distribution functions for normalized NDVI data (g-grassland) of 2000 compared with standard data validation sets (subset 2).

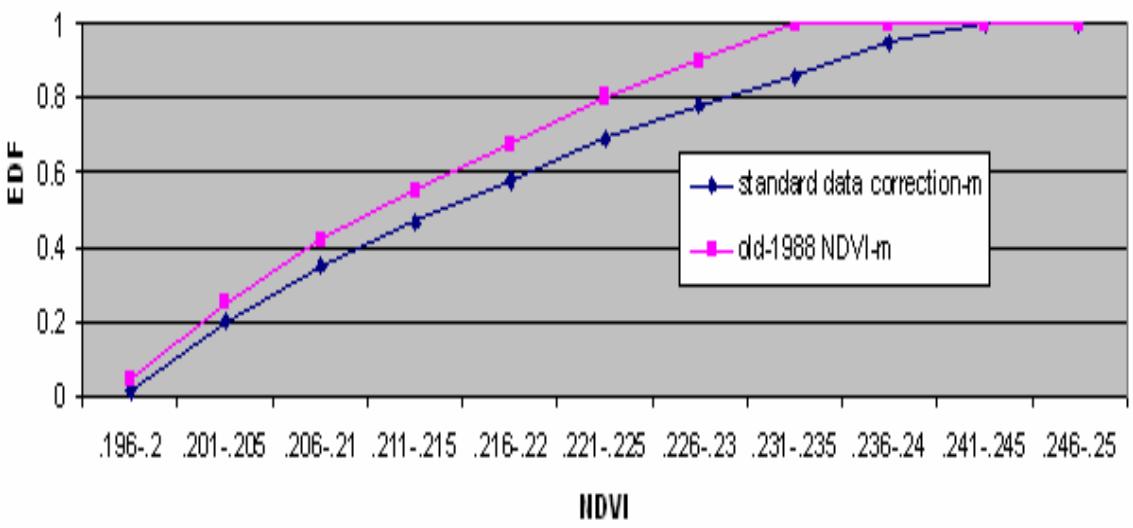

Figure 6.31 (a) Empirical distribution functions for unnormalized NDVI data (m-mixed) of 1988 compared with standard data correction sets (subset 1).

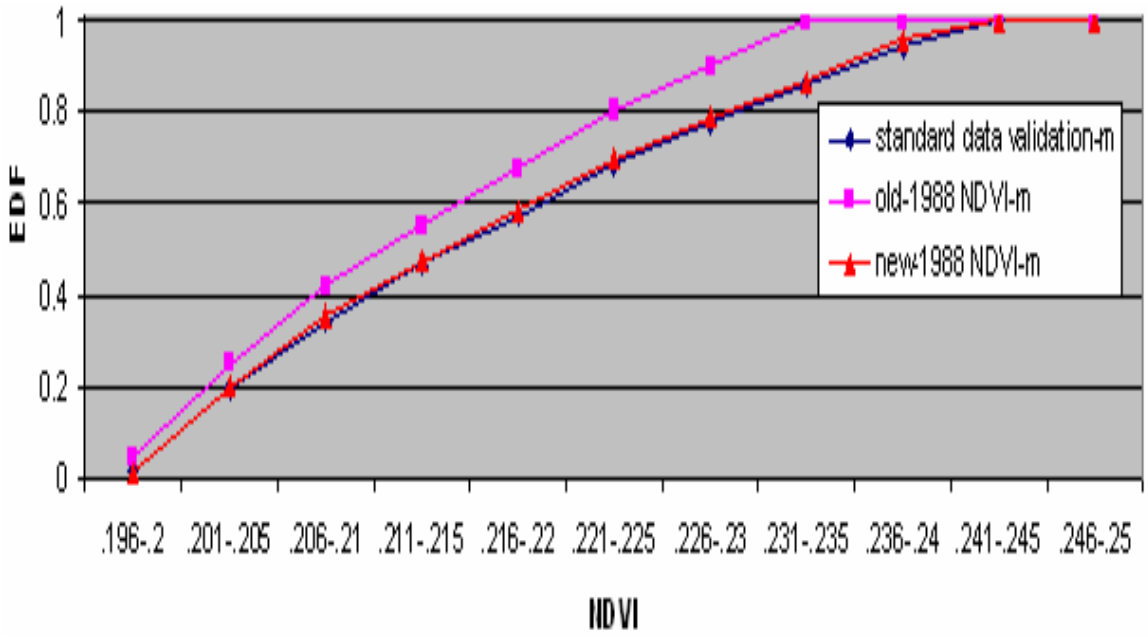

Figure 6.31 (b) Empirical distribution functions for normalized NDVI data (m-mixed) of 1988 compared with standard data validation sets (subset 2).

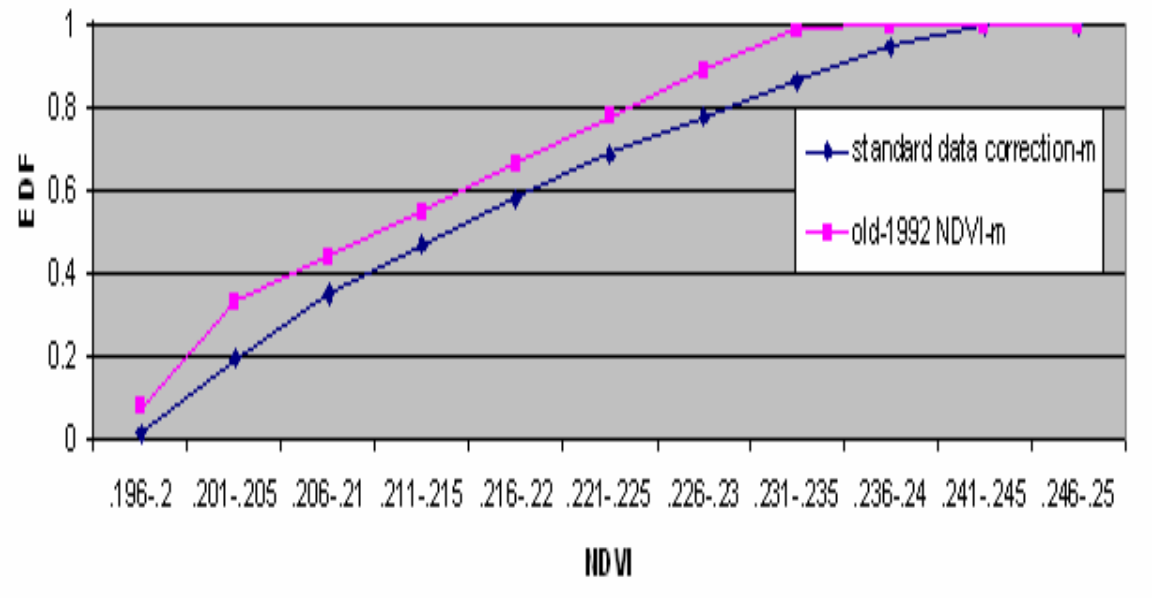

Figure 6.32 (a) Empirical distribution functions for unnormalized NDVI data (m-mixed) of 1992 compared with standard data correction sets (subset 1).

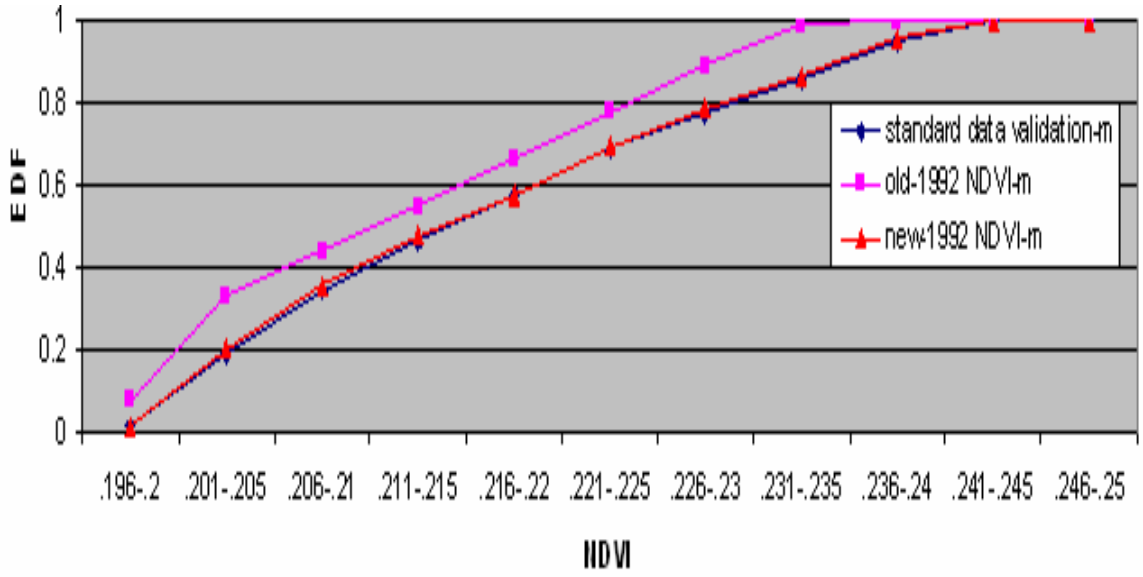

Figure 6.32 (b) Empirical distribution functions for normalized NDVI data (m-mixed) of 1992 compared with standard data validation sets (subset 2).

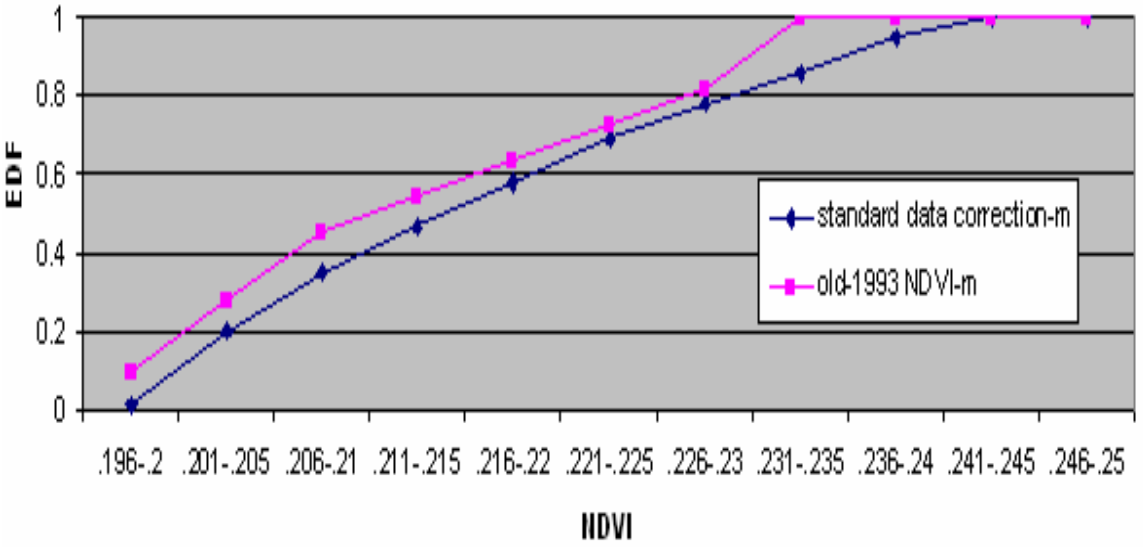

Figure 6.33 (a) Empirical distribution functions for unnormalized NDVI data (m-mixed) of 1993 compared with standard data correction sets (subset 1).

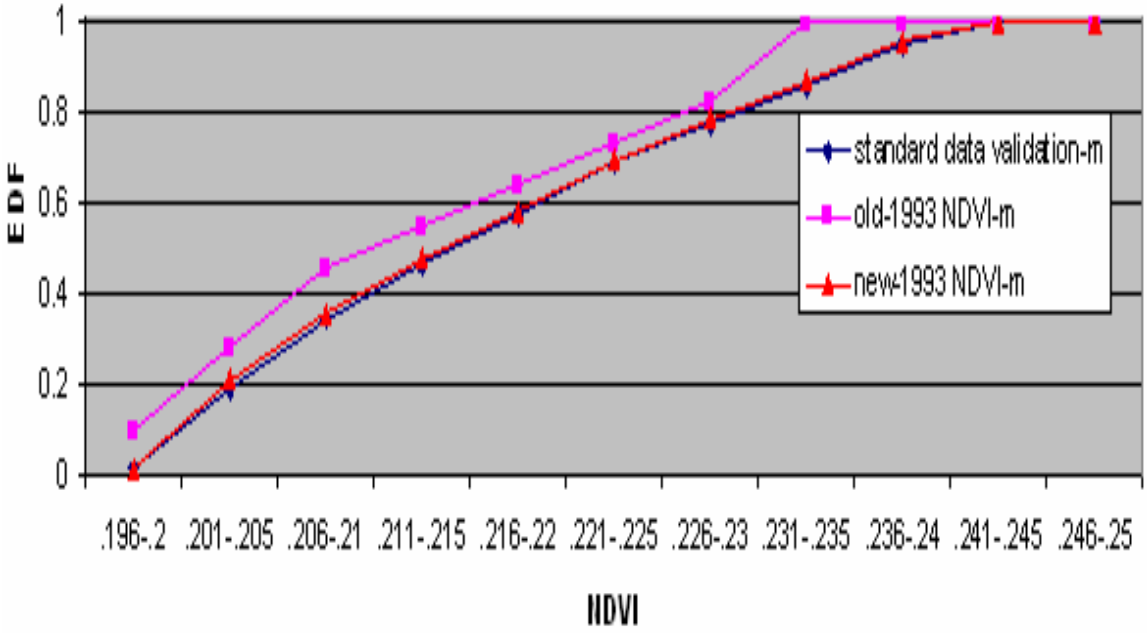

Figure 6.33 (b) Empirical distribution functions for normalized NDVI data (m-mixed) of 1993 compared with standard data validation sets (subset 2).

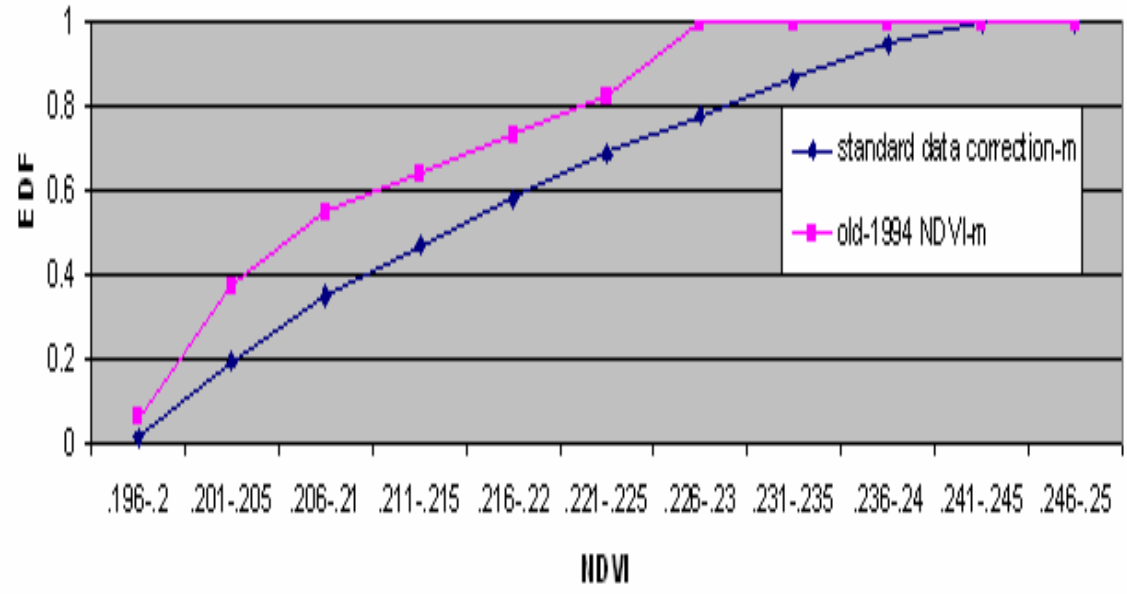

Figure 6.34 (a) Empirical distribution functions for unnormalized NDVI data (m-mixed) of 1994 compared with standard data correction sets (subset 1).

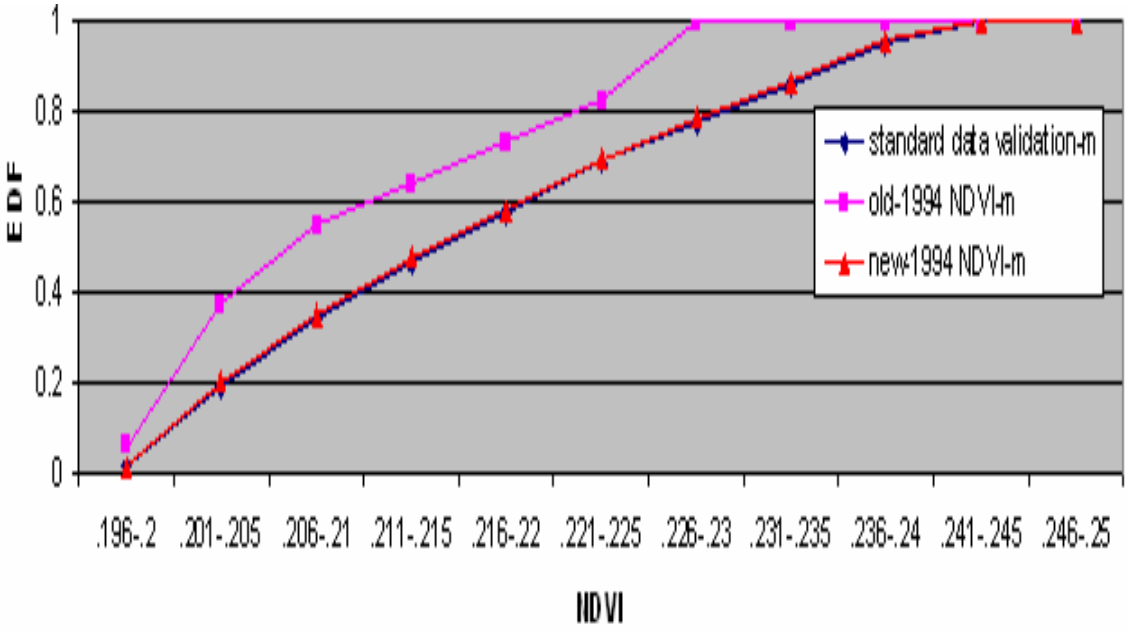

Figure 6.34 (b) Empirical distribution functions for normalized NDVI data (m-mixed) of 1994 compared with standard data validation sets (subset 2).

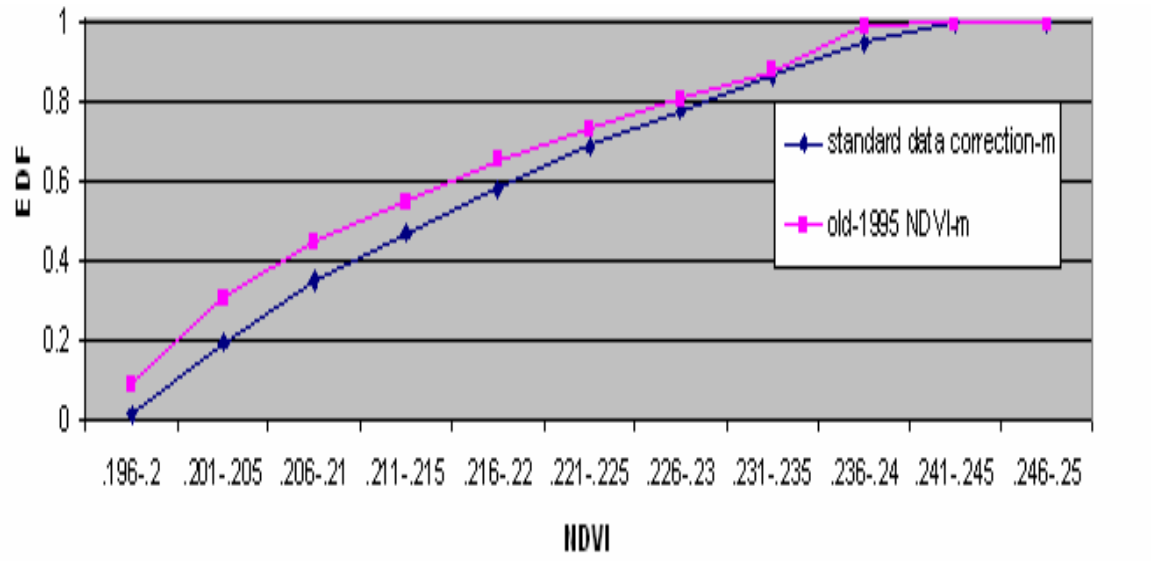

Figure 6.35 (a) Empirical distribution functions for unnormalized NDVI data (m-mixed) of 1995 compared with standard data correction sets (subset 1).

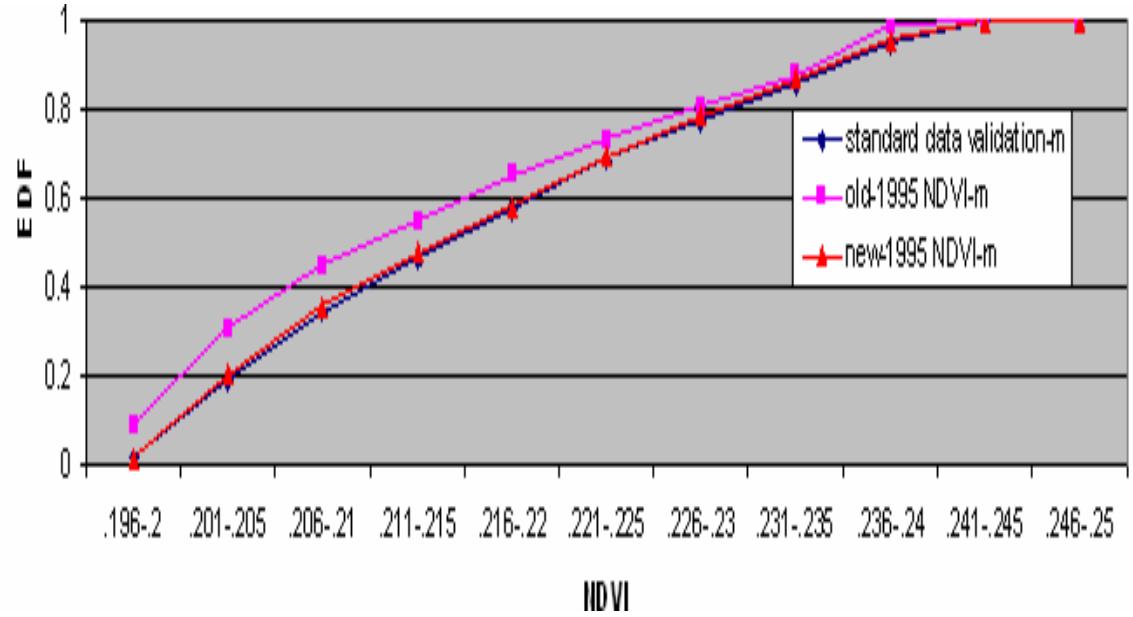

Figure 6.35 (b) Empirical distribution functions for normalized NDVI data (m-mixed) of 1995 compared with standard data validation sets (subset 2).

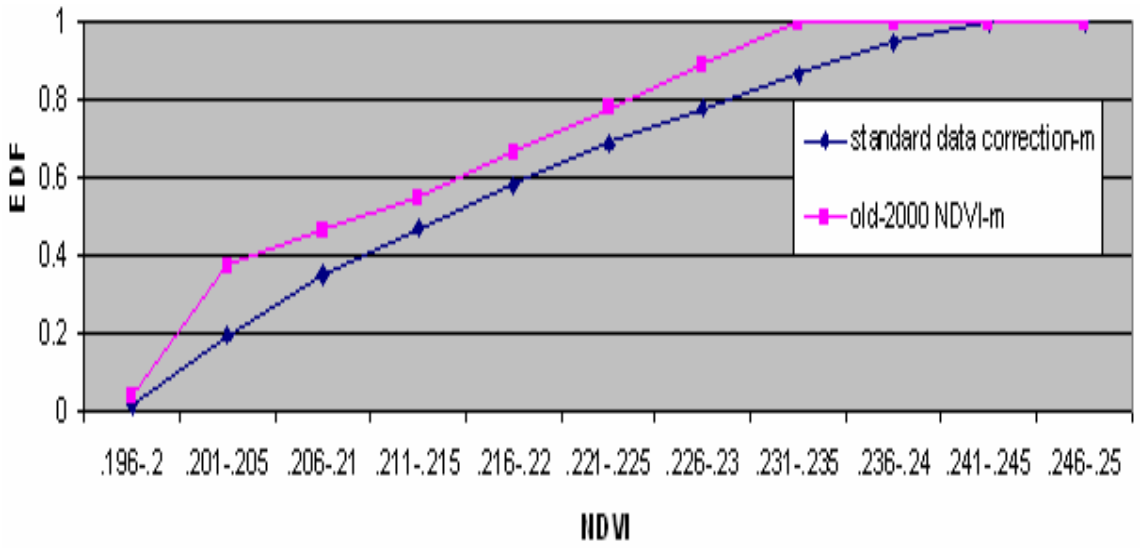

Figure 6.36 (a) Empirical distribution functions for unnormalized NDVI data (m-mixed) of 2000 compared with standard data correction sets (subset 1).

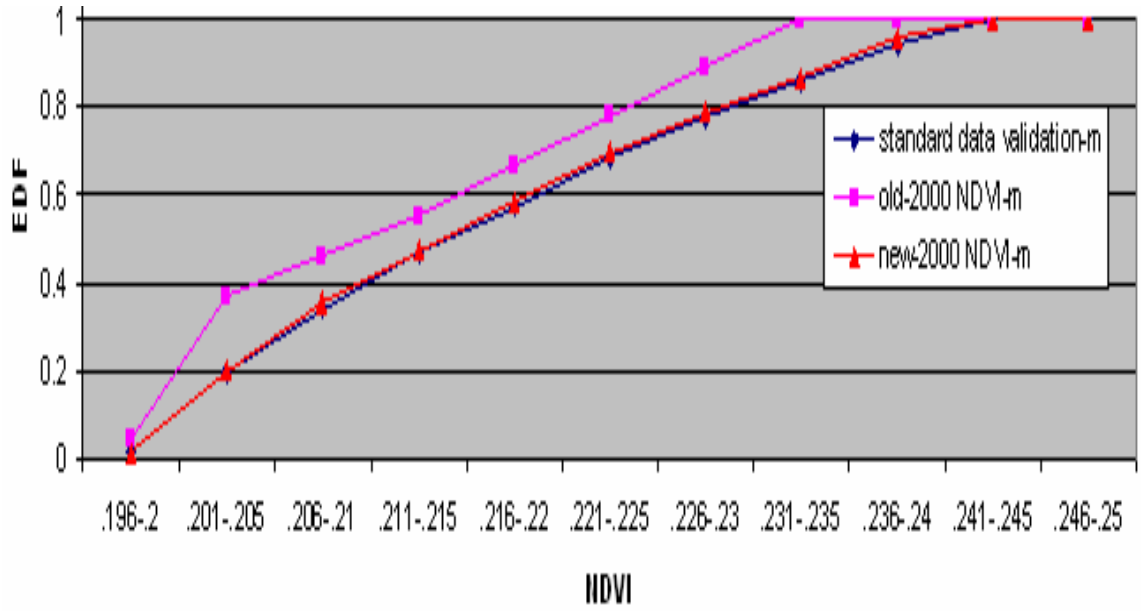

Figure 6.36 (b) Empirical distribution functions for normalized NDVI data (m-mixed) of 2000 compared with standard data validation sets (subset 2).

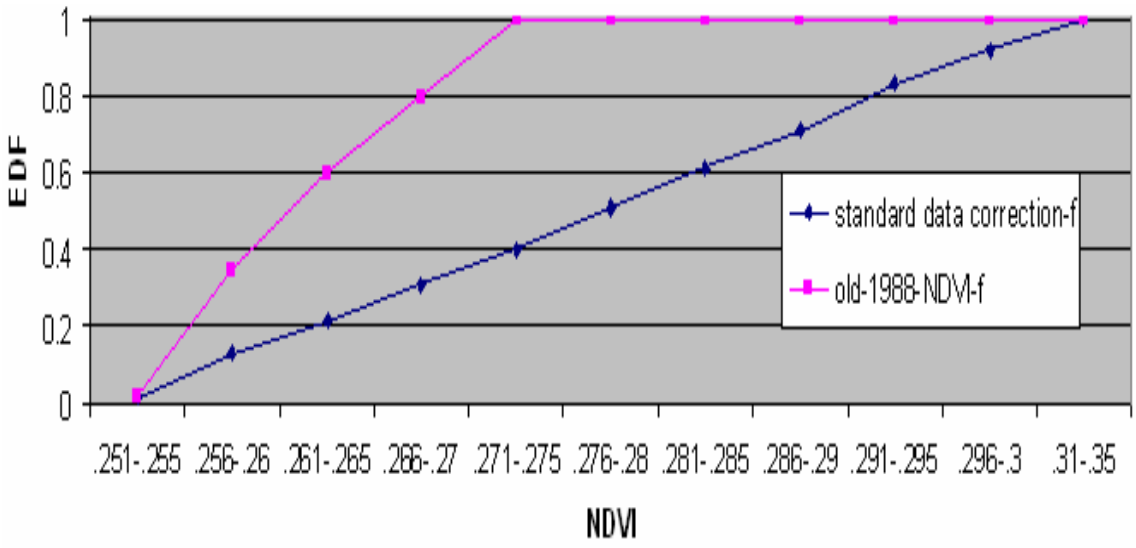

Figure 6.37 (a) Empirical distribution functions for unnormalized NDVI data (f-forest) of 1988 compared with standard data correction sets (subset 1).

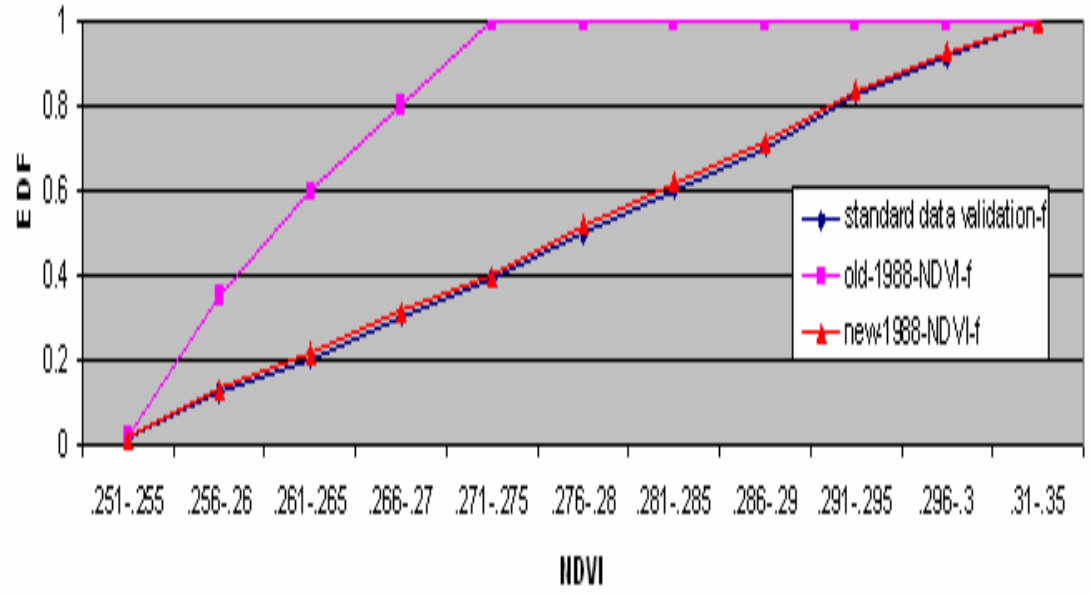

Figure 6.37 (b) Empirical distribution functions for normalized NDVI data (f-forest) of 1988 compared with standard data validation sets (subset 2).

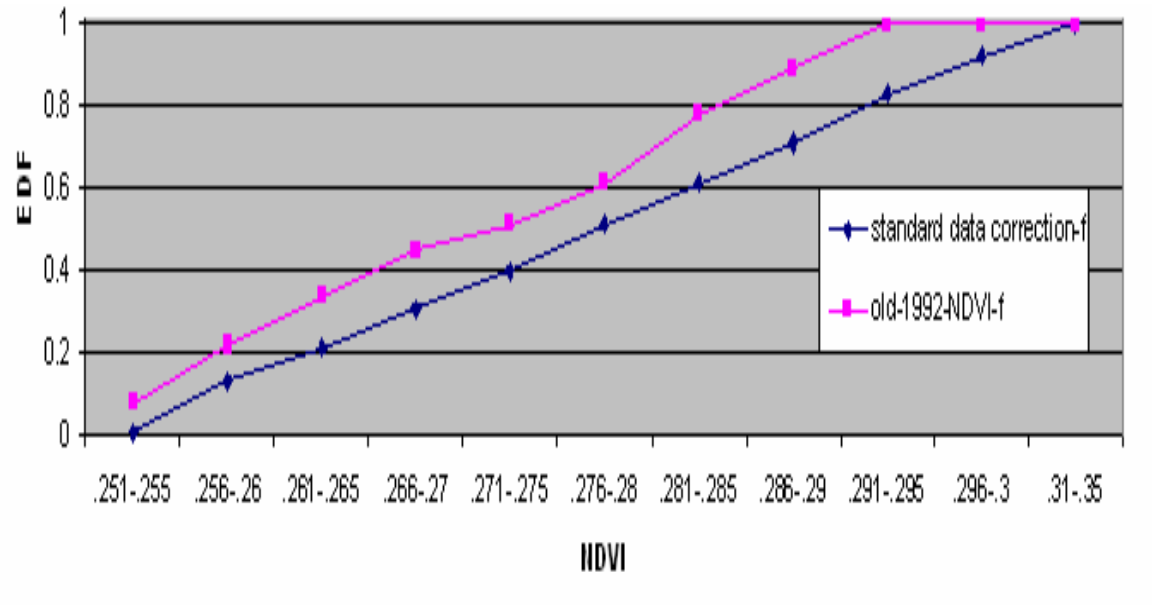

Figure 6.38 (a) Empirical distribution functions for unnormalized NDVI data (f-forest) of 1992 compared with standard data correction sets (subset 1).

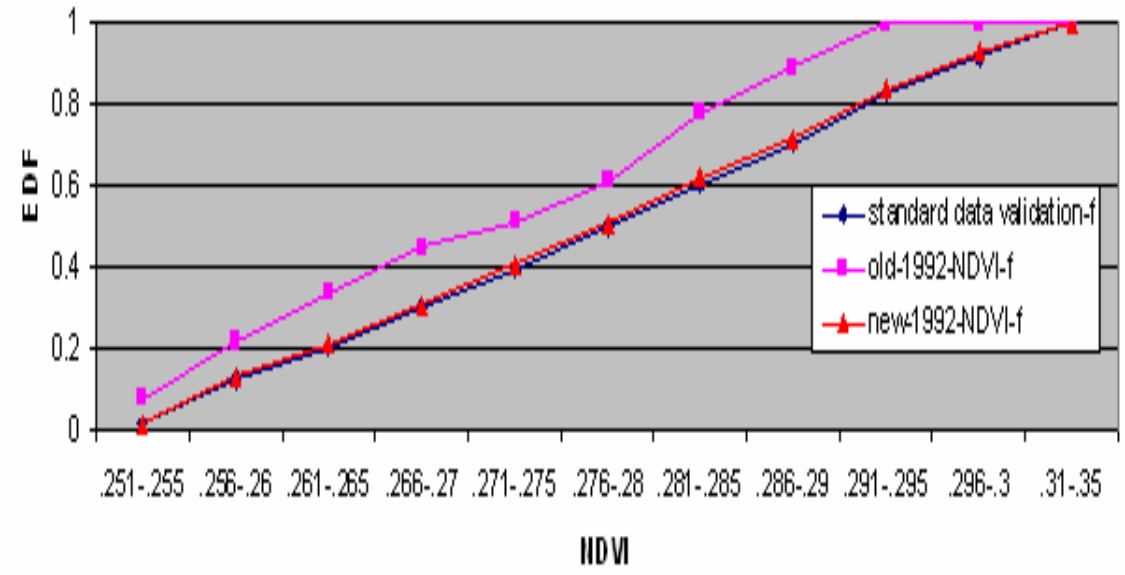

Figure 6.38 (b) Empirical distribution functions for normalized NDVI data (f-forest) of 1992 compared with standard data validation sets (subset 2).

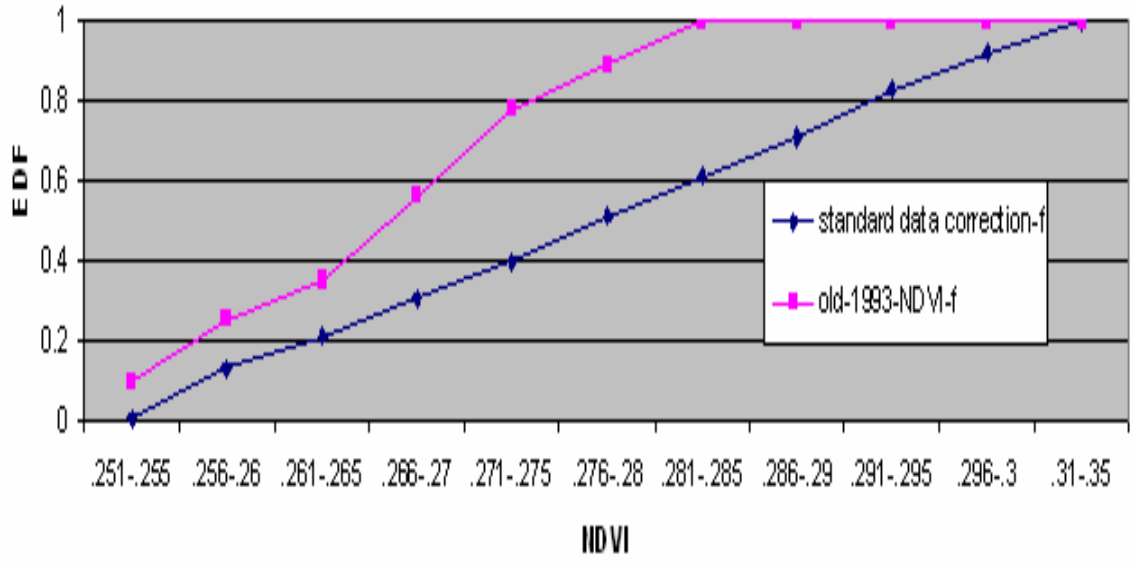

Figure 6.39 (a) Empirical distribution functions for unnormalized NDVI data (f-forest) of 1993 compared with standard data correction sets (subset 1).

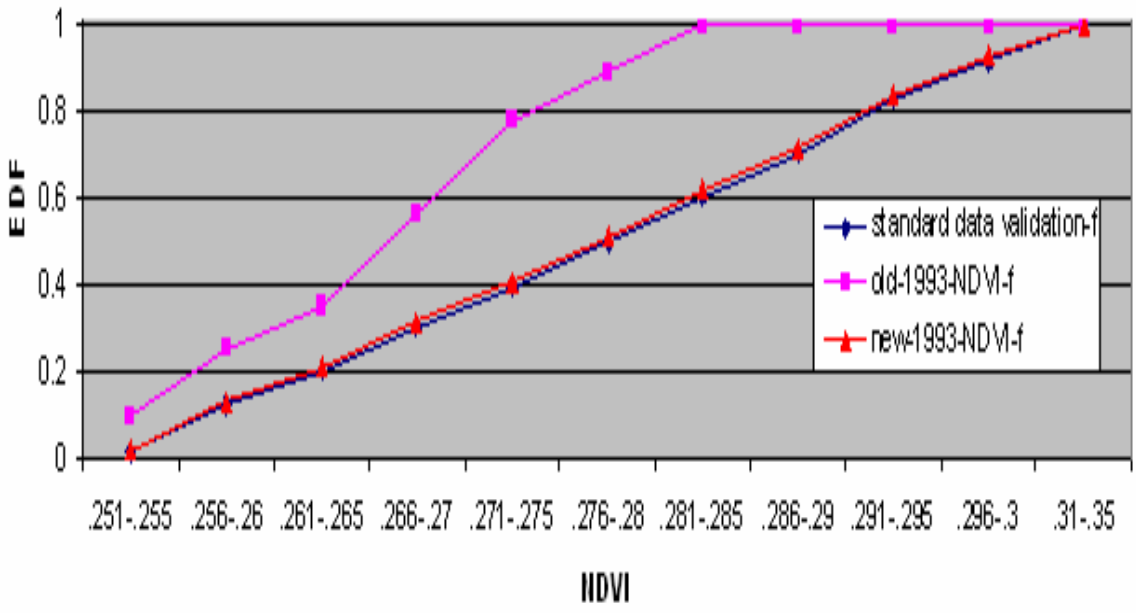

Figure 6.39 (b) Empirical distribution functions for normalized NDVI data (f-forest) of 1993 compared with standard data validation sets (subset 2).

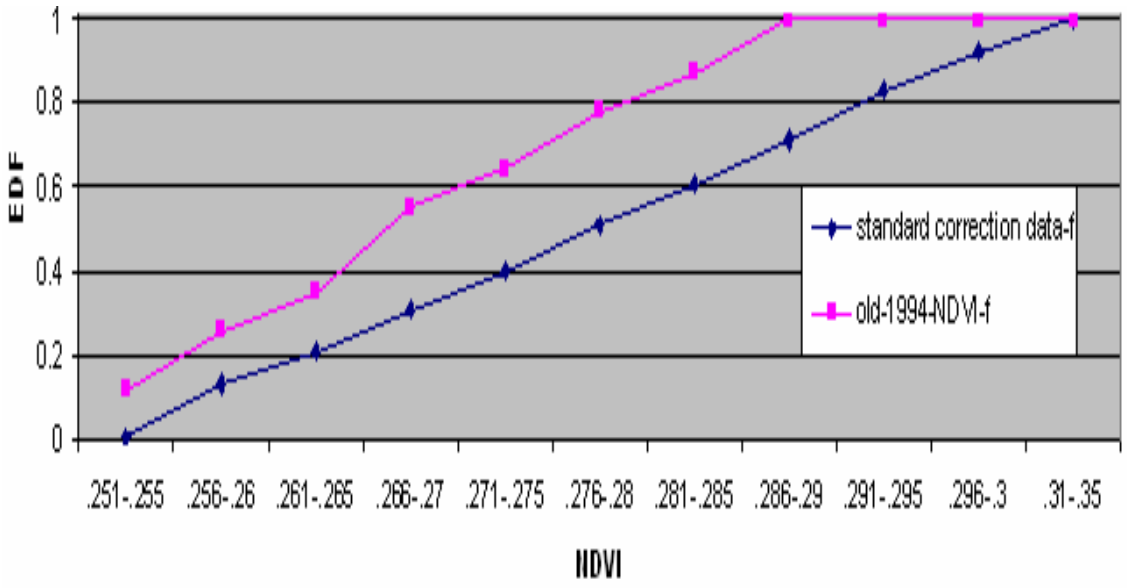

Figure 6.40 (a) Empirical distribution functions for unnormalized NDVI data (f-forest) of 1994 compared with standard data correction sets (subset 1).

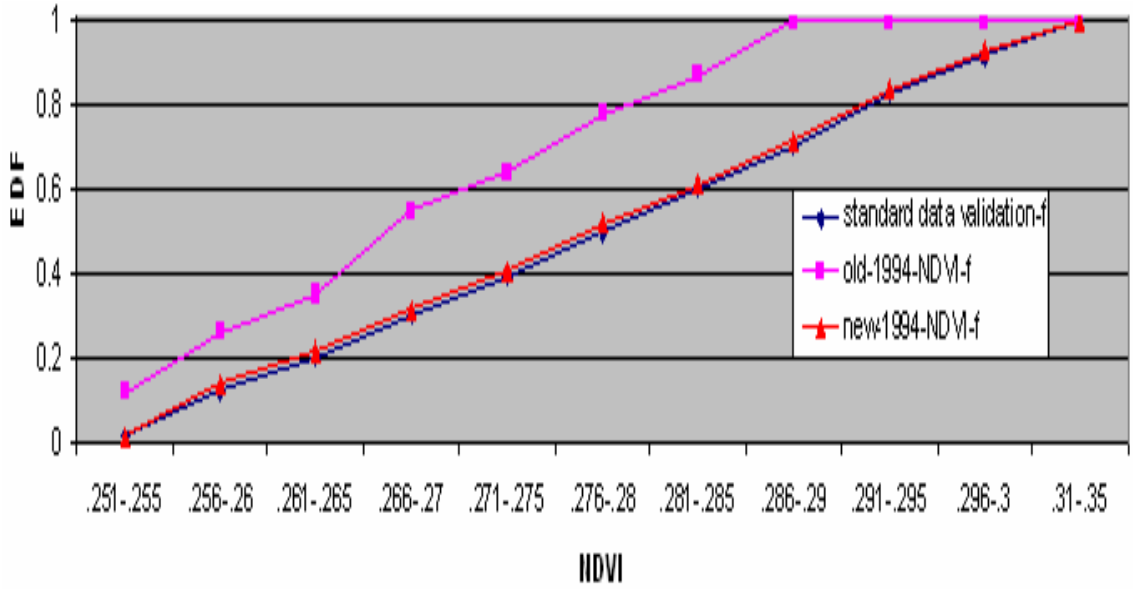

Figure 6.40 (b) Empirical distribution functions for normalized NDVI data (f-forest) of 1994 compared with standard data validation sets (subset 2).

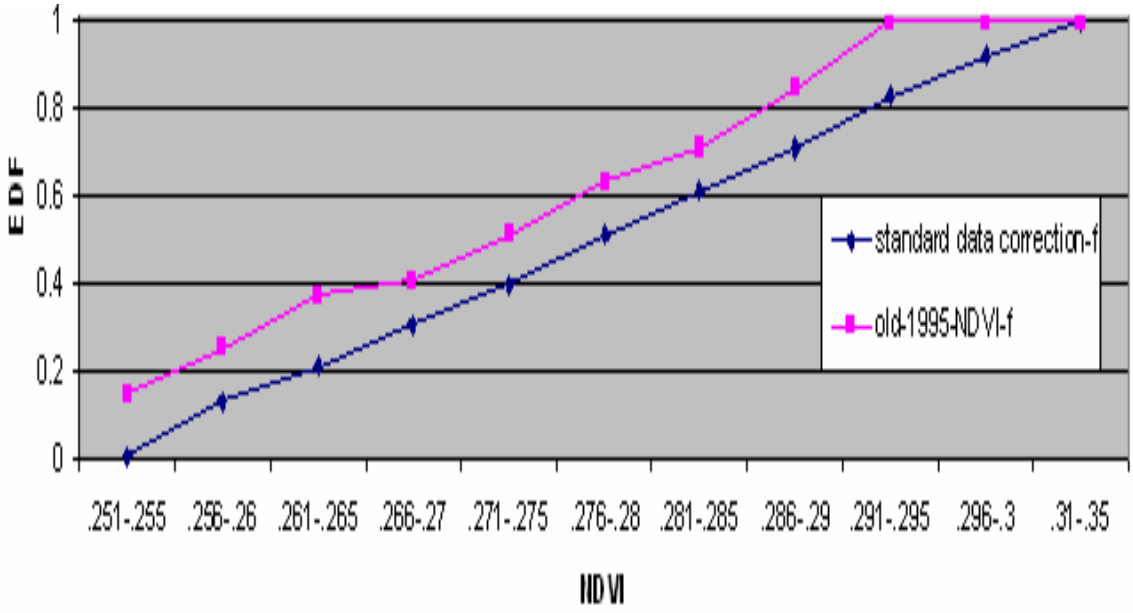

Figure 6.41 (a) Empirical distribution functions for unnormalized NDVI data (f-forest) of 1995 compared with standard data correction sets (subset 1).

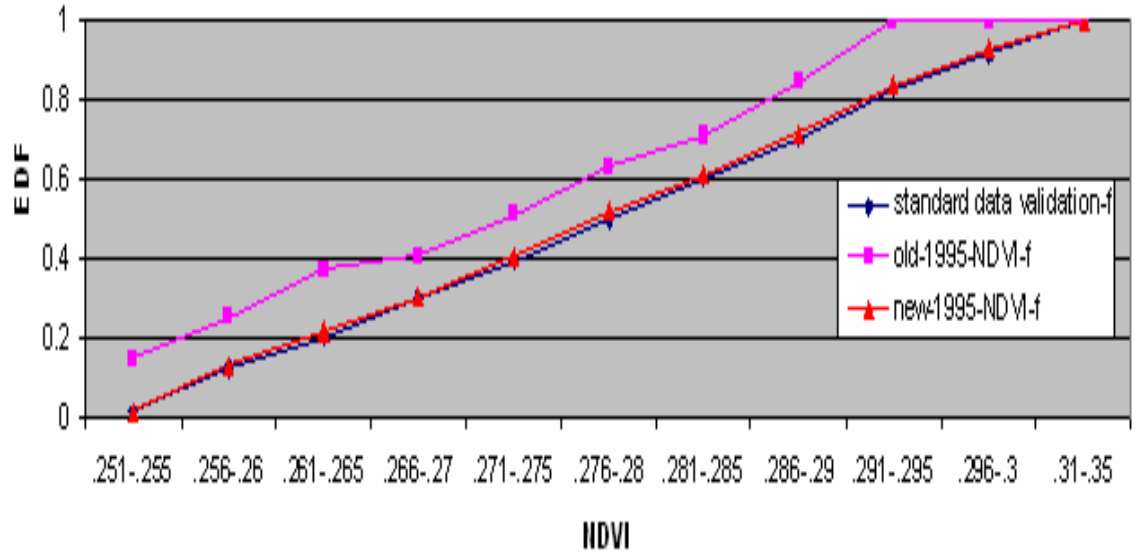

Figure 6.41 (b) Empirical distribution functions for normalized NDVI data (f-forest) of 1995 compared with standard data validation sets (subset 2)

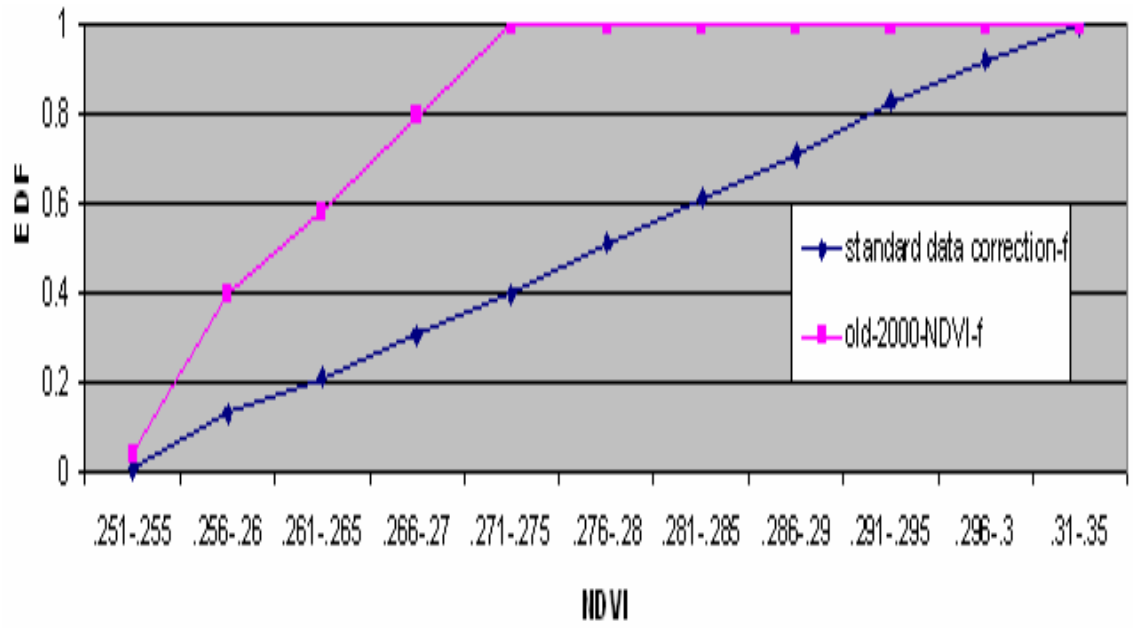

Figure 6.42 (a) Empirical distribution functions for unnormalized NDVI data (f-forest) of 2000 compared with standard data correction sets (subset 1).

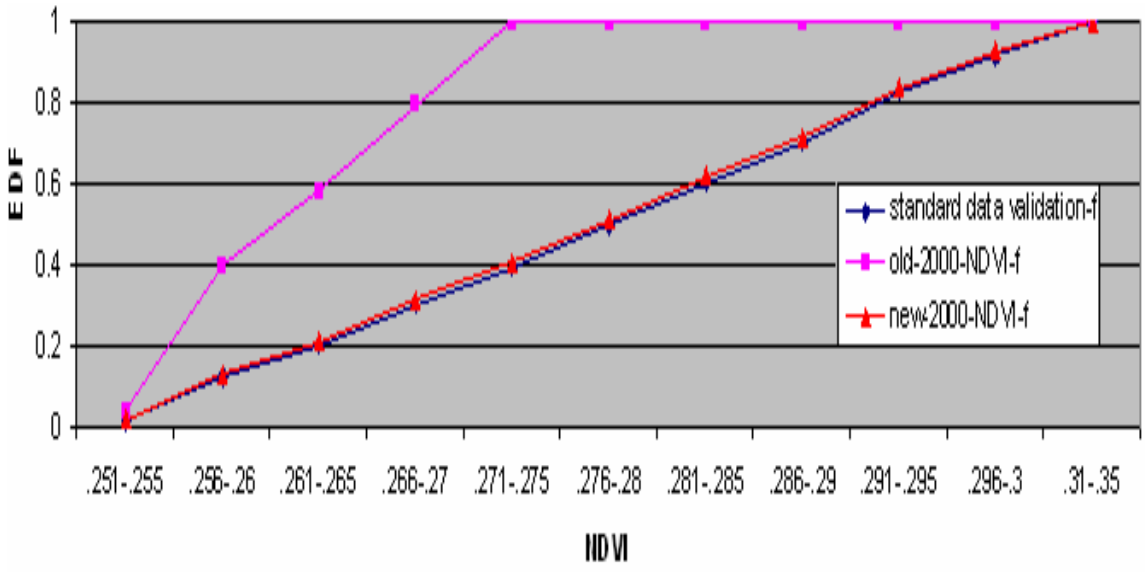

Figure 6.42 (b) Empirical distribution functions for normalized NDVI data (f-forest) of 2000 compared with standard data validation sets (subset 2).

Figure 6.19-6.42 shows data are normalized for only one week (26th week) of affected years. Similarly, we normalized NDVI data in every five week of affected years. Using this normalized data, we produce new NDVI time series for different ecosystems as shown in figure 6.43 which shows improvement of the NDVI data of 1988, 1992, 1993, 1994, 1995, and 2000.

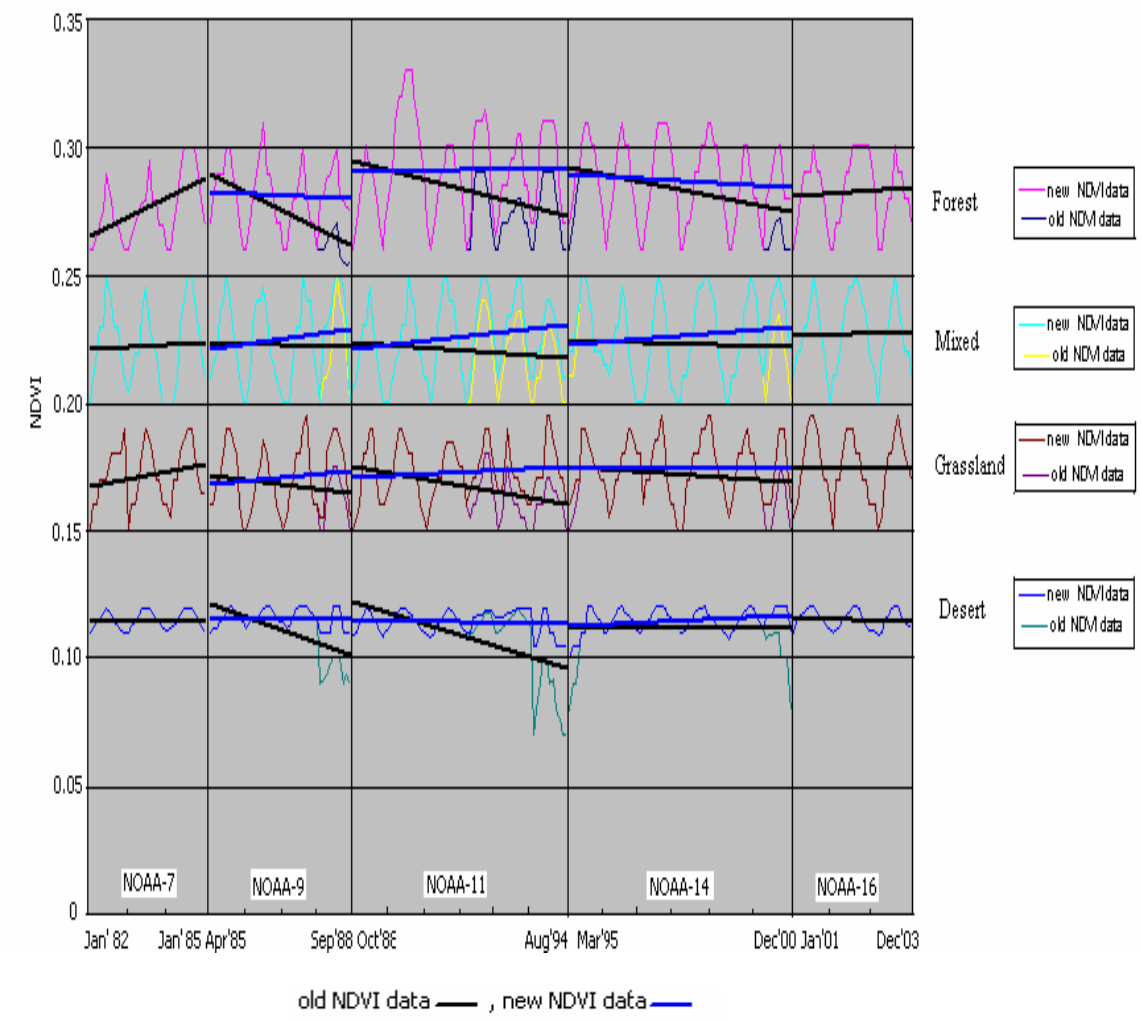

Figure 6.43 corrected NDVI time series (yearly) of different ecosystems in selected study area of China

NDVI trends for selected ecosystems of China and jumps between the satellites are illustrated in Figure 6.18 and 6.43 and the errors are estimated in Table 6.2. All targets show some NDVI trends for each satellite and jump from one satellite to the next one. Analysis shows that high rate of NDVI change for NOAA-9,-11, and -14 by reduction of NDVI in 1988, 1992-1994, and 2000 due to elevated amount of stratospheric aerosol from Mt. Pinatubo and considerable degradation of satellite orbit. High rate of NDVI change belong to desert and forest ecosystems (particularly NOAA-9, and -11). Vegetative ecosystems have generally small differences between NDVI at the beginning and the end of satellite life although some exceptions are seen for NOAA-9, -11, and -14. Regarding NDVI jump from one satellite to the next in Table 6.2(B), general tendency is a reduction of NDVI between beginning of NOAA-9 and the end of NOAA-7, between beginning of NOAA-16 and the end of NOAA-14. An increase in NDVI is observed only during satellite change from NOAA-9 to NOAA-11, NOAA-11 to NOAA-14, and NOAA-14 to NOAA-16 due to already mentioned sharp stratospheric aerosols increase and orbit drift of satellite. Therefore, desert and tropical forest target show the largest changes in NDVI during the time of satellite change. Again vegetative targets (except for desert and forest) show smaller NDVI jumps from one satellite to the next. After correction of NDVI, all target shows the significantly improve the NDVI trend and jumps between the satellites (new NDVI).

Table 6.2: Estimation of Errors in (A) NDVI trend at the End of a Satellite Life and (B) Jumps between the Satellites (% to the beginning level)

Ecosystems in selected study area of China		A			B			
		N-9	N-11	N-14	N-7/9	N-9/11	N-11/14	N-14/16
Desert	Old NDVI	-18	-20	0	5	21	18	-4
	New NDVI	-1	3	2	0	1	0	0
Grassland	Old NDVI	-5	-8	-3	-3	7	8	3
	New NDVI	2.5	0	0	-5	0	0	0
Mixed	Old NDVI	0	-2	-1	0	1	4	2
	New NDVI	4	3	3	0	0	-2	-1
Forest	Old NDVI	-11	-8	-5	1	13	6	4
	New NDVI	0	0	0	0	4	-1	-1

6.4 Analysis of BT Time Series for Study Area in China

We produce BT time series of five NOAA satellites are illustrated in figure 6.44 which shows BT data for 1988 (NOAA-9), 1992, 1993, 1994 (NOAA-11), and 1995, (week #1-8), 2000 (NOAA-14) are not stable enough compare to other years because of satellite orbital drift, Mt Pinatubo, and sensor degradation. Therefore, we need to correct the BT data for affected years.

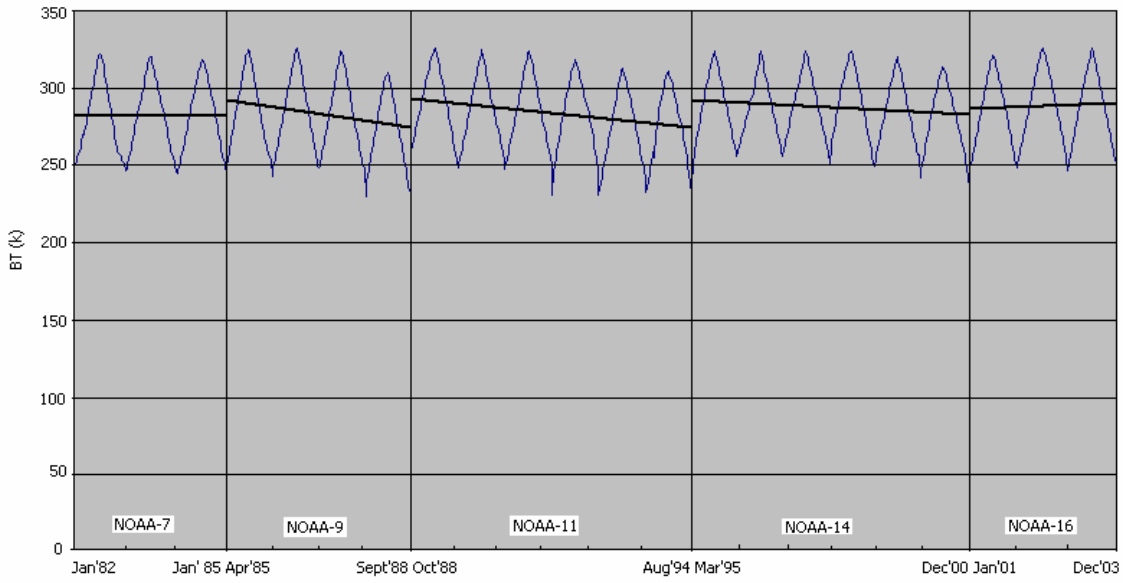

Figure 6.44 BT time series (Yearly) for study area in China

For this correction, we apply the method of empirical distribution functions for affected years. We normalize data by the EDF's compared with standard data correction sets (subset 1) according to equation 5.3 and 5.4. Then corrected or normalized data for this years compared with subset 2 (standard data validation sets) which provides BT data for these years that match in subset 2. Figure 6.45 shows how the procedure is applied in actual practice to generate normalization BT values. The figure shows idealized EDF's

for the standard data correction sets and 1988 year. As EDF are based on cumulative histogram, they are discrete. But in Figure 6.45 they are shown as continuous function.

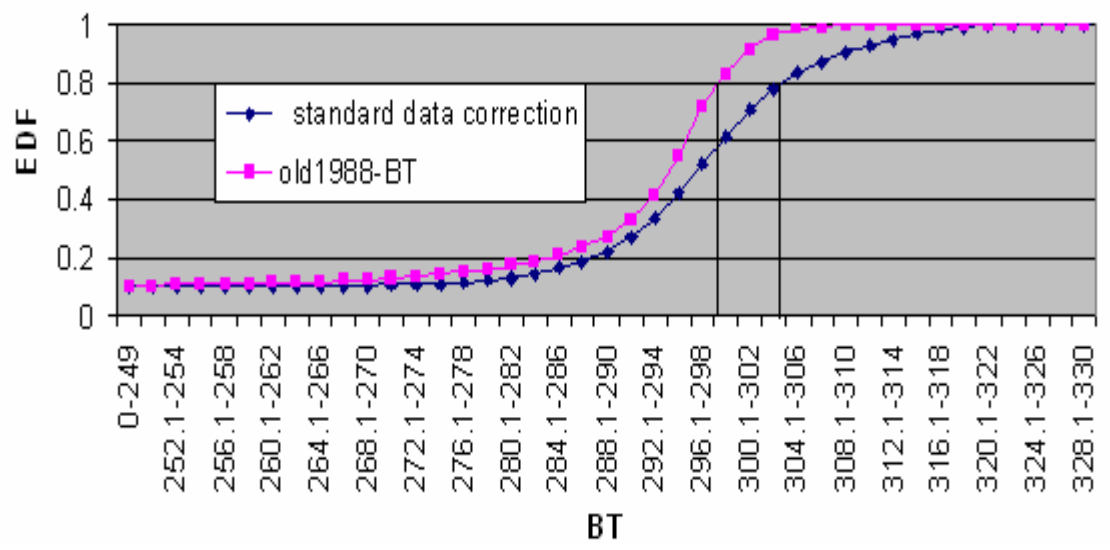

Figure 6.45 Illustration of procedure to generate normalization BT data

For example, for the BT value 300 in year 1988 find the EDF value from the EDF of year 1988. In the illustration it the EDF_{88} is 0.8. Then find the point on the standard data correction sets EDF with the same EDF value. According to eq. 5.4 the EDF value can also be expressed as $EDF_{standard}$ is 0.8. Finally, use the EDF of the standard data correction sets to find the normalized count value 306. Since the data are actually discrete, we will need to interpolate within the EDF of the standard data correction sets to find the value of 306, which must then be rounded to the nearest integer. We do interpolate with in the EDF of the standard data correction to find the normalized count value. After interpolated, we found the normalized BT value 300 in year 1988 is 306.

Therefore, 1988 new $300 = 300_{1988} + (306_{standard} - 300_{1988}) = 306$

Using this technique, we produce EDF's to normalize or correct data for the years 1988, 1992, 1993, 1994, 1995, and 2000 compared with standard data correction sets (subset 1) and then corrected or normalized data compared with standard data validation sets (subset 2) which are illustrated in following Figures.

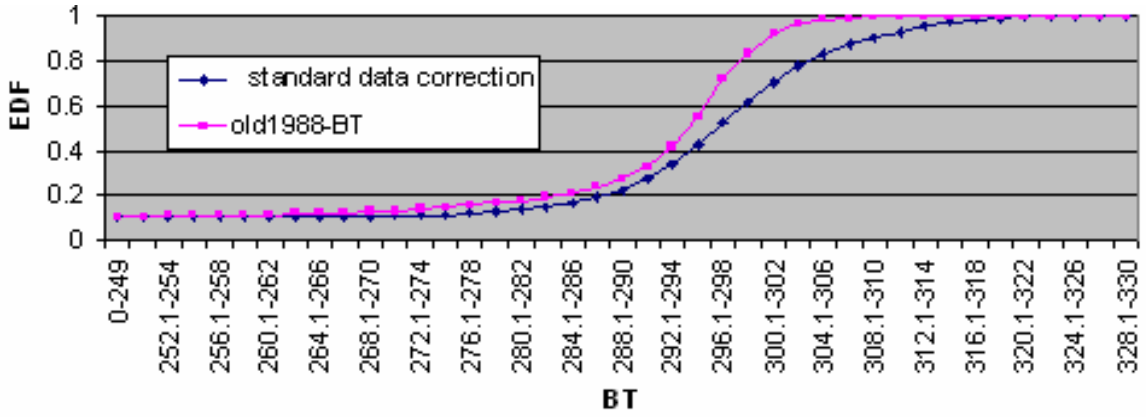

Figure 6.46 (a) Empirical distribution functions for unnormalized BT data of 1988 compared with standard data correction sets (subset 1).

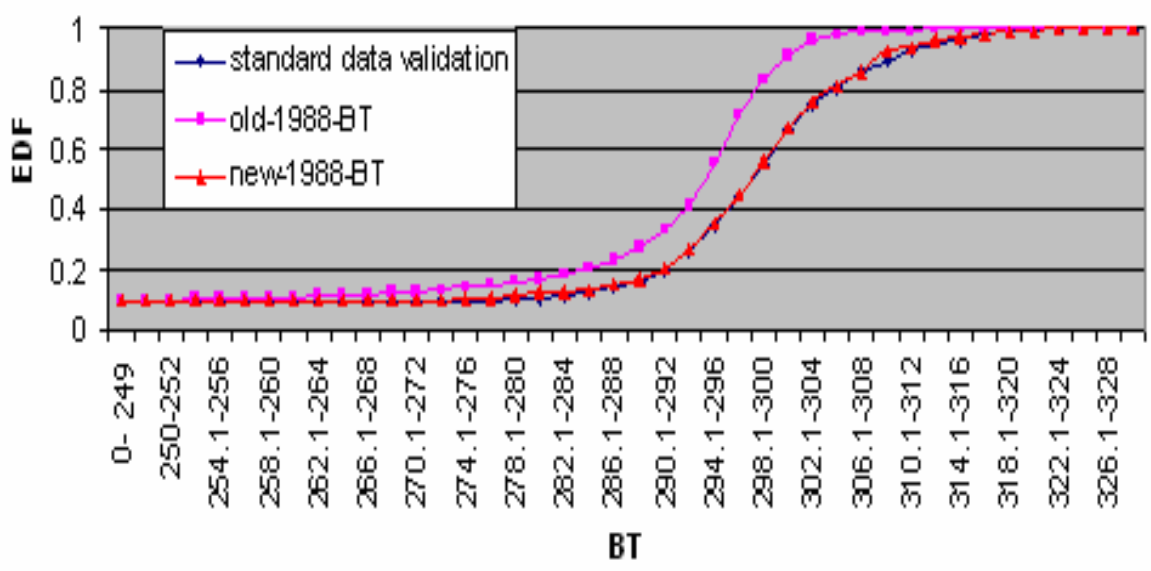

Figure 6.46 (b) Empirical distribution functions for normalized BT data of 1988 compared with standard data validation sets (subset 2).

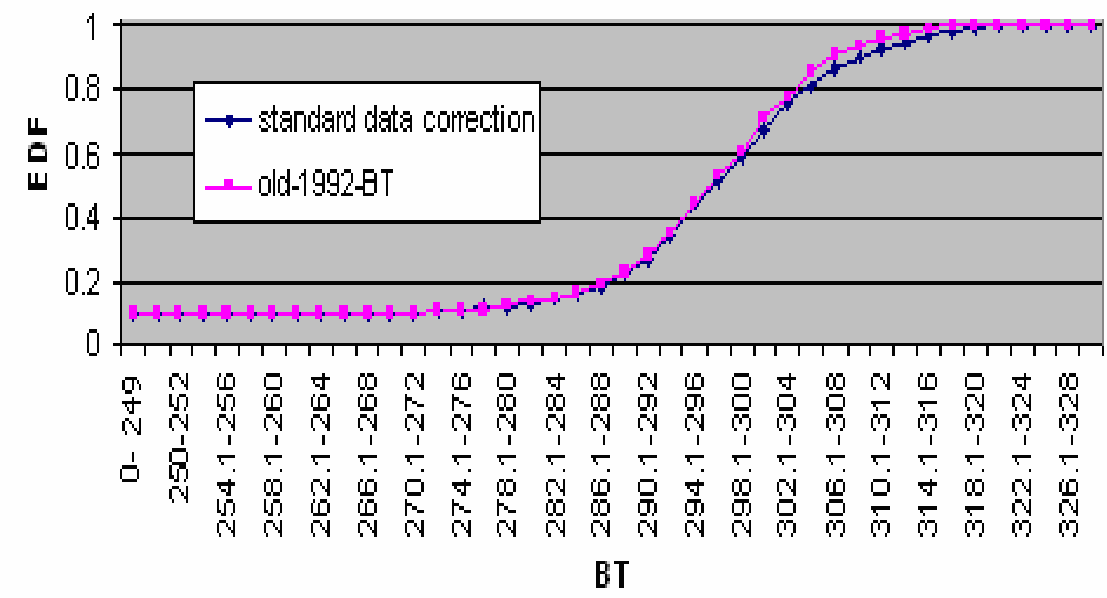

Figure 6.47 (a) Empirical distribution functions for unnormalized BT data of 1992 compared with standard data correction sets (subset 1).

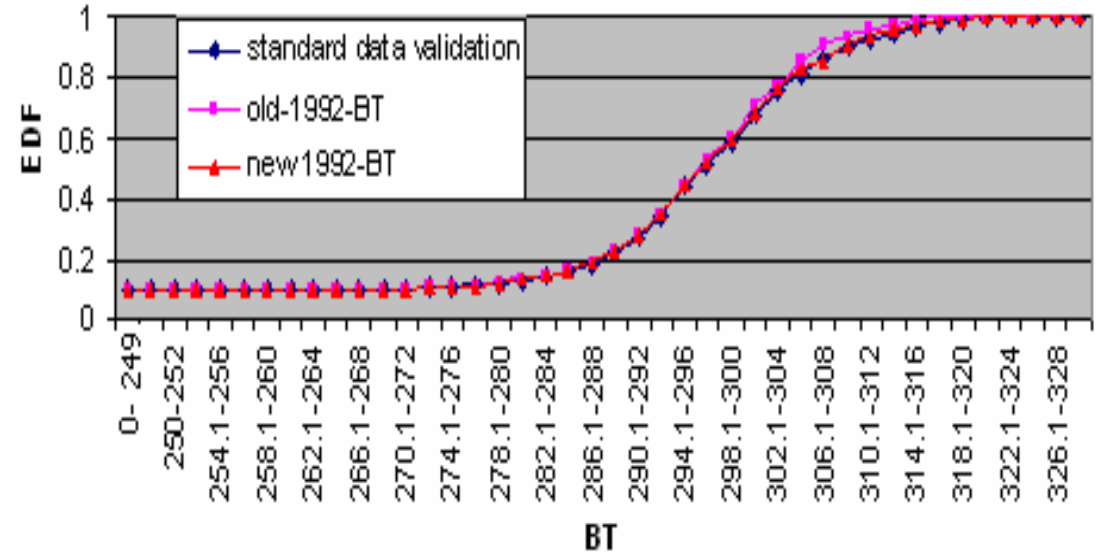

Figure 6.47 (b) Empirical distribution functions for normalized BT data of 1992 compared with standard data validation sets (subset 2).

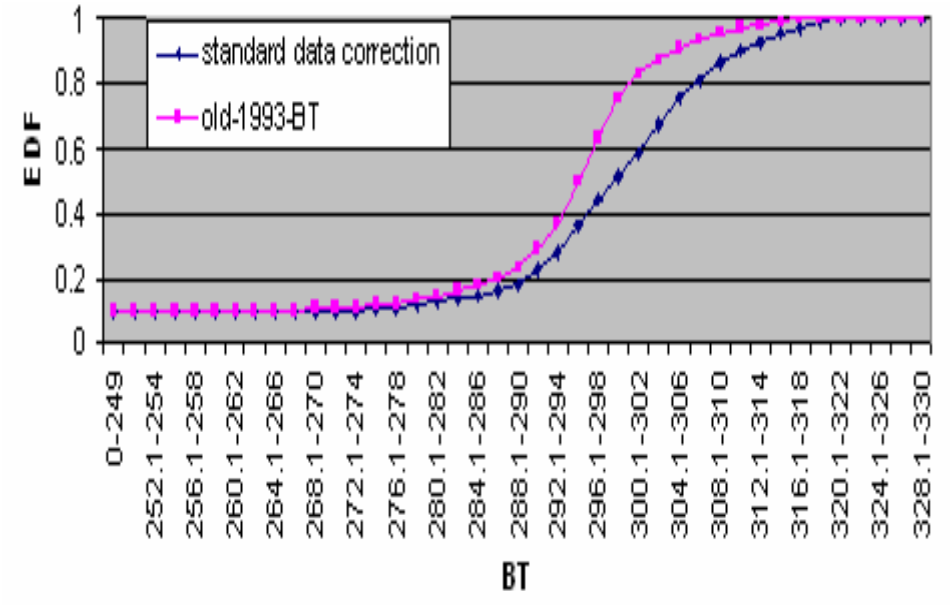

Figure 6.48 (a) Empirical distribution functions for unnormalized BT data of 1993 compared with standard data correction sets (subset 1).

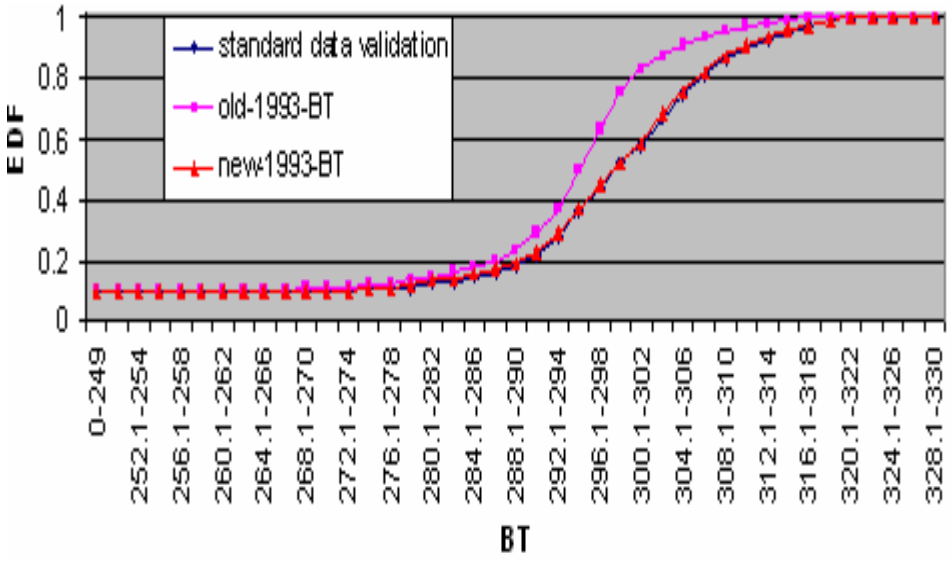

Figure 6.48 (b) Empirical distribution functions for normalized BT data of 1993 compared with standard data validation sets (subset 2).

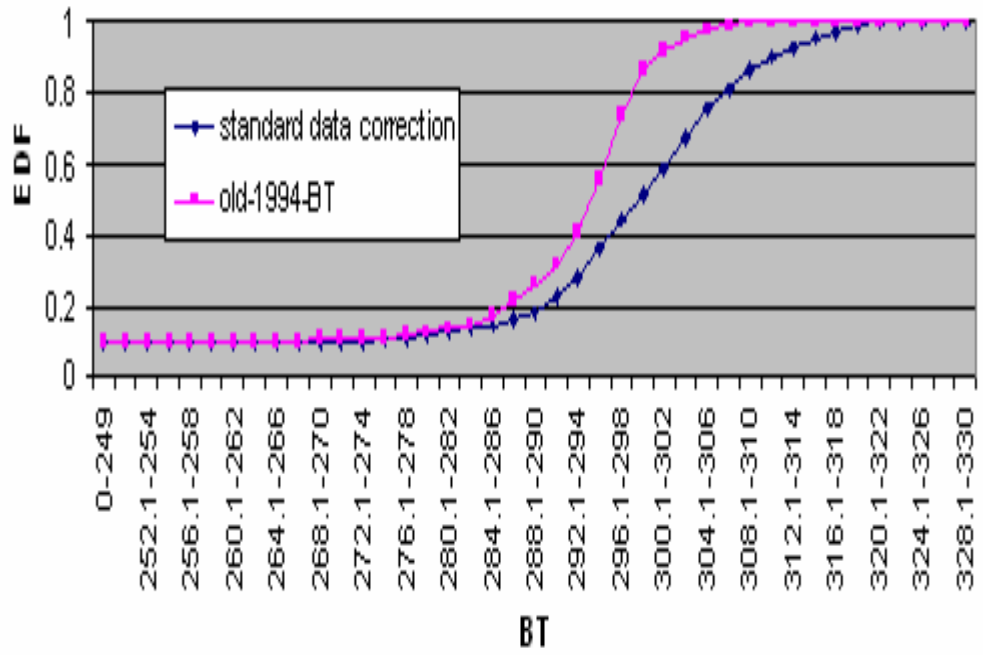

Figure 6.49 (a) Empirical distribution functions for unnormalized BT data of 1994 compared with standard data correction sets (subset 1).

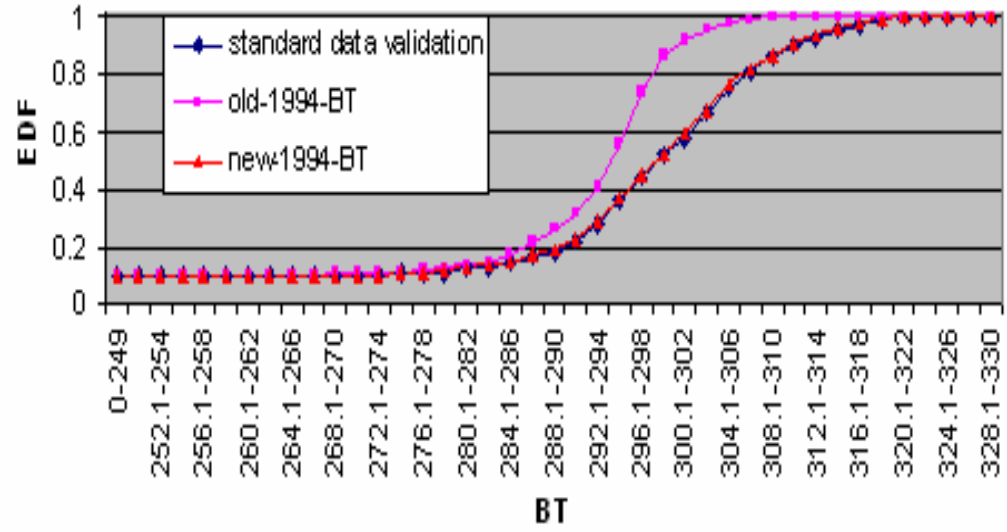

Figure 6.49 (b) Empirical distribution functions for normalized BT data of 1994 compared with standard data validation sets (subset 2).

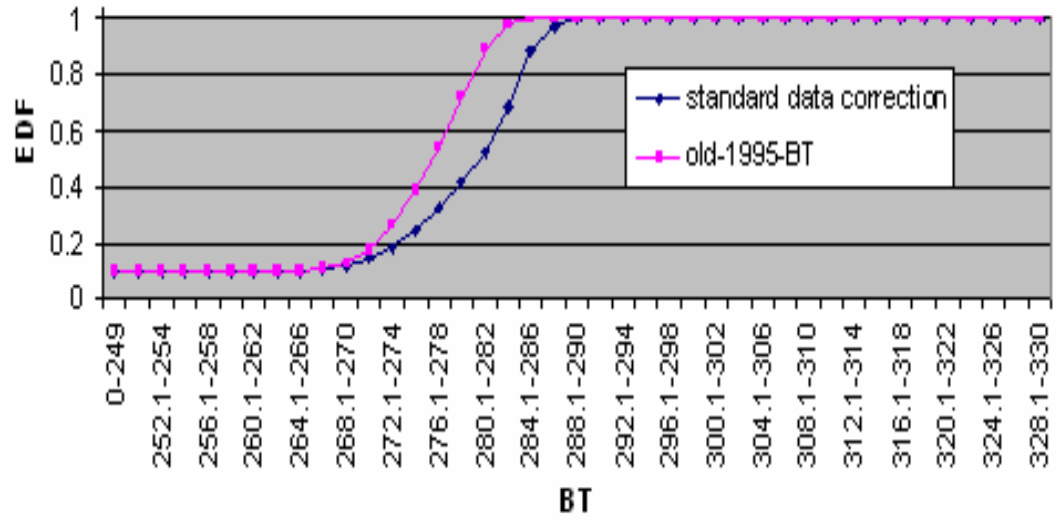

Figure 6.50 (a) Empirical distribution functions for unnormalized BT data of 1995 compared with standard data correction sets (subset 1).

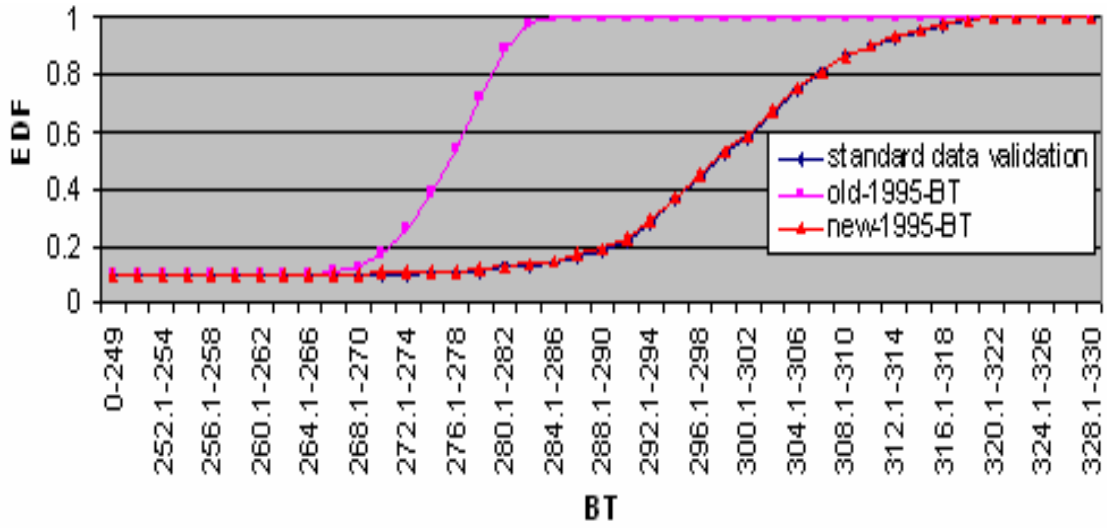

Figure 6.50 (b) Empirical distribution functions for normalized BT data of 1995 compared with standard data validation sets (subset 2)

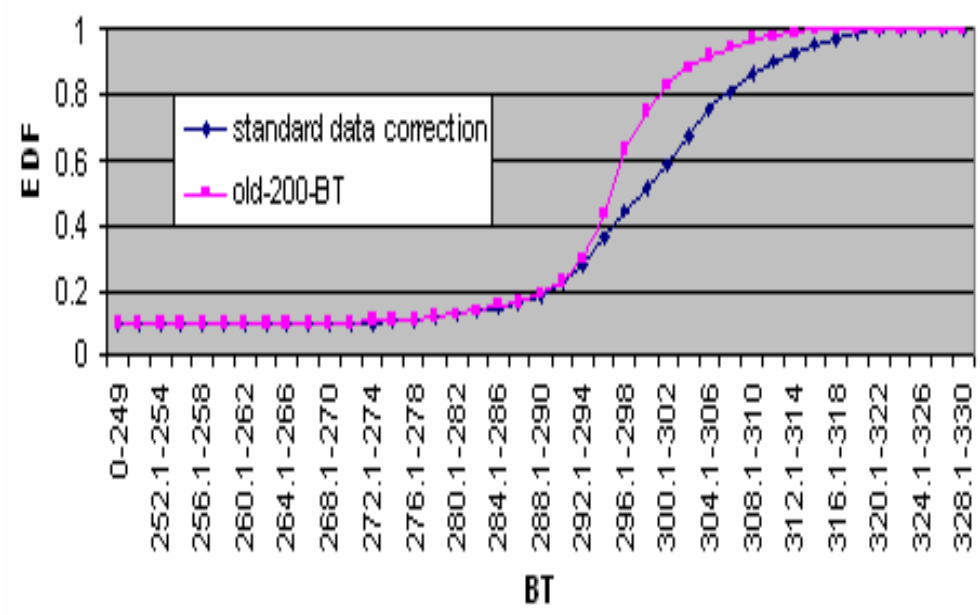

Figure 6.51 (a) Empirical distribution functions for unnormalized BT data of 2000 compared with standard data correction sets (subset 1).

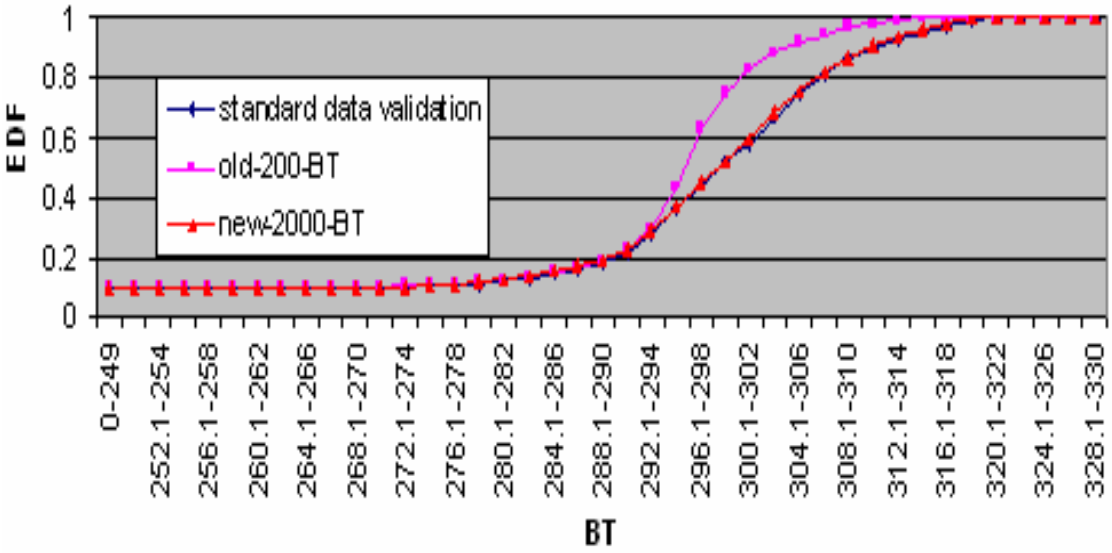

Figure 6.51 (b) Empirical distribution functions for normalized BT data of 2000 compared with standard data validation sets (subset 2).

Using normalized BT value, we produce new BT time series as shown in Figure 6.52 which shows improvement of BT data (pink line) of the year of 1988, 1992, 1993, 1994, 1995, and 2000.

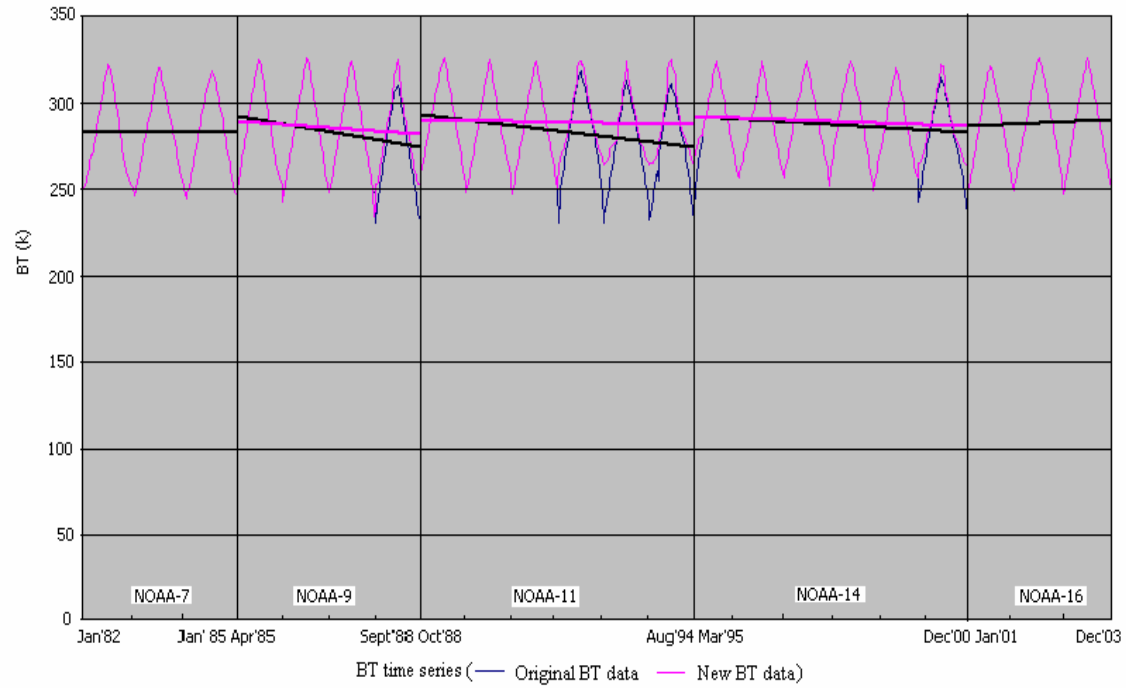

Figure 6.52 corrected BT time series (yearly) in study area of China

BT trends for selected study area of China and jumps between the satellites are illustrated in Figure 6.44 and 6.52 and the errors are estimated in Table 6.3. Figure 6.44 shows some BT trends for each satellite except NOAA-16 and jump from one satellite to the next one. Considering old BT trend (Table 6.3), for China, NOAA-9, -11, and -14 have negative trend and NOAA-7, -16 have positive or no trend. Therefore, NOAA-7, and -16 shows clear tendency to BT increase during its three years in operation. However, important is trend rate. Analysis shows that high rate of BT change for NOAA-9,-11, and -14 by

reduction of BT in 1988, 1992-1994, and 2000 due to elevated amount of stratospheric aerosol from Mt Pinatubo and considerable degradation of satellite orbit.

Regarding BT jump from one satellite to the next in Table 6.3(B), general tendency is a reduction of BT between beginning of NOAA-9 and the end of NOAA-7, between beginning of NOAA-16 and the end of NOAA-14. An increase in BT is observed only during satellite change from NOAA-9 to NOAA-11, NOAA-11 to NOAA-14, and NOAA-14 to NOAA-16 due to already mentioned sharp stratospheric aerosols increase and orbit drift of satellite.

After correction of BT, we also estimate errors in Table 6.3 for new BT. Figure 6.52 shows improvement to the BT trends for each satellite and jump from one satellite to the next one. But there remain other potential sources of error in BT such as an incomplete drift correction, inaccurate BT calculation, and influence from Mt. Pinatubo. The EDF method is designed to reduce errors due to orbit drift, the dominant uncertainty in temperature variation during the satellite life time [50]. However, it may be difficult to accurately and completely remove this effect and thus orbit remains as an error source, though at a reduced level. Another large uncertainty lies in BT calibration and Mt. Pinatubo which includes all errors such as incomplete atmospheric corrections, surface corrections, sensor degradation and volcanic eruptions.

Table 6.3: Estimation of Errors in (A) BT trend at the End of a Satellite Life and (B) Jumps between the Satellites (% to the beginning level)

Target		A			B			
		N-9	N-11	N-14	N-7/9	N-9/11	N-11/14	N-14/16
China	Old BT	-6	-6.5	-3	3.3	7	6.5	5.1
	New BT	-2	-1	-1.7	2	3	1.7	0

6.5 Analysis of BT Time Series for Different Ecosystems in China

We produce BT time series for different ecosystem in China such as desert, grassland, and forest as shown in figure 6.52. BT fluctuates due to weather changes from year to year in each ecosystem. BT will be higher mostly in dry and hot weather (desert) than in normal and wet weather such as grassland and forest. . Figure 6.53 shows 1988 (NOAA-9), 1992, 1993, 1994 (NOAA-11), 1995 (week #1-8), 2000 (NOAA-14) data are not uniform compare to other years because of satellite orbit drift, and sensor degradation.

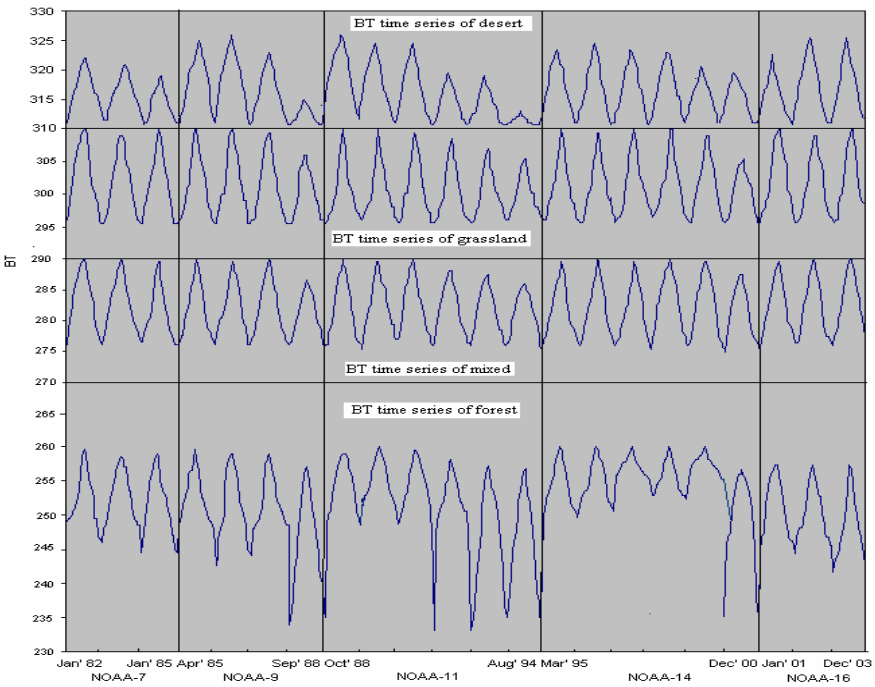

Figure 6.53 BT time series (yearly) for different ecosystem in China (— old BT data).

Therefore, we need to correct the data for affected years. We normalize data compared with standard data correction sets by the method of EDF's for affected years according to equation 5.3-5.4. Then corrected or normalized data for this years compared with subset 2 which provides BT data for these years that match in subset 2, are illustrated in following Figures.

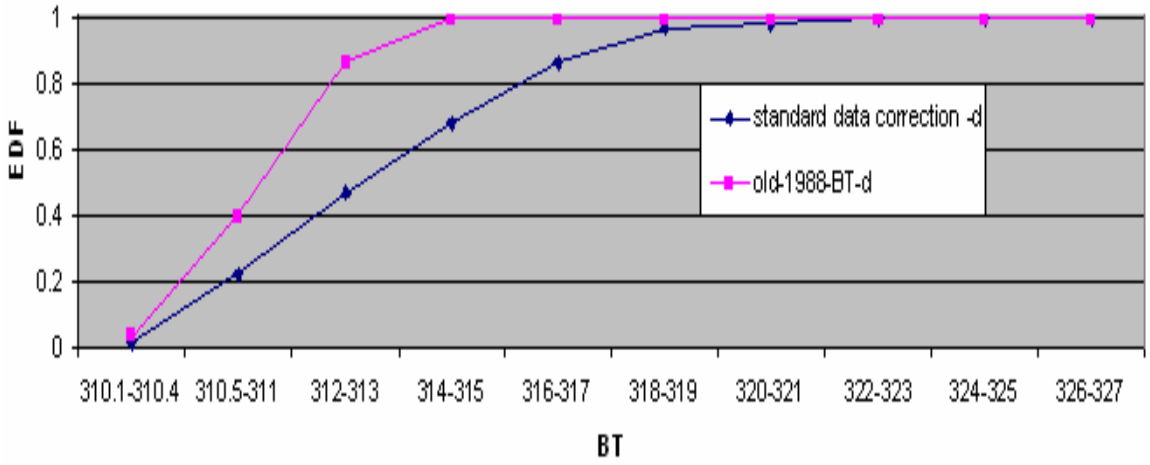

6.54 (a) Empirical distribution functions for unnormalized BT data (d-desert) of 1988 compared with standard data correction sets (subset 1).

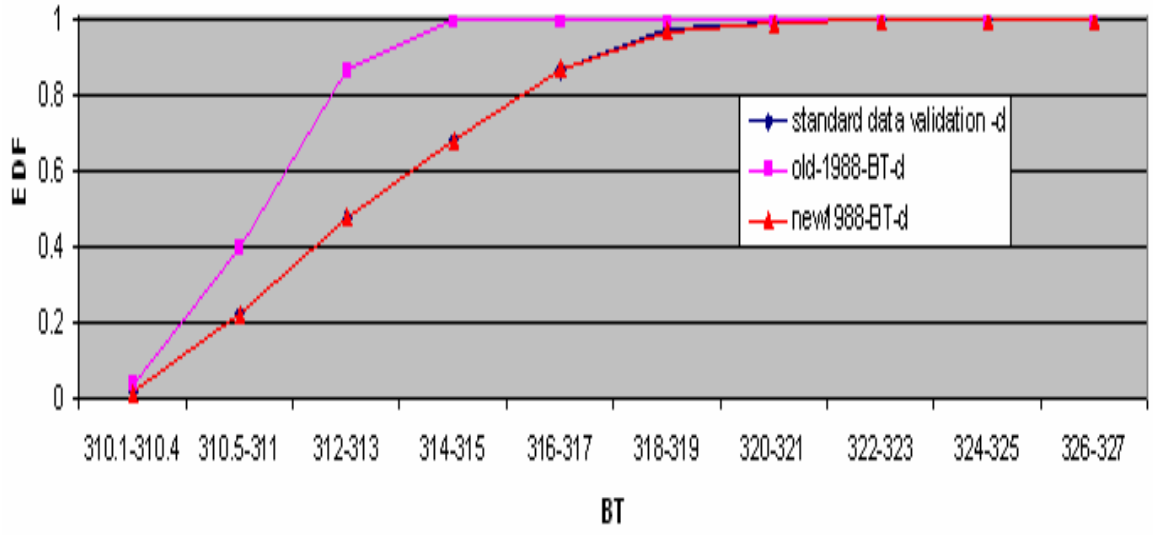

Figure 6.54 (b) Empirical distribution functions for normalized BT data (d-desert) of 1988 compared with standard data validation sets (subset 2).

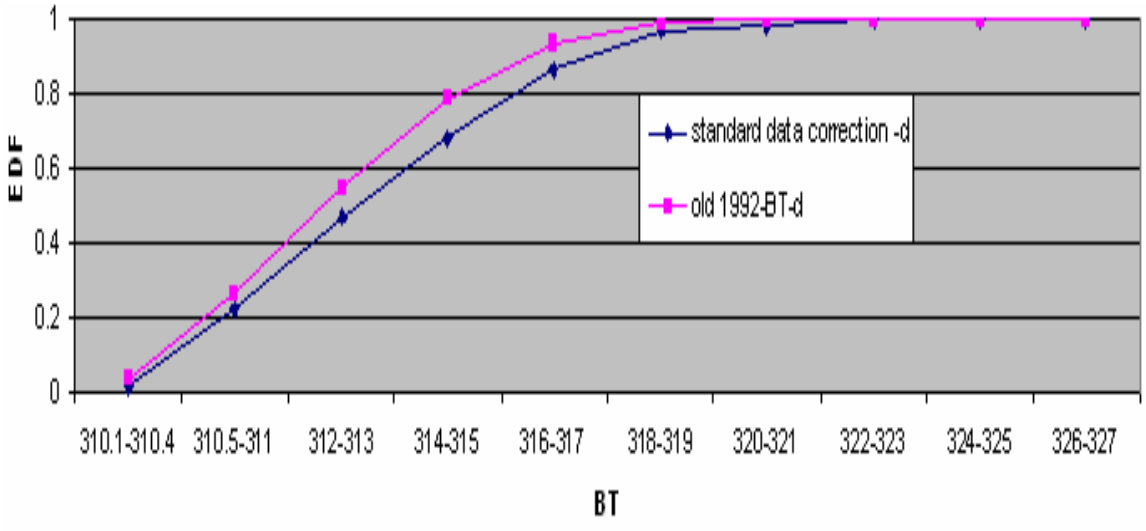

Figure 6.55 (a) Empirical distribution functions for unnormalized BT data (d-desert) of 1992 compared with standard data correction sets (subset 1).

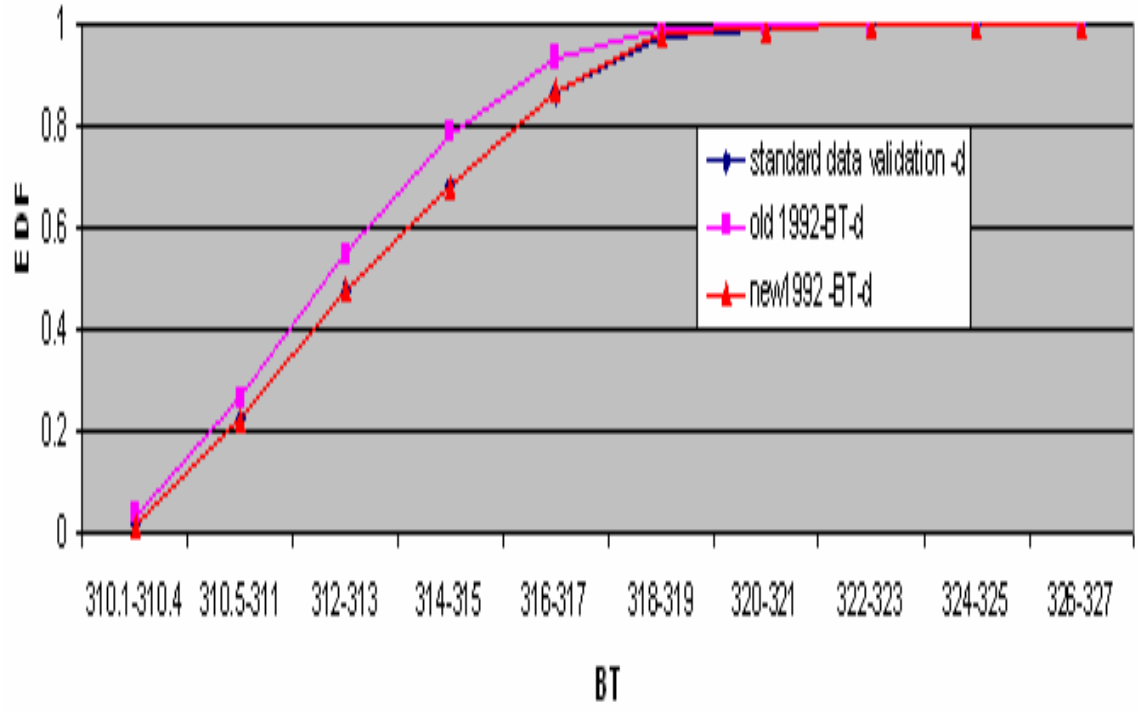

Figure 6.55 (b) Empirical distribution functions for normalized BT data (d-desert) of 1992 compared with standard data validation sets (subset 2).

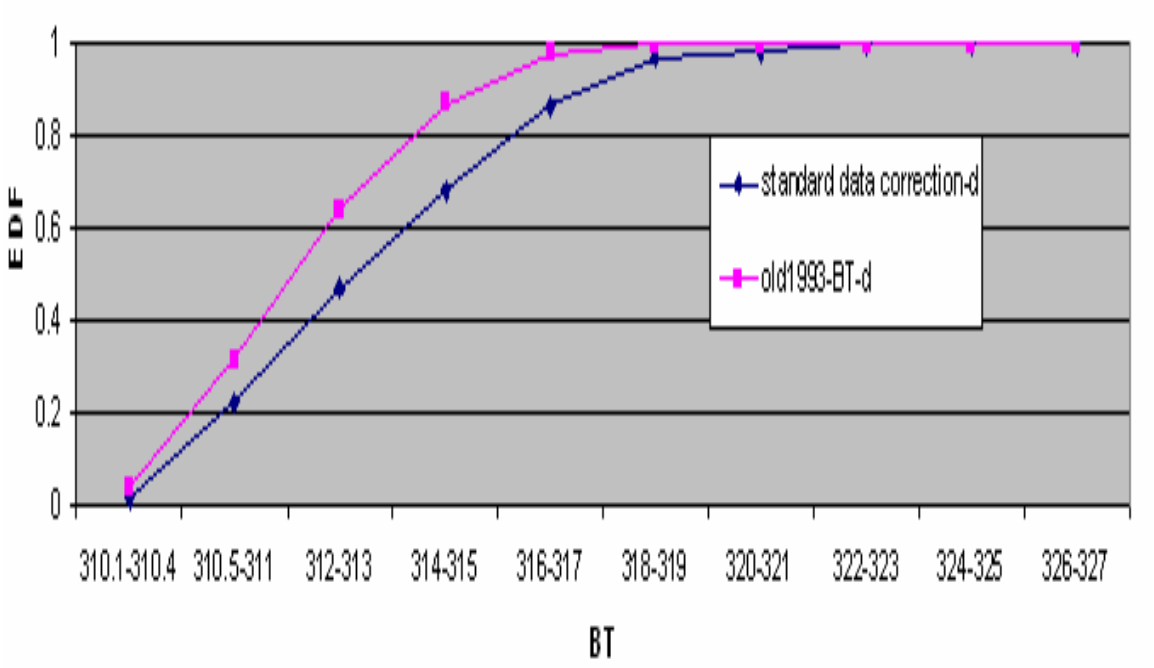

Figure 6.56 (a) Empirical distribution functions for unnormalized BT data (d-desert) of 1993 compared with standard data correction sets (subset 1).

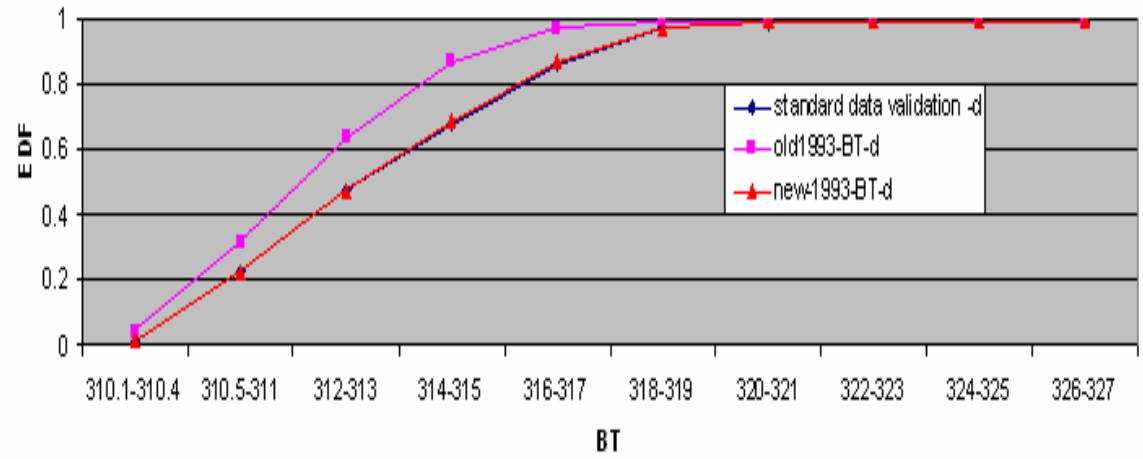

Figure 6.56 (b) Empirical distribution functions for normalized BT data (d-desert) of 1993 compared with standard data validation sets (subset 2)

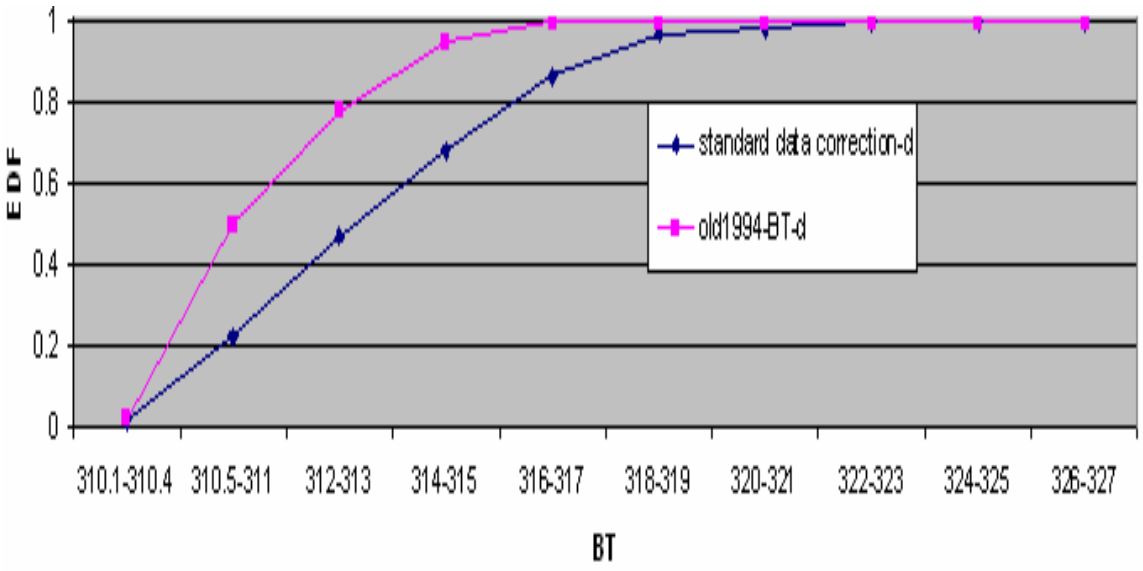

Figure 6.57 (a) Empirical distribution functions for unnormalized BT data (d-desert) of 1994 compared with standard data correction sets (subset 1).

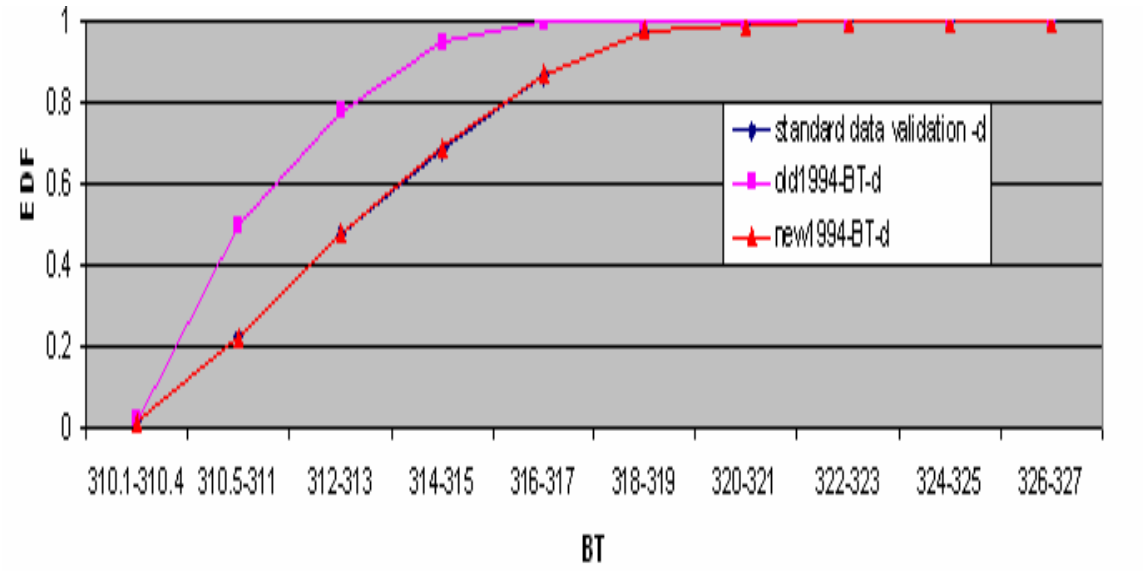

Figure 6.57 (b) Empirical distribution functions for normalized BT data (d-desert) of 1994 compared with standard data validation sets (subset 2).

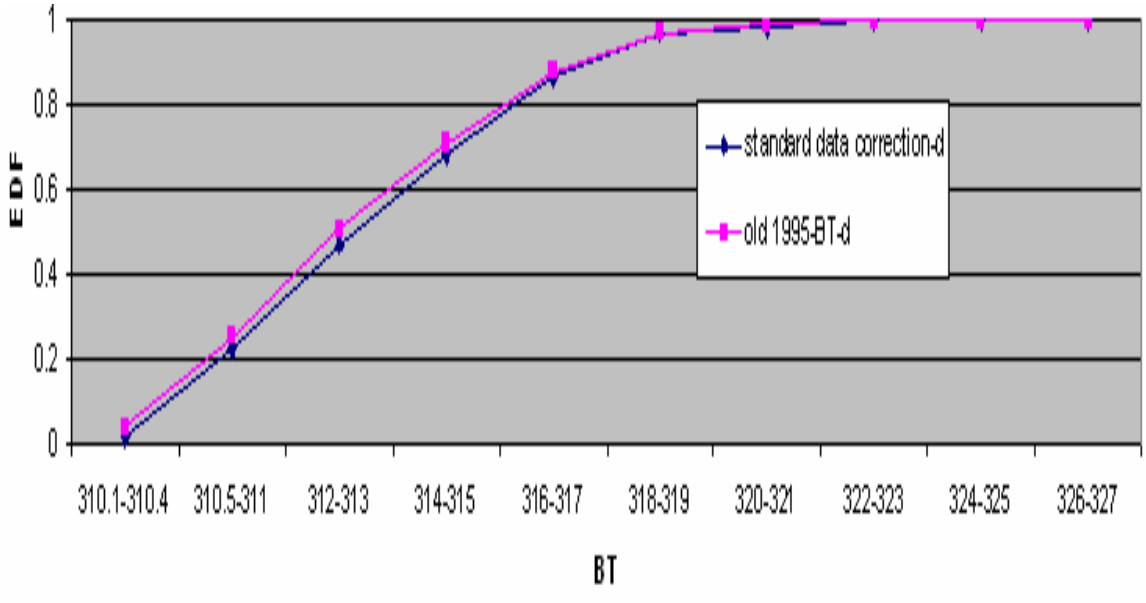

Figure 6.58 (a) Empirical distribution functions for unnormalized BT data (d-desert) of 1995 compared with standard data correction sets (subset 1).

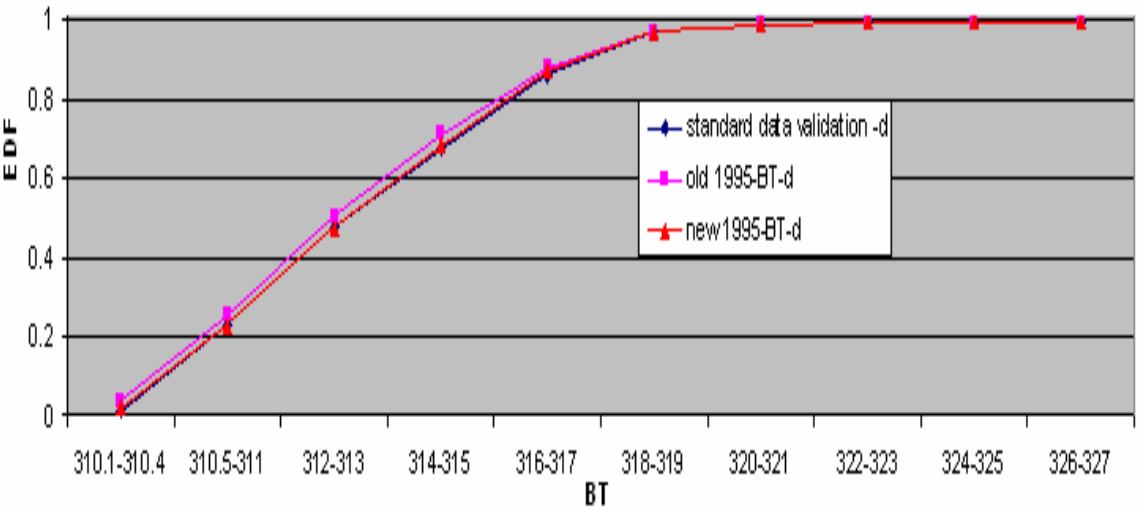

Figure 6.58 (b) Empirical distribution functions for normalized BT data (d-desert) of 1995 compared with standard data validation sets (subset 2).

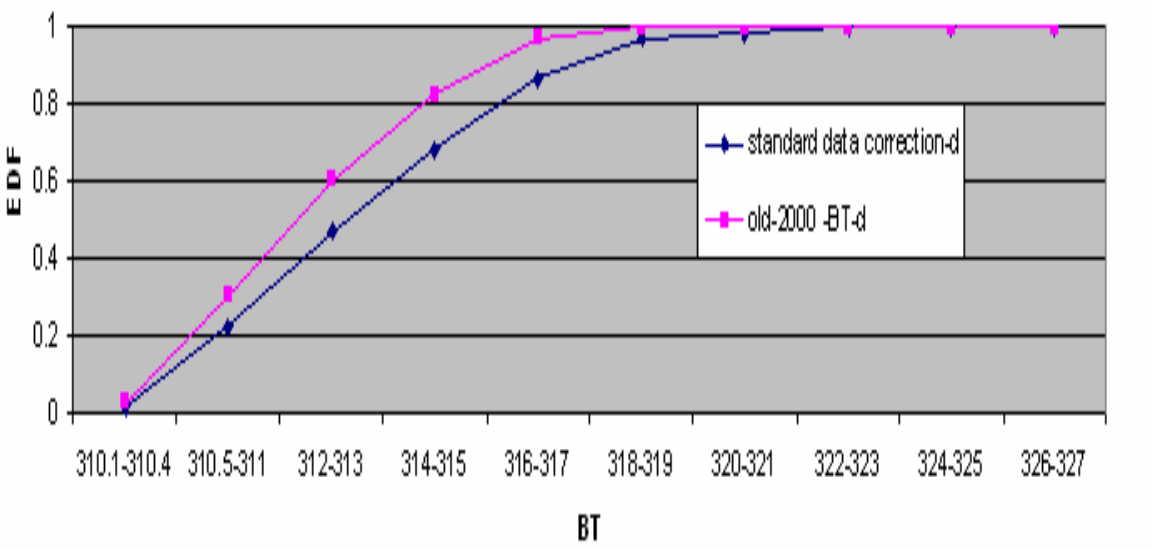

Figure 6.59 (a) Empirical distribution functions for unnormalized BT data (d-desert) of 2000 compared with standard data correction sets (subset 1).

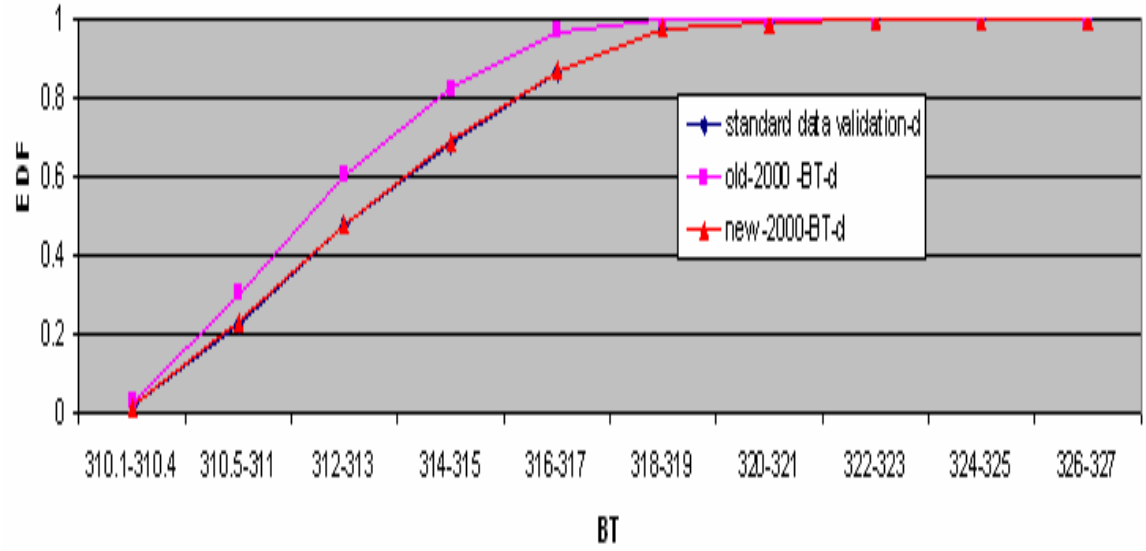

Figure 6.59 (b) Empirical distribution functions for normalized BT data (d-desert) of 2000 compared with standard data validation sets (subset 2).

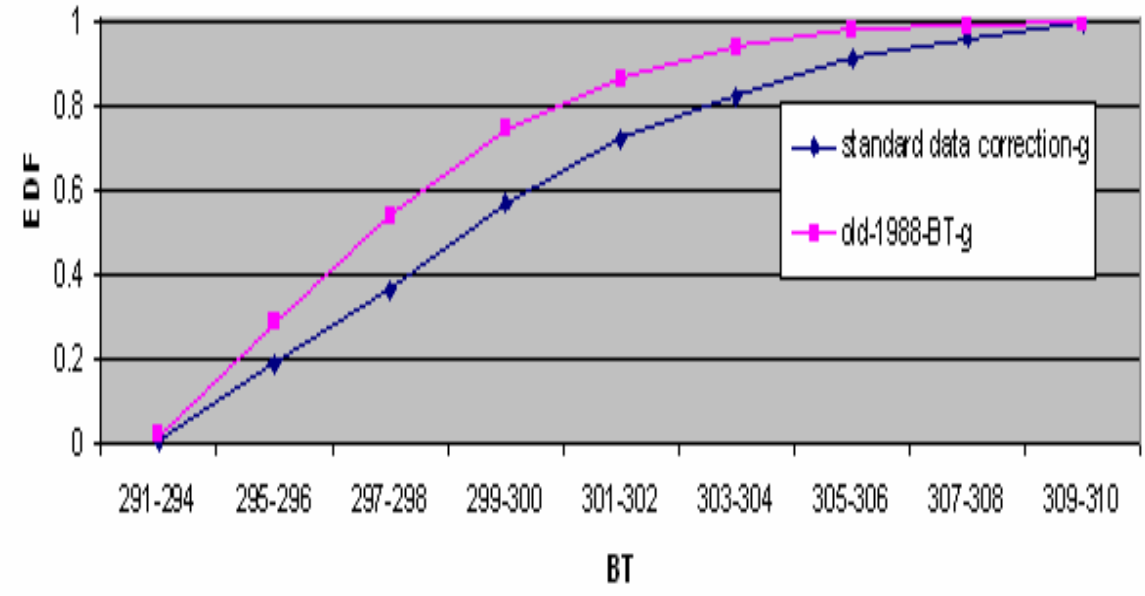

Figure 6.60 (a) Empirical distribution functions for unnormalized BT data (g-grassland) of 1988 compared with standard data correction sets (subset 1).

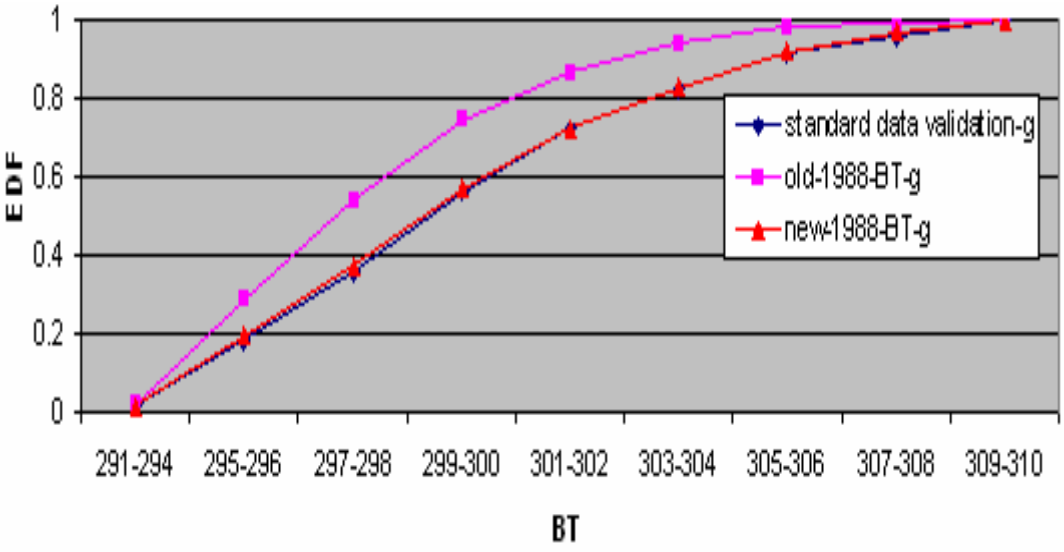

Figure 6.60 (b) Empirical distribution functions for normalized BT data (g-grassland) of 1988 compared with standard data validation sets (subset 2).

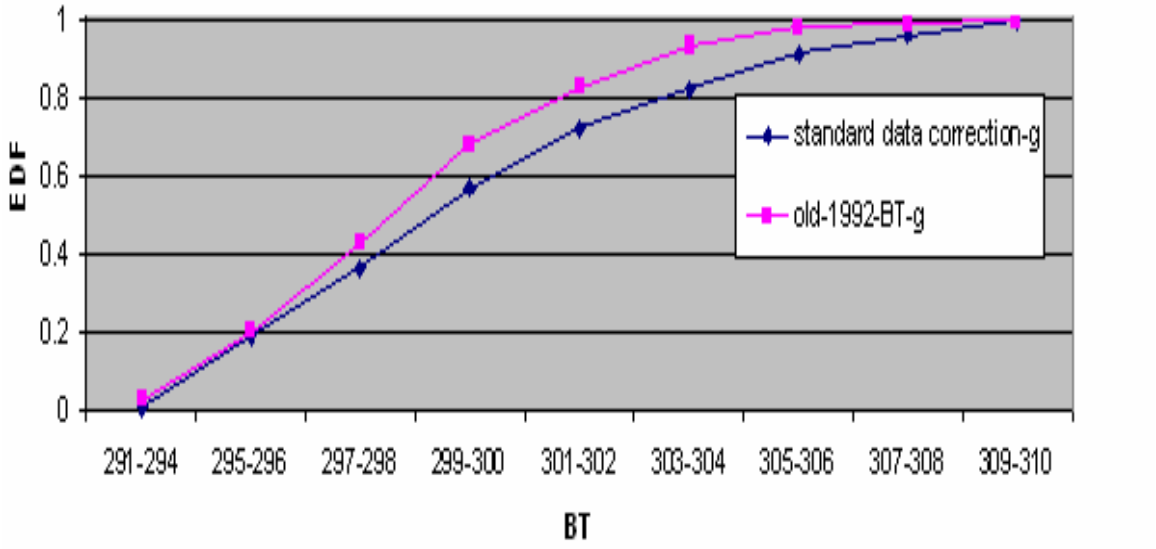

Figure 6.61 (a) Empirical distribution functions for unnormalized BT data (g-grassland) of 1992 compared with standard data correction sets (subset 1).

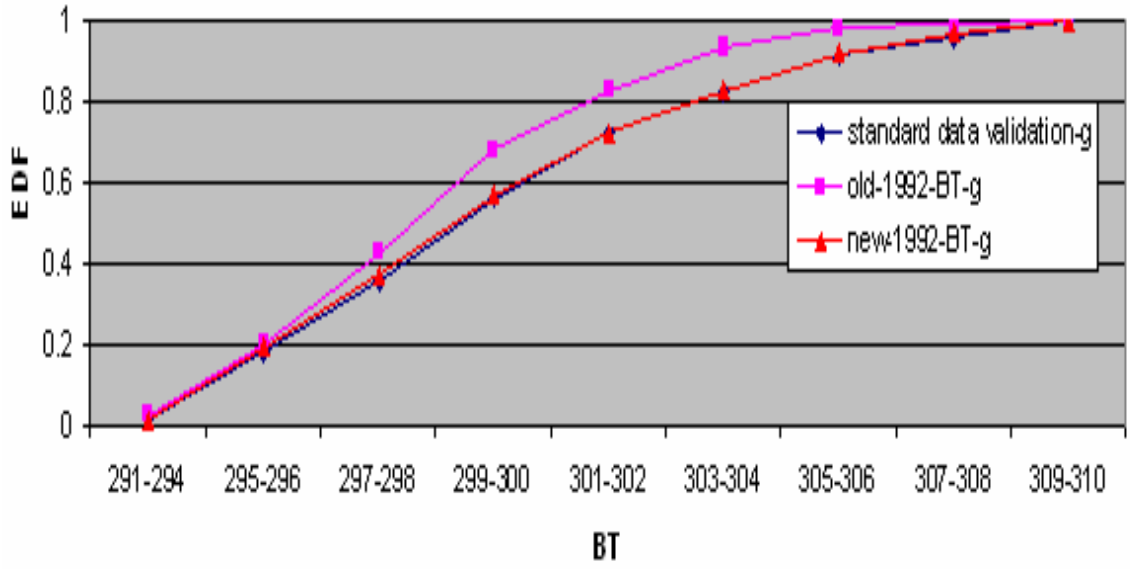

Figure 6.61 (b) Empirical distribution functions for normalized BT data (g-grassland) of 1992 compared with standard data validation sets (subset 2).

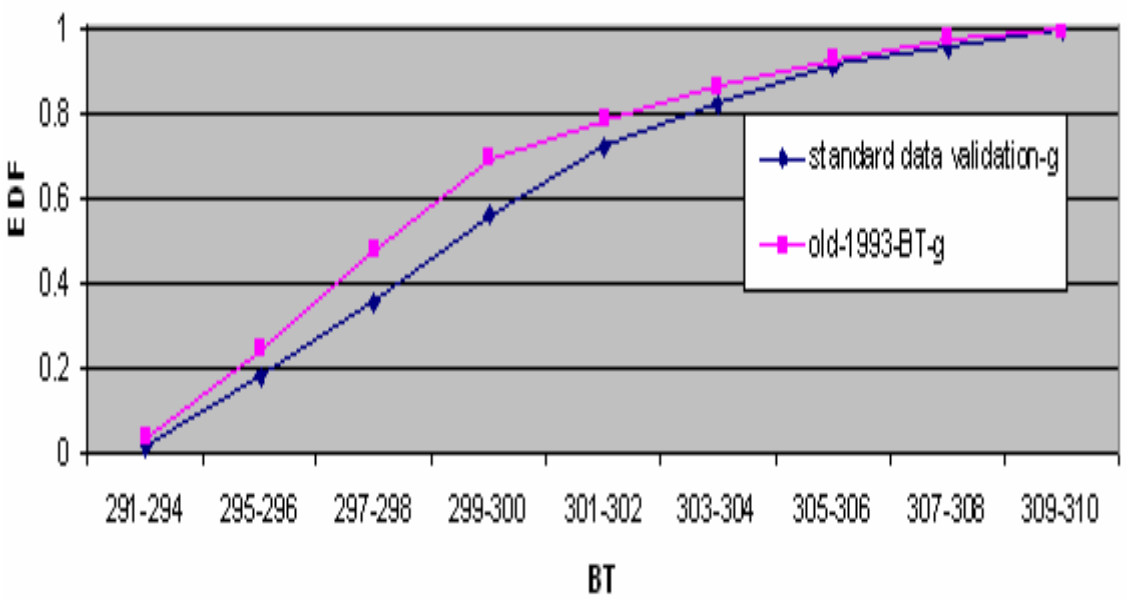

Figure 6.62 (a) Empirical distribution functions for unnormalized BT data (g-grassland) of 1993 compared with standard data correction sets (subset 1).

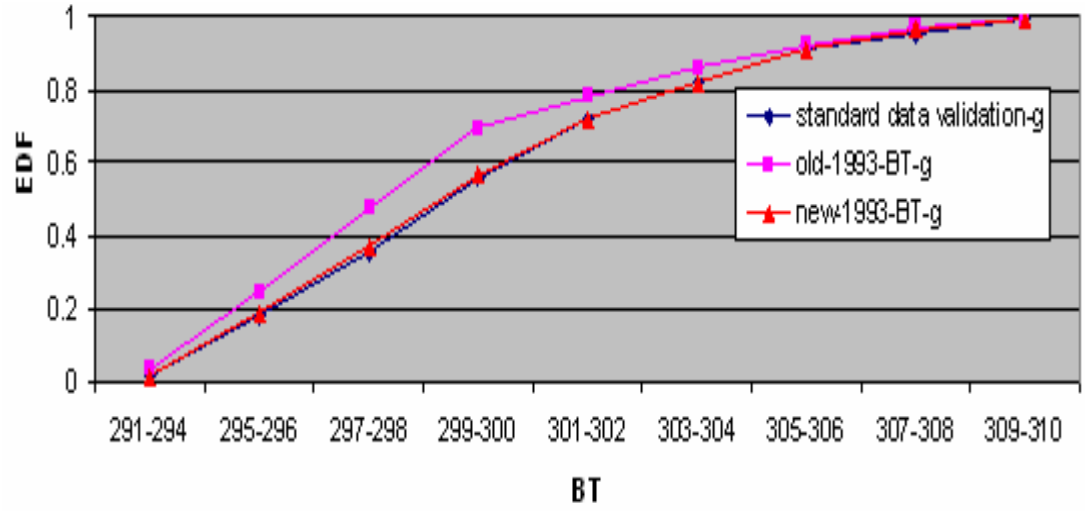

Figure 6.62 (b) Empirical distribution functions for normalized BT data (g-grassland) of 1993 compared with standard data validation sets (subset 2).

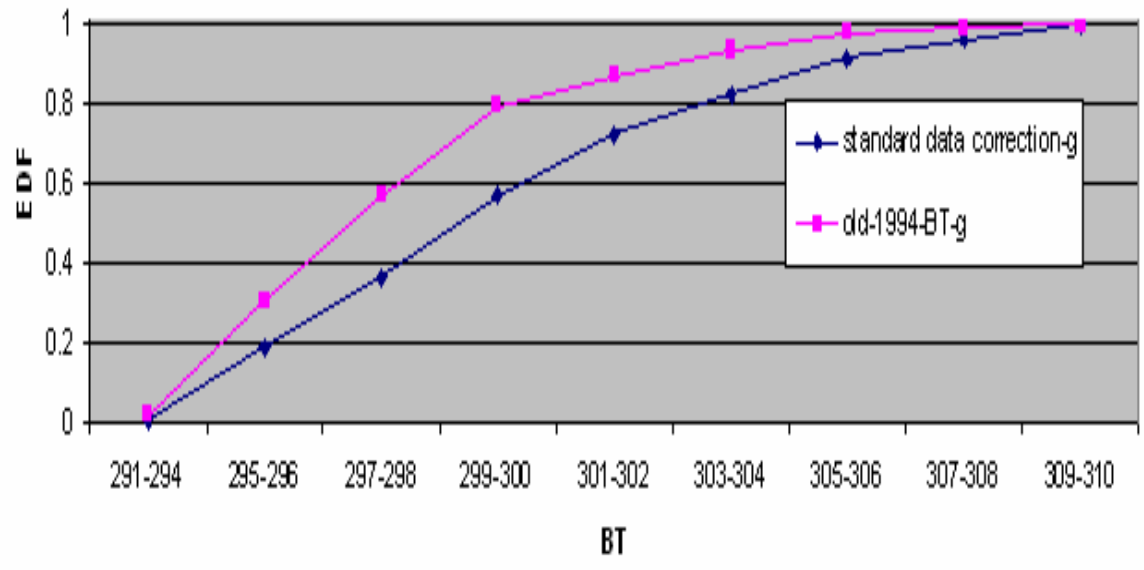

Figure 6.63 (a) Empirical distribution functions for unnormalized BT data (g-grassland) of 1994 compared with standard data correction sets (subset 1).

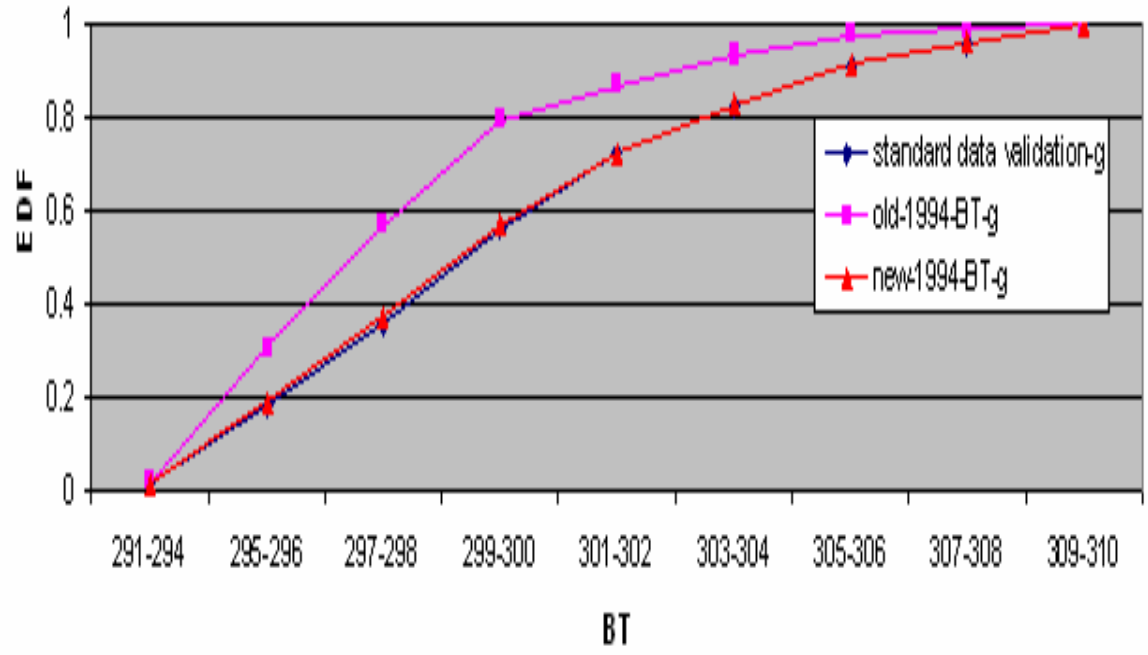

Figure 6.63 (b) Empirical distribution functions for normalized BT data (g-grassland) of 1994 compared with standard data validation sets (subset 2).

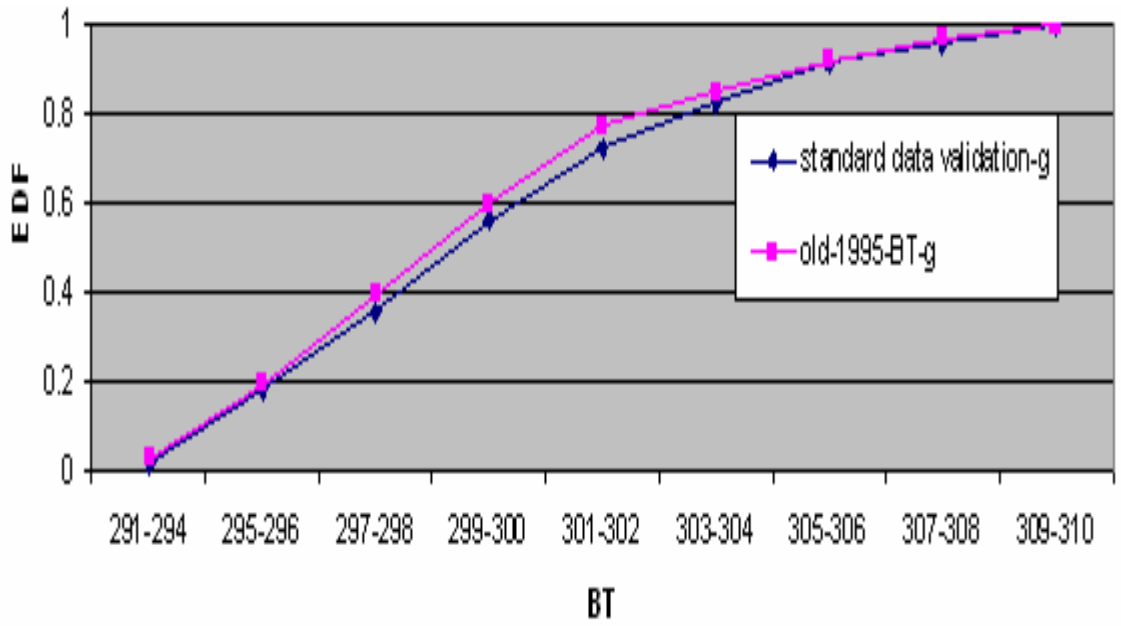

Figure 6.64 (a) Empirical distribution functions for unnormalized BT data (g-grassland) of 1995 compared with standard data correction sets (subset 1).

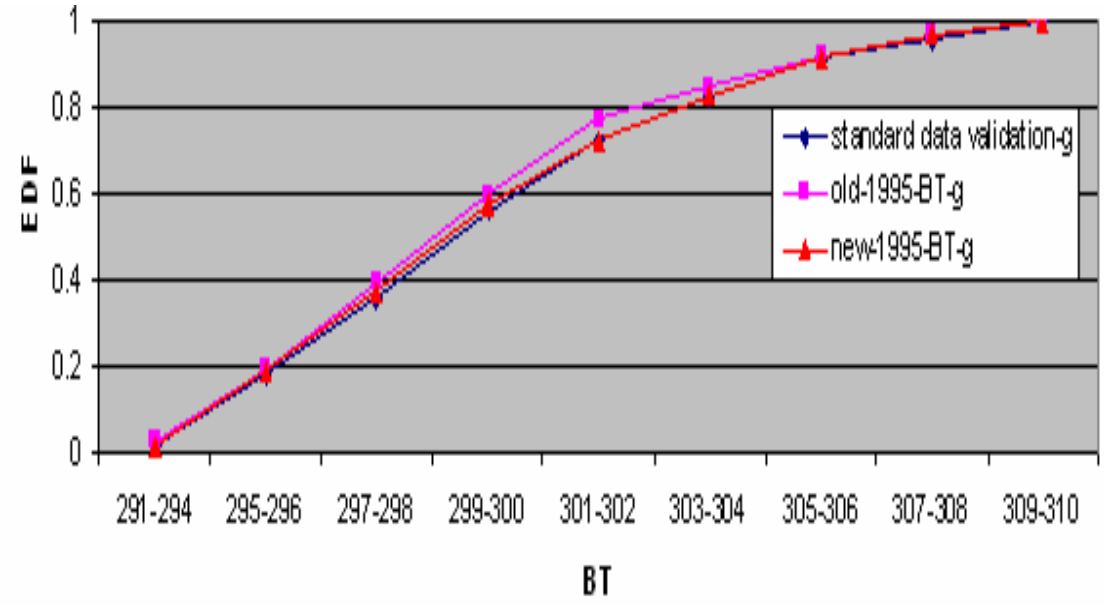

Figure 6.64 (b) Empirical distribution functions for normalized BT data (g-grassland) of 1995 compared with standard data validation sets (subset 2).

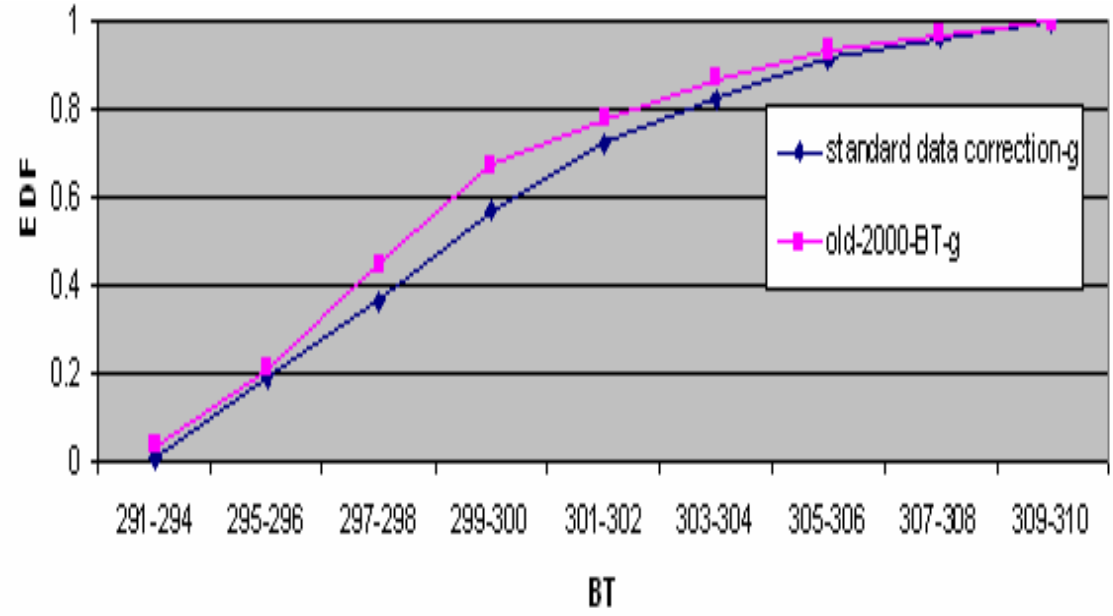

Figure 6.65 (a) Empirical distribution functions for unnormalized BT data (g-grassland) of 2000 compared with standard data correction sets (subset 1).

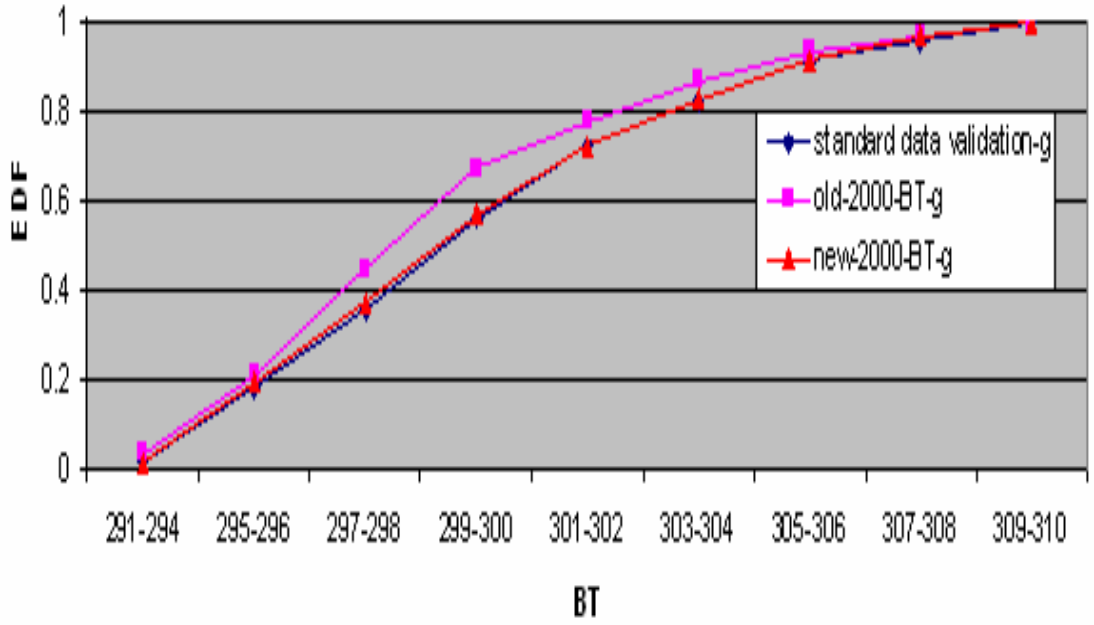

Figure 6.65 (b) Empirical distribution functions for normalized BT data (g-grassland) of 2000 compared with standard data validation sets (subset 2).

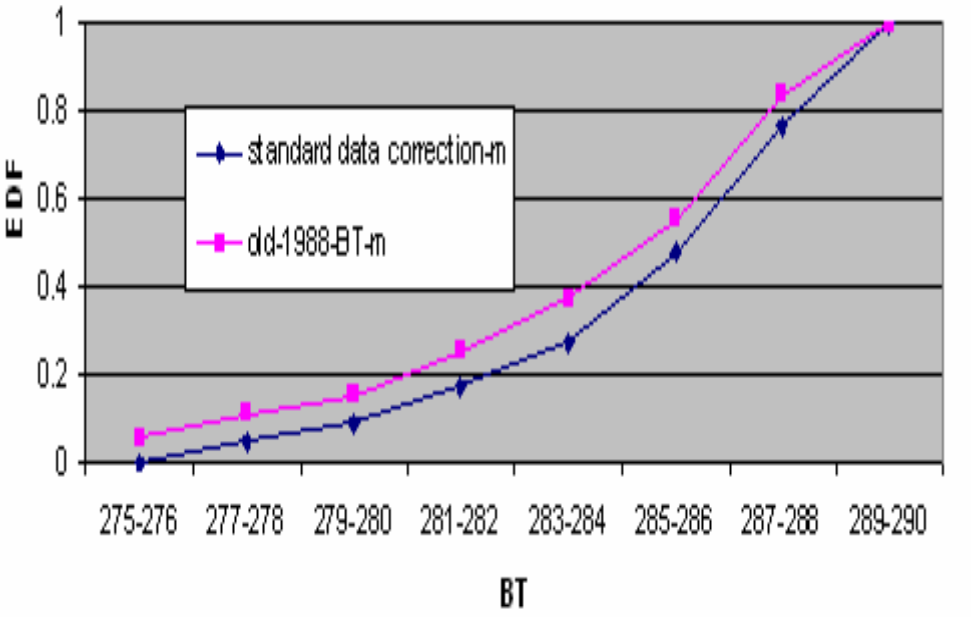

Figure 6.66 (a) Empirical distribution functions for unnormalized BT data (m-mixed) of 1988 compared with standard data correction sets (subset 1).

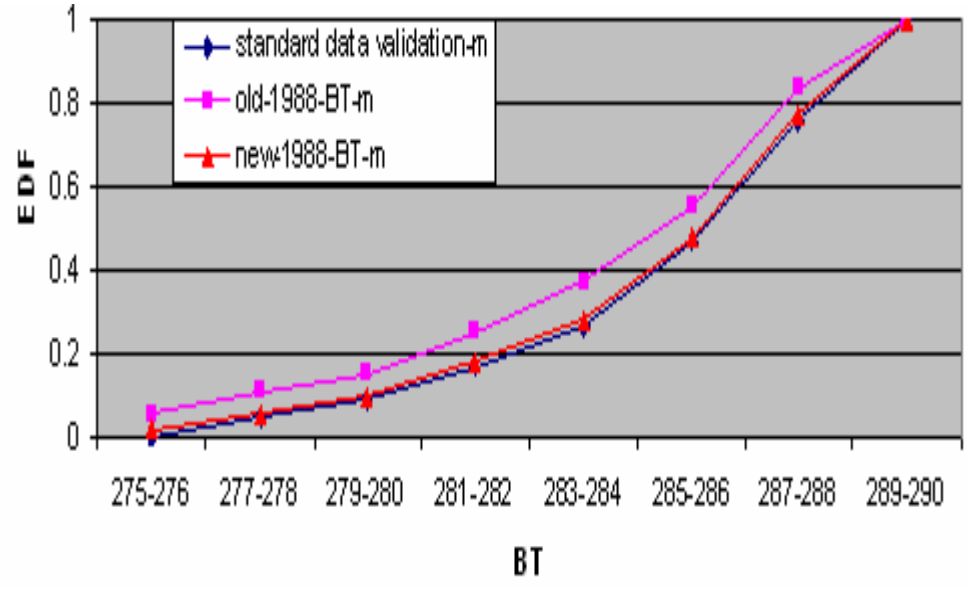

Figure 6.66 (b) Empirical distribution functions for normalized BT data (m-mixed) of 1988 compared with standard data validation sets (subset 2).

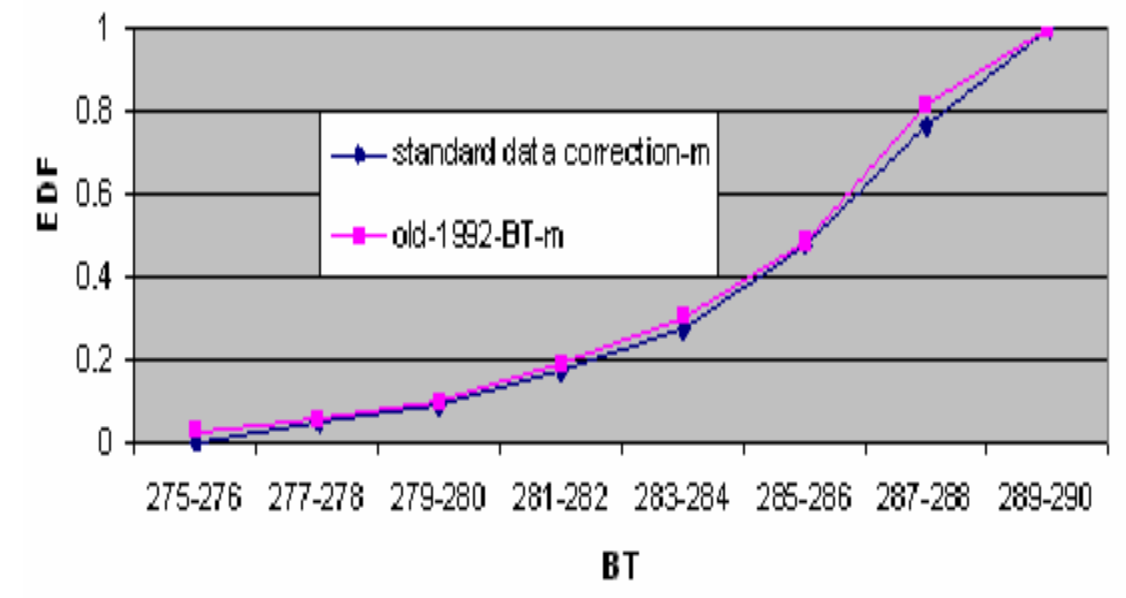

Figure 6.67 (a) Empirical distribution functions for unnormalized BT data (m-mixed) of 1992 compared with standard data correction sets (subset 1).

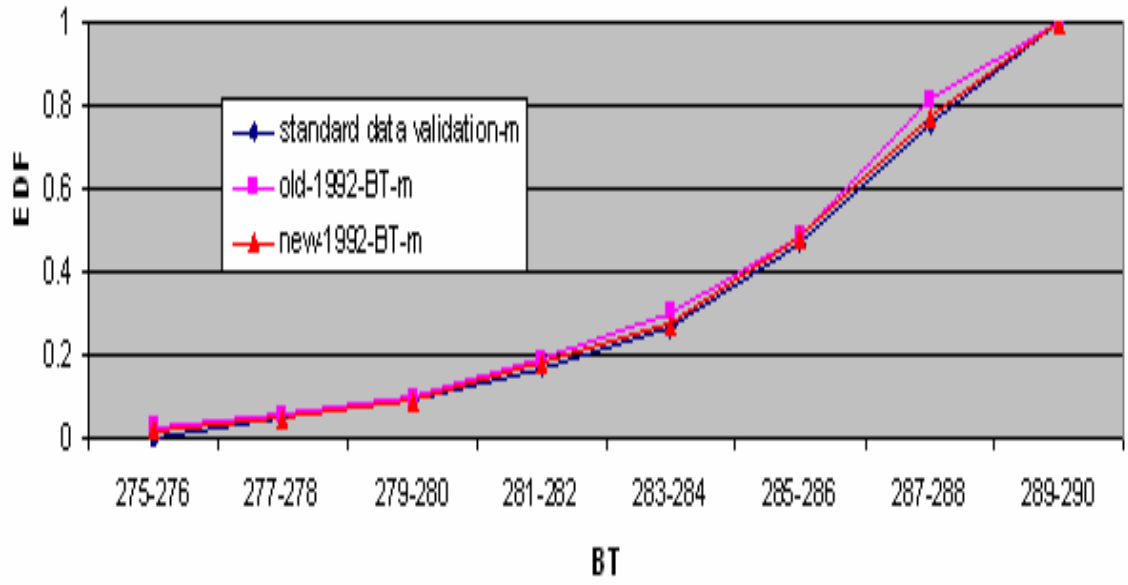

Figure 6.67 (b) Empirical distribution functions for normalized BT data (m-mixed) of 1992 compared with standard data validation sets (subset 2).

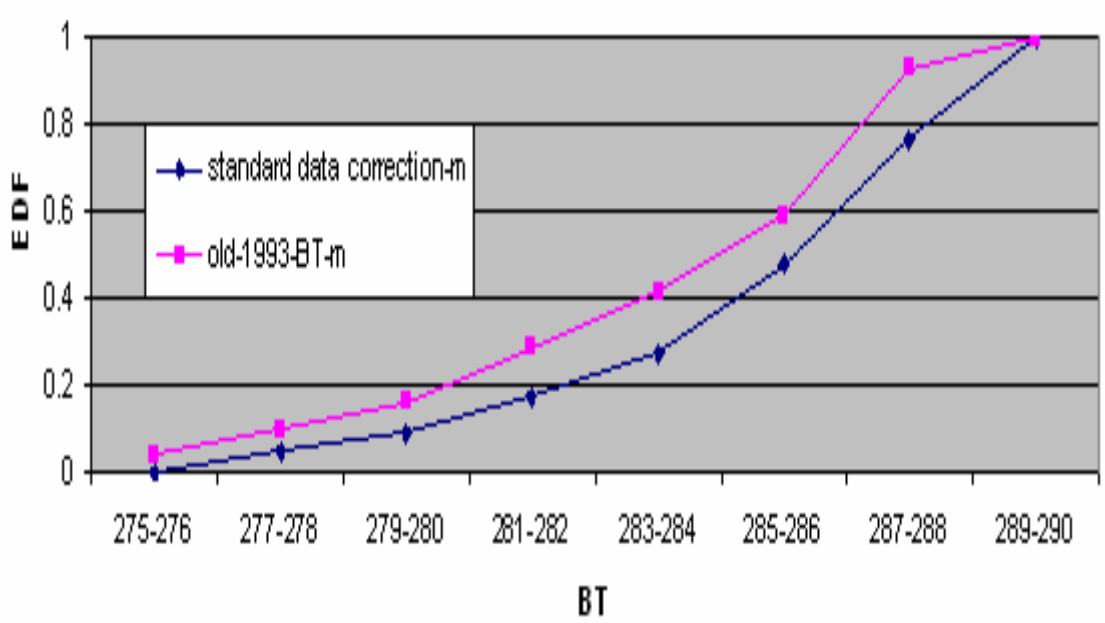

Figure 6.68 (a) Empirical distribution functions for unnormalized BT data (m-mixed) of 1993 compared with standard data correction sets (subset 1).

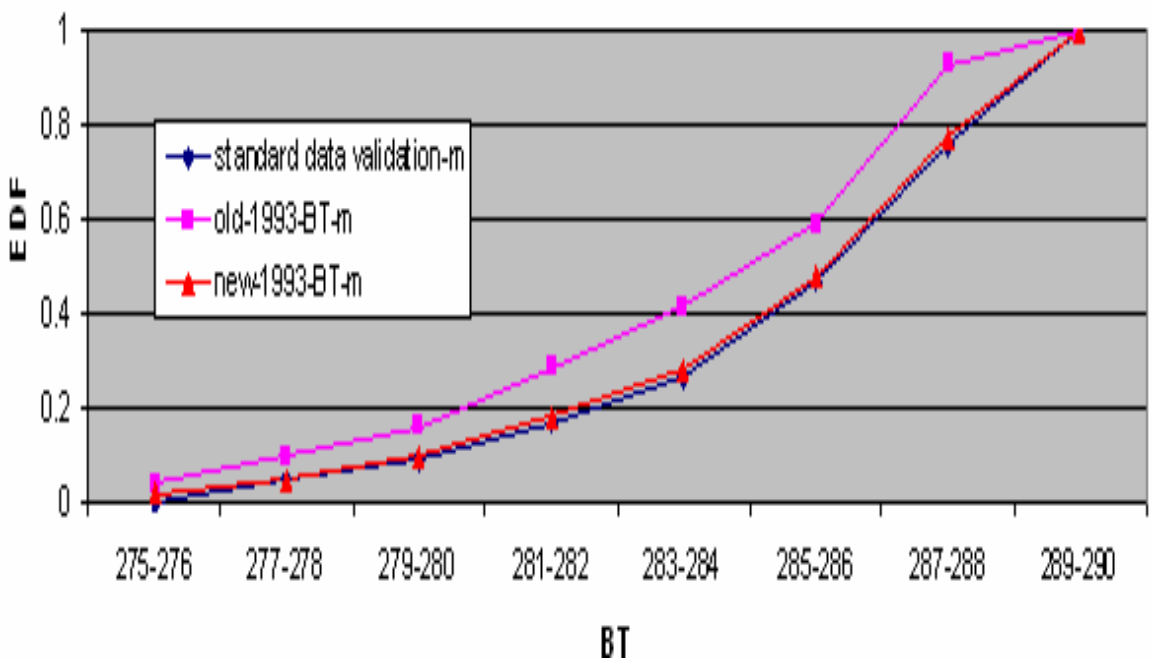

Figure 6.68 (b) Empirical distribution functions for normalized BT data (m-mixed) of 1993 compared with standard data validation sets (subset 2).

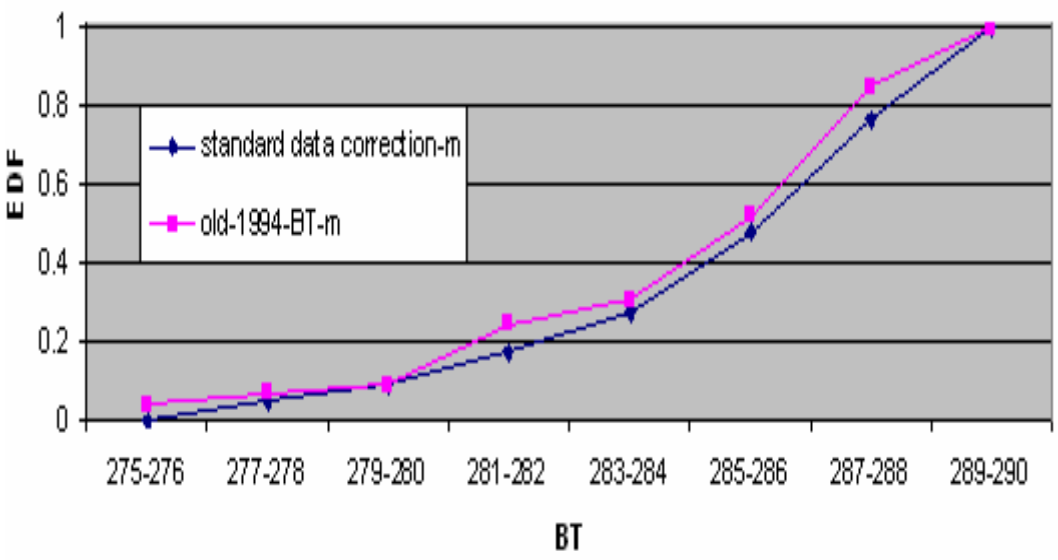

Figure 6.69 (a) Empirical distribution functions for unnormalized BT data (m-mixed) of 1994 compared with standard data correction sets (subset 1).

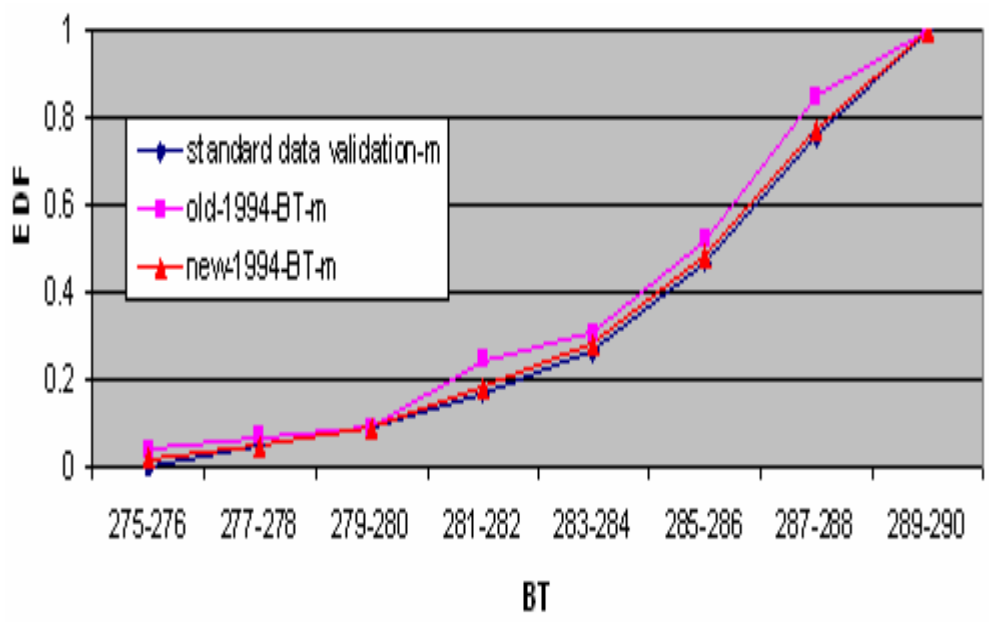

Figure 6.69 (b) Empirical distribution functions for normalized BT data (m-mixed) of 1994 compared with standard data validation sets (subset 2).

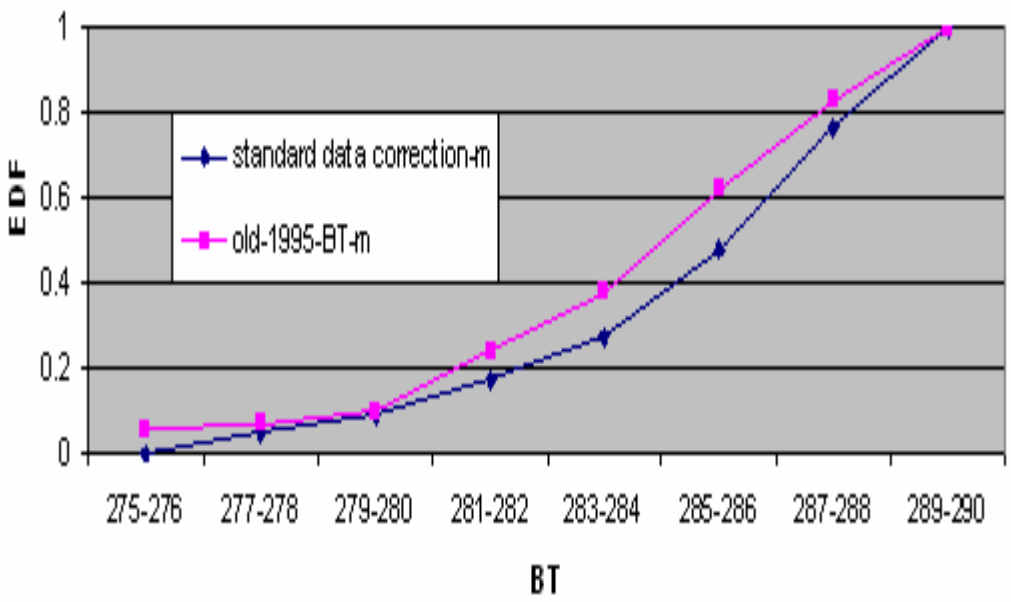

Figure 6.70 (a) Empirical distribution functions for unnormalized BT data (m-mixed) of 1995 compared with standard data correction sets (subset 1).

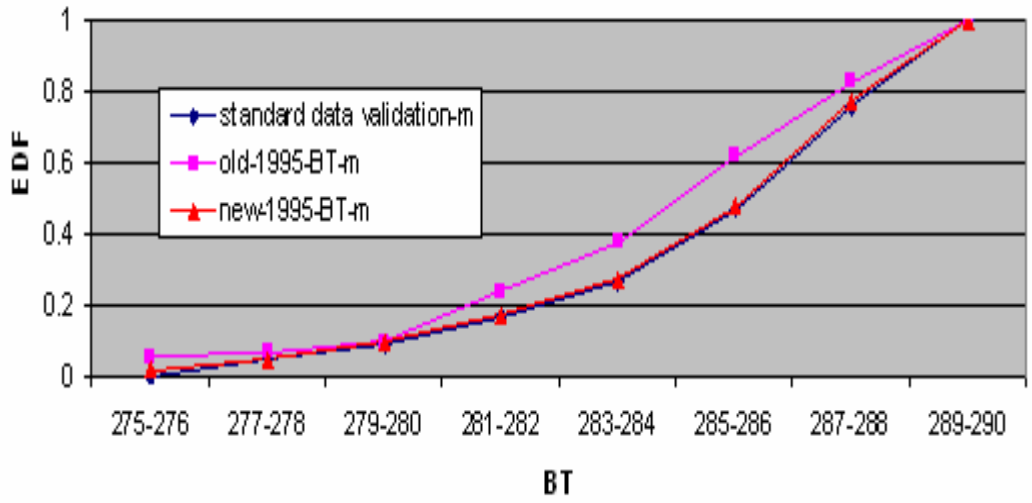

Figure 6.70 (b) Empirical distribution functions for normalized BT data (m-mixed) of 1995 compared with standard data validation sets (subset 2).

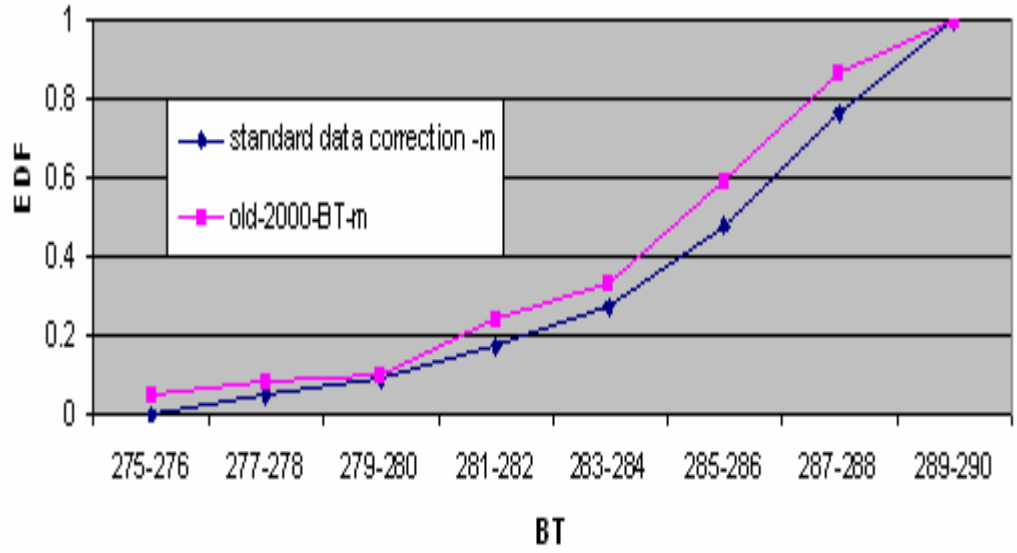

Figure 6.71 (a) Empirical distribution functions for unnormalized BT data (m-mixed) of 2000 compared with standard data correction sets (subset 1).

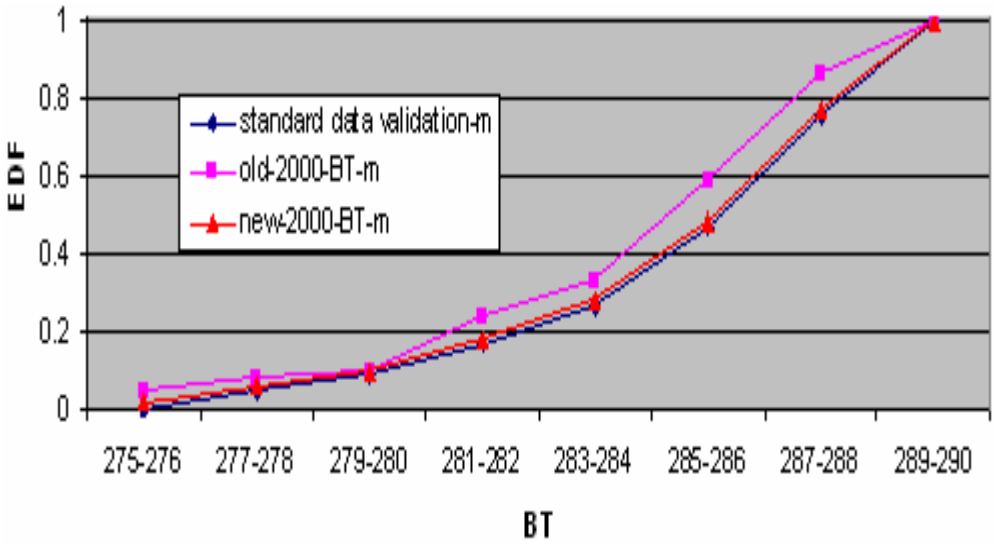

Figure 6.71 (b) Empirical distribution functions for normalized BT data (m-mixed) of 2000 compared with standard data validation sets (subset 2).

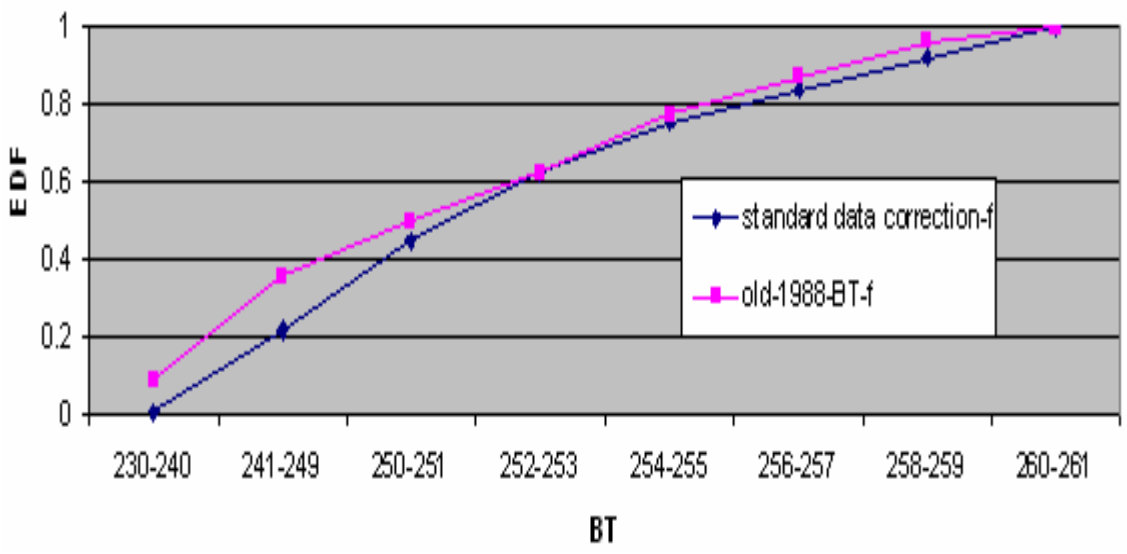

Figure 6.72 (a) Empirical distribution functions for unnormalized BT data (f-forest) of 1988 compared with standard data correction sets (subset 1).

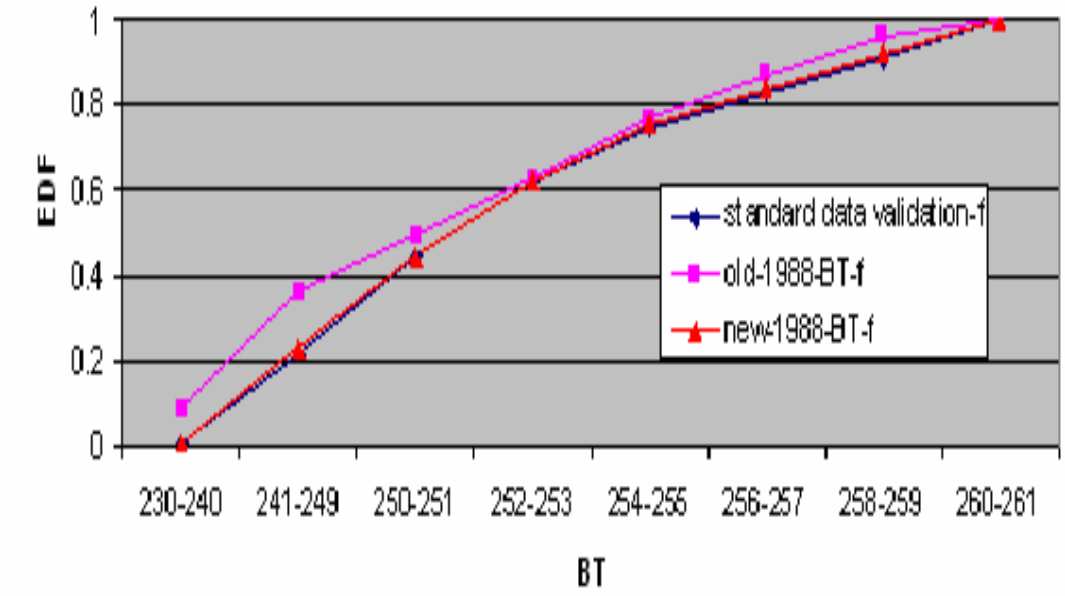

Figure 6.72 (b) Empirical distribution functions for normalized BT data (f-forest) of 1988 compared with standard data validation sets (subset 2).

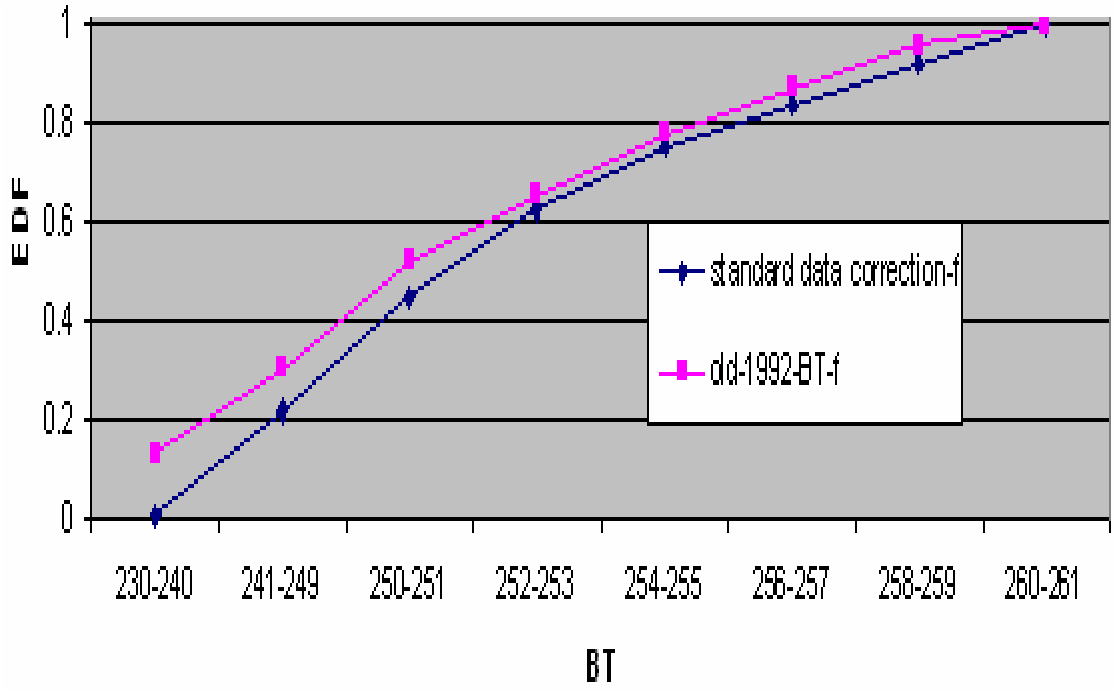

Figure 6.73 (a) Empirical distribution functions for unnormalized BT data (f-forest) of 1992 compared with standard data correction sets (subset 1).

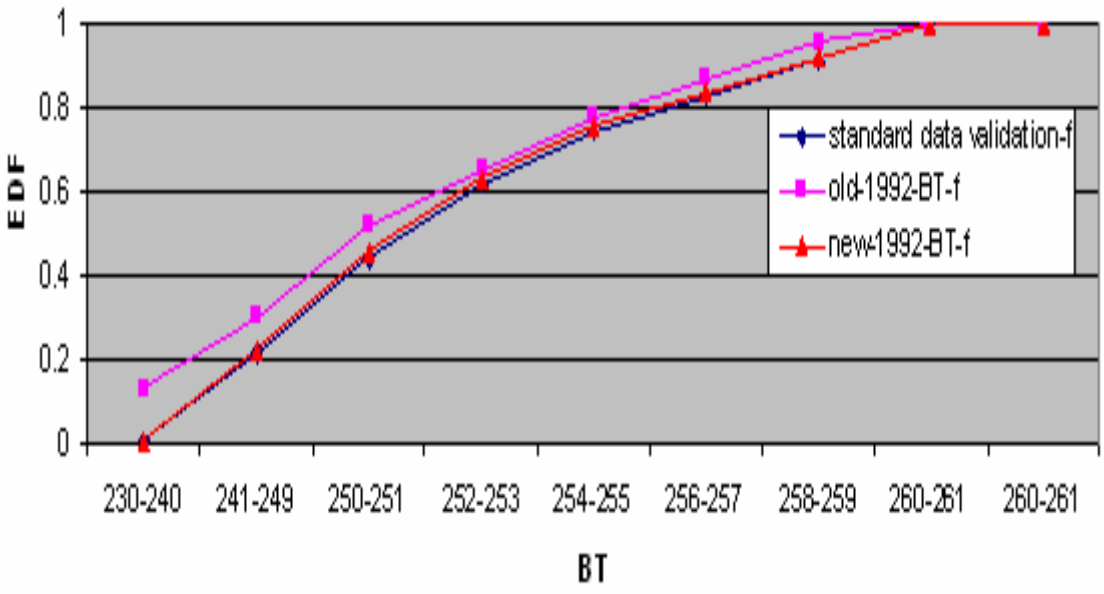

Figure 6.73 (b) Empirical distribution functions for normalized BT data (f-forest) of 1992 compared with standard data validation sets (subset 2).

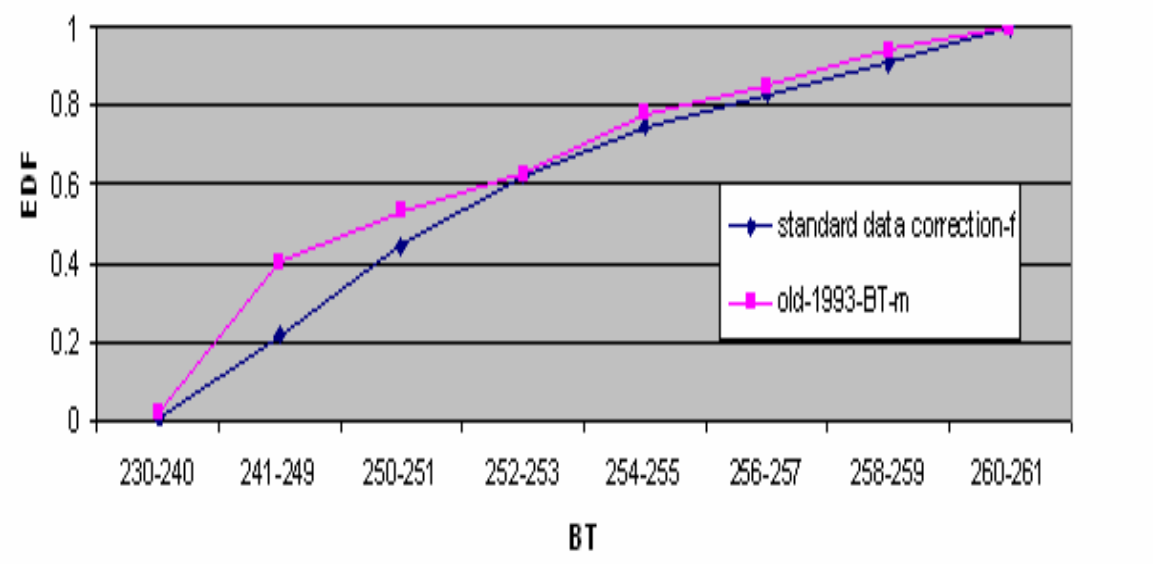

Figure 6.74 (a) Empirical distribution functions for unnormalized BT data (f-forest) of 1993 compared with standard data correction sets (subset 1).

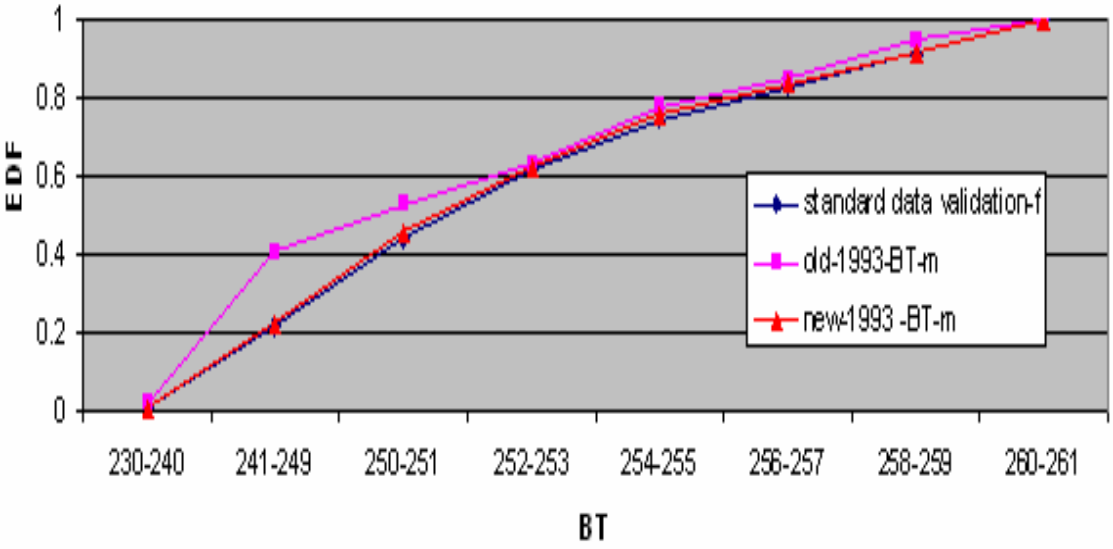

Figure 6.74 (b) Empirical distribution functions for normalized BT data (f-forest) of 1993 compared with standard data validation sets (subset 2).

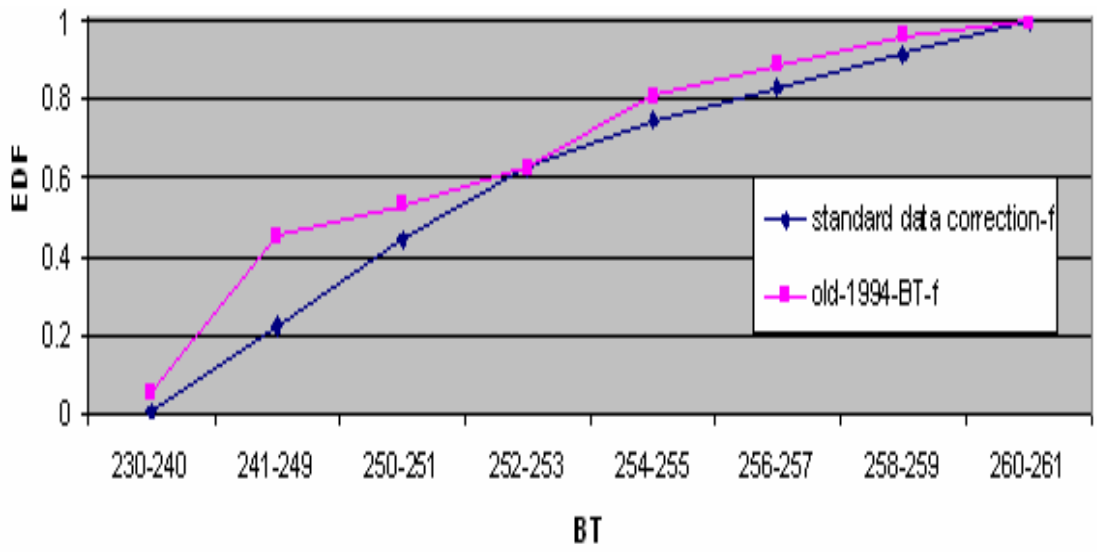

Figure 6.75 (a) Empirical distribution functions for unnormalized BT data (f-forest) of 1994 compared with standard data correction sets (subset 1).

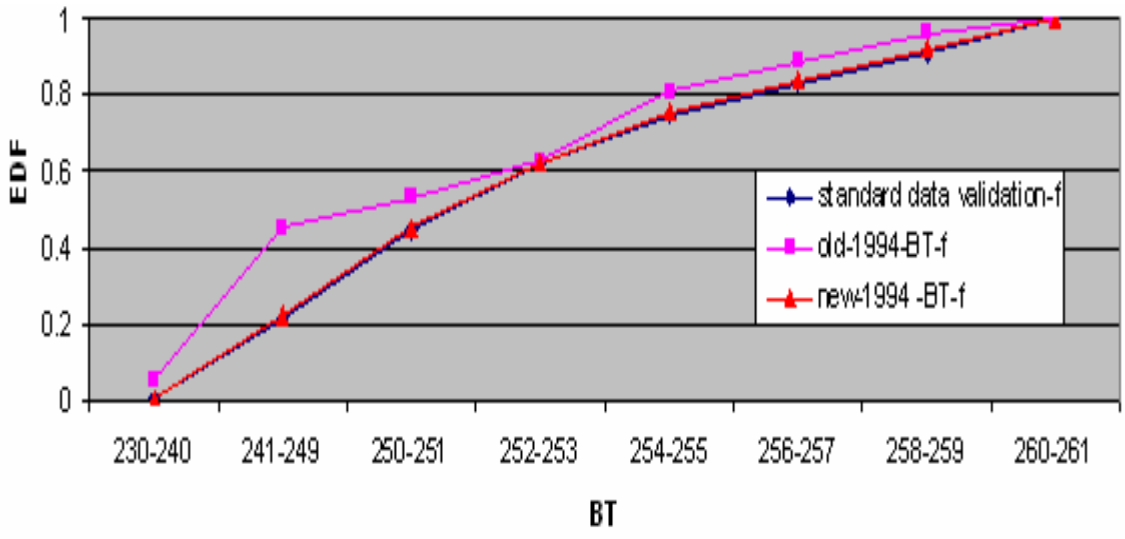

Figure 6.75 (b) Empirical distribution functions for normalized BT data (f-forest) of 1994 compared with standard data validation sets (subset 2).

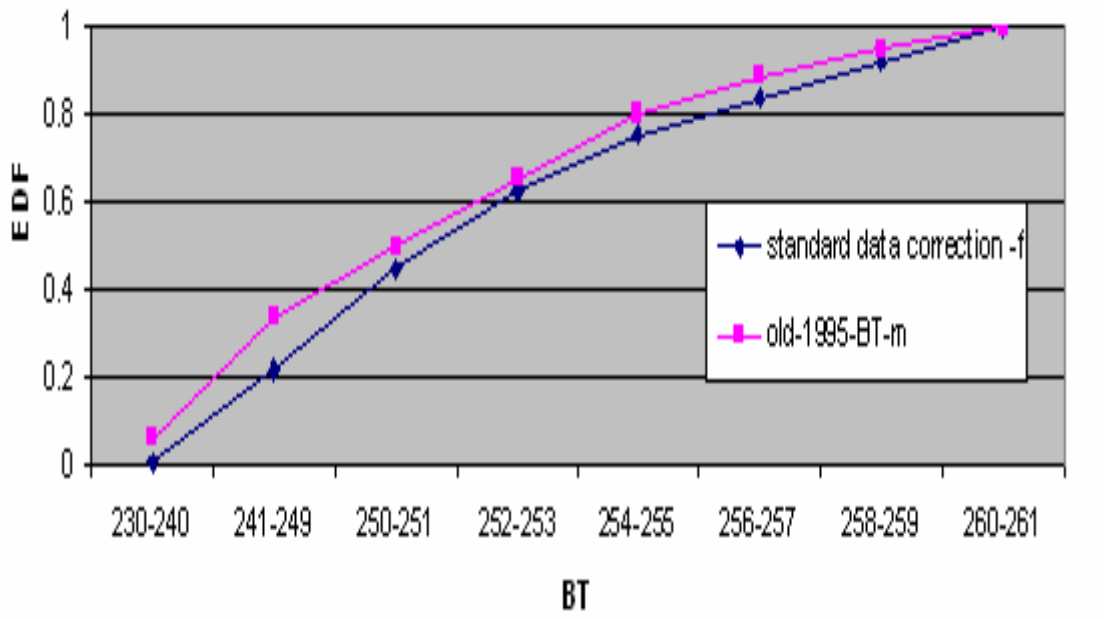

Figure 6.76 (a) Empirical distribution functions for unnormalized BT data (f-forest) of 1995 compared with standard data correction sets (subset 1).

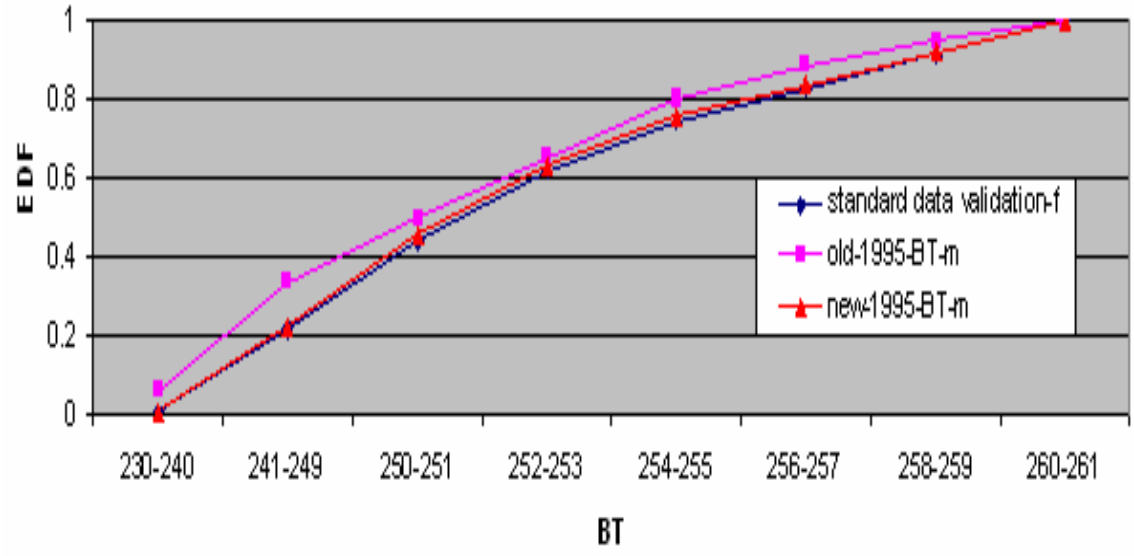

Figure 6.76 (b) Empirical distribution functions for normalized BT data (f-forest) of 1995 compared with standard data validation sets (subset 2).

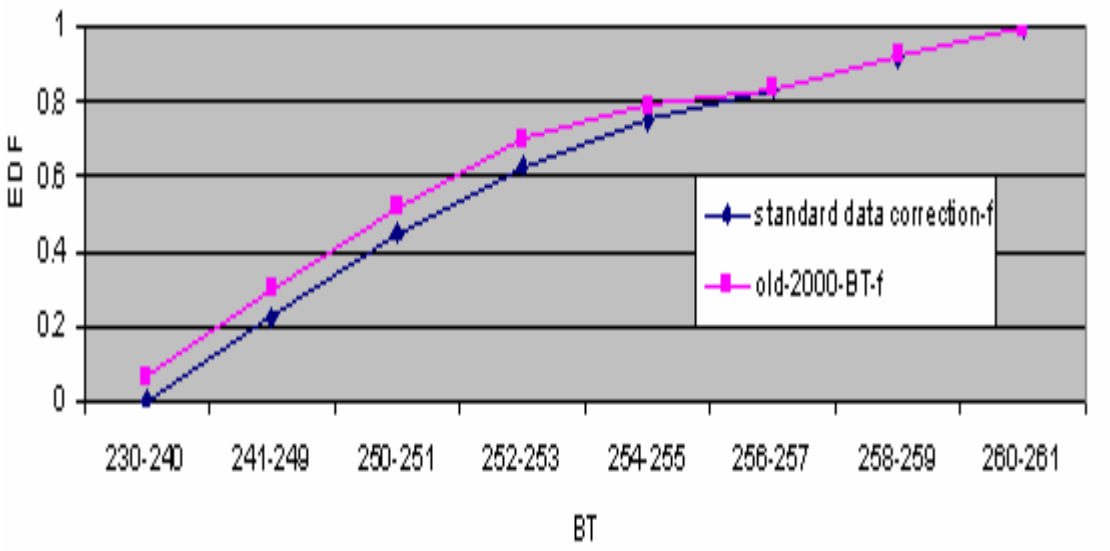

Figure 6.77 (a) Empirical distribution functions for unnormalized BT data (f-forest) of 2000 compared with standard data correction sets (subset 1).

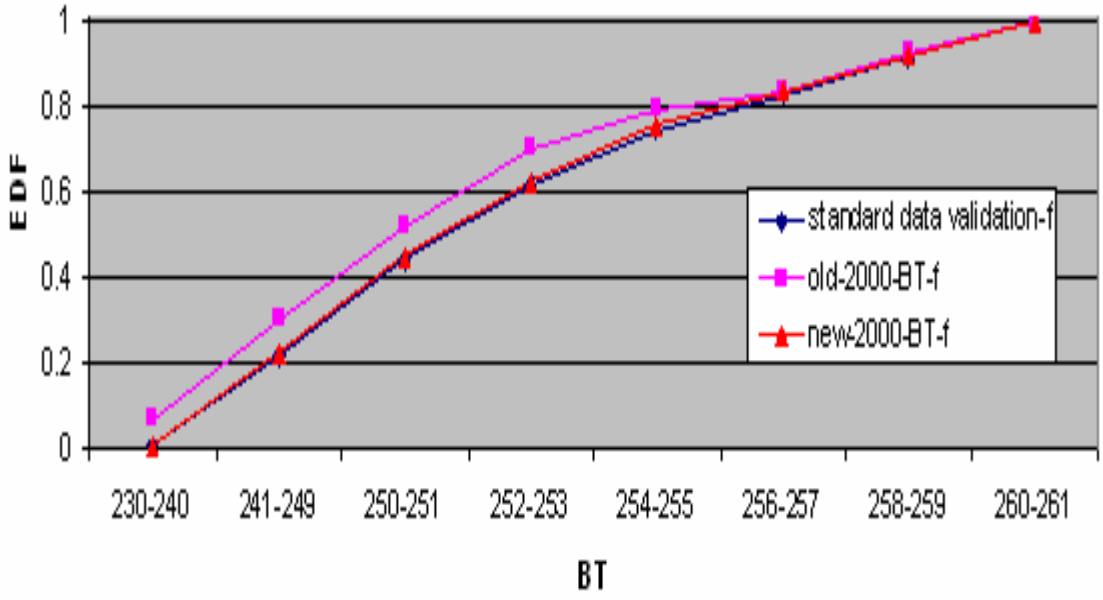

Figure 6.77 (b) Empirical distribution functions for normalized BT data (f-forest) of 2000 compared with standard data validation sets (subset 2).

Figure 6.54-6.77 shows that the normalization was successful in making the EDF's of the unnormalized and standard years nearly identical. Using normalized value, we produce new BT time series for different ecosystems as shown in Figure 6.78 which shows improvement of BT data (blue line) of the year of 1988, 1992, 1993, 1994, 1995, and 2000.

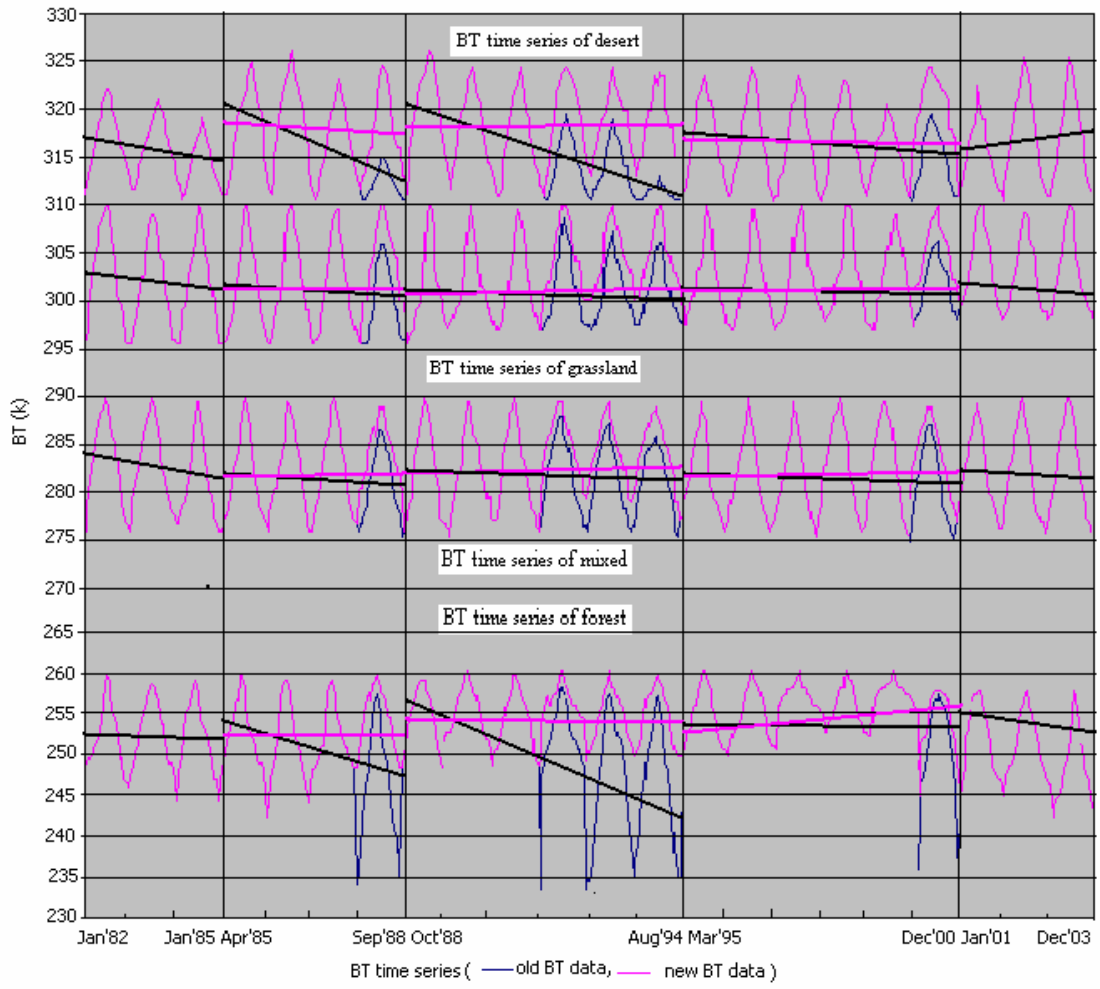

Figure 6.78 Corrected BT time series (yearly) for different ecosystems in China.

BT trends for selected ecosystems in China and jumps between the satellites are illustrated in Figure 6.78 and the errors are estimated in Table 6.4. All ecosystems show some BT trends for each satellite and jump from one satellite to the next one. Analysis shows that high rate of BT change for NOAA-9,-11, and -14 by reduction of BT in 1988, 1992-1994, and 2000 due to elevated amount of stratospheric aerosol from Mt Pinatubo and considerable degradation of satellite orbit. High rate of BT change belong to desert ecosystem. Vegetative ecosystems have generally small differences between BT at the beginning and the end of satellite life although some exceptions are seen for NOAA-9, -11, and -14.

Regarding BT jump from one satellite to the next in Table 6.4(B), general tendency is a reduction of BT between beginning of NOAA-9 and the end of NOAA-7, between beginning of NOAA-16 and the end of NOAA-14. An increase in BT is observed only during satellite change from NOAA-9 to NOAA-11, NOAA-11 to NOAA-14, and NOAA-14 to NOAA-16 due to already mentioned sharp stratospheric aerosols increase and orbit drift of satellite. Therefore, desert and tropical forest targets show the largest changes in BT during the time of satellite change. Again vegetative targets (except for desert and forest) show smaller BT jumps from one satellite to the next. After correction of BT, all target shows the significantly improve the BT trend and jumps between the satellites in table 6.4 (new BT).

Table 6.4: Estimation of Errors in (A) BT trend at the End of a Satellite Life and (B) Jumps between the Satellites (% to the beginning level)

Ecosystems in selected study area of China		A			B			
		N-9	N-11	N-14	N-7/9	N-9/11	N-11/14	N-14/16
Desert	Old BT	-2.1	-3	-1	1.8	2.3	2	0.3
	New BT	0	0	0	1.2	0.28	-0.3	-0.3
Grassland	Old BT	0.6	-0.3	-0.2	0.4	0.6	0.5	0.3
	New BT	0	0.3	0.13	0.2	0.3	-0.1	0.16
Mixed	Old BT	-0.2	-0.4	-0.17	0.5	0.4	0.4	-0.3
	New BT	0.3	0.45	0.33	0.3	-0.2	-0.3	-0.1
Forest	Old BT	-3	-5	-0.4	0.7	3.6	4.5	-0.3
	New BT	0	0	0.9	0.1	0.7	-0.5	0.5

6.6 Analysis of NDVI Image for Study Area in China

Figure 6.77 shows the NDVI image of 26th week number of (end of June), 1988, visually checked for navigation accuracy, remapped if necessary, and assembled into a time series. Formation of maximum value NDVI composite images minimizes atmospheric effects, scan angle effects, cloud contamination, and solar zenith angle effects without having to resort to an explicit atmospheric correction [3].

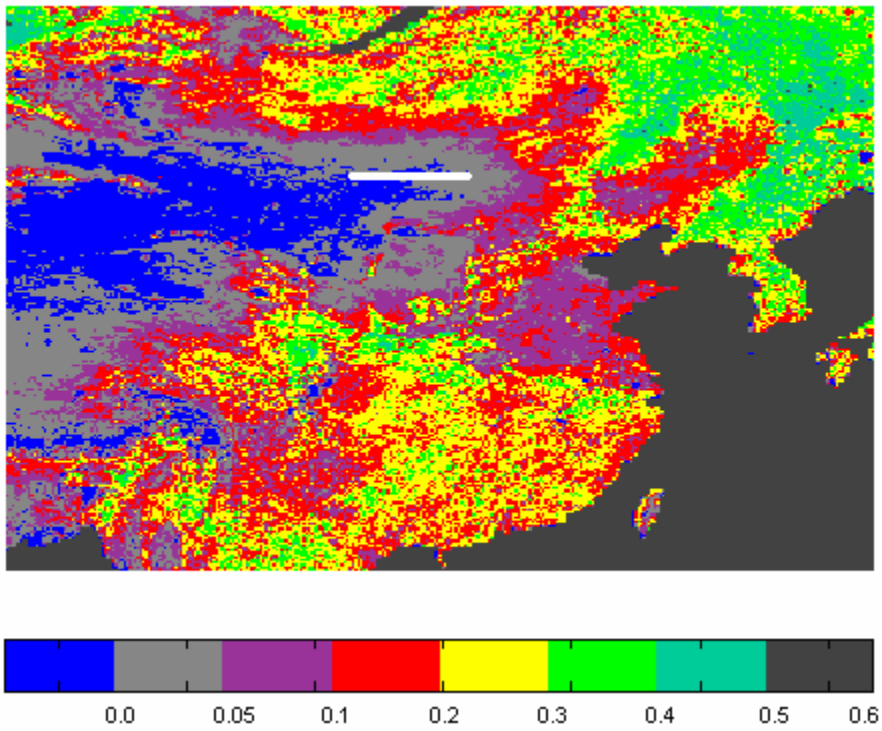

Figure 6.79 (a) NDVI image of old NDVI data of 1988.

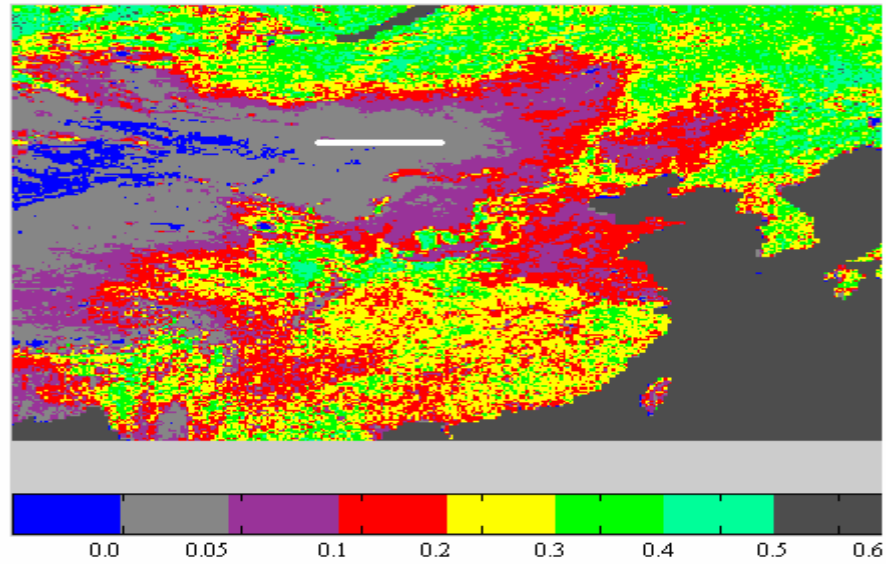

Figure 6.79 (b) NDVI images of new NDVI data (corrected) of 1988

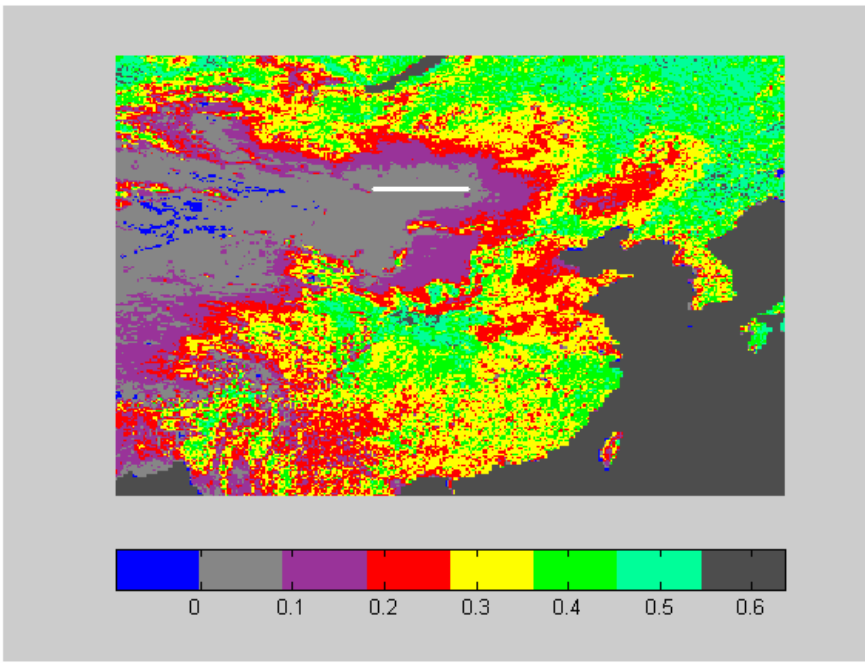

Figure 6.79 © NDVI images of standard

Figure 6.77 shows various ecosystems such as desert, grassland, forest and mixed in China based on the range of NDVI data. Desert targets; include both gray and purple color. Vegetative targets included grassland and forest (broadleaf, coniferous and tropical) ecosystems and also crop areas which are include green and yellow color. Blue color means water, soil, and rock. Red color means mixed between deserts and vegetative. Figure 6.77 (b) shows an example of the corrected NDVI image which is similar to standard NDVI data validation sets images (Figure 6.77(c)). Figure 6.77 (b) suggest over the China region, NDVI value generally increase after correction of the 26^{th} week number of 1988. Small increases are observed in tropical forest areas. Although the overall corrections are reasonable, fine straight lines are observed in Figure 6.77 over certain areas (for example, desert and water). We can also see from this figure the corrected NDVI distribution appears reasonable, suggesting that the artificial lines noted in this Figure, while undesirable, do not cause significant error on the corrected NDVI value and, therefore, the corrected data may still useful for further research application.

CHAPTER 7

VALIDATION

We investigate NDVI data stability of Mongolia, North Korea, Nepal, Bhutan, and India for validation compared to the original data set. For validation purpose, we extract the NDVI data for parts of Mongolia, North Korea, Nepal, Bhutan, and India. We use the same methodology (EDF) to improve the stability of NDVI data.

7.1 Mongolia

We extract the NDVI data for Mongolia area (bordered area in Figure 7.1) from the original data set using equations 6.1 and 6.2.

7.1.1 Geographical Location

Mongolia is situated in the central part of the Asiatic continent ($41^{O}35'N - 52^{O}09'N$ and $87^{O}44'E - 119^{O}56'E$). The country is bounded on the north by Russia and on the east, south, and west by China (Fig. 7.1). It has a total area of 1,565,000 sq. km (604,250 sq. mi) and a population of more than 2.3 million persons (in 1997). The capital is Ulaanbaatar with the population of 650,000 persons (in 1997). Cattle play a vital role in the Mongolian economy the population of which is 29 million. Agricultural area is more than 790,000 hectares.

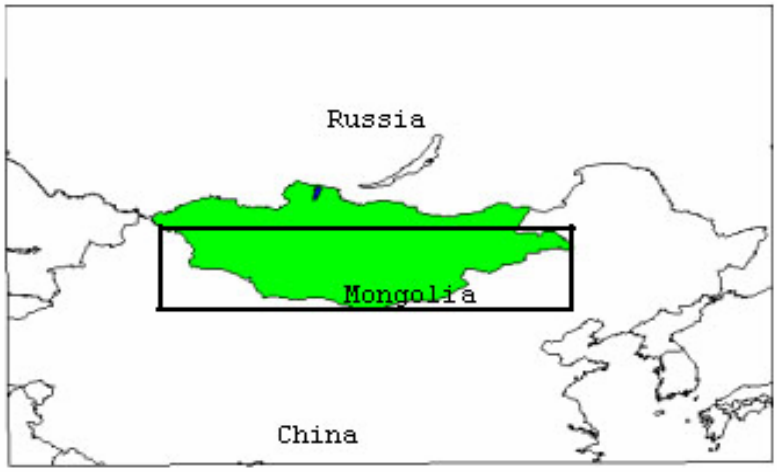

Figure 7.1 Geographical location of study area in Mongolia (bordered area)

7.1.2 Topography and Present Land Cover

Forests and grassland play an important role in the economic development of the country. Forest cover is only 10% and grassland cover is about 70-80% of all territory of Mongolia. The topography of Mongolia consists mainly of a plateau with the elevation ranging from 914 and 1524 m (about 3000 and 5000 ft) broken by mountain ranges in the north and west. The Altai Mountains in the southwest rise to heights above 4267 m (14,000 ft). The Gobi covers a wide arid tract in the central and southeastern areas. The most important rivers are the Selenge Mörön and its tributary, the Orhon Gol, in the north. Large lakes include the Har Us, Hyargas, Uvs, and Hövsgöl.

The country is having a mountainous, hills and wide steppe topography. The greater part of the highlands consist of mountainous areas with gentle to steep slopes, which are placed western, northern and south-west part of Mongolia. Eastern and southern parts of

Mongolia are wide plan steppe and gobi desert area. Steppe vegetation covers large area due to dry climate.

Mongolia can be separated into five major agro-ecological regions and sub-regions with significantly different environmental conditions, agricultural and livestock production potential, and ecological response to rate factors promoting anthropogenic induced degradation. They are: Mongol Altai region, Khangai - Hövsgöl region, Selenge - Onon region, Central and eastern steppe region and Gobi region.

Geographical position and associated climatic influences can be a negative environmental condition that affects sustainable use of land resources, especially pastoral livestock production.

7.1.3 Analysis of NDVI Time Series for Mongolia

We produce NDVI time series for Mongolia which is illustrated in Figure 7.2. The comparison of NDVI time series with the original NDVI time series (Figure 6.1) shows that both time series are almost similar but NDVI value varies from year to year. Most years show the NDVI values between 0.10 and 0.25 because major part of the study area is covered by desert and grassland, and few part of the study area is covered by forest. NDVI value is usually lower in dry and hot weather (desert) and higher in wet weather (forest) [36]. Based on our comparison of the two data sets, the NDVI data of Mongolia shows similar results. Figure 7.2 shows that NDVI data for 1988, 1992, 1993, 1994, and 2000 are not stable enough compared to other years because of satellite orbital drift, Mt Pinatubo, and sensor degradation. Therefore, we need to correct the NDVI data for

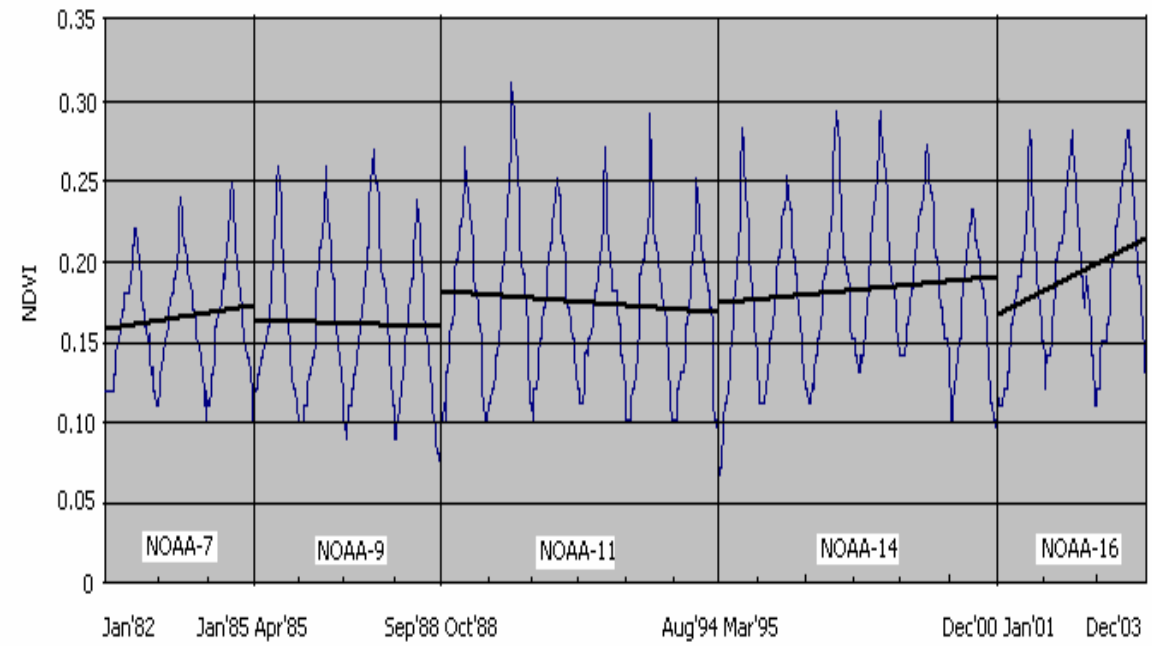

Figure 7.2. NDVI time series (yearly) of study area in Mongolia

affected years. For this correction, we apply the method of empirical distribution functions for affected years. We normalize data by the EDF's compared with standard data correction sets (subset 1) according to equations 5.3 and 5.4. Then corrected or normalized data for this years compared with subset 2 (standard data validation sets) which provides NDVI data for these years that match in subset 2.

Using this technique, we produce EDF's to normalize or correct data for the years 1988, 1992, 1993, 1994, and 2000 compared with standard data correction sets (subset 1) and then corrected or normalized data compared with standard data validation sets (subset 2) which are illustrated in following Figures

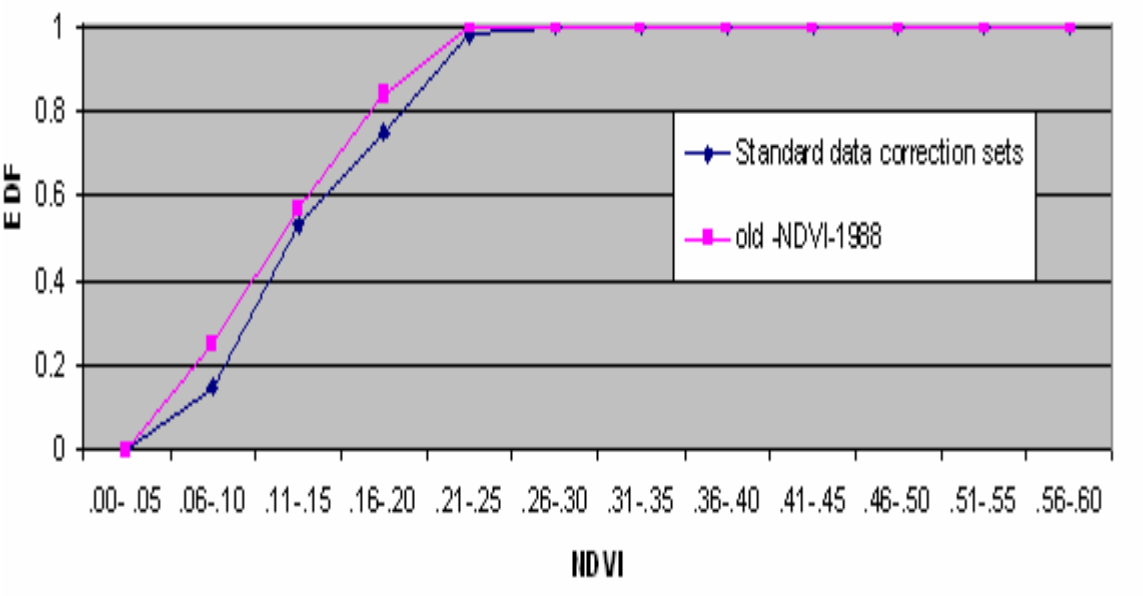

Figure 7.3 (a) Empirical distribution functions for unnormalized data of 1988 compared with standard data correction sets (subset 1).

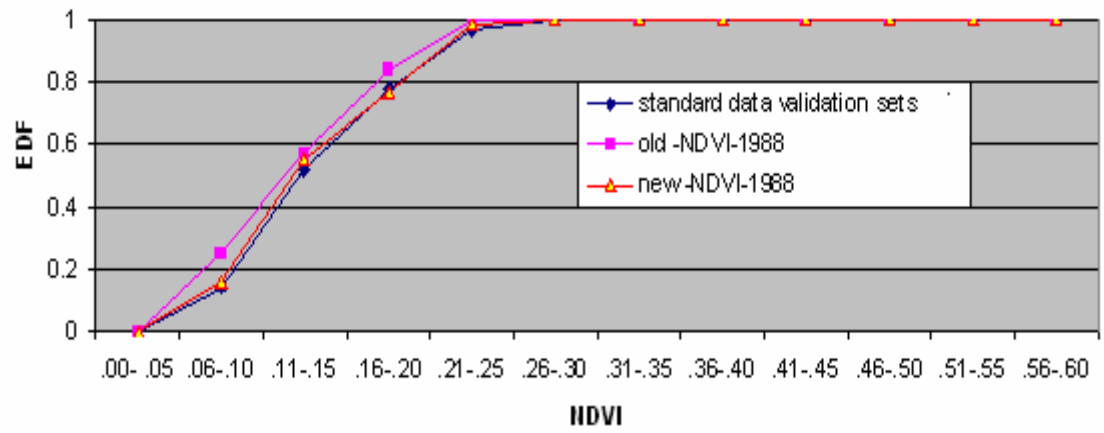

Figure 7.3 (b) Empirical distribution functions for normalized data of 1988 compared with standard data validation sets (subset 2).

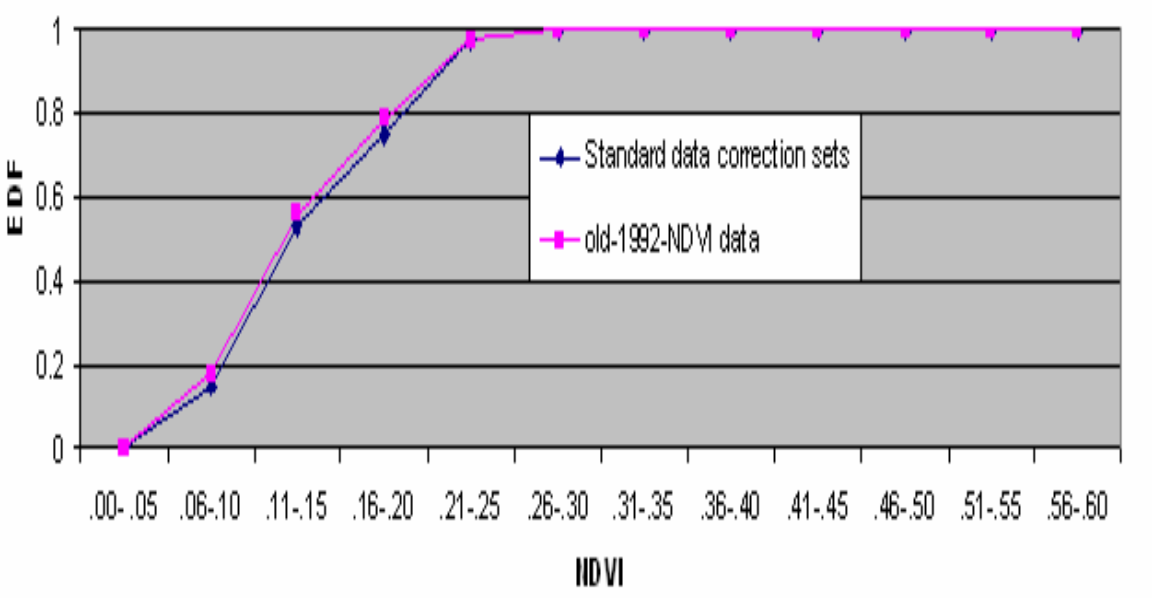

Figure 7.4 (a) Empirical distribution functions for unnormalized data of 1992 compared with standard data correction sets (subset 1).

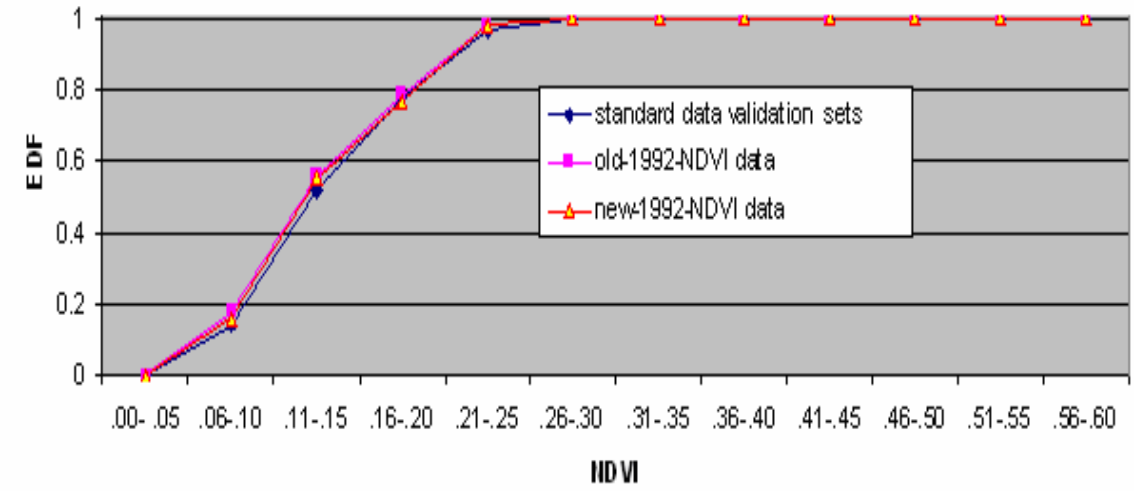

Figure 7.4 (b) Empirical distribution functions for normalized data of 1992 compared with standard data validation sets (subset 2).

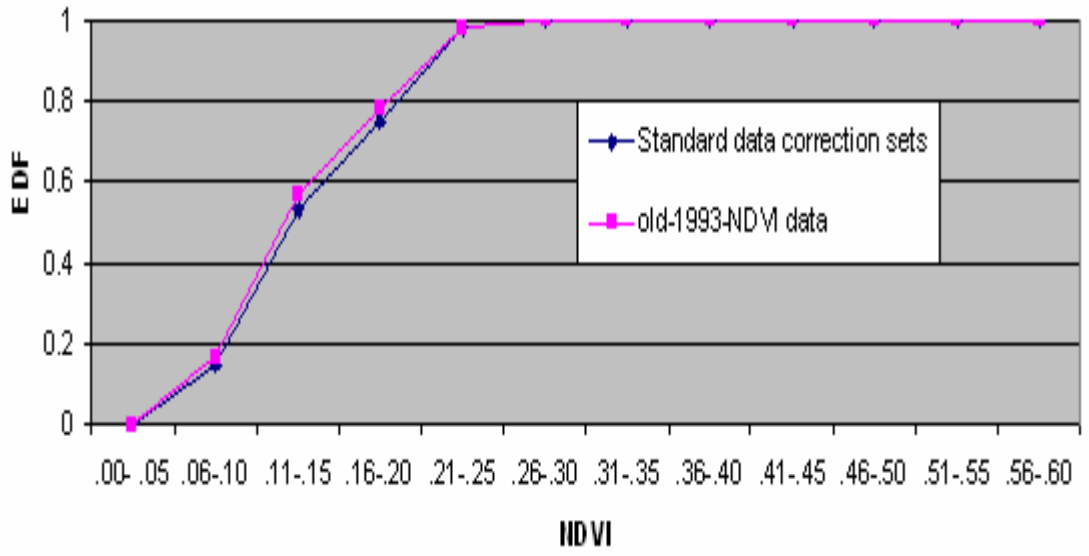

Figure 7.5 (a) Empirical distribution functions for unnormalized data of 1993 compared with standard data correction sets (subset 1).

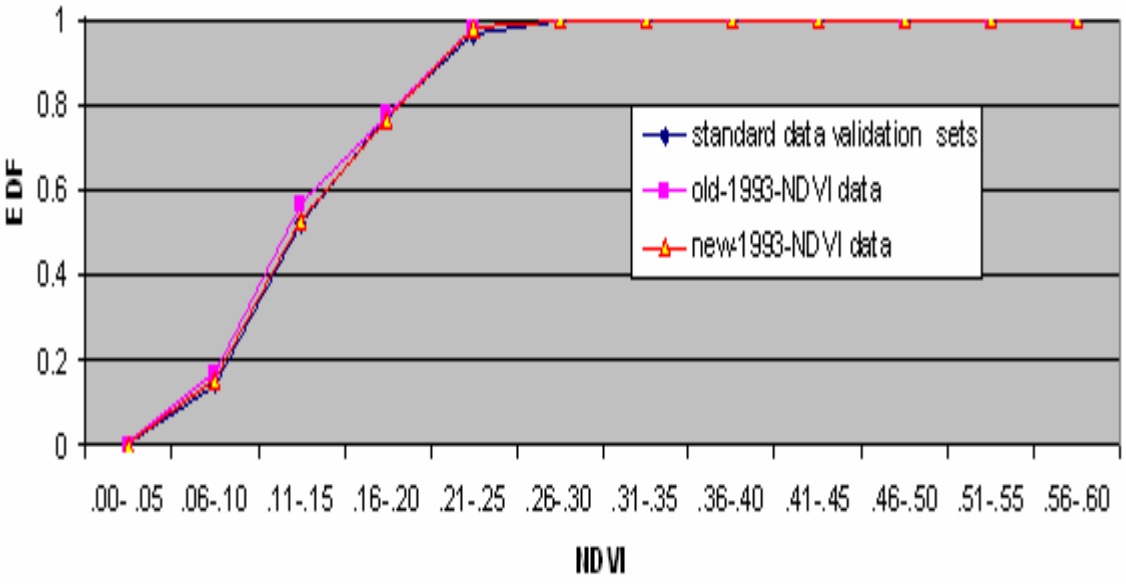

Figure 7.5 (b) Empirical distribution functions for normalized data of 1993 compared with standard data validation sets (subset 2).

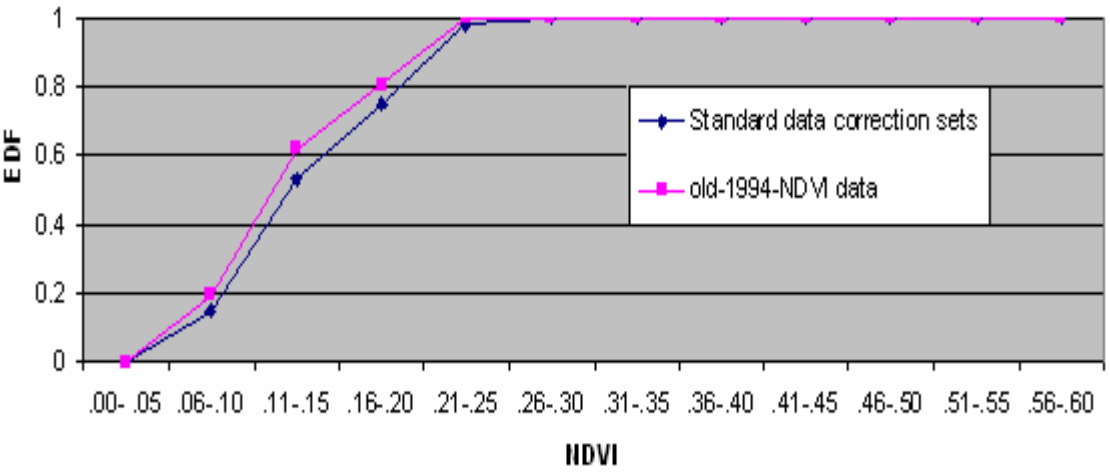

Figure 7.6 (a) Empirical distribution functions for unnormalized data of 1994 compared with standard data correction sets (subset 1).

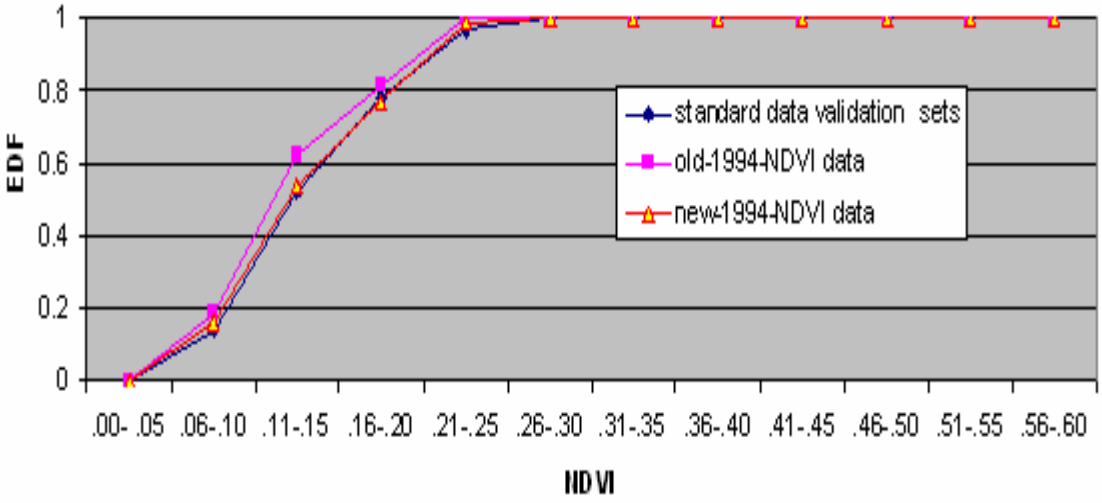

Figure 7.6 (b) Empirical distribution functions for normalized data of 1994 compared with standard data validation sets (subset 2).

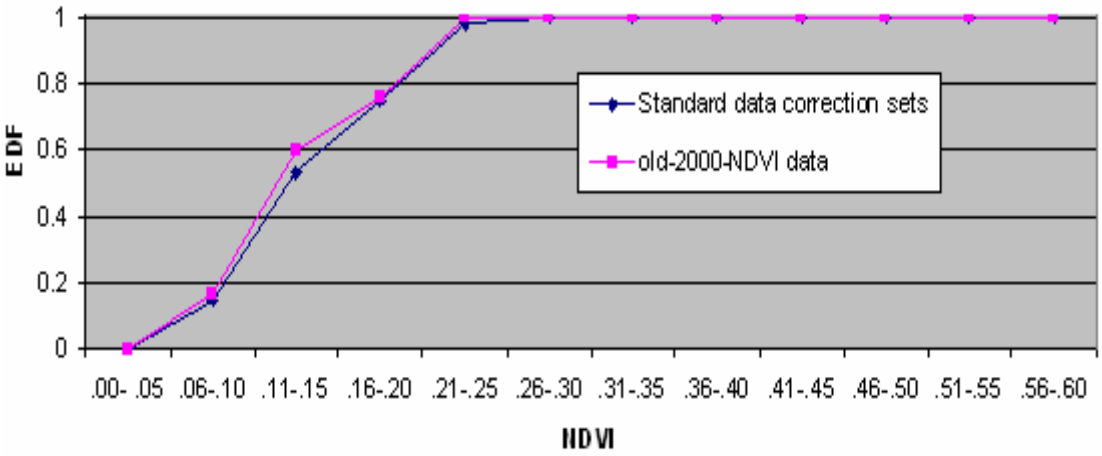

Figure 7.7 (a) Empirical distribution functions for unnormalized data of 2000 compared with standard data correction sets (subset 1).

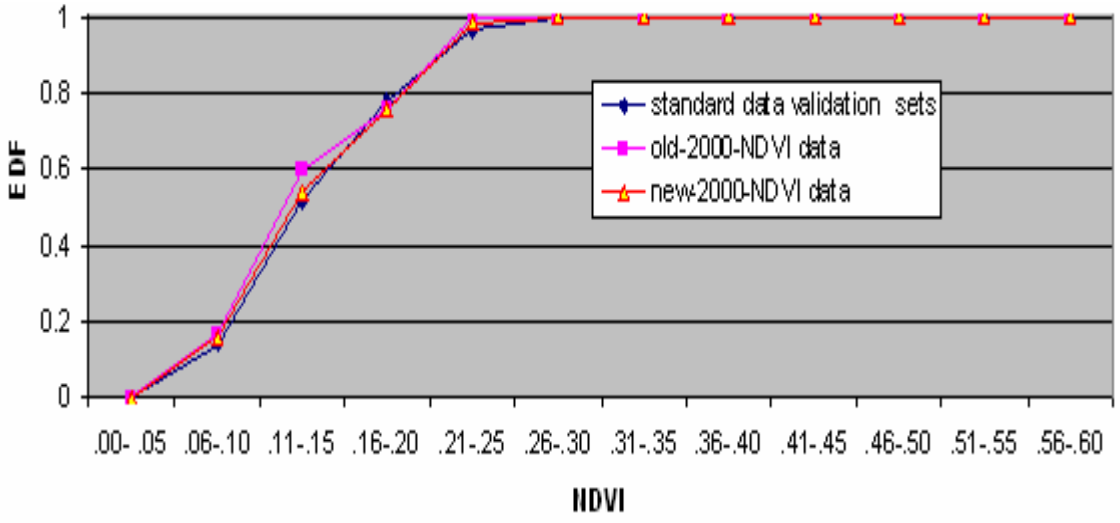

Figure 7.7 (b) Empirical distribution functions for normalized data of 2000 compared with standard data validation sets (subset 2).

Using normalized NDVI value, we produce new NDVI time series for Mongolia as shown in Figure 7.8 which shows improvement of the NDVI data (pink line) of the year of 1988, 1992, 1993, 1994, and 2000

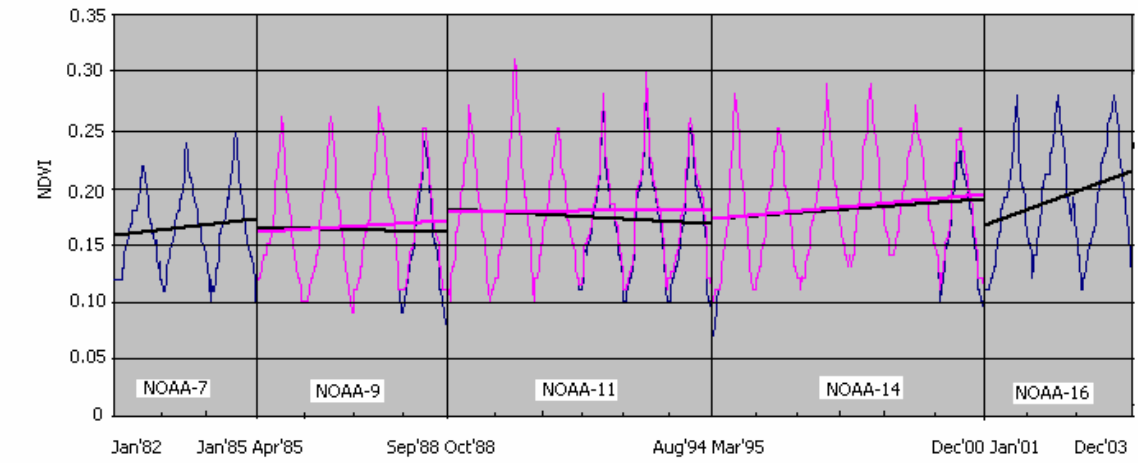

Figure 7.8 New NDVI time series (yearly) for study area in Mongolia

(old NDVI —, new NDVI —)

7.2 North Korea

We extract the NDVI data for North Korea (bordered area in Figure 7.9) for validation compared to the original data set using equations 6.1 and 6.2. North –East of China is separated from North Korea by Forest. Most of the study area of North-Korea is covered by forest.

7.2.1 Geographical Location

The Democratic People's Republic of Korea (DPRK) is located in the North East Asia. North Korea has land borders with Peoples' Republic of China and Federal Republic of Russia in the north, bounded by the Amnok and Tumen Rivers, and is bordered by seas on the east, west and south (Figure 7.9). It lies approximately between 39^0 N to 43^0 N in latitude and 122^0 E to 125^0 E in longitude. The terrain is predominately mountainous.

Figure 7.9 Geographical location of study area in North Korea (bordered area)

7.2.2 Topography and Present Land Cover

North Korea occupies about 55 percent of total land area of the Korean Peninsula, or approximately 120,410 hectares of land area. Approximately 80 percent of land area covers mountain ranges and uplands. The mountainous topography leaves few areas of cultivatable land. Only about 18 percent of the total landmass, or approximately 2 million hectares, is arable; the major portion of the country is rugged mountain terrain. The weather varies markedly according to elevation, and lack of precipitation, along with infertile soil, makes land at elevations higher than 400 meters unsuitable for purposes other than grazing. So, farming is concentrated in the flatland of the four west coast provinces, where a longer growing season, flat land, adequate rainfall, and good, irrigated soil permit the most intensive cultivation of crops. Fruit and nut orchards are common, occupying some 360,000 hectares of the low hill slopes (around 2.9% of total land area), where such crops as apples, pears, walnuts and persimmons dominate.

The Korean peninsular is dominated by a mountain chain which occupies almost 80% of total land. Total area of forest land in DPRK is reported to be approximately 7.5 millions hectares, of which 6.3 million hectares are natural and 1.2 million hectares are under plantation. To increase agricultural crops, forest land was reduced to 9.7 million hectares in 1970 to 7.5 million hectares in 1997. Another reason was government policies, to reduce the gap between urban and rural living standards, requires continued investment in the agricultural sector with developing forest land.

North Korea's forests have a variety of trees and other wildlife plants. Predominant trees include larch, poplar, oak, alder, pine, spruce, and fir. In the early 1990s, approximately 80 percent of the total area of the country, or 8.8 million hectares, was made up of forests

and woodlands; over 70 percent of these reserves were in the mountainous Hamgyong provinces, and in Yanggang and Chagang provinces. Much of this area was severely damaged by over cutting during the last 10 years. Round wood removals have been estimated by FAO. Log production was estimated at 4.5 million hectares in 1980, basically unchanged since the late 1980s. In 1997, however, timber production was estimated at 5 million hectares. Since early 1970s fuel use rate over 80% of total production.

7.2.3 Analysis of NDVI Time Series for North Korea

We produce NDVI time series for North Korea which is illustrated in Figure 7.10. We found the NDVI range between 0.15 and 0.45 approximately because major part of North Korea is covered by forest. As mentioned before, NDVI value is higher in most favorable weather (forest area). The comparison of NDVI time series for North Korea with the original NDVI time series (Figure 6.1) shows that both time series are almost similar, but NDVI value is higher for North Korea compared to the original NDVI data. Based on our comparison of the two data sets, the NDVI data of North Korea shows similar results.

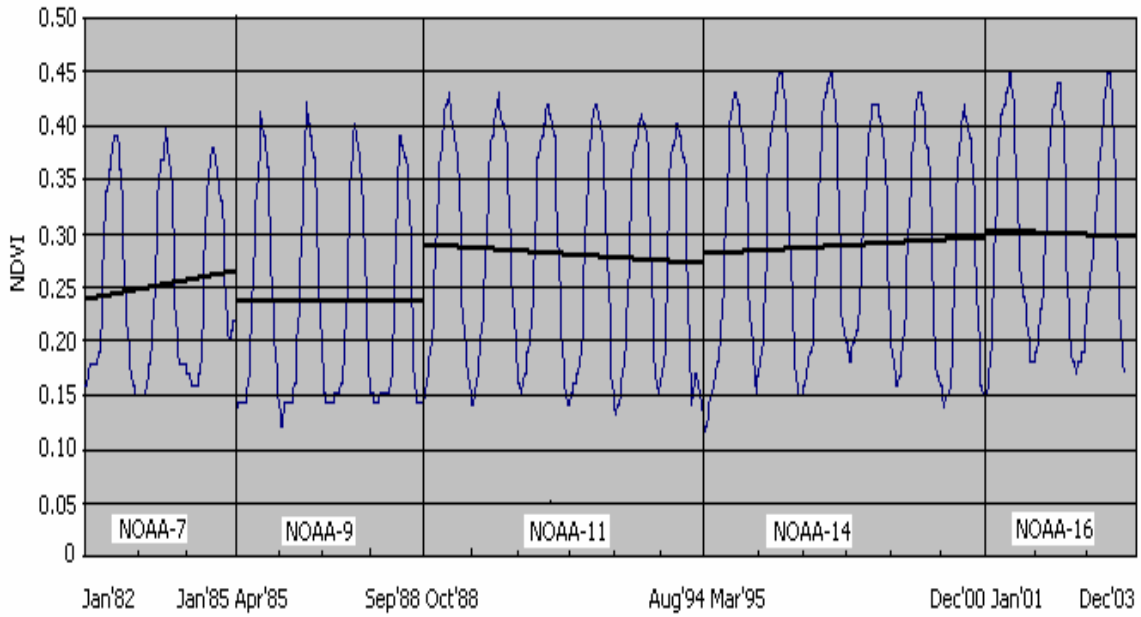

Figure 7.10 NDVI time series (yearly) of study area in North Korea

Figure 7.10 shows that NDVI data for 1988, 1992, 1993, 1994, and 2000 are not stable enough compared to other years. Therefore, we need to correct the NDVI data for affected years. In this case also, we apply EDF method to correct the NDVI data for these affected years which is illustrated in following Figures.

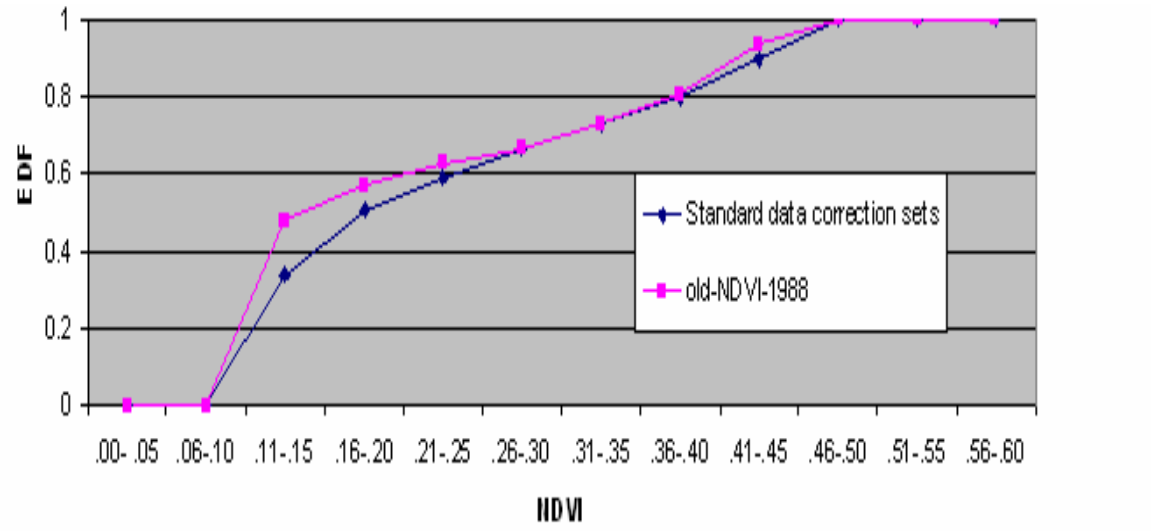

Figure 7.11 (a) Empirical distribution functions for unnormalized data of 1988 compared with standard data correction sets (subset 1).

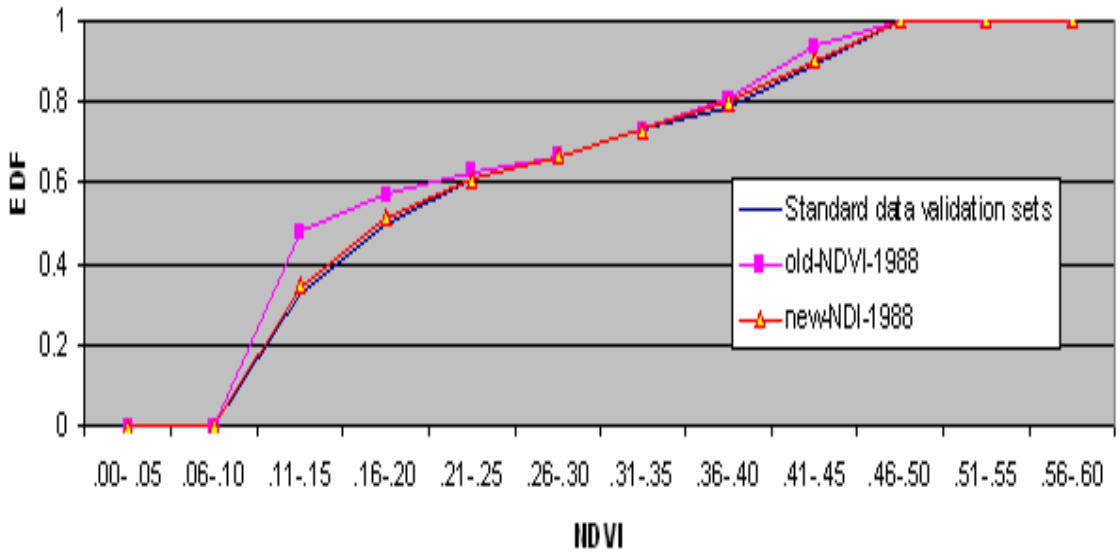

Figure 7.11 (b) Empirical distribution functions for normalized data of 1988 compared with standard data validation sets (subset 2).

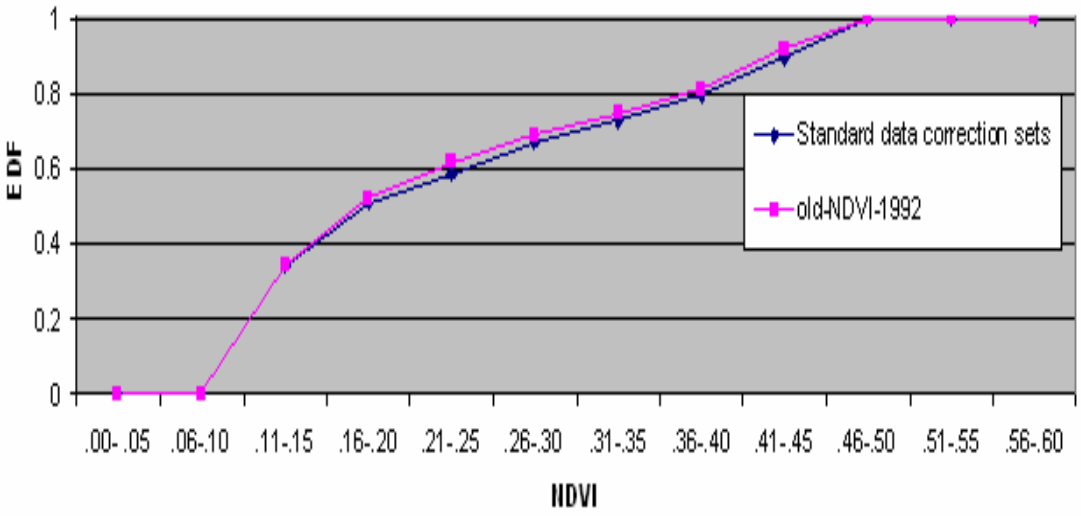

Figure 7.12 (a) Empirical distribution functions for unnormalized data of 1992 compared with standard data correction sets (subset 1).

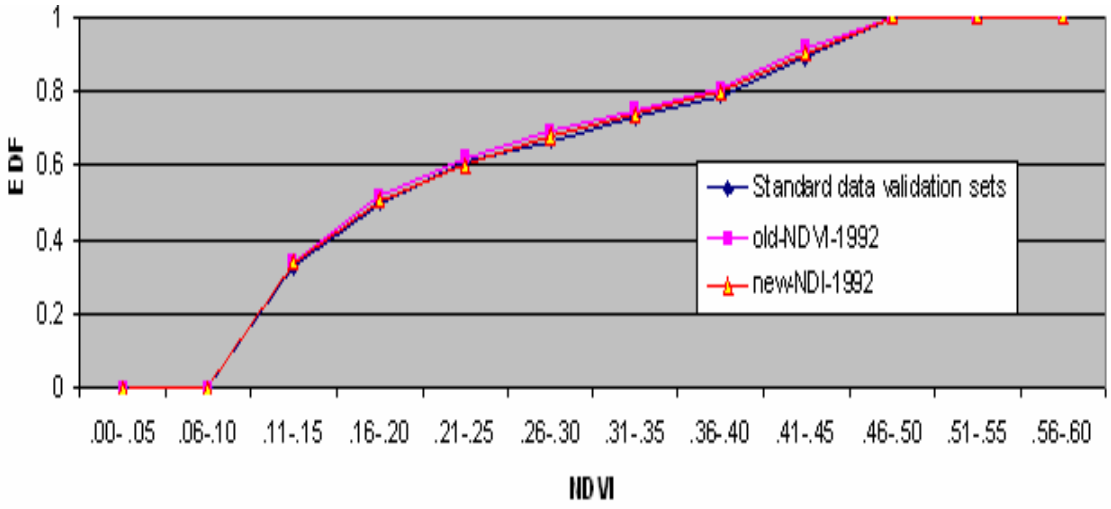

Figure 7.12 (b) Empirical distribution functions for normalized data of 1992 compared with standard data validation sets (subset 2).

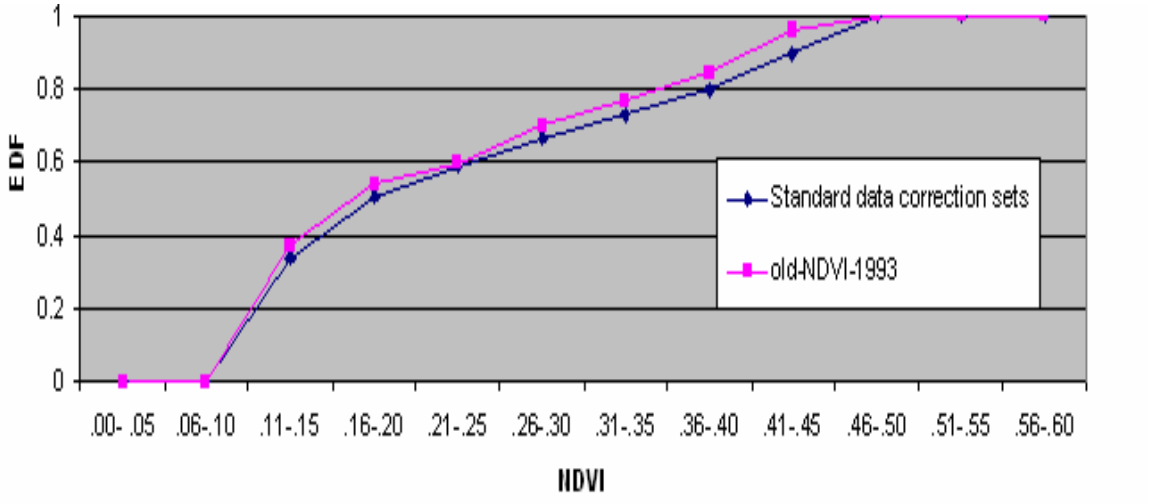

Figure 7.13 (a) Empirical distribution functions for unnormalized data of 1993 compared with standard data correction sets (subset 1).

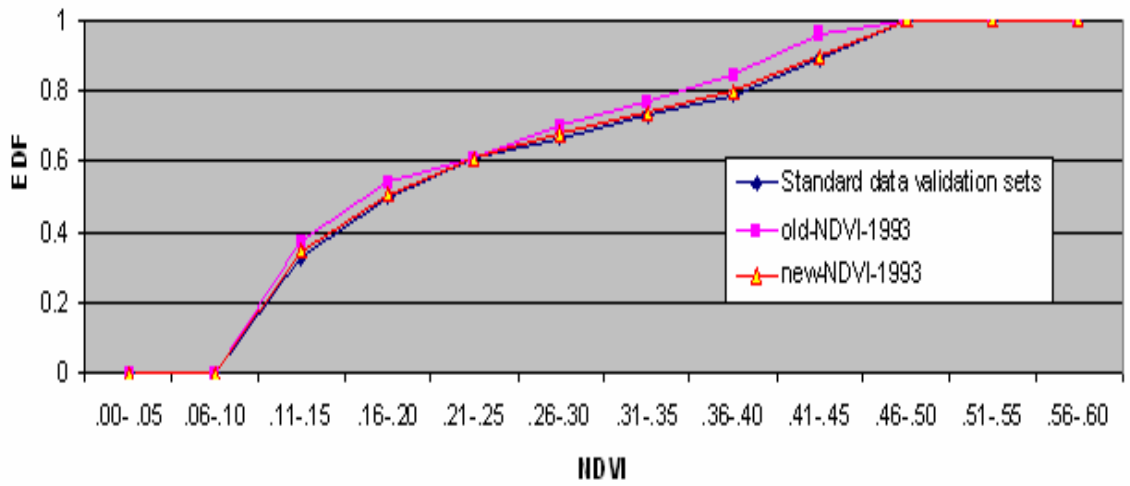

Figure 7.13 (b) Empirical distribution functions for normalized data of 1993 compared with standard data validation sets (subset 2).

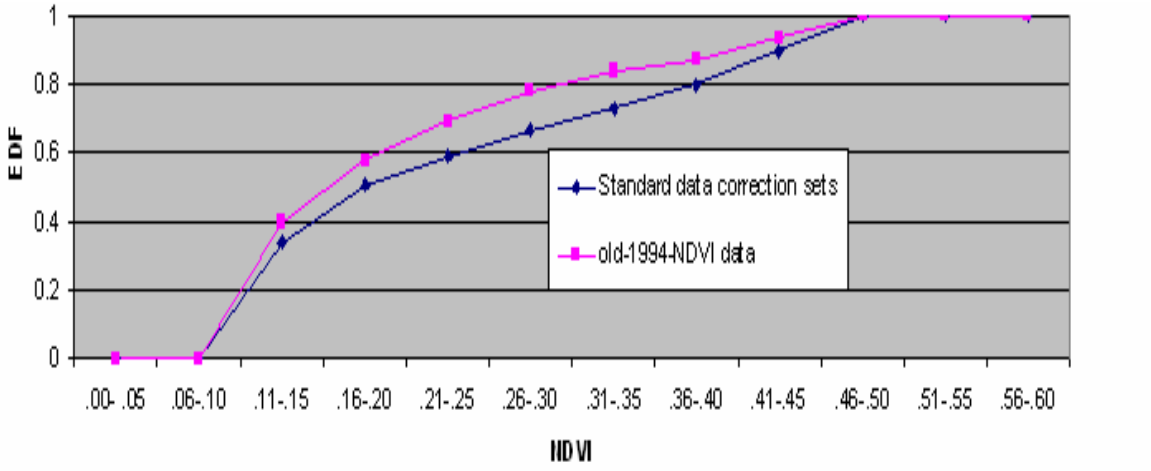

Figure 7.14 (a) Empirical distribution functions for unnormalized data of 1994 compared with standard data correction sets (subset 1).

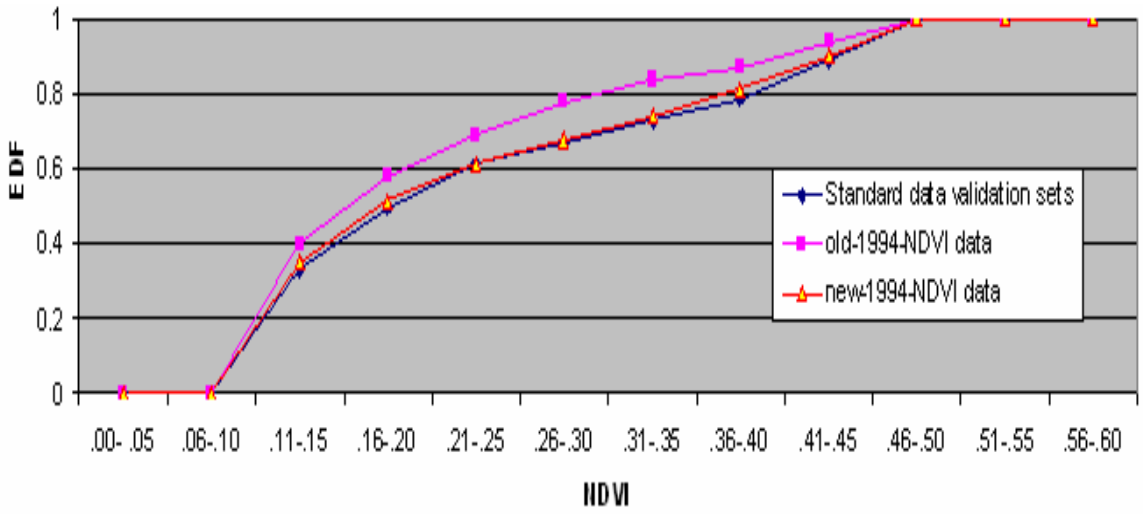

Figure 7.14 (b) Empirical distribution functions for normalized data of 1994 compared with standard data validation sets (subset 2).

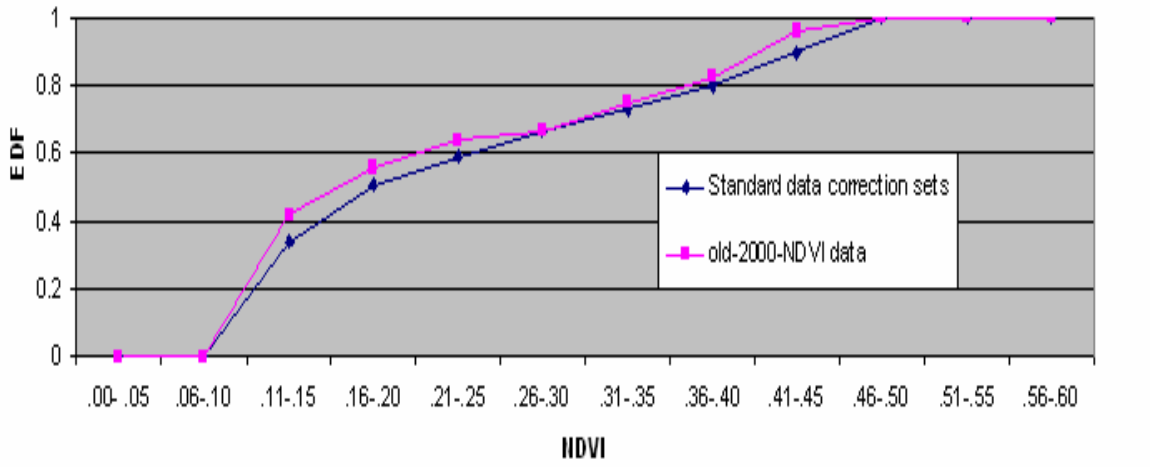

Figure 7.15 (a) Empirical distribution functions for unnormalized data of 2000 compared with standard data correction sets (subset 1).

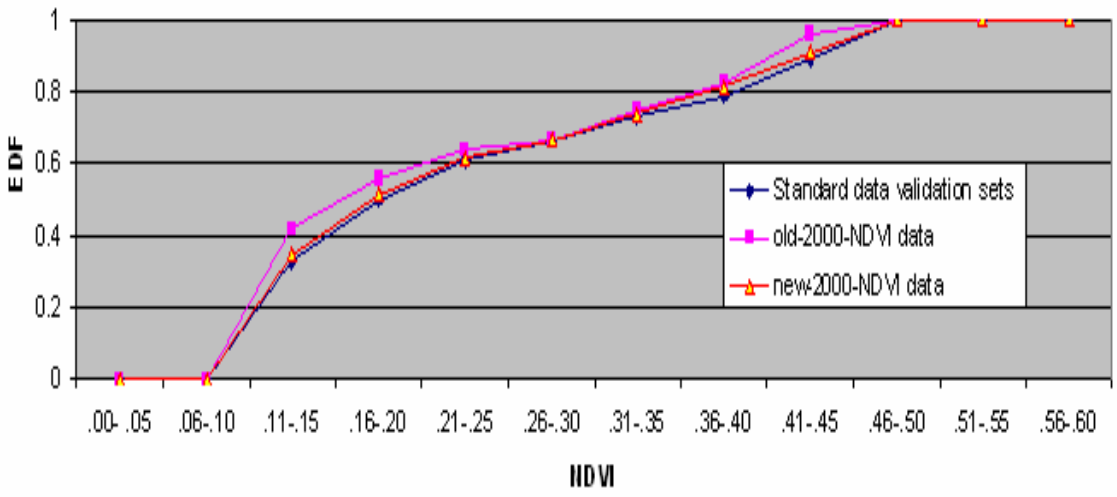

Figure 7.15 (b) Empirical distribution functions for normalized data of 2000 compared with standard data validation sets (subset 2).

Using normalized or corrected NDVI value, we produce new NDVI time series for North Korea as shown in Figure 7.16 which shows improvement of the NDVI data (pink line) of the year of 1988, 1992, 1993, 1994, and 2000

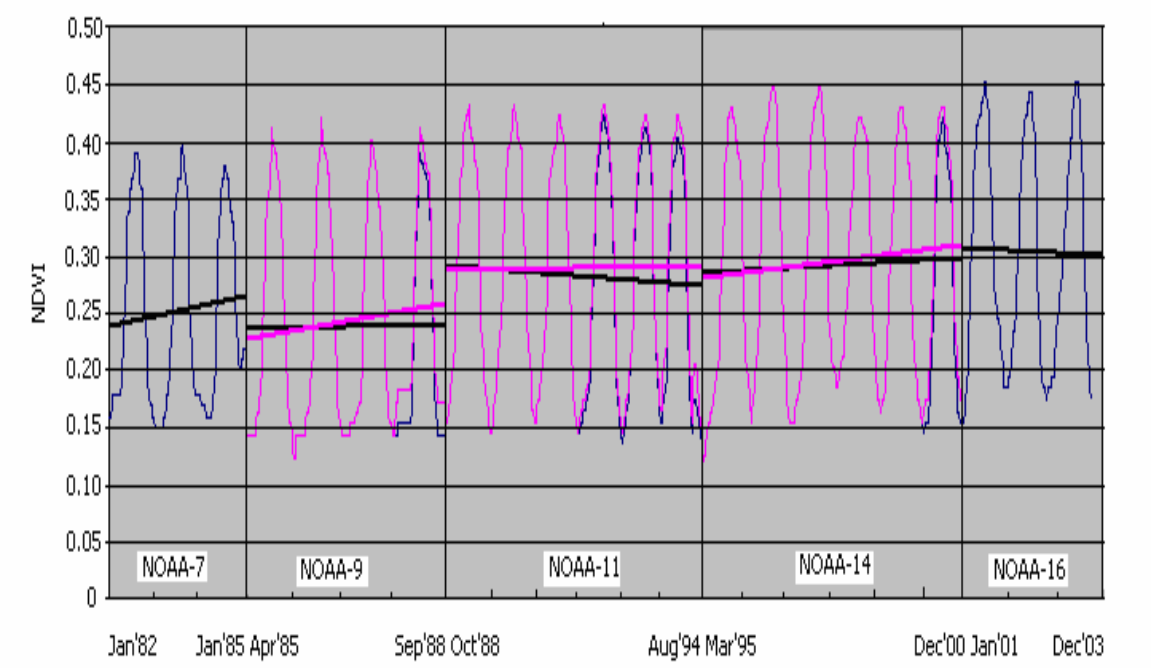

Figure 7.16 New NDVI time series (yearly) for study area in North Korea (old NDVI, new NDVI)

7.3 Nepal, Bhutan, and India

We investigate NDVI data of Nepal, Bhutan, and India (bordered area in Figure 7.17) for validation compared to the original data set. We extract the NDVI data for Nepal, Bhutan, and India from the original data set using equations 6.1 and 6.2. Most of this study area covers are upland hill, mountains, plateau, grassland and forest.

7.3.1 Nepal

7.3.1.1 Geographical Location

Nepal is in both the northern and eastern hemispheres. It's a landlocked country positioned on the Indian subcontinent of South Asia, and bordered by China (Tibet) and India.). It lies approximately between 27^0 N to 29^0 N in latitude and 74^0 E to 85^0 E in longitude.

Figure 7.17 Geographical location of study area in Nepal, Bhutan, and India (bordered area)

7.3.1.2 Topography and Present Land Cover

Nepal is divided into five major physiographic regions which run in more or less parallel bands from northwest to southeast. Each of these regions has a distinctive agricultural and forestry land utilization pattern. These regions are known as Terai, Siwaliks, Middle Mountains, High Mountains and High Himal from south to north direction. Nepal was once extensively covered by forests. Demand for fodder, overgrazing and uncontrolled cutting of timber and fuel wood, have significantly reduced the original forest cover. The composition of vegetation is closely related to the climate, which in turn is related to the physiographic region. There is not only a difference in vegetation from north to south, but also from east to west. The latter is caused by the decrease of monsoon rains in the western part and to some extent by the latitudinal differences between the eastern and western regions of Nepal.

a. The Terai - it forms a long strip of alluvial deposits along Nepal's southern border with India. The strip is an extension of the broad Gangetic Plain, and includes the Bhabar regions, which consist of alluvial fans of the Siwaliks. Originally, the Terai was covered with dense jungle, mainly composed of sal (Shorea robusta) and mixed hardwoods. Following a steady migration of population, most of the forest have been cleared for cultivation, predominantly of rice. Large tracts of forest in the Terai can be found in the Bhabar areas, which are well drained and have a low water table. The soils of the Bhabar areas are generally coarse in texture, subject to erosion if mismanaged, and are not therefore as suitable for agricultural production as

the other areas of the Terai. The Terai is not only important for its agricultural production, but also plays an important role in timber production and fuelwood supply. It also provides a rapid and economic east-west transportation corridor. Although the Terai represents only 14% of the total area of Nepal, it contains about 42% of the total cultivated land of the country. The forests consist mainly of high value sal and a mix of tropical and subtropical species.

b. The Siwaliks - its hillslopes have little potential for agricultural production. Soils are shallow and erodable.The majority of agricultural land is restricted to river terraces, alluvial valleys and, despite their limited areas to the Dun valleys. However, occasional hillslope cultivation may be found. The forests consist mainly of chir pine (Pinus roxburghii) and tropical mixed hardwoods of which sal is often a major component. The Siwaliks has very little agricultural land in the valley. The main crops are maize, millet, wheat and mustard. Rice is found where irrigation water is available.

c. Middle Mountains - this region has the highest population density in relation to cultivated land. The height of the Middle Mountains ranges from a few hundred meters to approximately 3,000 meters. The region is generally heavily dissected and has a great variety of soil types, geology and microclimates. Because of these, the area has many different agricultural landuse patterns. The farming systems incorporate a number of such land

patterns as well as extensively used public forest and grazing areas. The land in the Middle Mountains is intensively cultivated. Existing pasture land is heavily overgrazed and forests are stripped for fodder and fuelwood. Most slopes are terraced and support maize, millet, rice, wheat or potatoes. It was found that 85% of the cultivated land of the Middle Mountains consists of some form of hillslope cultivation. The badly degraded forests of the Middle Mountains consist mostly of hardwoods with some conifers, mainly pine.

d. High Mountains - unlike the boundary between the Terai and Siwaliks, there is no clearly defined boundary between the High Mountains and the Middle Mountains. The steep slopes of the High Mountains often show intensive agricultural terracing. River terraces are less extensive than they are in the Middle Mountains since rivers tend to develop deep incisions which leave little room for valley cultivation. Upper limits of agricultural land are reached in this physiographic unit. On large, gently sloping fields, one crop of potato, buckwheat or barley may be grown once every year or every two years. Many of the snow fields serve as buffer reservoirs for irrigation water used in the lower regions. Extensive areas of grazing land are found in the form of alpine pastures. Migrating livestock from lower areas utilize the pastures of this area during the monsoon. The forests of this region include both coniferous and hardwoods. Some of the least disturbed forest, especially the conifer forests including fir (Abies spectabilis) and hemlock (Tsuga dumosa) are found in this region. In the High Mountains, upper limits

of agriculture are found at about 4,200 meters. In the high regions, fields can support only one crop of buckwheat, barley or potato once a year or once every two years. The High Mountain forests contain a higher proportion of different conifers and in general, are in a better condition than forests elsewhere in the country.

e. High Himal - its climate is predominantly arctic, with permafrost, permanent snow fields and many glaciers. The little agricultural land available is found in the valleys and in some cases in sheltered pockets of the hillslopes. Pasture lands are used by migratory livestock in the High Mountain regions, and by yaks along the trade routes connecting Tibet.

7.3.2 Bhutan

7.3.2.1 Geographical Location

Bhutan is a small kingdom covering an area of 46,500 square kilometres in the eastern part of the Himalayan Range between latitudes 26^0 40' and 28^0 20' north and longitude 88^0 45' and 92^0 7' east. It is surrounded by the Tibetan Plateau in the north, the Bengal and Assam Plains in the south, Arunachal Pradesh in the east and the Darjeeling and the Sikkim Himalaya in the west (Figure 7.17)

7.3.2.2 Topography and Present Land Cover

The country is mountainous with elevations ranging from 150 up to 8,000 m. traversing south to north with a great diversity of environments. Of the 600,000 population

(estimates range from 600,000 to 810,000 to as high as 2.3M, but a figure of 1.5M is probably of the correct magnitude although the World Factbook suggests 2.3M for July 2006 with a growth rate of 2.1%), 90 percent are dependent on agriculture. Farming is essentially subsistence and the main crops grown are maize, rice, millet, buckwheat, barley, and mustard. However, the mountainous nature of the country makes only about 8 percent of the total land suitable for crops (LUPP, 1995). Furthermore land use is dictated by the diverse climate and topography.

The number of farming households in 1996 was estimated at 65,000 with an average of seven members. Average land holdings are 1.5 ha with 10 percent of households owning more than 5 ha (PPD, 1996). Most farming is subsistence with an integration of crops, forests and livestock.

7.3.3 India

7.3.3.1 Geographical Location

India is in both the eastern and northern hemispheres. It's positioned on the Indian subcontinent in south-central Asia. It's bordered by the Arabian Sea, Bay of Bengal, Gulf of Mannar, Indian Ocean, and the countries of Pakistan, Afghanistan, China, Nepal, Bhutan, Bangladesh and Burma (Myanmar) (Figure 7.17). It lies approximately between 15^0 N to 30^0 N in latitude and 65^0 E to 90^0 E in longitude.

7.3.3.2 Topography and Present Land Cover

A band of tropical grasslands (locally known as the terai and duars), now highly fragmented, extends across the plains of the Ganges and Brahmaputra rivers and into the adjacent Himalayan foothills. Eleven threatened grassland species occur there, including Bristled Grass-warbler, which is also known from scattered localities (away from the main grassland belt) in Pakistan and the Indian peninsula. Most of these birds inhabit damp lowland grasslands, but a few range into the hills, including Manipur Bush-quail and Slenderbilled Babbler in the Manipur basin, and Grey-crowned Prinia, which is found to well over 1,000 m and in forest edge as well as grasslands. Manipur Bush-quail, Marsh Babbler and Black-breasted Parrotbill have restricted ranges, and are confined to the Assam plains Endemic Bird Area, and Finn's Weaver is also highly localised in distribution. The Indo-Gangetic grasslands overlap with two wetland regions, W12 and W14.

7.3.3.4 Analysis of NDVI Time Series for Nepal, Bhutan, and India

Most of the study area in Nepal, Bhutan, and part of India are covers upland hill, mountains, forest and grassland area. We produce NDVI time series of five NOAA satellites which is illustrated in Figure 7.18

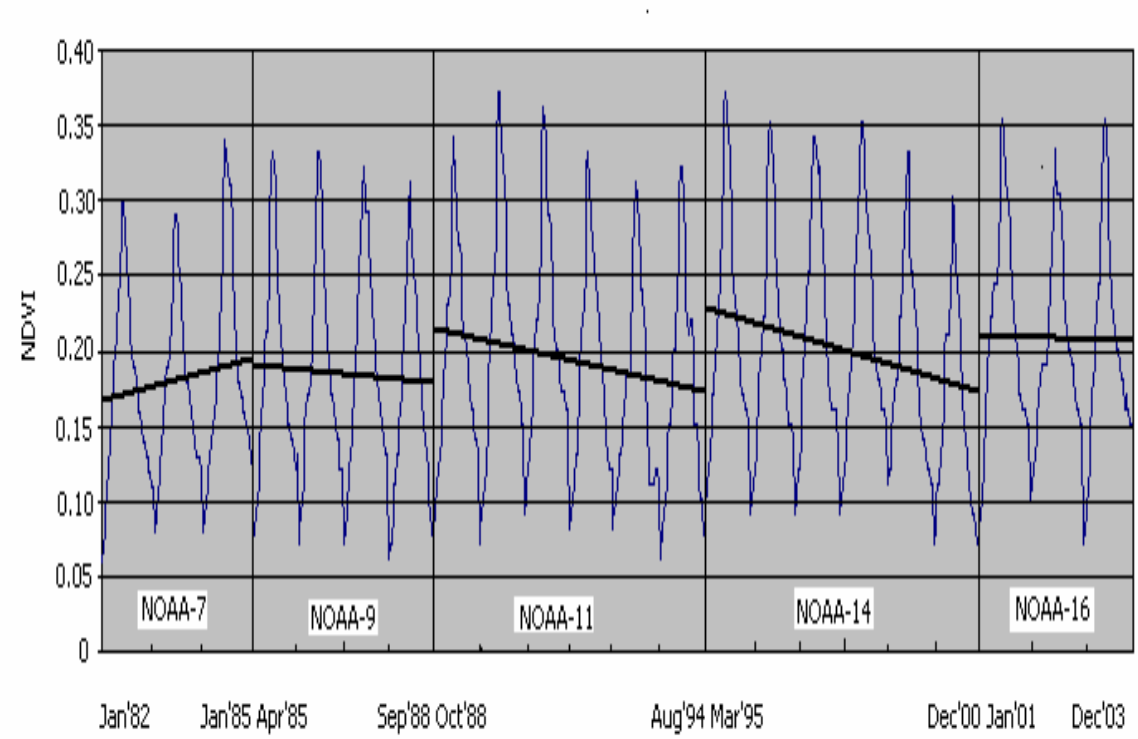

Figure 7.18 NDVI time series (yearly) of study area of Nepal, Bhutan, and part of India

We found the NDVI range between 0.07 and 0.35 approximately because major part of Nepal, Bhutan, and India cover grassland, upland hill, plateau, mountains and forest. The comparison of NDVI time series for Nepal, Bhutan, and India with the original NDVI time series (Figure 6.1) shows that both time series are almost similar, but NDVI value is varies from year to year. Based on our comparison of the two data sets, the NDVI data of Nepal, Bhutan, and India shows similar results.

Figure 7.18 shows that NDVI data for 1988, 1992, 1993, 1994, and 2000 are not stable enough compared to other years. Therefore, we need to correct the NDVI data for affected years. In this case also, we apply EDF method to correct the NDVI data for these affected years which is illustrated in following figures

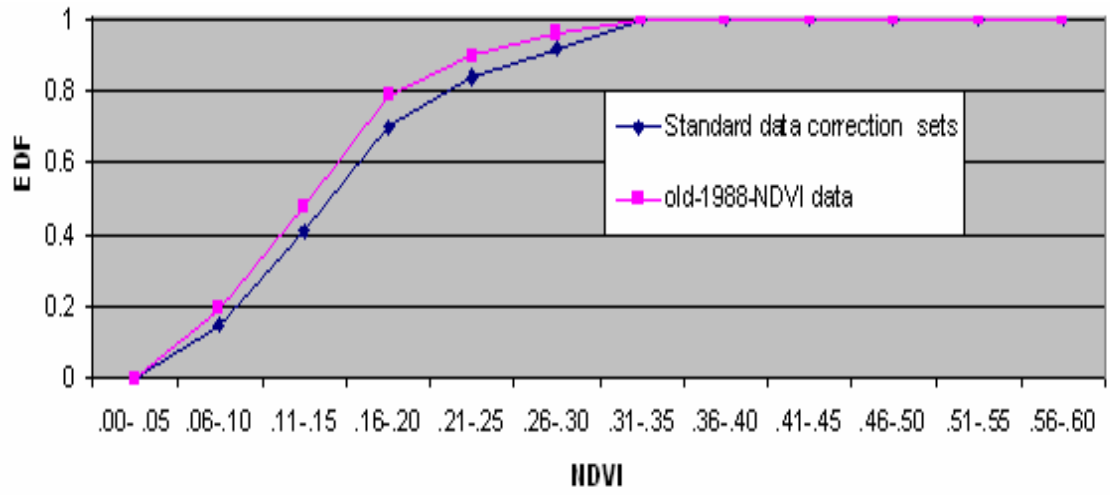

Figure 7.19 (a) Empirical distribution functions for unnormalized data of 1988 compared with standard data correction sets (subset 1).

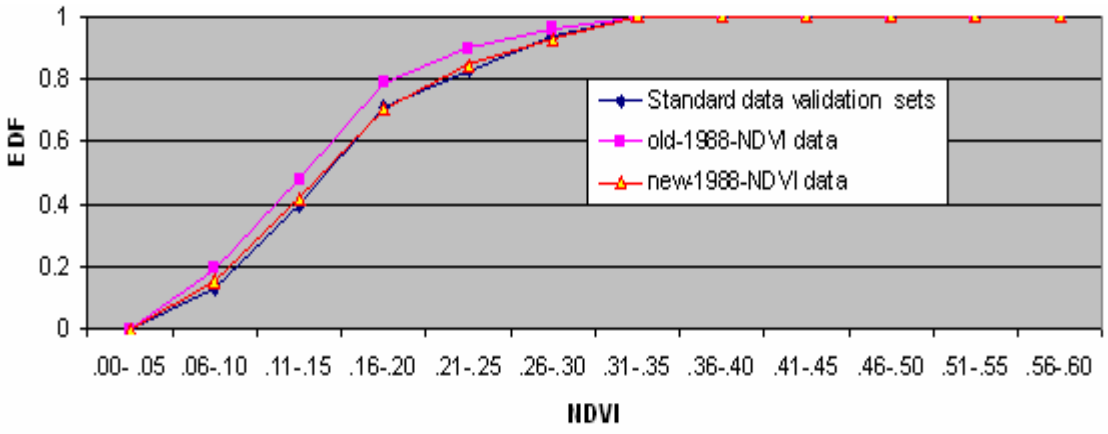

Figure 7.19 (b) Empirical distribution functions for normalized data of 1988 compared with standard data validation sets (subset 2).

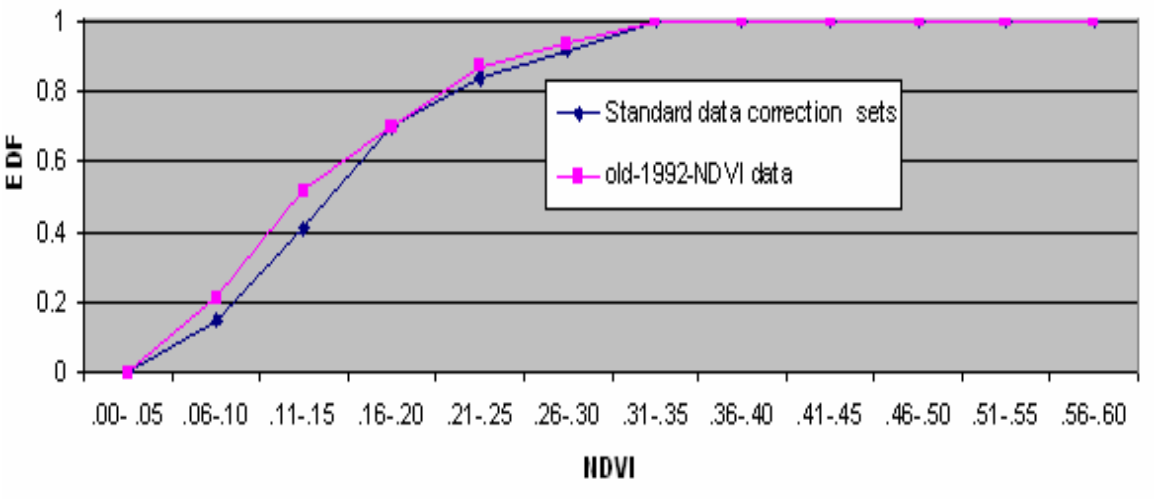

Figure 7.20 (a) Empirical distribution functions for unnormalized data of 1992 compared with standard data correction sets (subset 1).

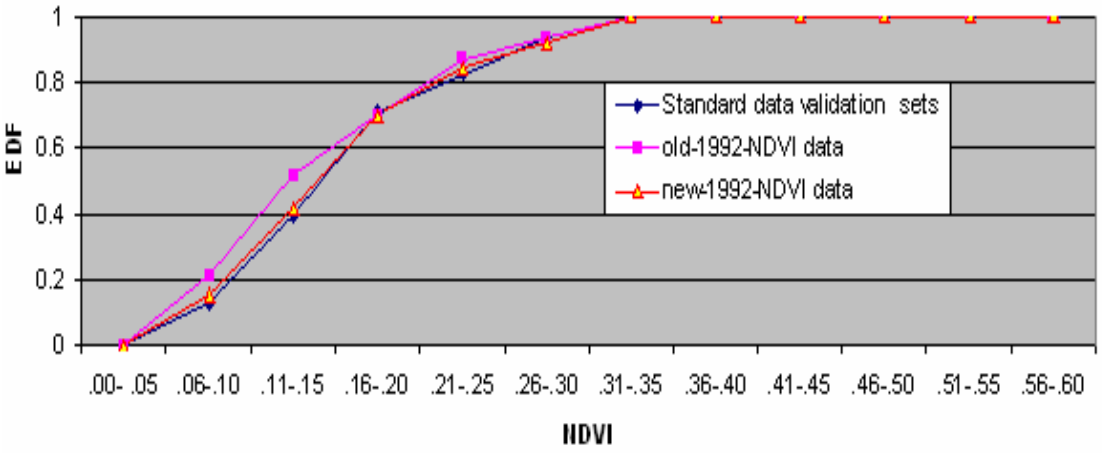

Figure 7.20 (b) Empirical distribution functions for normalized data of 1992 compared with standard data validation sets (subset 2).

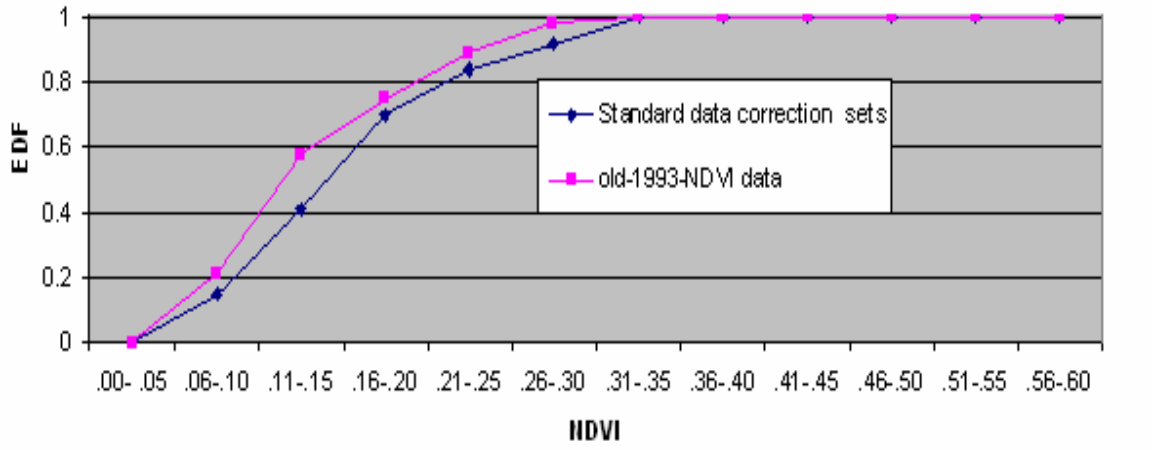

Figure 7.21 (a) Empirical distribution functions for unnormalized data of 1993 compared with standard data correction sets (subset 1).

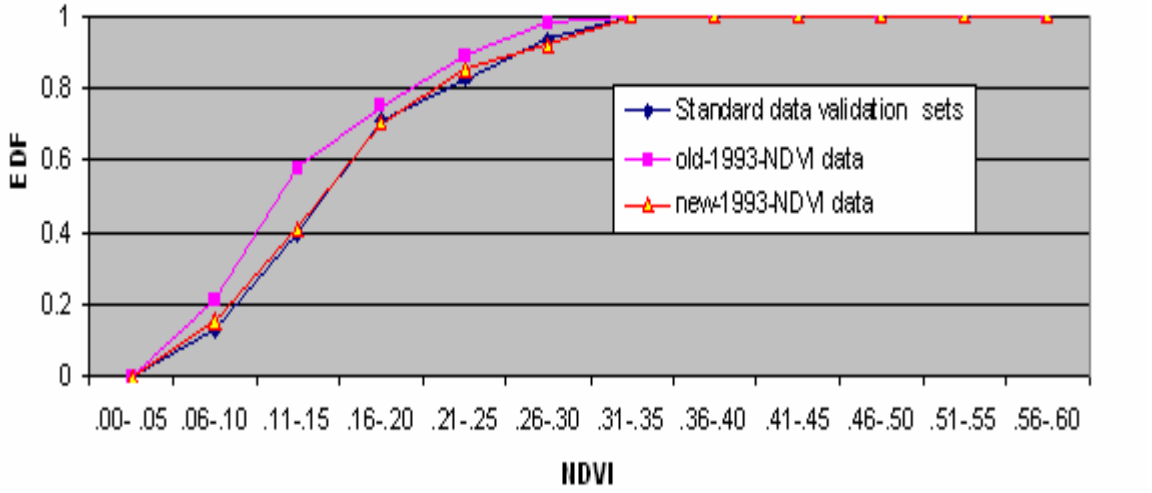

Figure 7.21 (b) Empirical distribution functions for normalized data of 1993 compared with standard data validation sets (subset 2).

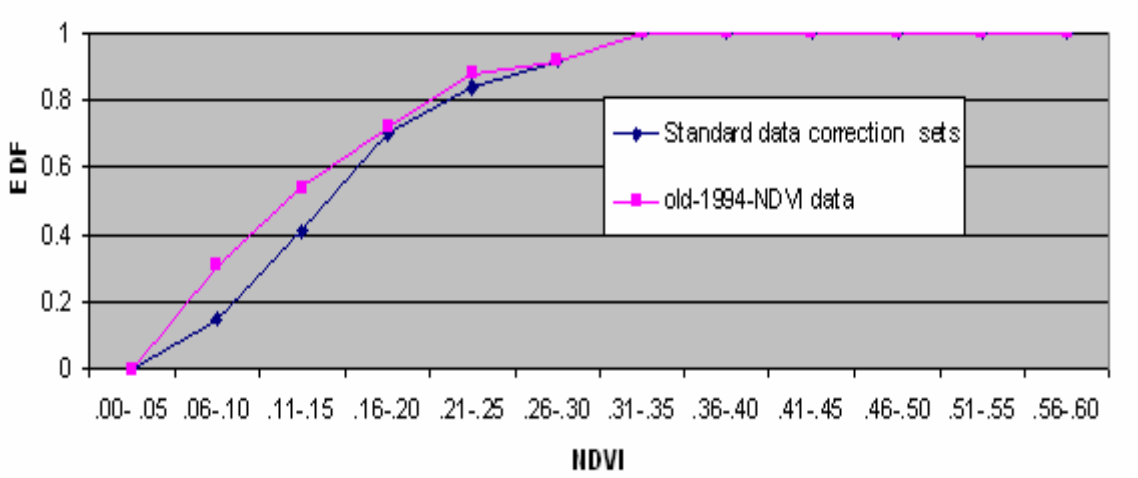

Figure 7.22 (a) Empirical distribution functions for unnormalized data of 1994 compared with standard data correction sets (subset 1).

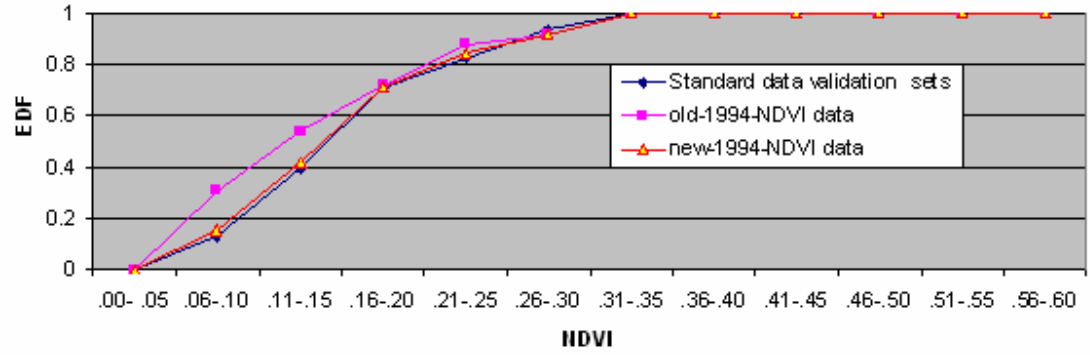

Figure 7.22 (b) Empirical distribution functions for normalized data of 1994 compared with standard data validation sets (subset 2).

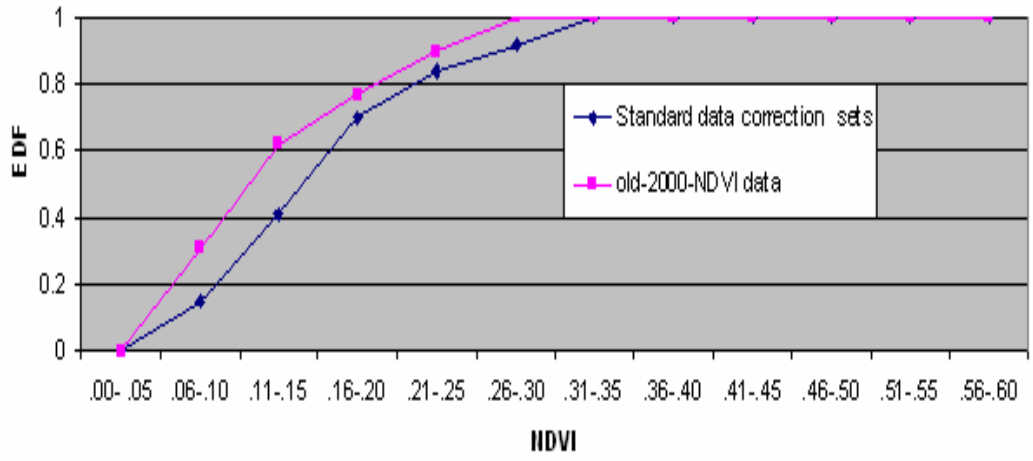

Figure 7.23 (a) Empirical distribution functions for unnormalized data of 2000 compared with standard data correction sets (subset 1).

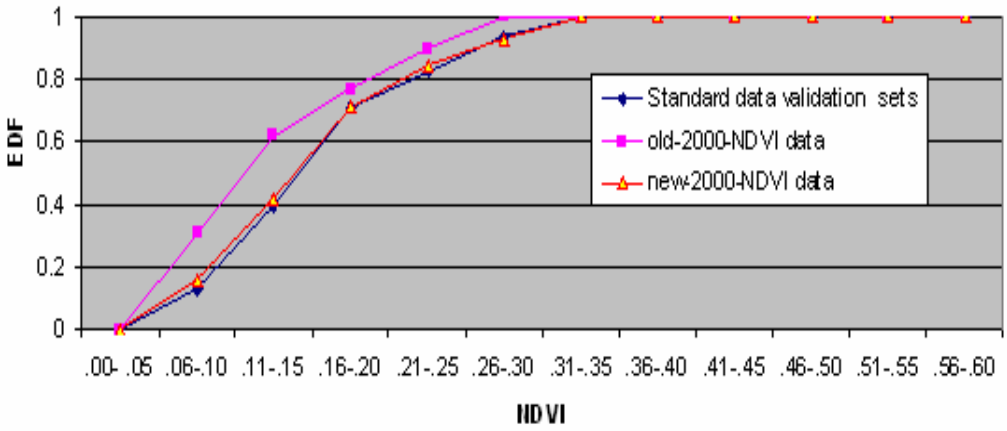

Figure 7.23 (b) Empirical distribution functions for normalized data of 2000 compared with standard data validation sets (subset 2).

Using normalized or corrected NDVI value, we produce new NDVI time series for Nepal, Bhutan, and India shown in Figure 7.24 which shows improvement of the NDVI data (pink line) of the year of 1988, 1992, 1993, 1994, and 2000

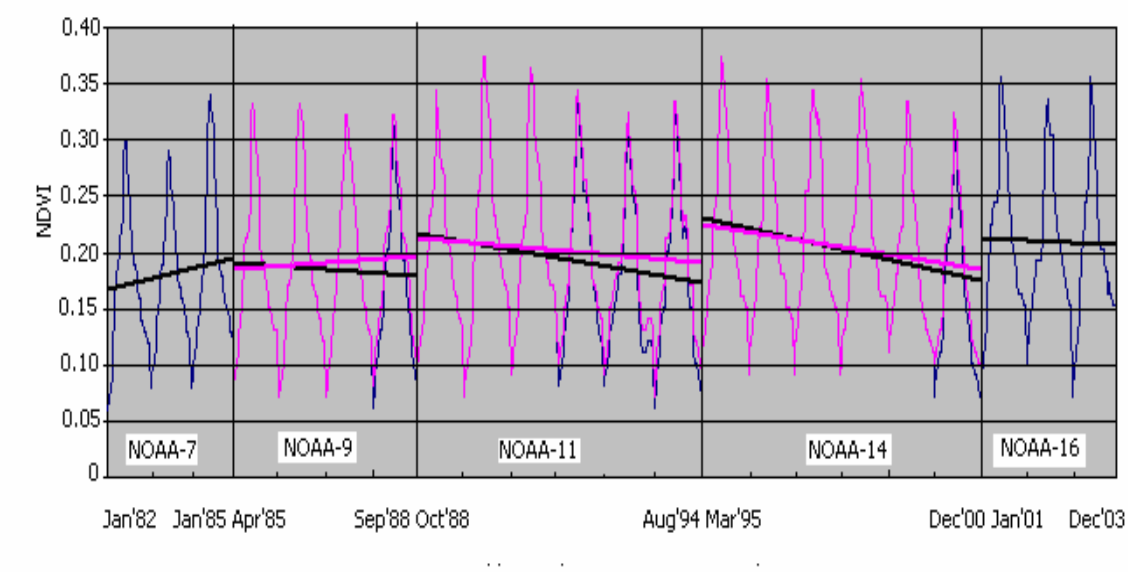

Figure 7.24. New NDVI time series (yearly) for study area in Nepal, Bhutan and India

(old NDVI, new NDVI)

Similarly, we can extract BT data from the original data set using equations 6.1 and 6.2. Then we can investigate BT data for validation compared to the original data set (Figure 6.53). BT fluctuates due to weather changes from year to year in each ecosystem. We assume for desert areas, the BT value will be greater than 310^0 K; for semi-desert (mixed) areas, the BT value will be between 295^0 K and 310^0 K; for grassland areas, the BT value will be between 275^0 K and 294^0 K; and for forest areas, the BT value will be less than 260^0 K as shown in Figure 6.78) because the BT will be higher mostly in dry and hot weather (desert) than in normal and wet weather (forest) [39]. To correct of BT data, we can apply the same methodology used to correct the BT data.

CHAPTER 8

CONCLUSIONS AND FUTURE RESEARCH

8.1 Conclusions

In this dissertation, the behavior of 22-year NOAA/NESDIS Global Vegetation Index (GVI) data are analyzed for improving the stability of the NDVI and BT. Degradation of NDVI and BT over time and shifts of NDVI and BT between the satellites was estimated China data set, for it includes a wide variety or different ecosystems represented globally. Data for the years 1988, 1992, 1993, 1994, 1995 (first eight weeks), and 2000 are not stable enough compared to other years due to satellite orbit drift, Mt Pinatubo volcanic eruption, AVHRR sensor degradation, and high sun elevation angle. The orbit drift of the NOAA series satellites, among other factors, has a significant effect on the magnitude of the energy signal measured by the satellite sensors, and consequently on the values of NDVI and BT.

To correct this error, we consider several possible techniques including empirical distribution functions, trend estimation method, typical patterns technique, weighted-least square method, solar zenith angle correction and calibration adjustments techniques. The analysis of available techniques compared to those of the most optimum EDF. To generate the normalized data, we begin by selecting samples of unnormalized earth-scene data covering as much of the range intensities as possible. For NOAA satellites, this selected area will be rectangular, extending several thousand pixels from desert to tropical forest (both east to west and north to south). Corresponding to the incoming radiance from any pixel, the instrument will respond with an output in digital counts. One can compile the discrete density function, i.e., the histogram, describing the relative

frequency of the occurrence of each possible count value, for each year. An empirical distribution function (EDF) can then be generated using the histogram which is also known as cumulative histogram of relative frequency. It is a non-decreasing function and its maximum value is unity. We produce EDF's for standard and affected years using the histogram analysis.

We assume data from NOAA-7(1982, 1983), NOAA-9 (1985, 1986), NOAA-11(1989, 1990), NOAA-14(1996, 1997), and NOAA-16 (2001, 2002) to be standard because theses satellite's equator crossing time falls between 1330 and 1500. Data from this particular period of the day maximized the value of coefficients. The crux of the proposed correction procedure consists of dividing standard year's data sets into two subsets. The subset 1(standard data correction sets) is used for correcting unstable years and then corrected data for this years compared with the standard data in the subset 2 (standard data validation sets). We test these EDF using data for the years 1988, 1992, 1993, 1994, 1995 and 2000, and compared with a standard data correction sets. We largely correct the NDVI and BT data effect due to orbit drift and sensor degradation, and thus produce temporally consistent NDVI and BT for a longer term time-series. We improved the NDVI and BT data over China and removed the drift effect by using the empirical distribution functions.

For validation purpose, we extract the NDVI data for parts of Mongolia, North Korea, Nepal, Bhutan, and India. Analysis of NDVI data for these various geographic areas produces similar results. This similarity of results shows that EDF is a robust method to correct the NDVI or BT data irrespective of geographic locations.

Based on our comparison with other methods for the normalization of AVHRR data in this research, EDF method is more accurate than the other methods. The main disadvantage of other methods is that they correct data for all years. But when using EDF Method, we do not need to correct data for the first two years for each satellite since the first two years produce data of good quality. In addition, EDF is an exact technique for satellite data normalization which depends on an adequate sample size for the approximations to be valid. Therefore, we use the EDF method to correct satellite data in this dissertation because normalized data are relatively closer to the standard data. Moreover, unlike other methods, we do not need to correct all year's data. These factors provide strong support to over contention that normalization by EDF is a more efficient method for removing the drift effect and sensor degradation.

Empirical distribution function (EDF) approach is based on the physical reality, that each ecosystem may be characterized by very specific statistical distribution, independent of the time of observation. EDF approach proposed here shows encouraging results which can be used globally to create vegetation index to improve the climatology. This method can also be derived from satellite observations such as GOES assuming the retrievals have proven quality. The correction of NDVI images (Figure 6.77 (b)) warrant additional comments. The AVHRR data are derived from seven-day composites using days when the maximum and minimum NDVI occurs. Therefore, the dataset containing the seven-day AVHRR data composites may itself be discrete. The line evident in the correction term seems to be more related to the standard (Figure 6.77(c)). This suggests that the dataset may still be useful in climate studies.

In most areas with vegetation, maximum NDVI and BT change by the end of satellite life is less compared to that for the desert. For climate and global change studies, NDVI and BT time series are not stable enough, specifically in desert and tropical forest areas. As both NDVI and BT data are distorted due to external forcing (e.g. stratospheric aerosols and satellite orbit degradation), NDVI and BT data for 1988 (NOAA-9), 1992, 1993, 1994 (NOAA-11), and 2000 (NOAA-14) may likely have distorted mean values and other statistics, and should be tested comprehensively before they are used for monitoring the environment.

Despite these advantages, EDF technique has several limitations: the EDF resolutions are limited by the available representative sample. For example, there are no data at the low and the high intensity ends. Our analysis shows that the EDF's of the normalized data for the years 1988, 1992, 1993, 1994, 1995, and 2000 compared with standard data validation sets. The largest differences occur when the EDF's of those years have steps, or flat spots. These are caused by the intensity levels with a zero frequency of occurrence in the histograms and are, therefore, an artifact of digitization or normalization. Perhaps the most serious limitation is that the distribution must be fully specified. That is, if location, scale, and shape parameters are estimated from the data, the critical region of the EDF technique is no longer valid. Typically it should be determined by simulation. In addition, EDF's are only applicable to continuous distribution.

EDF provide the best metric by approximating probabilistic distribution of the sample at hand. Error exists when EDF's of unnormalized year and the standard data validation years are not identical. As a quantitative measure of the error, we express the differences

in counts or percent, between the EDF of the standard and unnormalized years. Severity of the error was determined qualitatively from the AVHRR data and quantitatively with numerical measures of errors-- the empirical distribution functions themselves and count and percent difference among them.

8.2 Future Research

A strategy is proposed here to first generate and normalize the data using empirical distribution functions compared to standard and then to apply those normalized data to improve the NDVI and BT time series. Potential sources of error such as incomplete drift correction, inaccurate AVHRR data calibration, and influence from volcanic eruptions remain in NDVI and BT data even after applying the NDVI and BT correction. The empirical distribution functions are designed to reduce errors due to orbit drift, and dominant uncertainty in temperature variation during the satellite life time [50]. However, it may be difficult to accurately and completely remove these effects and, thus orbit remains as an error source, though at a reduced level. Another large uncertainty lies in AVHRR data calibration, which includes all errors introduced during the NDVI and BT calibration procedure, such as incomplete atmospheric corrections, sensor degradation, and change in solar zenith angle. Additionally, the lack of data for NOAA-11, due to the Mount Pinatubo aerosol contamination increases uncertainty. These issues can be further investigated in future research.

In future research, the corrected or normalized AVHRR data for a longer term series may be used to study climate change. For example, the maximum amount of vegetation (indicated by maximum value of NDVI) is developed in years with optimal weather because such weather stimulates efficient use of ecosystem resources (e.g., increase in the rate of soil nutrition uptake). Conversely, minimum vegetation (indicated by minimum NDVI data) develops in years with extremely unfavorable weather (mostly dry and hot) which suppresses vegetation growth directly and also through a reduction in the rate of ecosystem resources use. Therefore, the corrected maximum and minimum value of

NDVI and BT calculated from affected years of data that contain the extreme weather events (drought and nondrought years) can be used as criteria for estimating the favorable and unfavorable weather of the ecosystem resources.

Another potentially important application of the developed methodology is to apply it for correction and normalization of the GOES I-M satellite. Because the responses in the GOES I-M channels are expected to be linear and more nearly uniform compared to other satellites. Since the gains of the GOES I-M channels are expected to be more stable in time compared to other satellites, we would expect to normalized data from the EDF method to remain valid for even longer periods with GOES I-M [74].

PUBLICATIONS AND PRESENTATIONS

1. Md Z. Rahman, Leonid Roytman, and Felix Kogan**, "**Improving stability of NDVI data for NOAA environmental satellite," Proc. SPIE **Vol. 6412**, Paper No. 641217, December 2006

2. Md Z. Rahman, Leonid Roytman, and Felix Kogan, "Improving stability of NDVI data for NOAA environmental satellite," Oral Presentations, Fifth International Conference on Asia –Pacific Remote Sensing, Goa, India, November 2006

3. Md Z. Rahman, Leonid Roytman, and Felix Kogan, "Removing long-term errors from the AVHRR observations –based on NDVI**,"** Poster Presentation, Fourth conference on NOAA Educational Partnership Program, Florida A &M University, Tallahassee, Florida, October 2006.

4. Md Z. Rahman, Leonid Roytman, and Felix Kogan "Error correction of NDVI time series for NOAA environmental satellite," NOAA-CREST Day Conference, CCNY, New York, USA, October 2004

BIBLIOGRAPHY

[1] **A**nyamba, **A**., and **J.R E**astman, **I**nterannual variability of NDVI over Africa and its relation to EI Nino /Southern Oscillation, International Journal of Remote Sensing, **17**, 2533-2548, 1996

[2] **B**rest, **C. L**., and **W. B**. **R**ossow, **R**adiometric calibration and monitoring of NOAA AVHRR data for ISCCP, , International Journal of Remote Sensing, **13,** 235-273, 1992

[3] **B**ristor, **C. L**. (Ed.) (1975), **C**entral processing and analysis of geostationary satellite data, NOAA Tech. Mem. NESS **64**, National Oceanic and Atmospheric Administration, National Environmental Satellite Service, Washington, DC, 155 pp

[4] **B**rown, **S.A., M. F**olk, G. **G**oucher and **R**. **R**ew, Software for portable scientific data management. Computers in Physics, **7**:304-308, 1993.

[5] **B**rown, **O.W., B**rown, **J.W**. and **R.H**. **E**vans, Calibration of Advanced Very High Resolution Radiometer observations. Journal of Geophysical Research, **90**:11667-11677, 1985.

[6] **B**ocoum , **O**. Calibrage des canaux 1 & 2 de NOAA-AVHRR pour une comparison annuelle des donnes NDVI proceedings of 5th AVHRR data User's Meeting, Troms, Norway, 25-28 June 1991. EUM P 09 (Darmstadi- Eberstadt: EUMETSAT), pp. 35-40.

[7] **C**abot, **F**., and **G**. **D**edieu, Surface albedo from space: **C**oupling bidirectional models and remotely sensed measurements, Journal of Geophysical Research, **102, 19**,645-19,663, 1997.

[8] **C**ihlar, **J., J. M**. **C**hen, **Z. Li, F**. **H**uang. **R**. **L**atifovic, and **R**. **D**ixon , **C**an international land surface signal be discerned in composite AVHRR data, Journal of Geophysical Research, **103**, **23,** 163-23, 172, 1998.

[9] **D**i, **L**., and **D. A**. **H**astings, **T**emporal stability of some global NDVI products derived from NOAA/AVHRR GVI, , International Journal of Remote Sensing, **16,** 3569-3583, 1995.

[10] **D**esormeaux, **Y., W. B.** Rossow, **C. L. B**rest, and **G. G. C**ampbell, 1993: Normalization and calibration of geostationary satellite radiances for ISCCP. Journal of Atmospheric Oceanic Technology, **10,** 304–325.

[11] **F**leig, **A. J., D. F**. **H**eath, **K. F**. **K**lenk, **N**. **O**slik, K**. D**. Lee, **H**. Park, **P. K**. Bartia, and **D. G**ordon. 1983. User's Guide for the Solar Backscattered Ultraviolet (SBUV) and the Total Ozone Mapping Spectrometer (TOMS) RUT-S and RUT-T Data Sets: October 31, 1978 to November 1980. NASA Reference Publication **1112**.

[12] **F**etterer, **F. M.,** and **J. D**. **H**awkins. 1991. An AVHRR data set for the arctic leads ARI. Naval Oceanographic and Atmospheric Research Laboratory, Technical Note **118**, 61 p.

[13] **F**etterer, **F. M.,** and **J. H**awkins. 1993**.** Data set of arctic AVHRR imagery for the study of leads. Annals of Glaciology **17**:394-404.

[14] **G**ordon, **H.R**., **J.W. B**rown, and **R.H. E**vans, 1988. Exact Rayleigh scattering calculations for use with the Nimbus-7 coastal zone color scanner. Applied Optics **27**:2111-2122.

[15] **G**orman, **A. J**., and **J**. **M**acGregor, **S**ome considerations for using AVHRR data in climatological studies, 1, AVHRR instrument performance, International Journal of Remote Sensing, **15**, 549-565, 1994.

[16] **G**oward, **S. N**. **S**atellite bioclimatology, Journal of Climate **7**:710-720, 1989

[17] **G**oward, **S. N., B**. **M**arkham, **D. G**. **D**ye, **W**. **D**ulaney, and **J**. **Y**ang, **N**ormalized difference vegetation index measurements from the AVHRR, Remote Sensing of Environment, **35**, 257-277, 1991

[18] **G**oward, **S.N., D.G. D**ye, S. **T**urner, and **J. Y**ang, **O**bjective assessment of the NOAA global vegetation index data product. International Journal of Remote Sensing **14**:3365P3394, 1993

[19] **G**oward, **S. N., S**.**T**urner and **D.G**. **D**ye, The university of Maryland improved global vegetaion index product. International Journal of Remote Sensing (in press), 1994

[20] **G**utman, **G**. On the use of land surface temperatures with the NOAA/AVHRR: removing the effect of satellite orbit drift. , International Journal of Remote Sensing, **20**, 3407-3413, 1999

[21] **G**utman, **G**., and **A**. **I**gnatov, **G**lobal land monitoring from AVHRR: Potential an d limitations, International Journal of Remote Sensing, **16**, 2301-2309, 1995.

[22] **G**utman, **G**., **D**. **T**arpley, **A**., **A**. **I**gnatov, and **S**. **O**lson, **T**he enhanced NOAA global land data set from the AVHRR, **B**ulettin of **A**merican **M**eteorological **S**ociety, **76**, 1141-1156, 1995

[23] **G**utman, **G**. **G**arik, **O**n the use of long-term global data of land reflactances and vegetation indices derived from the AVHRR, Journal of Geophysical Research, 1**04**, 6, 6241-6255, 1999.

[24] **H**astings, **D. A.,** and **W. J**. **E**mery, The advanced very high resolution radiometer (AVHRR): a brief reference guide. Photogrammetric Engineering & Remote Sensing **58(8):**1183-1188, 1992

[25] **H**olben **B**N (1986) **C**haracteristics of maximum-value composite images from temporal AVHRR data, , International Journal of Remote Sensing, **7,** 1417-1434, 1986.

[26] **H**orn, **B.K. P**. and **W**oodham, R.J., **D**estriping LANDSAT MSS images by histogram modification, Computer Graphics and Image processing **10**: 69-83, 1979.

[27] **J**ackson, **R.D**., **P.N**. **S**later, and **P.J**. **P**inter, Discrimination of growth and water stress in wheat by various vegetation indices through clear and turbid atmospheres. Remote Sensing of the Environment, **15**:187-208, 1983.

[28] **J**ames, **M.E.** and **S.N.V K**alluri, The Pathfinder AVHRR land data set: An improved coarse resolution data set for terrestrial monitoring. International Journal of Remote Sensing, (in press)., 1994.

[29] **J**ustice, **C.O., B.L**. **M**arkham**, J.R.G. T**ownshend, and **R.L. K**ennard, 1989, Spatial degradation of satellite data. International Journal of Remote Sensing, **10**:1539-1561, 1989.

[30] **J**in, **M**englin, **R. E**. **T**rendon., Correcting the orbit drift effect on AVHRR land surface skin temperature measurements, , International Journal of Remote Sensing **23,** 4543-4558, 2003.

[31] **J**in, M,. and **D**ickerson, **R. E** Interpolation of surface radiative temperature measured from polar orbiting satellite to a diurnal cycle. Part 1, without clouds. Journal of Geophysical Research, **104,** 2105-2116, 1999.

[32] **K**idwell, **K. B.,** *NOAA* Polar Orbiter Data Users Guide. U.S. Department of Commerce. National Oceanic and Atmospheric Administration, Satellite Data Services Division, Washington, D.C., 1991.

[33] **K**idwell, **K. B.** NOAA Polar Orbiter Data Users Guide: NOAA Polar Orbital Environmental Satellites (POES). U.S. Department of Commerce. National Oceanic and Atmospheric Administration, Satellite Data Services Division, Washington, D.C. 1995.

[34] **K**idwell, K., **G**lobal **V**egetation **U**ser's **G**uide, NOAA, **N**atl. **E**nviron. **S**atellite **D**ata and **I**nf. **S**erv. Natl. Clim. Data Cent., Dep. Of **C**ommer., Washington, D. C., 1997.

[35] **K**ogan, **F.N., R**emote sensing of weather impacts on vegetation in non-homogeneous area. , International Journal of Remote Sensing, **11,** 1405-1419, 1990

[36] **K**ogan, **F.N., D**raught of the late 1980s in the United States as derived from NOAA polar orbiting satellite data. **B**ulettin of **A**merican **M**eteorological **S**ociety*,* **76**, 655-668, 1995

[37] **K**ogan, **F.N., G**lobal draught watch from space, **B**ulettin of **A**merican Meteorological Society*,* **78**, 621-636, 1997.

[38] **K**ogan, **F.N., A** typical pattern of vegetation conditions in southern Africa during EI Nino years detected from AVHRR data using three-channel numerical index. , International Journal of Remote Sensing , **18,** 3689-3695, 1998.

[39] **K**ogan, **F.N., G**lobal Drought Detection and Impact Assessment from space in Drought: A Global Assessment Ed. By D.A Wilhite, vol.1, Hazard and Disaster Series, pp. 196-210, Routledge, London-New York, 2000.

[40] **K**ogan, **F.N**., and **X. Z**hu, **E**volution of long-term errors in NDVI time series, Adv. Space Res. Vol. **28**, No 1, pp. 149-153, 2001.

[41] **L**oeb, **N. G., I**n-flight calibration of NOAA AVHRR visible and near-IR bands over Greenland And Antarctica, , International Journal of Remote Sensing, **18,** 477-490, 1997.

[42] **L**os, **S. O., C**alibration adjustment of the NOAA AVHRR normalized difference vegetation index without recourse to component channels, International Journal of Remote Sensing, 14**,** 1907-1917, 1993.

[43] **M**acGregor, **J**., and **A. J**. **G**orman, **S**ome considerations for using AVHRR data in climatological studies, 1, AVHRR instrument performance, International Journal of Remote Sensing, **15**, 549-565, 1994.

[44] **M.P**. **W**einreb, **R.X**ie, **J.H**. **L**ienesch, and **D.S C**rosby; **R**emoving Stripes in GOES Images by Matching Empirical Distribution Functions, NOAA Technical Memorandum NESDIS **26**, Washington, D.C, May 1989

[45] METEO- France, French Research in Meteorology, 2006

[46] (Nasa Earth Observatory Web Reference [1])
http://earthobservatory.nasa.gov/Library/MeasuringVegetation/measuring_vegetation_2.html

[47] NOAA KLM USER'S GUIDE, , National Oceanic and Atmospheric Administration/ National Environmental Satellite, Data, and Information Service, September 2006, Section 3.1.

[48] **P**rice, **J. C., C**alibration of satellite radiometers and the comparison of vegetation indices. Remote Sensing of Environment**, 21**, 15-27, 1987a

[49] **P**rice, **J. C.,R**adiometric calibration of satellite sensors in the visible and near infrared: history and outlook, Remote Sensing of Environment**, 22**, 3-9, 1987b

[50] **P**rice, **J. C., T**iming of NOAA afternoon passes, International Journal of Remote Sensing,**12**, 193-198, 1991.

[51] **P**rince, **S. D**., and **S. N**. **G**oward, **E**valuation of the NOAA/NASA Pathfinder AVHRR Land data set for global primary production modeling, International Journal of Remote Sensing, **17,** 217-221, 1996.

[52] **P**rivette, J. L., Fowler, C., Wick, G. A., Baldwin, D., and Emery, W. J., Effects of orbital drift on AVHRR products: Normalized difference vegetation index and sea surface temperature. Remote Sensing of Environment, **53**, 164-171, 1995

[53] **P. C**racknell, **T**he Advanced Very High Resolution Radiometer, Taylor & Francis, page 90-97, 1997

[54] **R**ao, **C.R.N**. and **J.C**hen, Nonlinearity corrections for the thermal infrared channels of the Advanced Very High Resolution Radiometer: assessment and recommendations. NOAA Technical Report NESDIS 69 (Washington DC: US Department of Commerce, 1993a

[55] **R**ao, **C.R.N**. , **D**egradation of the visible and near infrared channels of the Advanced Very High Resolution Radiometer on the NOAA –9 spacecraft: assessment and recommendations for corrections. NOAA Technical Report NESDIS 70 (Washington DC: US Department of Commerce). 1993b

[56] **R**ao, **C.R.N.** and **J.C**hen, Post-launch calibration of the visible and near-infrared channels of the Advanced Very High Resolution Radiometer on NOAA-7, -9, and -11 spacecraft. NOAA Technical Report NESDIS 78 (Washington, DC: US Department of Commerce). 1994

[57] **R**ao, **C.R.N.** and **J.C**hen, **I**nter-satellite Calibration Linkages for the Visible and Near-infrared Channels of the Advanced Very High Resolution Rdiometer on the NOAA –7, -9, and –11 Spacecrafts, , International Journal of Remote Sensing, **16**, 1931-1942, 1995.

[58] **R**ao, **C.R.N.** and **J.C**hen, Postlaunch calibration of the visible and near-infrared channels of the advanced very high resolution radiometer on the NOAA 14 spacecraft, 1**,** , International Journal of Remote Sensing, **7**, 2743-2747, 1996.

[59] **R**ao, **C.R.N**. and **J.C**hen, **R**evised post-launch Calibration of the visible and Near-infrared Channels of the Advanced Very High Resolution Radiometer on the NOAA-14 Spacecraft, , International Journal of Remote Sensing, **20**, 3485-3491, 1999

[60] **R**ouse, **J. W., R. H.** Haas, **J. A.** Schell and **D.W. D**eering, 1974. Monitoring Vegetation Systems in the Great Plains with ERTS.

[61] **R**ossow, **W. B.,** and **R. A. S**chiffer, ISCCP could data products, **B**ulettin of **A**merican **M**eteorological **S**ociety, **72,** 2-20,1991.

[62] **R**oderic, M., Smith, R., and Lodwick, G., Calibrating long-term AVHRR-derived NDVI omagery, Remote Sensing of Environment**, 58,** 1-12, 1996

[63] **S**towe, **L.L., E.P. M**cClain, R. **C**arey, **P**. Pellegrino, G. G. **G**utman, P. **D**avis, **C**. **L**ong, and **S**. **H**art, Global distribution of cloud cover derived from NOAA/AVHRR operational satellite data. Advances in Space Research, **3**:51-54., 1991.

[64] **S**teyn-**R**oss, **D.A., M.** L. **S**teyn-**R**oss, and **S**. **C**lift, Radiance calibrations for Advanced Very High Resolution Radiometer infrared channels. Journal of Geophysical Research, **97**:5551-55568, 1992.

[65] **S. L**iang., land cover classification methods for multi-year AVHRR data, International Journal Remote Sensing, 2001, **22**, 1479-1493

[66] **S**chiffer, **R. A.,** and **W. B**. **R**ossow, 1983: ISCCP global radiance data set: A new resource for climate research. **B**ulettin of **A**merican **M**eteorological **S**ociety, **66,** 1498–1505.

[67] **T**anre, **D. B.N. H**olben, and **Y**. **K**aufman, Atmospheric Correction Algorithm for NOAA-AVHRR Products: Theory and Application. IEEE Transactions on Geoscience and Remote Sensing, **30**:231-248., 1992.

[68] **T**ucker, **C.J**. **R**ed and photographic infrared linear combinations for monitoring vegetation, Remote Sensing of the Environment **8,** 127-150, 1979.

[69] **T**ucker, **C. J. M**aximum normalized difference vegetation index images for Sub-Saharan Africa for 1983 to 1985**,** International Journal of Remote Sensing, **7,** 1383-1384, 1986.

[70] **T**ucker, **C. J., W. W. N**ewcomb, S. O. Los, and S. D. Prince, Mean and inter-year variation of growing-season normalized difference vegetation index for the Sahel 1981-1989. International Journal of Remote Sensing, **12**:1113-1115., 1991.

[71] **T**arpley, **D**. Extraction of climate parameters from operational polar orbiting spacecraft. Proceeding of 6th AVHRR Data User's Meeting, Belgirate, Italy, 29 July 1993. EUM p 12 (Darmstadi-Eberstadi: EUMETSAT), pp. 3-8.

[72] **V**iovy, **N., O**. **A**rino, and **A. S. B**elward, The best index slope extraction (BISE): A method for reducing noise in NDVI time series, International Journal of Remote Sensing, **13,** 1585-1590, 1992

[73] **W**einreb, **M.P., G**. **H**amilton, **S**. **B**rown, and **R.J**. **K**oczor, Nonlinearity corrections in calibration of Advanced Very High Resolution Radiometer infrared channels, Journal of Geophysical Research, **95**:7381-7388, 1990.

[74] **W**einreb, **M.P**, RXie, J.H.Lienesch, D.S Crosby . Removing stripes in GOES images by Matching Empirical Distribution Functions, NOAA Technical Memorandum NESDIS 26, May 1989

[75] **W**eatherhead, **E.C., et al**., Factors affecting the detection of trends: Statistical considerations and applications to environmental data. Journal of Geophysical Research, **103,** 17,149-17,161, 1998

[76] **W**hitlock C. H., and **C**oauthors, 1990: AVHRR and VISSR satellite instrument calibration results for both cirrus and marine stratocumulus IFO periods. FIRE Science Rep. 1988, NASA CP-3083, 450 pp. [Available from NASA Center for Aerospace, Information, 800 Elkridge Landing Rd., Linthicum, MD 21090.]

[77] NOAA/NASA AVHRR Pathfinder land Data User's Mannual 3.1, September 1994

[78] **W**. **B R**ossow, **B**rest, **C. L**., and **M. D R**oiter, Update of radiance calibrations for ISCCp, J. Atmos. Oceanic Technol., **14**, 1091-1109, 1997